STRETCHING DIRECTIONS IN CISLUNAR SPACE: STATIONKEEPING AND AN APPLICATION TO TRANSFER TRAJECTORY DESIGN

by

Vivek Muralidharan

A Dissertation

Submitted to the Faculty of Purdue University

In Partial Fulfillment of the Requirements for the degree of

Doctor of Philosophy

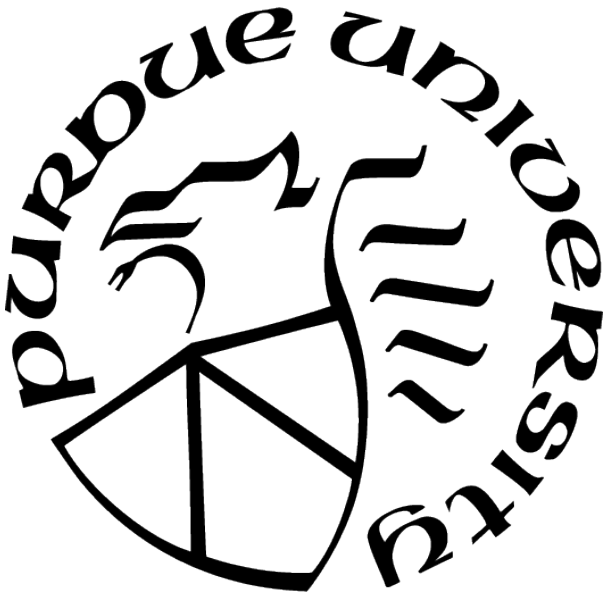

School of Aeronautics and Astronautics

West Lafayette, Indiana

August 2021

THE PURDUE UNIVERSITY GRADUATE SCHOOL
STATEMENT OF COMMITTEE APPROVAL

Dr. Kathleen C. Howell, Chair

School of Aeronautics and Astronautics

Dr. David A. Spencer

School of Aeronautics and Astronautics

Dr. Carolin E. Frueh

School of Aeronautics and Astronautics

Dr. Davide Guzzetti

Department of Aerospace Engineering, Auburn University

Approved by:

Dr. Gregory A. Blaisdell

ACKNOWLEDGMENTS

Firstly, I express my profound gratitude to my adviser and mentor, Professor Kathleen Howell, for providing me endless opportunities to learn and evolve. I greatly appreciate your constant guidance and feedback on my research and your time and effort in editing my writings. Your advice has always been invaluable, both personally and professionally.

Sincere thanks to my committee members, Professor David A. Spencer, Professor Carolin Frueh and Professor Davide Guzzetti, for reviewing my research documents and offering me constructive advice and feedback. Professor Guzzetti, you have been an approachable instructor. I was fortunate to learn the fundamentals of Astrodynamics while you were teaching.

All the members of the Multi-Body Dynamics research group, both past, and present, have been excellent technical support and great friends. Special thanks to Bonnie, you are a wonderful friend and great support. I also want to particularly acknowledge Anish, Beom, David, Emily, Fouad, Juan, Kenza, Nadia, Chris, and Ted. Sincere thanks to the School of Aeronautics and Astronautics at Purdue University, and the staff. I appreciate the facility at the Rune and Barbara Eliasen Visualization Laboratory.

I am grateful to the Purdue University Minority Engineering Program (MEP) for supporting me with a Graduate Assistantship to continue my doctoral studies at Purdue. Ms. Virginia Booth Womack and Dr. Darryl Dickerson, thank you for trusting me. The entire MEP staff, including Dr. Jacqueline Gatson, Ms. Mary Kenner, Mr. Derrick Williams-Bacon, Ms. Heather Coar, Dr. Carol Stwalley, Ms. Tamara Markey, Ms. Himani Shah, Mr. Richard Womack, Bonnie Prado Pino, Tasha Zepherin, and Kenneth Idem, you all have been extremely humble and approachable. I cherish the time spent with you all.

I sincerely thank Dr. Uroš Kalabić for providing me with an opportunity to intern at Mitsubishi Electric Research Laboratories (MERL) during my doctoral studies. Dr. Avishai Weiss and other MERL scientists and staff have been great resources.

Special mention to Anjaly, you were more than just a friend to me. Thank you for being there during different stages of my life, and imparting some knowledge in chemistry and life science beyond engineering.

I want to thank my parents for their unconditional support. I appreciate my brother, Varun, for showing confidence in me. Nileena, how our paths crossed is a lucky accident, 'serendipity' as you say. I want to thank you for the support you offer and for alleviating me during challenging times. Finally, gratitude to all my extended family members, friends, and well-wishers.

TABLE OF CONTENTS

LIST OF TABLES

LIST OF FIGURES

ABSTRACT

The orbits of interest for potential missions are stable or nearly stable to maintain long term presence for conducting scientific studies and to reduce the possibility of rapid departure. Near Rectilinear Halo Orbits (NRHOs) offer such stable or nearly stable orbits that are defined as part of the L1 and L2 halo orbit families in the circular restricted three-body problem. Within the Earth-Moon regime, the L1 and L2 NRHOs are proposed as long horizon trajectories for cislunar exploration missions, including NASA's upcoming Gateway mission. These stable or nearly stable orbits do not possess well-distinguished unstable and stable manifold structures. As a consequence, existing tools for stationkeeping and transfer trajectory design that exploit such underlying manifold structures are not reliable for orbits that are linearly stable. The current investigation focuses on leveraging stretching direction as an alternative for visualizing the flow of perturbations in the neighborhood of a reference trajectory. The information supplemented by the stretching directions are utilized to investigate the impact of maneuvers for two contrasting applications; the stationkeeping problem, where the goal is to maintain a spacecraft near a reference trajectory for a long period of time, and the transfer trajectory design application, where rapid departure and/or insertion is of concern.

Particularly, for the stationkeeping problem, a spacecraft incurs continuous deviations due to unmodeled forces and orbit determination errors in the complex multi-body dynamical regime. The flow dynamics in the region, using stretching directions, are utilized to identify appropriate maneuver and target locations to support a long lasting presence for the spacecraft near the desired path. The investigation reflects the impact of various factors on maneuver cost and boundedness. For orbits that are particularly sensitive to epoch time and possess distinct characteristics in the higher-fidelity ephemeris model compared to their CR3BP counterpart, an additional feedback control is applied for appropriate phasing. The effect of constraining maneuvers in a particular direction is also investigated for the 9:2 synodic resonant southern L2 NRHO, the current baseline for the Gateway mission. The

stationkeeping strategy is applied to a range of L1 and L2 NRHOs, and validated in the higher-fidelity ephemeris model.

For missions with potential human presence, a rapid transfer between orbits of interest is a priority. The magnitude of the state variations along the maximum stretching direction is expected to grow rapidly and, therefore, offers information to depart from the orbit. Similarly, the maximum stretching in reverse time, enables arrival with a minimal maneuver magnitude. The impact of maneuvers in such sensitive directions is investigated. Further, enabling transfer design options to connect between two stable orbits. The transfer design strategy developed in this investigation is not restricted to a particular orbit but applicable to a broad range of stable and nearly stable orbits in the cislunar space, including the Distant Retrograde Orbit (DROs) and the Lunar Orbits (LO) that are considered for potential missions. Examples for transfers linking a southern and a northern NRHO, a southern NRHO to a planar DRO, and a southern NRHO to a planar LO are demonstrated.

1. INTRODUCTION

In pursuit for scientific discoveries and a broader understanding of the universe, space missions are expanding beyond the geocentric space. As a result of expanding technology, humans are gaining confidence in venturing into deep space with both crewed and robotic missions. A wide variety of destinations are sought in support of ever-expanding and increasingly complex goals. A much wider range of solutions beyond the Keplerian motion are leveraged using multi-body dynamical environments in support for space exploration. In recent times, Lunar missions that exploit such complex multi-body dynamics continue to generate serious interest among various space organizations across the globe. Moreover, with increasing research activities in the field of space physics, the investigation of the celestial body nearest to the Earth, i.e., the Moon, offers significant potential for scientific discoveries. In addition, with a focus on expanding the human presence in the region, NASA's Gateway mission, formerly the Deep Space Gateway (DSG) or Lunar Orbital Platform-Gateway (LOP-G) mission, delivers a hub-like facility that is currently planned to move along a Near Rectilinear Halo Orbit (NRHO) in the lunar vicinity [1], [2]. Near rectilinear halo orbits are members of the halo orbit family in the L1 and L2 (equilibrium points) regions in the Earth-Moon circular restricted three-body problem [3], [4]. A cost-efficient stationkeeping strategy as well as the ability to transfer from one orbit to another relatively quickly is of high priority.

1.1 Objective

Motion along an NRHO is characterized by a reasonably close lunar passage and a large out-of-plane amplitude relative to the Earth-Moon orbit plane, appropriate for investigating the polar regions of the Moon. In addition, spacecraft along some NRHOs offer a nearly uninterrupted link for relay communications to various landing sites for planned lunar landing missions [5], [6]. The NRHOs are stable or nearly stable as characterized by the linear variational flow. Due in part to these stability characteristics, NRHOs offer candidate orbits suitable for any long-term cislunar operations. Some of the dynamical structures such as the unstable and stable manifolds are either non-existent or not well-defined for the stable or

nearly stable orbits [7]. As a consequence, various strategies that rely on the unstable and stable manifold structures for long-term orbit maintenance, or insertion or departure from the orbit provide diminishing results.

The overarching goal of this investigation is exploring the underlying multi-body dynamics to leverage structures that are useful for two contrasting applications, especially for stable or nearly stable orbits. The stationkeeping problem requires maintaining a spacecraft near a reference orbit for a significantly long duration. In contrast, a transfer trajectory design problem relies on rapid insertion and departure from a reference orbit. The research objectives are met through the following:

1. Understand the flow dynamics in the vicinity of a reference solution that lack well-defined unstable and stable manifold structures.

   Ability to visualize the impact of a state change at an initial time, over some propagated time downstream, offers insight into the underlying motion in the neighborhood of a reference trajectory. Certain directions are more sensitive to state changes compared to the others. Reliable and unsophisticated mathematical tools must be developed to identify such sensitive directions. A prior information about the sensitivity of the dynamical flow assists in developing strategies for stationkeeping and transfer trajectory design.

2. Effect of underlying dynamics near a reference trajectory for stationkeeping and transfer design applications.

   - Stationkeeping Process

     A stationkeeping process is designed to overcome any navigational errors and unmodeled perturbations, thereby ensuring that the spacecraft remains bounded in the vicinity of a reference orbit for a long duration, and in a cost-effective way. The understanding of the flow in the neighborhood of a reference solution is crucial to study the influence of various parameters within the stationkeeping process. This investigation examines a current strategy from the context

of the dynamical foundations and structures that enable the strategy to generally succeed. Furthermore, a systematic and straightforward approach to select parameters suitable for impulsive stationkeeping is explored.

- Transfer Trajectory Design

  Perturbations near a stable orbit does not amplify rapidly. However, for transfer trajectory design applications, a trajectory in the neighborhood that departs relatively quickly, and also arrives swiftly, are desired. This investigation explores the sensitive directions in the neighborhood of a reference orbit that are then exploited to design transfers between stable orbits in the cislunar regime.

3. Application for various stable orbits.

   Stationkeeping and transfer trajectory design applications exploit certain sensitive directions in the neighborhood of a stable reference orbit. The current investigation examines the stationkeeping strategy for a range of stable and nearly stable halo orbits in the L1 and L2 regions within the Earth-Moon system. Moreover, the transfer trajectory design methodology offers an infrastructure to transfer between a number of stable orbits, both planar and three-dimensional.

The substantiation of these objectives yield reliable scheme that enhances the stationkeeping and transfer design process. The approaches illustrated in this investigation offers promising results that can be expanded for a wide range of orbits in the multi-body regime.

1.2 Previous Contributions

1.2.1 Multibody Dynamics

A simplified two-body planetary motion was postulated by Johannes Kepler (1571 - 1630) as three laws, also known as Kepler's laws of planetary motion, that enhanced the heliocentric theory given by Nicolaus Copernicus [8], [9]. Later, in 1687, Sir Isaac Newton (1642 - 1727) formulated the Universal Laws of Gravitation in *PhilosophiæNaturalis Principia Mathematica* [10] that explained Kepler's laws. Although a very simplified model, the two-body problem, in general, is a good approximation of the planetary motion in the helio-

centric space. Since there are numerous bodies in space, each applying a mutual gravitational force on the others, a model with a central gravitational body, such as the Sun, is perhaps not sufficient to explain the complex dynamics of space. Leonhard Euler (1707 - 1783) in 1767 formulated a simple restricted three-body problem [11], that was more comprehensive than the two-body problem and overcame some of the challenges of the two-body problem. The existence of equilibrium points in the nonlinear dynamical regime of Euler's three-body problem was derived by Joseph-Louis Lagrange (1736 - 1813) in 1772 [12]. A number of astronomers and mathematicians improved the existing models. Carl Gustav Jacob Jacobi (1804 - 1851) computed the integral of motion in CR3BP, that is now known as Jacobi Constant or Jacobi integrals [13]. Jules Henri Poincaré (1854 - 1912) formulated a visualization technique to represent different dynamical behavior of the trajectories as noted by saddle, focus, center or nodes, using maps in 1899 [14], now identified as Poincaré maps. In 1967, Victor Szebehely's *Theory of Orbits* [15] summarizes the advancements in the circular restricted three-body problem and validates theories with appropriate numerical results.

The nonlinear dynamics of the circular restricted three-body problem (CR3BP) offers different dynamical structures suitable for space missions. Farquhar in 1968, described a 3-dimensional halo orbit that exists close to the collinear equilibrium points in the Sun-Earth system [16]. Such an orbit served as the baseline for the first libration point mission, the ISEE-3 mission, in 1978. Later in 1973, Farquhar and Kamel, calcluated analytical solutions to represent quasi-periodic motion along an orbit using Lindstedt-Poincaré approach [17]. Richardson offered an analytical solution to represent halo orbits for ISEE-3 mission in 1980 [18]. Howell in 1984 developed a numerical computation technique for precise halo orbit construction [19]. Howell and Pernicka formulated numerical techniques to determine Lissajous trajectory in CR3BP [20]. Following the success of ISEE missions [21] and further development of the multi-body dynamical regimes and advancement in technology more librations missions have been launched. The WIND mission in 1994, the Solar Heliospheric Observatory (SOHO) in 1995 and the Advanced Composition Explorer (ACE) in 1997 [22] have supported helio-physics research while positioned at the Sun-Earth L1 halo orbits. Furthermore, the Genesis spacecraft [23] and the Wilkinson Microwave Anisotropy Probe

(WMAP) [24] have explored the Sun-Earth L1 and L2 Lagrange point orbits, respectively. In recent times, with evolving computational techniques, Pavlak describes a method for generating long baseline solutions in complex space using multiple shooting technique [25]. With the launch in 2007, the ARTEMIS P1 and P2 (formerly THEMIS) [26] became the earliest probes to explore the Lagrange point orbits in the Earth-Moon system. The proposed NASA Gateway mission is planned to operate in a stable orbit in the cislunar space [1], [2].

1.2.2 Orbit Maintenance Strategies

A number of stationkeeping strategies have been developed in support of various libration point missions in the past. One of the early stationkeeping operations for the ISEE-3 mission are discussed by Farquhar et al. [21], [27]. Other studies on ISEE-3 are found in [28]–[32]. Rodriguez and Hechler [33] offers insight on SOHO mission design and control while Sharer et al. offer design and control strategies for the WIND Trajectory [34]. Other stationkeeping studies in the Sun-Earth system is found in [35]–[37]. Some of the early orbit maintenance strategies in the Earth-Moon system are discussed by Breakwell et al. [38], [39], Colombo [40], as well as Euler and Yu [41]. Recent investigations on the orbit maintenance strategies for the ARTEMIS mission were conducted by Folta et al. [42]–[44] as well as Howell and Pavlak [45].

Many of the libration point missions in the past have explored unstable halo orbits as baseline. As a consequence, a number of stationkeeping strategies exploit the dynamical structures near the unstable orbits. Howell and Pernicka [30], [31], Howell and Gordon [46], [47], [48], [49] as well as Muralidharan [50] have worked on Target Point Approach that are proven to be effective along unstable orbits in the Sun-Earth L1 and L2 region. Existing stationkeeping strategies that are based on manifold theory, for example, Floquet mode approaches used by a number of authors produce a maneuver to nullify any unstable components of the perturbations. Gomez et al. [51], [52], Howell and Keeter [53], Simo et al. [54], [55], Howell and Pavlak [45], Meng et al. [56], and Muralidharan [50] have used Floquet mode approach for various applications. Without reliable numerical computation of manifolds, such an approach cannot generally be leveraged for stationkeeping in support of

activities in stable or nearly stable orbits. An alternate strategy, one that is based on the near symmetry of the orbits in the CR3BP system, is widely employed for stationkeeping in the halo orbit region, including the stable NRHOs [4], [57]–[60]. The alternate technique is commonly identified as an x-axis crossing control strategy and is proven to be effective in low-cost stationkeeping for orbits that lack well-distinguished stable and unstable manifolds.

Other strategies that are applicable for stable orbits are analyzed by Guzzetti et al. [4] and Muralidharan [50] using the Cauchy-Green tensor approach. Variants of Linear Quadratic Regulator and Model Predictive Control techniques are offered by various authors [61]–[63] A summary of few orbit maintenance techniques for libration point orbits has been provided by Shirobokov et al. [64].

1.2.3 Transfer Trajectory Design

Transfer design applications involving unstable orbits has leveraged the underlying manifold structures to assist in departure and arrival on the orbits, along an almost ballistic trajectory [65]–[69]. With the lack of usable manifold structures, transfer to orbits that are stable have been addressed by alternate strategies, both with low-thrust and impulsive maneuvers. Parish et al. demonstrate low-thrust transfers between Distant Retrograde Orbits (DROs) and the halo orbits in the Earth-Moon system [70]. Pritchett et al. use collocation algorithm for low thrust transfers [71]. Pino et al. use energy surfaces to identify intermediate orbits to transition between two orbits with low-thrust engines [72]. Das et al. illustrate trajectory design techniques using reinforcement learning [73]. McCarty et al. leverage a low-thrust transfers from NRHO to DRO [74]. Many transfer options between stable orbits using one or more impulsive maneuvers have been demonstrated by several authors. Vutukuri investigated techniques using intermediate resonant arcs and their manifolds to transfer between orbits, including those that are stable [75]. Capdevilla and Howell developed a transfer network linking Earth, Moon, and their triangular libration point regions using impulsive maneuvers [76]. Zimovan et al. use intermediate dynamical structures using higher-period orbits as options to transfer between stable orbits [77]. Several transfers between NRHOs

and Lunar Orbits (LOs) with two or more impulsive maneuvers are demonstrated in the literature [78]–[80].

1.3 Present Work

Distinct unstable, stable and oscillatory modes are either non-existent or not well-defined for linearly stable orbits [7]. Any existing strategies that are based on manifold theory are not reliable for stationkeeping or transfer trajectory design process. An alternate strategy that leverages other dynamical structures are explored in this investigation and demonstrated for stationkeeping and transfer trajectory design applications. The dynamical flow along the orbit is visualized using the stretching directions, rather than using stable and unstable manifolds [81]–[83]. Variants of the stretching directions are employed for multiple space applications, for example, identification of stationkeeping maneuvers using a Cauchy-Green tensor approach [4], the trajectory design phase for the EQUULEUS mission [84], [85], sensitivity analysis along quasi-satellite orbits [86], patch-point placements along sensitive trajectories [87], as well as monitoring perturbation growth along trajectories [88].

The goal for the stationkeeping problem is to maintain a spacecraft in the neighborhood of a reference trajectory for a long duration. Within the stationkeeping framework, the stretching directions offer insight on the interactions between parameters, including maneuver locations, time duration between successive maneuvers as well as the target horizon time. Such information assist in identifying combinations of parameters that facilitates the success of the stationkeeping algorithm. Further, insights from the stretching directions of the flow enhance the control algorithm. This investigation examines the current stationkeeping strategy from the context of the dynamical foundations and structures that enable the strategy to generally succeed. The effect of various parameters on orbit maintenance cost and on the boundedness of the spacecraft motion near the desired path are explored.

A contrasting application is to depart from the vicinity of a reference path rapidly, as well as rapid insertion on the orbit. Disposal of logistic modules while avoiding any collisions is also a concern. Previous transfer trajectory design approaches, between stable orbits, exploit

intermediate segments of known orbits, resonant arcs as well as manifolds of known unstable orbits, however, the most productive types of intermediate orbits are not known *a priori*. In this investigation, the dynamical flow is visualized using the principal stretching directions. An alternate strategy that offers reliable departure and arrival analysis from stable orbits are explored, one that leverages the maximum stretching directions. An effective departure from the orbit serves as a preliminary step for the disposal problem as well as a basis for transfers to other spatial locations.

The investigation focuses on developing mathematical tool to characterize the sensitive directions in form of stretching directions, and utilize the understanding of the dynamical flow near a reference trajectory to enhance stationkeeping and transfer trajectory design strategies. The study is summarized as follows:

- Chapter 2

  The dynamical flow beyond a two-body conic problem is developed in the circular restricted three-body problem (CR3BP). The equations of motion for CR3BP are modeled based on a few fundamental assumptions. The equilibrium solutions and the limit cycles in the nonlinear system in form of periodic orbits are calculated. An energy-like constant, that is the integral of motion is defined. Such a quantity determines the accessible regions for a spacecraft motion. Behavior in the neighborhood of a reference solution is identified using linear variational equations. A higher-fidelity model using n-gravitational bodies is formulated to replicate a real-world scenario. Further, procedures to transform between different coordinate systems are derived.

- Chapter 3

  The CR3BP is a nonlinear dynamical system. As a consequence, determining an accurate initial condition that reaches a desired final state is non-intuitive. Tools are developed using the Dynamical Systems Theory (DST). A linear State Transition Matrix (STM) is calculated along a chosen reference solution. Differential correction techniques utilizes the STM for identification of precise initial conditions. Likewise, single shooting and multiple shooting techniques for complex trajectory corrections

are derived. Application of the shooting algorithms in a higher-fidelity model is also discussed. Such tools are applied for stationkeeping and transfer design process.

- Chapter 4

  An overview of the orbit maintenance process is discussed in this chapter. Impact of the orbit determination process on the state uncertainty of a spacecraft along an NRHO is identified. Navigational errors and solar radiation pressure errors that influences the spacecraft motion is summarized. Insight into the Monte Carlo process is provided, along with an explanation on the impact of sample size on confidence intervals.

- Chapter 5

  In this chapter, the interaction between the dynamical flow evolving between two successive maneuver locations and the dynamical flow from the maneuver location to the target is analyzed from the context of the stretching directions. Further, the impact of the stretching directions along the L1 and L2 NRHOs are analyzed to offer insight on the performance of the x-axis crossing control strategy. Certain members of the halo orbit families are particularly sensitive to epoch dates and possess distinct characteristics in the higher-fidelity ephemeris model in comparison to their CR3BP counterpart. As a result, targeting conditions that are not synchronized and in phase are observed to be ineffective in stationkeeping. Additionally, certain events, such as eclipse avoidance require a certain phasing. The influence of an additional feedback constraint for appropriate phasing is investigated within the framework of a stationkeeping problem.

- Chapter 6

  A strategy that offers reliable departure and arrival analysis from stable orbits are explored in this chapter, one that leverages the maximum stretching directions. Impact of maneuver directions and their location along an NRHO is presented. A strategy that leverages maneuvers along maximum stretching directions to transfer between stable orbits is demonstrated. Some examples of transfers between stable orbits such as, a southern NRHO to a northern NRHO (3D to 3D), a southern NRHO to a DRO (3D to planar) and a southern NRHO to a Lunar Orbit (3D to planar) are illustrated.

- Chapter 7

  Some of the concluding remarks from the stationkeeping strategy and the transfer trajectory design process are detailed. Some peculiar observations are highlighted. Recommendations for future work are offered.

2. SYSTEM MODELS

The "two-body problem" represents the behavior of two point masses due to their mutual gravitational forces. The two-body problem is expressed mathematically with relatively straight forward differential equations and an analytical solution is available. Any additional gravitational bodies taken into consideration increases the complexity of the problem and an analytical solution ceases to exist. Some characteristics of the system behavior are revealed by numerical propagation of the governing differential equations. The three-body problem incorporates an additional gravitational source than the two-body problem and serves as a foundation for more complex motion.

2.1 Circular Restricted Three-Body Problem (CR3BP)

The solar system comprises of infinitely many gravitational bodies that mutually influence the motion of each other. The motion of a body influenced by '$n-1$' other bodies in the solar system is modeled as the 'the n-body problem.' To formulate the n-body problem define each of the 'n' bodies as P_{i} with mass m_{i} where $\mathrm{i} = 1, 2, ..., n$. Assuming all the n bodies are spherically symmetric, Newton's Laws of motion are applied to compute the force acting on the particle of interest. Let orthonormal unit vectors $\hat{X}, \hat{Y}, \hat{Z}$ represent the coordinates of the inertially fixed frame, $\underline{\mathcal{I}}$, with O as the inertially fixed base point or the origin. The vector $\bar{r}_{\mathrm{i}}$ describes the position of body P_{i} with respect to the base point O while the vector $\bar{r}_{q\mathrm{i}}$ describes the position of body P_{i} with respect to the body P_q as shown in Figure 2.1. Therefore, as expressed in [89], the total force acting on the body P_{i} as a result of all the other bodies is

$$\bar{F}_{\mathrm{i}} = -\tilde{G} \sum_{\mathrm{j}=1,\ \mathrm{j}\neq\mathrm{i}}^{n} \frac{m_{\mathrm{i}} m_{\mathrm{j}}}{r_{\mathrm{ji}}^{3}}\ \bar{r}_{\mathrm{ji}} \tag{2.1}$$

such that, $\tilde{G}$ is the scalar gravitational constant given by $6.67408 \times 10^{-11}\ m^3 kg^{-1} s^{-2}$ [90] and $\bar{F}_{\mathrm{i}}$ is the force vector acting on body P_{i}.

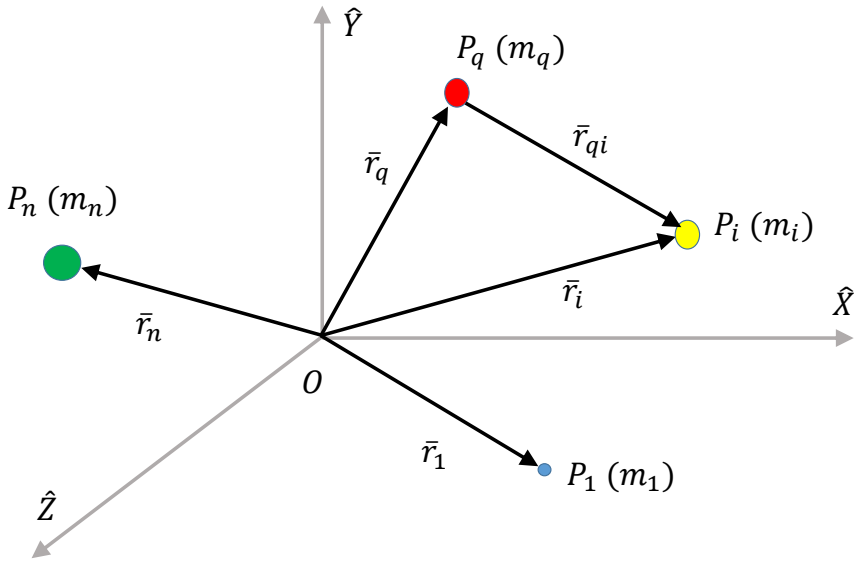

Figure 2.1. Gravitational interactions between n bodies in space.

The motion of a body is systematically expressed in terms of kinematic quantities. Using Newton's second law of motion, equation (2.1) is expressed in terms of the acceleration of body P_{i} in the inertial frame, $\underline{\mathcal{I}}$, as

$$\bar{F}_{\mathrm{i}} = m_{\mathrm{i}}\ddot{\bar{r}}_{\mathrm{i}} = -\tilde{G}\sum_{\substack{\mathrm{j}=1\\ \mathrm{j}\neq\mathrm{i}}}^{n}\frac{m_{\mathrm{i}}m_{\mathrm{j}}}{r_{\mathrm{ji}}^{3}}\ \bar{r}_{\mathrm{ji}} \tag{2.2}$$

such that,

$$\ddot{\bar{r}}_{\mathrm{i}} = -\tilde{G}\sum_{\substack{\mathrm{j}=1\\ \mathrm{j}\neq\mathrm{i}}}^{n}\frac{m_{\mathrm{j}}}{r_{\mathrm{ji}}^{3}}\ \bar{r}_{\mathrm{ji}} \tag{2.3}$$

where $\ddot{\bar{r}}_{\mathrm{i}}$ represents the acceleration of body P_{i} due to the gravitational forces of all other bodies in the n-body system. It is the second derivative of the position vector with respect to the dimensional time as observed in the inertial frame.

For a system with two or more gravitational bodies, an analytical solution does not exist. Gaining some insight into the system behavior is challenging but a priority. For the n-body system, each of the bodies are sensitive to changes in position, velocity and acceleration due to the influence of all the other bodies in the solar system, hence, a generic equation

of motion cannot be formulated that is independent of time. A multi-body problem with selected number of bodies about a fixed epoch date and real time data describing the states, called the ephemeres model, offers some insight. A less complex, time invariant mathematical model with three gravitational bodies is formulated with certain assumptions making a reliable framework to understand the characteristic behavior of the system. The Circular Restricted Three-Body Problem (CR3BP) is a commonly used approach for formulating the equations of motion of a body influenced by two other bodies, independent of time. The solution delivered by the CR3BP model is used as an initial guess for the higher-fidelity model.

2.1.1 Assumptions

The Circular Restricted Three-Body Problem is a time-invariant specific case of the n-body problem with a total of three bodies. Equation (2.3) delivers the expression of an n-body system, so for $n = 3$,

$$\ddot{\bar{r}}_3 = -\tilde{G}\left[\frac{m_1}{r_{13}^3}\,\bar{r}_{13} + \frac{m_2}{r_{23}^3}\bar{r}_{23}\right] \tag{2.4}$$

where the position vectors $\bar{r}_{13}$ and $\bar{r}_{23}$ are given as

$$\bar{r}_{13} = \bar{r}_3 - \bar{r}_1 \tag{2.5}$$

$$\bar{r}_{23} = \bar{r}_3 - \bar{r}_2 \tag{2.6}$$

such that, $\bar{r}_{\mathrm{i}}$ is the position vector of body 'i' with respect to the origin. To solve for the differential equation, time history of $\bar{r}_1$ and $\bar{r}_2$ are to be known, but such information is not available as states of P_1 and P_2 are simultaneously influenced by $\bar{r}_3(t)$. The three-body problem requires 18 integrals of motion to be solved simultaneously, i.e., 6 states (3 position and 3 velocity states) for each of the 3 bodies, but only 10 integrals are known. A two-body problem has a closed form solution but with the addition of just one more gravitational body, i.e., $n = 3$, a closed form solution ceases to exist, however, with certain additional

assumptions, a refined model is described that illustrates the underlying behavior of a number of systems. The assumptions are as stated:

- $m_3 << m_1, m_2$

  Let the three bodies P_1, P_2 and P_3 be point mass bodies with masses m_1, m_2 and m_3, such that $m_3 << m_1, m_2$. The two bodies P_1 and P_2 are considered as primaries that are massive in comparison to the third body, P_3. The assumption of an infinitesimally small body P_3 is valid for bodies like a spacecraft, a comet, etc. The assumption is further extended to $m_1 < m_2$ to represent a larger primary body and a smaller primary body.

- P_3 does not influence the motion of P_1 and P_2

  When P_3 is modeled as an infinitesimally small body in comparison to the primaries it is assumed that the gravitational force due to mass m_3 does not influence the motion of bodies, P_1 and P_2, with masses m_1 and m_2 respectively. This results in an isolated two-body system with primary body m_1 and secondary body m_2, for which an analytical solution is known in form of a conic. P_3 is known to coexist within the stable system of P_1 and P_2.

- P_1 and P_2 move on circular orbits about their mutual barycenter

  Further it is assumed that the primary bodies, P_1 and P_2, move in a circular orbit about their mutual barycenter. This assumption is not necessary but simplifies the model from an elliptic restricted three-body problem. As a result, the barycenter is regarded as inertially fixed and treated as the origin for developing the equations of motion in the circular restricted three-body problem.

To formulate the circular restricted three-body problem, consider the bodies to be oriented as shown in Figure 2.2. Let orthonormal unit vectors $\hat{X}, \hat{Y}, \hat{Z}$ represent the coordinates of the inertially fixed frame, $\underline{\mathcal{I}}$, with origin at the barycenter (B) of the primaries. Since P_1 and P_2 have a conic solution, the motion of the primaries are fixed in $\hat{X}\hat{Y}$ plane. The angular momentum vector of the motion of the primaries is along the positive $\hat{Z}$ direction.

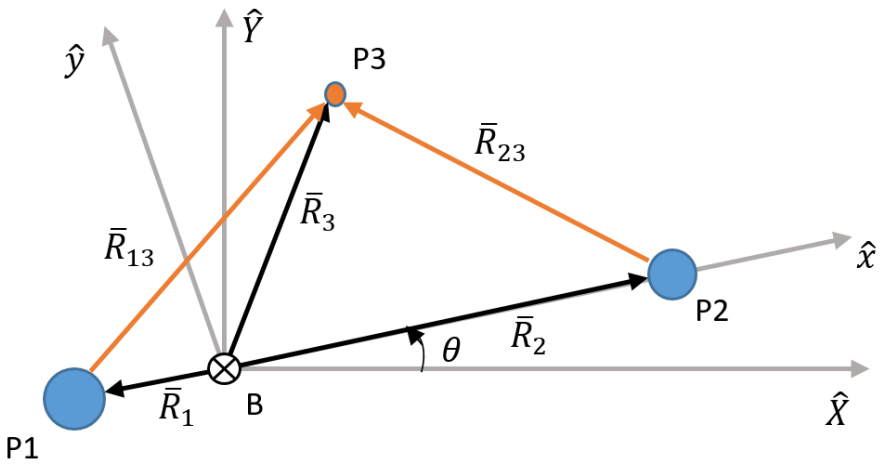

Figure 2.2. Three-body orientation in space, with respect to an inertial and a rotating frame.

2.1.2 Equations of Motion

Since the primaries is assumed to revolve in a circular orbit about their mutual barycenter observed in the inertial frame, the angular velocity of its motion is fixed. Let $\dot{\theta}$ represent the angular velocity or the mean motion. The motion of the primaries are defined in the inertial fixed frame as a function of time, t, as

$$\bar{R}_1 = R_1 \left[-cos(\dot{\theta}t)\hat{X} - sin(\dot{\theta}t)\hat{Y} \right] \tag{2.7}$$

$$\bar{R}_2 = R_2 \left[cos(\dot{\theta}t)\hat{X} + sin(\dot{\theta}t)\hat{Y} \right] \tag{2.8}$$

where $\bar{R}_1$ and $\bar{R}_2$ are the position vectors from the barycenter towards primary bodies P_1 and P_2 respectively. The magnitude of each of the vectors $\bar{R}_1$ and $\bar{R}_2$ are described by R_1 and R_2 respectively. In this investigation, non-bold italicized letters represents the scalar magnitude of a quantity while the non-bold italicized letters with a bar sign on top represents a vector quantity. The position vector of the third body P_3 denoted by $\bar{R}_3$ is free to change in all three spatial directions. Computing the states $\bar{R}_3$ and $\dot{\bar{R}}_3$ in the inertial frame requires computation of the position and velocity states of the primary bodies at all times. A rotating coordinate frame, $\underline{\mathcal{R}}$, that rotates with the primary bodies remove the necessity

to evaluate the states of the primaries that are explicit functions of time. The energy of the system in the rotating frame, $\underline{\mathcal{R}}$, remains conserved as in the inertial frame, $\underline{\mathcal{I}}$. Define $\hat{x}, \hat{y}, \hat{z}$ as the unit vectors that define the coordinates of the rotating frame of reference, such that $\hat{x}$ points in the direction from primary body P_1 to P_2. The direction $\hat{z}$ points along the angular momentum of the primaries, also aligned along the positive $\hat{Z}$ axis. Finally, the direction $\hat{y}$ completes the right hand coordinate system.

To further generalize the equations of motions for various three-body systems and minimize the possibility of round-off errors during numerical integration, the terms of the equations of motion are non-dimensionalized by corresponding characteristic quantities. All quantities of distance are reduced by the characteristic length, all quantities of mass are reduced using the characteristic mass and quantities of time with the characteristic time. The characteristic length, l^*, is defined as the distance between the two primaries such as

$$l^* = R_1 + R_2, \tag{2.9}$$

the characteristic mass, m^*, is the total mass of the system, given as

$$m^* = m_1 + m_2 \tag{2.10}$$

and the characteristic time is defined as the reciprocal of the mean motion,

$$t^* = \frac{1}{\dot{\theta}} = \sqrt{\frac{l^{*3}}{\tilde{G}m^*}} \tag{2.11}$$

where the subscript 1 denotes the characteristic properties of primary P_1 while subscript 2 denotes properties of primary P_2. Let the system mass ratio, μ, be another defining quantity, given as,

$$\mu = \frac{m_2}{m_1 + m_2} = \frac{m_2}{m^*} \tag{2.12}$$

hence, $m_2 = \mu m^*$ and $m_1 = (1 - \mu)m^*$. The characteristic quantities and the system mass ratio are sufficient to describe the nature of a system. The circular restricted three-body is

therefore simplified in the non-dimensional units. The differential equation that governs the motion of body P_3 as given by equation (2.4), is non-dimensionalized as

$$\ddot{\bar{r}}_3 = \frac{1-\mu}{r_{13}^3}\,\bar{r}_{13} + \frac{\mu}{r_{23}^3}\bar{r}_{23} \tag{2.13}$$

where $\bar{r}_3$ is now expressed in the rotating frame as $\bar{r}_3 = x\hat{x} + y\hat{y} + z\hat{z}$. The vectors $\bar{r}_{13}$ and $\bar{r}_{23}$ given as

$$\bar{r}_{13} = \bar{r}_3 - \bar{r}_1 = (x-\mu)\hat{x} + y\hat{y} + z\hat{z} \tag{2.14}$$

$$\bar{r}_{23} = \bar{r}_3 - \bar{r}_2 = (x-1+\mu)\hat{x} + y\hat{y} + z\hat{z} \tag{2.15}$$

depends on the location of the primaries along the $\hat{x}$ axis, i.e., $\bar{r}_1 = -\mu\hat{x}$ and $\bar{r}_2 = (1-\mu)\hat{x}$. The derivatives, i.e., $\dot{\bar{r}}_3$ and $\ddot{\bar{r}}_3$ are with respect to non-dimensional time τ where $\tau = t/t^*$.

To formulate the equations of motion in the rotating frame, the derivatives are taken in the rotating frame, $\underline{\mathcal{R}}$, with respect to an inertial frame, $\underline{\mathcal{I}}$. The Basic Kinematic equation (BKE) correlates the derivatives in the rotating frame to the inertial frame as

$$\frac{{}^I d\bar{r}_3}{d\tau} = \frac{{}^R d\bar{r}_3}{d\tau} + {}^I\omega^R \times \bar{r}_3 \tag{2.16}$$

where ${}^I\omega^R = \dot{\theta}\hat{z}$ gives the angular velocity of the rotating frame about $\hat{z}$ axis. The velocity of the body P_3 therefore becomes

$$\begin{aligned} {}^I\dot{\bar{r}}_3 &= \dot{x}\hat{x} + \dot{y}\hat{y} + \dot{z}\hat{z} + [\dot{\theta}\hat{z}] \times [x\hat{x} + y\hat{y} + z\hat{z}] \\ &= (\dot{x} - \dot{\theta}y)\hat{x} + (\dot{y} + \dot{\theta}x)\hat{y} + \dot{z}\hat{z} \end{aligned} \tag{2.17}$$

in the rotating frame, $\underline{\mathcal{R}}$. The second derivative of the position vector $\bar{r}_3$, yields

$${}^I\ddot{\bar{r}}_3 = (\ddot{x} - 2\dot{\theta}\dot{y} - \dot{\theta}^2 x)\hat{x} + (\ddot{y} + 2\dot{\theta}\dot{x} - \dot{\theta}^2 y)\hat{y} + \ddot{z}\hat{z} \tag{2.18}$$

where ${}^I\ddot{\bar{r}}_3$ is the instantaneous acceleration in the rotating frame. Substituting the equations, (2.14), (2.15) and (2.18) into equation (2.13) along with non-dimensional value of mean

motion, $\dot{\theta}$, that is 1 for CR3BP, yields the three scalar equations of motion for P_3 in the rotating frame, $\underline{\mathcal{R}}$, given by

$$\ddot{x} - 2\dot{y} - x = -\frac{1-\mu}{d^3}(x+\mu) - \frac{\mu}{r^3}(x-1+\mu) \tag{2.19}$$

$$\ddot{y} + 2\dot{x} - y = -\frac{1-\mu}{d^3}y - \frac{\mu}{r^3}y \tag{2.20}$$

$$\ddot{z} = -\frac{1-\mu}{d^3}z - \frac{\mu}{r^3}z \tag{2.21}$$

such that,

$$d = r_{13} = \sqrt{(x+\mu)^2 + y^2 + z^2} \tag{2.22}$$

$$r = r_{23} = \sqrt{(x-1+\mu)^2 + y^2 + z^2} \tag{2.23}$$

where d represents the non-dimensional distance from P_3 to primary body P_1 and r represents the non-dimensional distance from P_3 to smaller primary body P_2.

2.1.3 Jacobi Constant

The conservation of energy principle does not apply for a non inertial system. A similar quantity that is conserved in the rotating frame is of high significance. A *potential function (U)* represents the work done to displace a unit mass from infinity to that particular point. For CR3BP, this is given by,

$$U = \frac{1-\mu}{d} + \frac{\mu}{r} \tag{2.24}$$

such that, $\bar{\nabla} U_{\mathrm{i}} = m_{\mathrm{i}} \ddot{\bar{r}}_{\mathrm{i}}$ for a unit mass m_{i}. Similarly a *pseudo-potential function (U^*)* is defined such that,

$$U^* = U + \frac{1}{2}\left(x^2 + y^2\right) = \frac{1-\mu}{d} + \frac{\mu}{r} + \frac{1}{2}\left(x^2 + y^2\right) \tag{2.25}$$

where U and U^* are both functions of only positions and give useful insights about the motion of the spacecrafts. The scalar equations of motion in equations (2.19), (2.20) and (2.21) when rendered as a function of pseudo-potential function, given by

$$\ddot{x} - 2\dot{y} = \frac{\partial U^*}{\partial x} \tag{2.26}$$

$$\ddot{y} + 2\dot{x} = \frac{\partial U^*}{\partial y} \tag{2.27}$$

$$\ddot{z} = \frac{\partial U^*}{\partial z} \tag{2.28}$$

indicates that the acceleration in the x and y directions, as in equations (2.26) and (2.27), are decoupled from any out of plane components in the z direction; implying that the xy planar motion evolves independently of the out of plane motion and vice-versa. Any motion in the orbit plane of primaries continue to remain in the same plane unless any out of plane maneuver is applied. Both U and U^* do not remain conserved in the rotating frame.

An energy integral is computed by integrating the dot product of the velocity and the acceleration components of the third body in motion, due to the gravitational forces exerted on it by the two primaries. In the rotating frame, this is given by

$$\begin{aligned} \dot{\bar{r}}_3 \cdot \ddot{\bar{r}}_3 &= [\dot{x}\hat{x} + \dot{y}\hat{y} + \dot{z}\hat{z}] \cdot [\ddot{x}\hat{x} + \ddot{y}\hat{y} + \ddot{z}\hat{z}] \\ &= \dot{x}\ddot{x} + \dot{y}\ddot{y} + \dot{z}\ddot{z} \\ &= \frac{\partial U^*}{\partial x}\dot{x} + \frac{\partial U^*}{\partial y}\dot{y} + \frac{\partial U^*}{\partial z}\dot{z} \\ &= \frac{\partial U^*}{\partial t} \end{aligned} \tag{2.29}$$

which is the time derivative of the pseudo-potential function. The integration of the partials in equation (2.29) yields,

$$\dot{\bar{r}}_3^2 = v^2 = 2U^* - C \qquad \rightarrow \qquad C = 2U^* - v^2 \tag{2.30}$$

here C is the constant of integration and v is the velocity of the third body P_3 in the rotating frame. The constant C, known as *Jacobi Constant* represents a conserved energy-like quantity in the rotating frame. An increase in the energy of the system relative to the rotating frame represents a decrease in the Jacobi constant and vice-versa. Jacobi constant has various uses in the circular restricted three-body problem. It is used to determine accuracy of numerical integration by monitoring the change in the value of C, to identify the change in energy required for transfer trajectories, to understand the energy limits of families of orbits and many more.

2.1.4 Equilibrium Solutions

Determining equilibrium solutions helps gain further insight into the CR3BP. The equilibrium solutions correspond to the positions where the third body, free from any initial acceleration or velocity remains stationary in the rotating frame for an indefinite period of time. Consequently, all the time derivatives are zero, i.e., $\dot{x} = \dot{y} = \dot{z} = \ddot{x} = \ddot{y} = \ddot{z} = 0$. Substituting this relation into the equations (2.26)-(2.28) indicates that the gradient of pseudo-potential function is zero, i.e., $\nabla U^* = 0$. Therefore, the equilibrium solutions are solved using the following equations

$$\frac{\partial U^*}{\partial x} = \frac{\partial U^*}{\partial y} = \frac{\partial U^*}{\partial z} = 0 \tag{2.31}$$

using numerical schemes. The equilibrium points are also commonly described as *Lagrange points* or *Libration points*, (Li). Each libration points 'Li' are found by numerically solving the equation (2.31) that yields,

$$\frac{\partial U^*}{\partial x} = -\frac{1-\mu}{d_{L_i}^3}(x_{L_i} + \mu) - \frac{\mu}{r_{L_i}^3}(x_{L_i} - 1 + \mu) + x_{L_i} = 0 \tag{2.32}$$

$$\frac{\partial U^*}{\partial y} = -\frac{1-\mu}{d_{L_i}^3} y_{L_i} - \frac{\mu}{r_{L_i}^3} y_{L_i} + y_{L_i} = 0 \tag{2.33}$$

$$\frac{\partial U^*}{\partial z} = -\frac{1-\mu}{d_{L_i}^3} z_{L_i} - \frac{\mu}{r_{L_i}^3} z_{L_i} = 0 \tag{2.34}$$

where $d^3_{L_i}$ and $r^3_{L_i}$ are the distances from the libration point 'Li' to each of the two primaries while the coordinates of the equilibrium points are $(x_{L_i}, y_{L_i}, z_{L_i})$.

Each combination of $(x_{L_i}, y_{L_i}, z_{L_i})$ correspond to a libration point, 'Li'. Equation (2.34) is satisfied with $z_{L_i} = 0$, thus all libration points lie in the orbit plane of the primaries. Similarly, $y_{L_i} = 0$, is a solution of the equation (2.33), hence one or more equilibrium solutions exists on the rotating x-axis given by $(x_{L_i}, 0, 0)$ that satisfies equation (2.32) as

$$-\frac{1-\mu}{|x_{L_i}+\mu|^3}(x_{L_i}+\mu) - \frac{\mu}{|x_{L_i}-1+\mu|^3}(x_{L_i}-1+\mu) + x_{L_i} = 0 \tag{2.35}$$

but equation (2.35) has no closed form solution, therefore, roots are computed numerically that yields three real solutions. Imaginary solutions are neglected as physical locations cannot be represented by imaginary numbers. The three possible solutions of equation (2.35) are represented in terms of the displacement from the nearest primary using γ_i. Coordinates of the three collinear libration points are given as $(x_{L_i}, y_{L_i}, z_{L_i})$, such that,

$$L_1 : \qquad (1-\mu-\gamma_1, \quad 0, \quad 0) \tag{2.36}$$

$$L_2 : \qquad (1-\mu+\gamma_2, \quad 0, \quad 0) \tag{2.37}$$

$$L_3 : \qquad (\quad -\mu-\gamma_3, \quad 0, \quad 0) \tag{2.38}$$

where γ_i indirectly depends on the value of μ, i.e., different values of γ_i for different three-body systems. The values of γ_i are solved by iterating the equation (2.35) at each of the collinear Li, specifically

$$-\frac{1-\mu}{(1-\gamma_1)^2} + \frac{\mu}{\gamma_1^2} + 1 - \mu - \gamma_1 = 0 \tag{2.39}$$

$$-\frac{1-\mu}{(1+\gamma_2)^2} - \frac{\mu}{\gamma_2^2} + 1 - \mu + \gamma_2 = 0 \tag{2.40}$$

$$\frac{1-\mu}{\gamma_3^2} + \frac{\mu}{(1+\gamma_3)^2} - \mu + \gamma_3 = 0 \tag{2.41}$$

for different system mass ratio μ. Libration point L1 lies between the two primaries, L2 lies to the right of smaller primary while L3 lies to the left of larger primary as shown in Figure 2.3. Each of the libration points are numbered according to the convention followed in literature.

Besides the three collinear solution, two other equilibrium solutions exists in the CR3BP. Equations (2.32) and (2.33) are also satisfied simultaneously for $d = r = 1$ that completes the equilateral triangle with the distance between the primaries as the side of an equilateral triangle. As a result, two equilibrium points lie on either side of the $x - z$ plane equidistant from both the primaries as shown in Figure 2.3. By virtue of their location, these points are labelled as triangular or equilateral Libration points. As per the convention, coordinates of the triangular libration points are

$$L_4 : \qquad \left(\frac{1}{2} - \mu, \quad \frac{\sqrt{3}}{2}, \quad 0\right) \tag{2.42}$$

$$L_5 : \qquad \left(\frac{1}{2} - \mu, \quad -\frac{\sqrt{3}}{2}, \quad 0\right) \tag{2.43}$$

where L4 is located in the positive $\hat{y}$ region while L5 is located in the negative $\hat{y}$ region.

2.1.5 Zero Velocity Curves

Within the CR3BP, the motion of P_3, under the influence of the two primary bodies, is bounded by the total energy it possesses. The value of the Jacobi Constant along with the equilibrium solutions render the boundaries of motion. From equation (2.30), $v^2 = 2U^* - C$, leads to the conclusion that the velocity of P_3 will become imaginary if $C > 2U^*$ which is mathematically possible but physically absurd. The region where the velocity becomes imaginary is physically inaccessible hence it is termed as the forbidden region. The motion

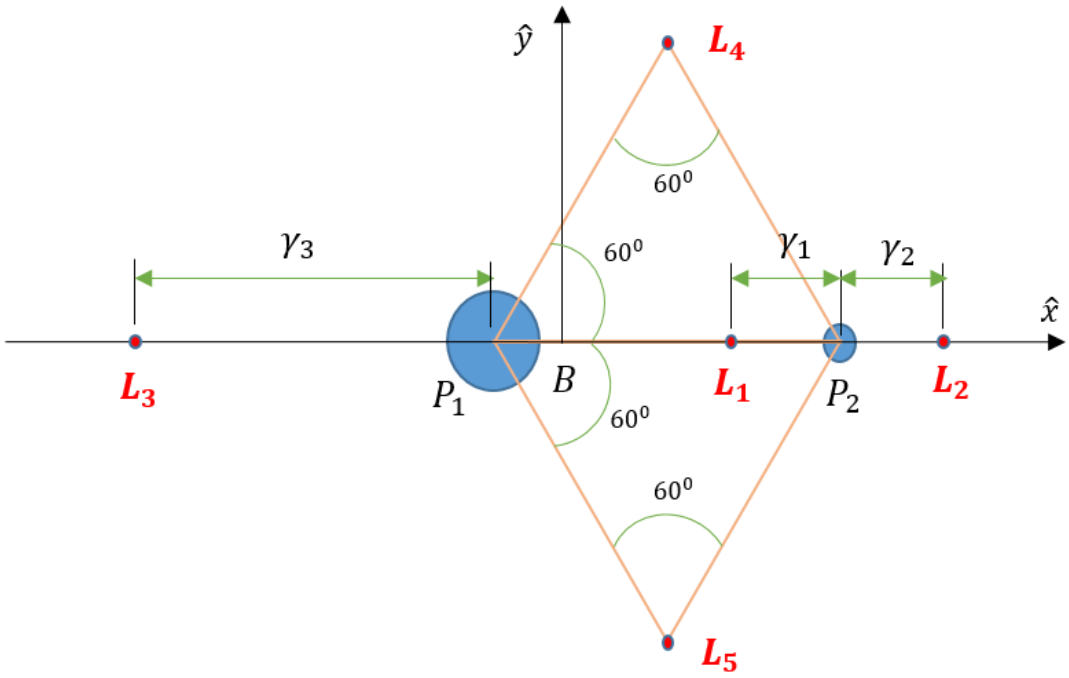

Figure 2.3. Equilibrium locations in the CR3BP.

of the third body P_3 is confined within the region where $C \leq 2U^*$. The boundary occurs where P_3 is theoretically stationary with zero velocity or

$$C = 2U^* = \frac{2(1-\mu)}{d} + \frac{2\mu}{r} + \left(x^2 + y^2\right) \tag{2.44}$$

where infinitely many combinations of (x, y, z) satisfy the equation (2.44) forming a three-dimensional surface called the *Zero Velocity Surface (ZVS)*. An example of a ZVS in the Earth-Moon system is illustrated in Figure 2.4.

A two-dimensional curve formed out of a cross section of the ZVS is called the *Zero Velocity Curves (ZVC)*. To examine a planar motion, a cross section of the Zero Velocity Surface is considered along the $x - y$ plane forming a Zero Velocity Curve representing the boundary for the planar motion. The Zero Velocity Curves for different energy levels (or different Jacobi values) decide the boundaries of motion for P_3 in the plane. Each equilibrium point corresponds to a Jacobi Value (C_{L_i}). As the ZVCs evolve for different Jacobi values, it

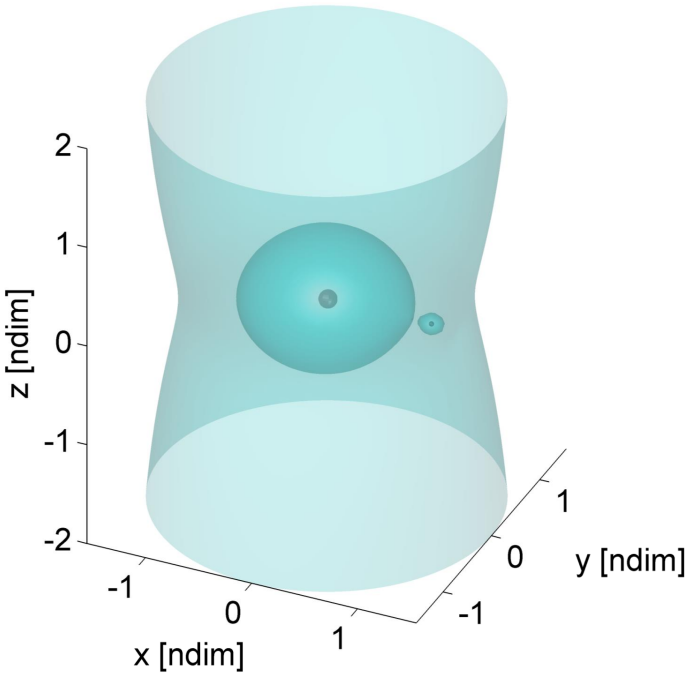

Figure 2.4. Zero Velocity Surface in the Earth-Moon system for $C = 3.2$. (Earth and Moon not to scale)

is insightful to monitor the changes in the ZVCs as it crosses each C_{L_i}. Figure 2.5 illustrates the evolution of ZVCs for different Jacobi values in comparison to the Jacobi values at the Lagrange points mentioned as C_{L_i} for the Earth Moon (EM) system, and its impact on the accessible regions in space.

The Jacobi constant at the Lagrange points, C_{L_i}, are critical factors that impact the shape of the ZVCs. The changing geometry is as explained:

- $C_{L_1} < C$

  For an energy level less than at L1, i.e., $C_{L_1} < C$, the third body P_3 is bounded within the vicinity of either one of the primary bodies as indicated in Figure 2.5(a). If P_3 is initially present near main primary then it continues to remain in the vicinity of the main primary. Similarly, if P_3 is present near the second primary then it remains bounded near the second primary. The energy of P_3 is not high enough to cross the

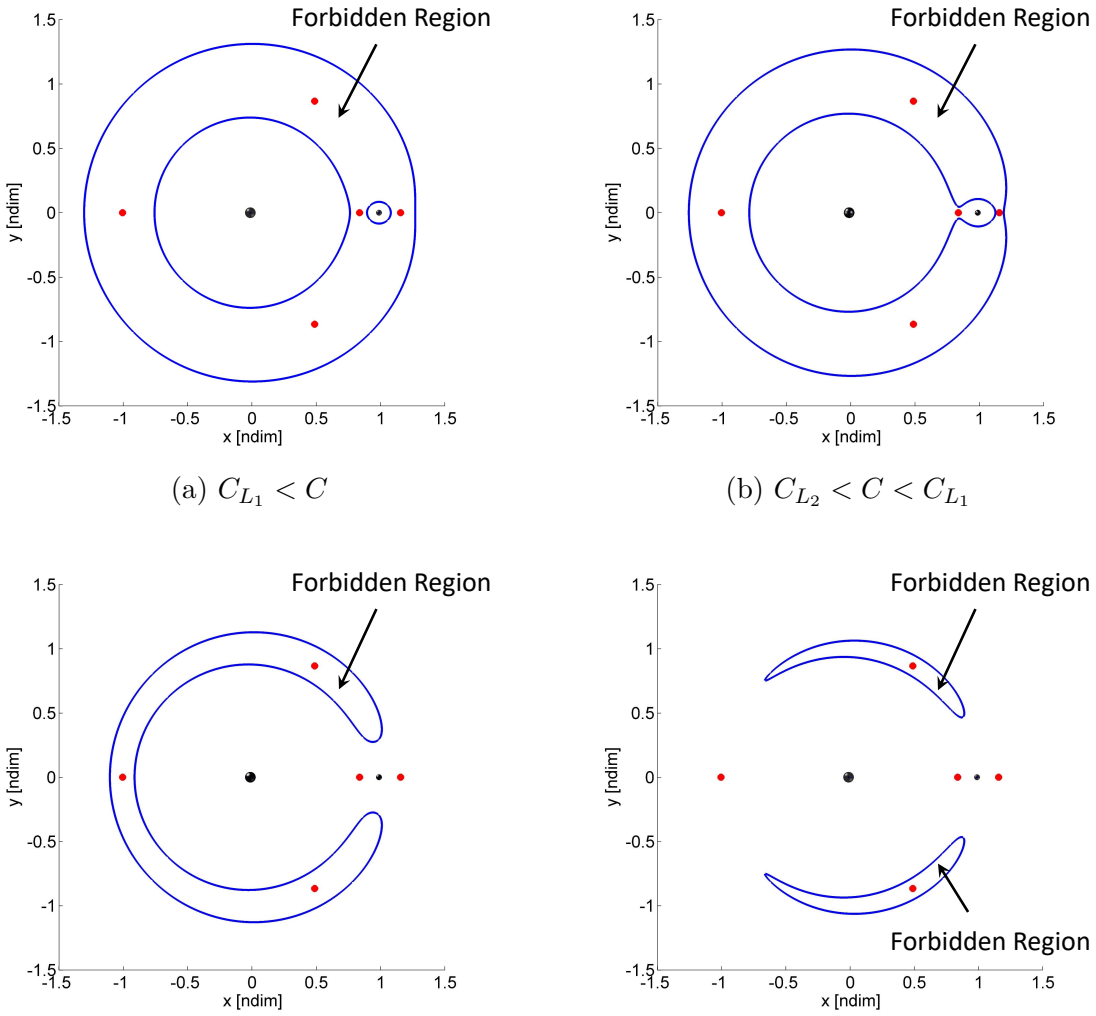

(a) $C_{L_1} < C$

(b) $C_{L_2} < C < C_{L_1}$

(c) $C_{L_3} < C < C_{L_2}$

(d) $C_{L_{4,5}} < C < C_{L_3}$

Figure 2.5. Zero Velocity Curves in the $x-y$ plane for different Jacobi values in the Earth-Moon (EM) system.

forbidden region near the Lagrange point L1 to transit from the vicinity of one primary body to the other.

- $C_{L_2} < C < C_{L_1}$

  For ZVCs with Jacobi values between the Jacobi at L1 and L2, as seen in Figure 2.5(b), a gateway appears near L1 offering connections between the two primaries. The body P_3, however still does not possess enough energy to escape to outer space.

- $C_{L_3} < C < C_{L_2}$

  With increase in energy level more than L2, gateway opens up near L2 allowing P_3 to escape to outer space near the second primary. Forbidden region still persists towards the left of the main primary, thus access to outer space is possible only along the positive x direction.

- $C_{L_{4,5}} < C < C_{L_3}$

  The ZVC splits near L3 at Jacobi level C_{L_3} opening gateway to outer space near L3 as well. In this range of Jacobi values, P_3 has enough energy to move out of the vicinity of both the primaries in either direction. The forbidden regions eventually contracts towards L4 and L5.

- $C < C_{L_{4,5}}$

  For lower Jacobi values less than at L4 or L5, the ZVC ceases to exist in the $x - y$ plane. This does not imply that P_3 is free to move anywhere, it just means that $P - 3$ is free to traverse anywhere in the planar space but there are still out-of-plane regions that are inaccessible. It is important to note that at this range of Jacobi values the Zero Velocity Surface splits into two distinct surfaces at L4 and L5 in the out-of-plane directions. With a decrease in C values, the two distinct Zero Velocity Surfaces continues to shrink in the direction away from the $x - y$ plane.

The Zero Velocity Surfaces provides practicable information especially for mission design. For example, a maneuver is performed to increase the energy level to reach from one primary to another by opening a gateway near L1, similarly an energy reduction maneuver facilitates capture in the vicinity of the primaries by closing the gateways near L1 and L2.

2.2 Linearized Model

Any nonlinear system is difficult to analyze. A linearized model offers understanding of the local behavior of the system in the vicinity of equilibrium solutions. The behavior of certain states in the nonlinear system close to an already known solution is predicted using the linearized model without actually requiring to propagate the selected states. With the same intention the equations of motion of CR3BP are linearized about its equilibria.

2.2.1 Linearized Variational Equations of Motion

The motion in the circular restricted three-body problem is governed by coupled, second order nonlinear differential equations that does not have a closed form analytical solution. Linearized solutions are generated near the equilibrium points to realize the local behavior. All the six states are perturbed about the equilibrium points to develop the linearized equations of motion. Let (x_{eq}, y_{eq}, z_{eq}) represent the location of the equilibrium points and (ξ, η, ζ) be the perturbations in $(\hat{x}, \hat{y}, \hat{z})$ directions respectively such that,

$$x = x_{eq} + \xi \tag{2.45}$$

$$y = y_{eq} + \eta \tag{2.46}$$

$$z = z_{eq} + \zeta \tag{2.47}$$

where (x, y, z) are the new states in the vicinity of the equilibrium points. For any state q, such that $q = q_{eq} + \delta q$, where δq is a small deviation from reference solution q_{eq}, the derivative is expressed as

$$\dot{q} = f(q, t) \tag{2.48}$$

which is approximated to the first order derivative term using Taylor Series. As a result, equation (2.48) becomes,

$$\dot{q_{eq}} + \dot{\delta q} \approx f(q_{eq} + \delta q, t) = f(q_{eq}, t) + \left.\frac{\partial f}{\partial q}\right|_{q_{eq}} dq + H.O.T.s \tag{2.49}$$

where, $H.O.T.s$ represents the higher order terms that are neglected here for approximating the integration to first order, assuming perturbations are very small. The first order approximation yields

$$\delta\dot{q} = \left.\frac{\partial f}{\partial q}\right|_{q_{eq}} \delta q = A(t)\delta q \tag{2.50}$$

where $A(t)$ is known as the Jacobian Matrix and contains the partials of f with respect to state q. Using equation (2.50), the time derivatives of the position and velocity states near equilibrium points in CR3BP is also written in the same form,

$$\dot{x} = \dot{x}_{eq} + \dot{\xi} = \dot{\xi} \tag{2.51}$$

$$\dot{y} = \dot{y}_{eq} + \dot{\eta} = \dot{\eta} \tag{2.52}$$

$$\dot{z} = \dot{z}_{eq} + \dot{\zeta} = \dot{\zeta} \tag{2.53}$$

$$\ddot{x} = \ddot{x}_{eq} + \ddot{\xi} = \ddot{\xi} \tag{2.54}$$

$$\ddot{y} = \ddot{y}_{eq} + \ddot{\eta} = \ddot{\eta} \tag{2.55}$$

$$\ddot{z} = \ddot{z}_{eq} + \ddot{\zeta} = \ddot{\zeta} \tag{2.56}$$

since $[\dot{x}_{eq}, \dot{y}_{eq}, \dot{z}_{eq}, \ddot{x}_{eq}, \ddot{y}_{eq}, \ddot{y}_{eq}]^T = \bar{0}$, as the equilibrium points are stationary in CR3BP. The variational equations are developed by taking the derivatives of the equations (2.26), (2.27) and (2.28) and expressed in terms of pseudo potential function, U^*, as

$$\ddot{\xi} - 2\dot{\eta} = U^*_{xx}\xi + U^*_{xy}\eta + U^*_{xz}\zeta \tag{2.57}$$

$$\ddot{\eta} + 2\dot{\xi} = U^*_{yx}\xi + U^*_{yy}\eta + U^*_{yz}\zeta \tag{2.58}$$

$$\ddot{\zeta} = U^*_{zx}\xi + U^*_{zy}\eta + U^*_{zz}\zeta \tag{2.59}$$

where each $U^*_{\mathrm{ij}} = \dfrac{\partial^2 U^*}{\partial \mathrm{i} \partial \mathrm{j}}$ are the second order partials of U^* with respect to the directions expressed as the subscripts. For each $\mathrm{i}, \mathrm{j} \in \{x, y, z\}$, the partials are expanded as

$$U^*_{xx} = 1 - \frac{1-\mu}{d^3} - \frac{\mu}{r^3} + \frac{3(1-\mu)(x+\mu)^2}{d^5} + \frac{3\mu(x-1+\mu)^2}{r^5} \tag{2.60}$$

$$U^*_{yy} = 1 - \frac{1-\mu}{d^3} - \frac{\mu}{r^3} + \frac{3(1-\mu)y^2}{d^5} + \frac{3\mu y^2}{r^5} \tag{2.61}$$

$$U^*_{zz} = -\frac{1-\mu}{d^3} - \frac{\mu}{r^3} + \frac{3(1-\mu)z^2}{d^5} + \frac{3\mu z^2}{r^5} \tag{2.62}$$

$$U^*_{xy} = \frac{3(1-\mu)(x+\mu)y}{d^5} + \frac{3\mu(x-1+\mu)y}{r^5} = U^*_{yx} \tag{2.63}$$

$$U^*_{xz} = \frac{3(1-\mu)(x+\mu)z}{d^5} + \frac{3\mu(x-1+\mu)z}{r^5} = U^*_{zx} \tag{2.64}$$

$$U^*_{yz} = \frac{3(1-\mu)yz}{d^5} + \frac{3\mu yz}{r^5} = U^*_{zy} \tag{2.65}$$

where d, r and μ retain their original definitions.

In the CR3BP, the natural motion of P_3 is represented by 6 state variables, $[\xi, \eta, \zeta, \dot{\xi}, \dot{\eta}, \dot{\zeta}]^T$. The linearized variational equations of motion are expressed in first order state space form as

$$\begin{pmatrix} \dot{\xi} \\ \dot{\eta} \\ \dot{\zeta} \\ \ddot{\xi} \\ \ddot{\eta} \\ \ddot{\zeta} \end{pmatrix} = \begin{bmatrix} 0 & 0 & 0 & 1 & 0 & 0 \\ 0 & 0 & 0 & 0 & 1 & 0 \\ 0 & 0 & 0 & 0 & 0 & 1 \\ U^*_{xx} & U^*_{xy} & U^*_{xz} & 0 & 2 & 0 \\ U^*_{yx} & U^*_{yy} & U^*_{yz} & -2 & 0 & 0 \\ U^*_{zx} & U^*_{zy} & U^*_{zz} & 0 & 0 & 0 \end{bmatrix} \begin{pmatrix} \xi \\ \eta \\ \zeta \\ \dot{\xi} \\ \dot{\eta} \\ \dot{\zeta} \end{pmatrix} \tag{2.66}$$

that is numerically integrated to determine the 6 states required to express the motion of a spacecraft uniquely. For ease of representation, if $\delta\bar{q}$ denotes the states $[\xi, \eta, \zeta, \dot{\xi}, \dot{\eta}, \dot{\zeta}]^T$, then $\delta\dot{\bar{q}} = A(t)\delta\bar{q}$ portrays equation (2.66), such that $A(t)$ is the 6x6 Jacobian matrix that is reduced to smaller 3x3 submatrices as,

$$A(t) = \begin{bmatrix} O_{3\times3} & I_{3\times3} \\ U_{XX} & \Omega_{3\times3} \end{bmatrix} \tag{2.67}$$

where O, I, U_{XX} and Ω are 3x3 submatrices of 6x6 Jacobian matrix in equation (2.66). Here, O denotes a zero matrix while I indicates an identity matrix.

2.2.2 Stability of the Equilibrium Points

The stability charactersitics of the linearized equations of motion facilitates the analysis of the local motion near the equilibrium points. There are numerous ways to define the stability of a solution depending on the objective of the given problem. An equilibrium point

is considered stable if the motion of a body that is subjected to any small perturbations remains bounded in the near neighborhood of the equilibrium point. The definition of the stability in this case is in lieu with Lyapunov Stability Criteria. Mathematically, an equilibrium point ψ_{e} is Lyapunov Stable if for all $\epsilon > 0$ there exists $\delta > 0$, such that if at time, $t = 0$, $||\psi(0) - \psi_{\mathrm{e}}|| < \delta$, then for $t \geq 0$, $||\psi(t) - \psi_{\mathrm{e}}|| < \epsilon$. Alternatively, if an initial perturbation δ is given about the equilibrium point then subsequent motion should remain bounded within a defined ϵ. Furthermore, the solution is said to be asymptotically stable if the solution satisfies the Lyapunov Stability, and, for an initial perturbation within some $\delta > 0$, i.e., at $t = 0$, $||\psi(0) - \psi_{\mathrm{e}}|| < \delta$, there exists,

$$\lim_{t \to \infty} ||\psi(0) - \psi_{\mathrm{e}}|| = 0 \tag{2.68}$$

indicating a convergent behavior.

The Lyapunov stability of a linearized system defined as $\delta\dot{\bar{q}} = A\delta\bar{q}$, is computed by inspecting the eigenvalues of the Jacobian Matrix A (assuming A constant). The eigenvalues λ_{i} are the roots of the characteristics equation of A for which the determinant $||\lambda I - A|| = 0$ is evaluated. A system is classified as unstable, marginally stable or asymptotically stable based on the eigenvalues. The criteria are

- **Unstable**: If at-least one of the eigenvalues have a positive real part, i.e., $\mathscr{R}(\lambda_{\mathrm{i}}) > 0$, then the linearized system is unstable. The corresponding nonlinear system is also unstable.

- **Marginally Stable**: If all of the eigenvalues are purely imaginary, i.e., $\mathscr{R}(\lambda_{\mathrm{i}}) = 0$, then the linearized system is marginally stable. A marginally stable linearized system is bounded but not asymptotically stable. No conclusions can be made about the stability of the corresponding nonlinear system.

- **Asymptotically Stable**: If all of the eigenvalues have negative real part, i.e., $\mathscr{R}(\lambda_{\mathrm{i}}) < 0$, then the linearized system is marginally stable. The corresponding nonlinear system is stable in the local vicinity.

The linearized equations of motion are computed about the equilibrium points to assess the stability. The equilibrium points computed in section 2.1.4 indicate that all of them lie in the plane of the primaries, i.e., $z = 0$. Therefore, partials given in equations (2.64) and (2.65) become $U^*_{xz} = U^*_{yz} = U^*_{zx} = U^*_{zy} = 0$. The linearized equations in (2.57) - (2.59) are simplified to three equations

$$\ddot{\xi} - 2\dot{\eta} = U^*_{xx}\xi + U^*_{xy}\eta \tag{2.69}$$

$$\ddot{\eta} + 2\dot{\xi} = U^*_{yx}\xi + U^*_{yy}\eta \tag{2.70}$$

$$\ddot{\zeta} = U^*_{zz}\zeta \tag{2.71}$$

with fewer number of partials. The linearized equations of motion about the equilibrium solutions expressed in equations (2.69) - (2.71) indicate that the motion of spacecraft in the out-of-plane direction, i.e., z direction given in (2.71) is decoupled from equations (2.69) and (2.70) that relate to the in-plane motion. Subsequently implying that the motion in the out-of-plane direction evolves independent of the motion in the plane of primaries.

Since the equation (2.71) is decoupled from the equations (2.69) and (2.70), the out of plane motion and the in-plane motion are analyzed independently. For all equilibrium points, $U^*_{zz} < 0$, hence out of plane motion in the vicinity of all equilibrium points undergo simple harmonic motion like a spring mass system. Moreover, the eigenvalues $\lambda_z = \pm i\omega_z = \pm i\sqrt{|U^*_{zz}|}$, implying marginal stability with the frequency of the out-of-plane motion given by $\omega_z = \sqrt{|U^*_{zz}|}$. For Lagrange points L4 and L5, the value of $|U^*_{zz}| = 1$, i.e., $\omega_z = 1$, hence the period of the out-of-plane motion $\wp = 2\pi/\omega_z = 2\pi$ (in non-dimensional unit) which is same as the period of the primaries. For variational in-plane motion about the equilibrium points, the states are given by $\delta\bar{q} = [\xi, \eta, \dot{\xi}, \dot{\eta}]^T$ such that,

$$\delta\dot{\bar{q}} = A_{xy}\delta\bar{q} \tag{2.72}$$

$$A_{xy} = \begin{bmatrix} O_{2\times2} & I_{2\times2} \\ U_{XX,2\times2} & \Omega_{2\times2} \end{bmatrix} \tag{2.73}$$

where A_{xy} denotes the Jacobian matrix of the in-plane motion, with submatrices as

$$U_{XX,2\times2} = \begin{bmatrix} U^*_{xx} & U^*_{xy} \\ U^*_{yx} & U^*_{yy} \end{bmatrix} \tag{2.74}$$

$$\Omega_{2\times2} = \begin{bmatrix} 0 & 2 \\ -2 & 0 \end{bmatrix} \tag{2.75}$$

while $O_{2\times2}$ is a 2×2 zero matrix and $I_{2\times2}$ is a 2×2 identity matrix. The eigenvalues of the in-plane system near the equilibrium points are the roots of the characteristic equations given by determinant $||\lambda I - A_{xy}|| = 0$, i.e.,

$$\lambda^4 + (4 - U^*_{xx} - U^*_{yy})\lambda^2 + (-2U^*_{xy} + 2U^*_{yx})\lambda + (U^*_{xx}U^*_{yy} - U^*_{xy}U^*_{yx}) = 0 \tag{2.76}$$

where the values U^*_{xx}, U^*_{xy} and U^*_{yx} are different for different equilibrium points. Consequently, each equilibrium point has different stability properties that are analyzed separately.

2.2.3 Motion near the Collinear Equilibrium Points

The collinear equilibrium points L1, L2 and L3 lie along the x-axis. Since $y_{L_i} = z_{L_i} = 0$, some of the terms in the linear variational equations of motion are nullified in the vicinity of these collinear Lagrange points, i.e., $U^*_{xy} = U^*_{yx} = 0$. Thus, the characteristic equation for the in-plane motion as in equation (2.76) simplifies to

$$\lambda^4 + (4 - U^*_{xx} - U^*_{yy})\lambda^2 + (U^*_{xx}U^*_{yy}) = 0 \tag{2.77}$$

with fewer variables. The eigenvalues corresponding to the system are the roots of the characteristic equations that are given by,

$$\lambda_{1,2} = \pm\sqrt{-\beta_1 + (\beta_1^2 + \beta_2^2)^{1/2}} \tag{2.78}$$

$$\lambda_{3,4} = \pm\sqrt{-\beta_1 - (\beta_1^2 + \beta_2^2)^{1/2}} \tag{2.79}$$

where, for simplicity β_1 and β_2 are defined as

$$\beta_1 = 2 - \frac{U^*_{xx} + U^*_{yy}}{2} \tag{2.80}$$

$$\beta_2^2 = -U^*_{xx}U^*_{yy} \tag{2.81}$$

that are functions of the pseudo-potential evaluated at the corresponding equilibrium point Li. Further, for additional simplicity, define

$$s = \sqrt{\beta_1 + (\beta_1^2 + \beta_2^2)^{1/2}} \tag{2.82}$$

$$\beta_3 = \frac{s^2 + U^*_{xx}}{2s} \tag{2.83}$$

as constants for representation. The analytical solution of the variational equations in terms of the position along x and y directions near the equilibrium points are expressed as

$$\xi = \sum_{\mathrm{i}=1}^{4} A_{\mathrm{i}} \mathrm{e}^{\lambda_{\mathrm{i}} t} \tag{2.84}$$

$$\eta = \sum_{\mathrm{i}=1}^{4} B_{\mathrm{i}} \mathrm{e}^{\lambda_{\mathrm{i}} t} \tag{2.85}$$

where A_{i} and B_{i} are coefficients corresponding to stimulated eigenvector with λ_{i} as the corresponding eigenvalue. Here, A_{i} and B_{i} are related to each other as

$$B_{\mathrm{i}} = \alpha_{\mathrm{i}} A_{\mathrm{i}} \tag{2.86}$$

$$\alpha_{\mathrm{i}} = \frac{\lambda_{\mathrm{i}}^2 - U^*_{xx}}{2\lambda_{\mathrm{i}}} \tag{2.87}$$

because of coupled xy motion. To identify the motion along a particular direction, the linearized variational model is perturbed along the corresponding eigenvector direction. It is important to note here that $\lambda_{3,4} = \pm is$ where s is as defined in equation (2.82) implying that $\lambda_{3,4}$ are purely imaginary indicating marginal stability, while $\lambda_{1,2}$ exists as positive and negative real pair. A periodic solution in the linearized system exists only along the eigenvalues $\lambda_{3,4}$, therefore any component of perturbations are nullified along directions

corresponding to eigenvalues $\lambda_{1,2}$ that potentially destabilizes the system due to its unstable component. Henceforth, conditions such that, $A_1 = A_2 = 0$ are set to modify equations (2.84) and (2.85) to

$$\xi = A_3 e^{\lambda_3 t} + A_4 e^{\lambda_4 t} \tag{2.88}$$

$$\eta = B_3 e^{\lambda_3 t} + B_4 e^{\lambda_4 t} = \alpha_3 A_3 e^{\lambda_3 t} + \alpha_4 A_4 e^{\lambda_4 t} \tag{2.89}$$

resulting in a solution may potentially be periodic in the vicinity of the collinear libration points. On evaluating, A_3 and A_4 in terms of $s, \alpha_3, \xi_0, \eta_0$, the analytical representation of the periodic behavior of the motion of the spacecraft in the vicinity of the collinear equilibrium points are given by

$$\xi = \xi_0 \, cos(s(\tau - \tau_0)) + \frac{\eta_0}{\beta_3} \, sin(s(\tau - \tau_0)) \tag{2.90}$$

$$\eta = \eta_0 \, cos(s(\tau - \tau_0)) - \xi_0 \beta_3 \, sin(s(\tau - \tau_0)) \tag{2.91}$$

$$\dot{\xi} = -\xi_0 s \, sin(s(\tau - \tau_0)) + \frac{\eta_0}{\beta_3} s \, cos(s(\tau - \tau_0)) \tag{2.92}$$

$$\dot{\eta} = -\eta_0 s \, sin(s(\tau - \tau_0)) - \xi_0 \beta_3 s \, sin(s(\tau - \tau_0)) \tag{2.93}$$

where, τ represents the non-dimensional time. The linearized variational equations of motion are developed given the initial perturbation in position (ξ_0, η_0) and in velocity $(\dot{\xi_0}, \dot{\eta_0})$, in the x and y directions respectively at initial non-dimensional time τ_0. The time period of formed orbit is given by

$$\wp = \frac{2\pi}{s} \tag{2.94}$$

as expressed in non-dimensional time.

2.2.4 Motion near the Triangular Equilibrium Points

Similar to collinear libration points, analytical linearized variational equations of motion are used to leverage the dynamics in the proximity of the triangular libration points. The out-

of-plane motion is decoupled from the in-plane motion, and hence, they evolve independently. As discussed in section 2.2.2, the period of the out-of-plane motion is same as the period of the primaries about the barycenter. While, the in-plane motion is given by the characteristic equation given in equation (2.76). For equilibrium points L4 and L5, the partials of the pseudo-potential functions are evaluated as

$$U^*_{xx} = \frac{3}{4} \tag{2.95}$$

$$U^*_{yy} = \frac{9}{4} \tag{2.96}$$

$$U^*_{xy} = U^*_{yx} = \pm\frac{3\sqrt{3}}{2}\left(\mu - \frac{1}{2}\right) \tag{2.97}$$

where U^*_{xy} and U^*_{yx} are positive for L4 and negative for L5. On substituting these in equation (2.76), the characteristic equations for the in-plane motion becomes,

$$\lambda^4 + \lambda^2 + \frac{27}{4}\mu\left(1-\mu\right) = 0 \tag{2.98}$$

that is a function of the system mass ratio, μ. The roots of the characteristic equation are computed as

$$\lambda_{1,2} = \pm\sqrt{\frac{1}{2}\left(-1+\sqrt{g}\right)} \tag{2.99}$$

$$\lambda_{3,4} = \pm\sqrt{\frac{1}{2}\left(-1-\sqrt{g}\right)} \tag{2.100}$$

such that,

$$g = 1 - 27\mu\left(1-\mu\right) \tag{2.101}$$

is a constant value defined for simplicity.

The eigenvalues that determine the stability of the system depends on the value of g that is a function of system mass ratio μ, therefore the stability characteristics of the triangular

equilibrium points in various three-body systems are different. The stability characteristics alter at certain critical system mass ratios as explained.

- $0 < g < 1$ or $0 < \mu < 0.03852$

  On careful inspection, it is evident that for all values of $0 < \mu < 0.03852$, $\lambda_{1,2}$ and $\lambda_{3,4}$ are purely imaginary, hence the motion of the third body about the triangular equilibrium points is periodic in linear sense. The eigenvalues are represented in terms of their frequencies, i.e., $\lambda_{1,2} = \pm \mathrm{i}\omega_1$ and $\lambda_{3,4} = \pm \mathrm{i}\omega_2$, where ω_1 is the smaller frequency that corresponds to long period motion ($\wp = 2\pi/\omega_1$) and ω_2 is the larger frequency that corresponds to short period motion ($\wp = 2\pi/\omega_2$). The motion near the Lagrange points L4 and L5 are a linear combination of the short period motion and the long period motion. Stability in the nonlinear system is however not determined. The characteristics remain same for $0.96148 < \mu < 1$ except that the positions of the primaries bodies are interchanged.

- $g = 0$ or $\mu = 0.03852$

  At this critical mass ratio, $\lambda_{1,2} = \lambda_{3,4} = \pm \left(1/\sqrt{2}\right) \mathrm{i}$, which means that one of the short period or long period motion is eliminated. Additionally in the linear model, repeated imaginary eigenvalues results in an unstable system.

- $g < 0$ or $0.03852 < \mu$

  For any three-body system with mass ratio μ such that, $0.03852 < \mu$ (or $\mu < 1 - 0.03852 = 0.96148$), the eigenvalues exists in the form

$$\lambda_{1,2} = \pm\sqrt{\frac{1}{2}\left(-1 + \sqrt{g}\right)} = \pm\sqrt{\frac{1}{2}\left(-1 \pm \mathrm{i}\delta\right)} \tag{2.102}$$

$$\lambda_{3,4} = \pm\sqrt{\frac{1}{2}\left(-1 - \sqrt{g}\right)} = \pm\sqrt{\frac{1}{2}\left(-1 \mp \mathrm{i}\delta\right)} \tag{2.103}$$

  where $\sqrt{g} = \pm \mathrm{i}\delta$. The eigenvalues for this range of μ value system exist in the form $\lambda_{\mathrm{i}} = p + \mathrm{i}q$, with two positive real and two negative real part, making the system unsta-

ble. Nevertheless, initial conditions selected wisely in the direction of the eigenvector corresponding to the negative real eigenvalue results in an asymptotically stable linear system in the local vicinity of the equilibrium points. The third body undergoes a spiral motion eventually approaching the triangular equilibrium point.

- $g \geq 1$ or $\mu \leq 0$, $1 \leq \mu$
  Such mass ratio indicates negative mass for either of the primary body. Such system cannot exist physically.

2.3 Higher-Fidelity Ephemeris Model

The circular restricted three-body problem fundamentally captures the motion of a spacecraft due to concurrent gravitational interaction with two main primary bodies. The presence of other non-finite gravitational bodies affects the motion of the spacecraft. The higher fidelity model is a more accurate representation of the complex dynamical regime, that exhibits characteristics similar to the CR3BP, and used to represent accurate trajectory designs and compute orbit maintenance costs with reduced errors. Using the n-body relative equations of motion, a more accurate representation of the spacecraft motion is rendered, one that accommodates the time-varying relative location of the celestial bodies in modeling the gravitational forces acting on the spacecraft. DE421 planetary ephemerides from NASA Jet Propulsion Laboratory (JPL) is used to identify the position and velocity of different celestial bodies used in simulating in the higher-fidelity model. The inclusion of precise orbit eccentricities and inclination in the ephemeris model improves the authenticity of the solutions unlike in the lower fidelity CR3BP model where such parameters are either ignored or assumed constant.

2.3.1 *n*-body Dynamical Model

For improved accuracy, the governing equations of motion of the body of interest is derived in the n-body dynamical regime. The additional higher-fidelity force terms enhances the solution over the restricted three-body problem. The objective of the ephemeris model is

to investigate the motion of a body P_{i} in an n-body gravitational model. In section 2.1, the differential equations of motion of a n-body model are written with respect to an inertially fixed base point. Since the DE421 planetary ephemerides data provides relative location of a celestial body with respect to another, it is practically convenient to formulate the equations of motion with respect to a central body P_q as portrayed in Figure 2.6. The central body is denoted by subscript q, the object of interest or the spacecraft as i, while the remaining of the n bodies are labeled as j. The vector $\bar{r}_{q\mathrm{i}}$ represents the relative position of spacecraft with respect to the central body.

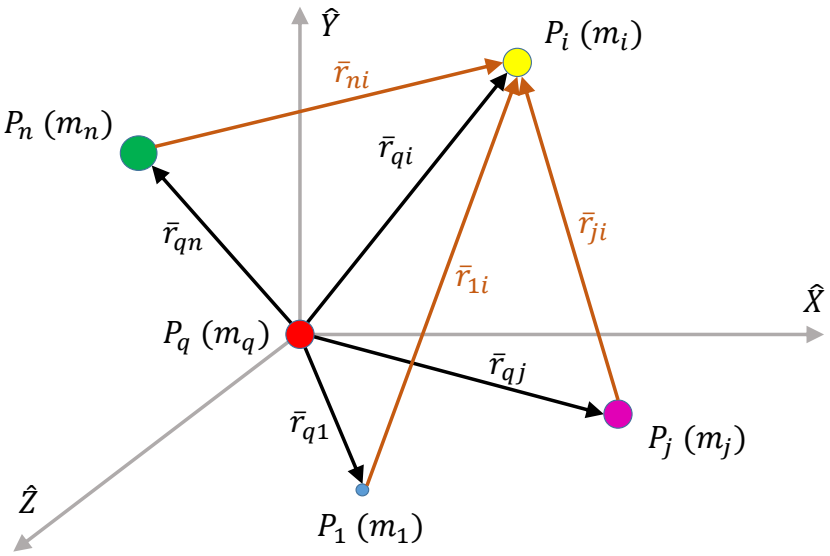

Figure 2.6. Geometry of the n-body problem.

A second order vector differential equation that governs the motion of the spacecraft relative to the central body is derived using the instantaneous position vectors $\bar{r}_{\mathrm{ij}}$ and $\bar{r}_{q\mathrm{j}}$, as demonstrated in Figure 2.6, as

$$\ddot{\bar{r}}_{q\mathrm{i}} = -\frac{\tilde{G}(m_{\mathrm{i}} + m_q)}{r_{q\mathrm{i}}^3}\bar{r}_{q\mathrm{i}} + \tilde{G}\sum_{\substack{\mathrm{j}=1 \\ \mathrm{j}\neq \mathrm{i},q}}^{n} m_{\mathrm{j}}\left(\frac{\bar{r}_{\mathrm{ij}}}{r_{\mathrm{ij}}^3} - \frac{\bar{r}_{q\mathrm{j}}}{r_{q\mathrm{j}}^3}\right) \tag{2.104}$$

where the vector $\bar{r}_{q\mathrm{j}}$ is directly obtained from DE421 ephemerides data while the vector $\bar{r}_{\mathrm{ij}}$ is obtained by vector operation, i.e.,

$$\bar{r}_{\mathrm{ij}} = \bar{r}_{q\mathrm{j}} - \bar{r}_{q\mathrm{i}} \tag{2.105}$$

where the vector $\bar{r}_{q\mathrm{i}}$ is the position of the spacecraft relative to the central body. Additionally, $\bar{r}_{\mathrm{ij}} = -\bar{r}_{\mathrm{ji}}$ denotes the relative location of the perturbing body P_{j} with respect to the body of interest P_{i}.

The n-body equations of motion as given in equation (2.104) are expressed in dimensional units, however, for practical use and ease of numerical computation, these terms are non-dimensionalized using corresponding characteristic quantities of the most relevant CR3BP system. The accuracy of this model is further improved by additional force models such as Solar Radiation Pressure and J2 perturbations incorporated into Equation (2.104), i.e.,

$$\ddot{\bar{r}}_{q\mathrm{i}} = -\frac{\tilde{G}(m_{\mathrm{i}} + m_q)}{r_{q\mathrm{i}}^3}\bar{r}_{q\mathrm{i}} + \tilde{G}\sum_{\substack{\mathrm{j}=1 \\ \mathrm{j}\neq \mathrm{i},q}}^{n} m_{\mathrm{j}}\left(\frac{\bar{r}_{\mathrm{ij}}}{r_{\mathrm{ij}}^3} - \frac{\bar{r}_{q\mathrm{j}}}{r_{q\mathrm{j}}^3}\right) + \mathrm{a}_{SRP}\hat{r}_{Sun,\mathrm{i}} + \bar{\varrho}_{J2,q\mathrm{i}} \tag{2.106}$$

such that $-\dfrac{\tilde{G}(m_{\mathrm{i}} + m_q)}{r_{q\mathrm{i}}^3}\bar{r}_{q\mathrm{i}}$ is the dominant gravitational acceleration due to body P_q, while $-\tilde{G}m_{\mathrm{j}}\dfrac{\bar{r}_{\mathrm{ij}}}{r_{\mathrm{ij}}^3}$ is the direct perturbing acceleration and $\tilde{G}m_{\mathrm{j}}\dfrac{\bar{r}_{q\mathrm{j}}}{r_{q\mathrm{j}}^3}$ is the indirect perturbing acceleration due by body P_{j} on spacecraft P_{i}. The sum of the direct and indirect perturbing acceleration, i.e., $-\tilde{G}m_{\mathrm{j}}\left(\dfrac{\bar{r}_{\mathrm{ij}}}{r_{\mathrm{ij}}^3} - \dfrac{\bar{r}_{q\mathrm{j}}}{r_{q\mathrm{j}}^3}\right)$ is the resultant net gravitational acceleration on spacecraft P_{i} due to body P_{j}. The quantity $\mathrm{a}_{SRP}\hat{r}_{Sun,\mathrm{i}}$ is the acceleration due to solar radiation pressure acting on the spacecraft in the direction away from the Sun, and, finally, $\bar{\varrho}_{J2,q\mathrm{i}}$ is the J2 perturbing acceleration on the spacecraft due to oblateness of body P_q. It is further assumed that the J2 perturbing accelerations due to non-central bodies are negligible and therefore not included in Equation (2.106).

In a circular restricted three-body problem, the coordinate system is defined about the barycenter of the two primary bodies P_1 and P_2, and, therefore, it is sometimes convenient

to compare the magnitude of gravitational forces acting on the spacecraft with respect to the barycenter. Such gravitational acceleration quantities are given by

$$\ddot{\bar{r}}_{B\mathrm{i}} = (1-\mu)\ddot{\bar{r}}_{1,\mathrm{i}} + \mu\ddot{\bar{r}}_{2,\mathrm{i}} \tag{2.107}$$

where $\ddot{\bar{r}}_{P_1\mathrm{i}}$ and $\ddot{\bar{r}}_{P_2\mathrm{i}}$ are values calculated using Equation (2.106) for central bodies $P1$ and $P2$ respectively. The magnitudes of gravitational forces thus determined, offer insight into the most influencing forces that must be considered while modeling a real scenario.

2.3.2 Solar Radiation Pressure

The effect of the solar radiation pressure (SRP) on a spacecraft depends on its mass, sectional area facing the Sun, and the coefficient of reflectivity. Of course, the orientation of the spacecraft impacts the acceleration due to SRP, however, unless the specific dimensions and the orientation of the spacecraft is unknown it is challenging to model the effects of SRP. A simple and convenient cannonball model is assumed to model the spacecraft. An equivalent spherical model overcomes the effect of the orientation of the spacecraft as the sectional area facing the Sun is a constant. The effect of an additional perturbing force due to solar radiation pressure (SRP) acting on the spacecraft surface is trivial if modeled as a point mass. In reality, however, the area of the spacecraft is non-zero. For a spacecraft with a perfectly reflective surface, the mass to area ratio, $\sigma^*_{MAR} = 1.53 \times 10^{-3}$ kg/m^2 is the critical value at which the solar radiation pressure acting on the spacecraft is exactly equal to the gravitational force acting due to the Sun. A dimensionless sail lightness parameter β_{sail} (or sail loading parameter) is defined as

$$\beta_{sail} = \frac{\sigma^*_{MAR}}{\sigma_{MAR}} \tag{2.108}$$

that is effectively the ratio between the solar radiation pressure acting on the spacecraft to the gravitational force due to the Sun [91], [92]. The value of $\beta_{sail} = 0$, represent a point

mass object. The acceleration due to the solar radiation pressure acting on the spacecraft is given as

$$\mathrm{a}_{SRP} = \beta_{sail} \left(\frac{C_r}{2}\right) \frac{\tilde{G} M_S}{R_{S-s/c}^2} \, cos^2(\alpha) \, \hat{n}_{sail} \tag{2.109}$$

where, α is the angle between the direction of incident photons and the normal to the surface of the spacecraft, $\hat{n}_{sail}$ is the direction normal to the surface of the spacecraft, $\tilde{G}$ is the universal gravitational constant, M_S is the mass of the Sun, $R_{S-s/c}$ is the distance from the Sun to the spacecraft while C_r is a material parameter such that $0 \leq C_r \leq 2$ where $C_r = 2$ indicates perfectly reflective surface while $C_r = 0$ indicates perfectly light absorbing surface [91], [92]. For convenience, it is assumed that the surface of the spacecraft is perfectly reflective, i.e., $C_r = 2$, and the maximum area of the spacecraft is facing the Sun at all times, i.e., $\alpha = 0^o$, consequently incorporating the maximum impact of the solar radiation pressure. Of course, errors in SRP is simulated by altering the coefficient of reflectivity, C_r, and the sectional area of the spacecraft facing the Sun. In general, if the mass to area ratio (σ_{MAR}) of the spacecraft is small, i.e., a less dense spacecraft, then the effect of the SRP is more prominent.

2.4 Coordinate Frame

Newton's laws of motion hold true in an inertial frame of reference; one that is not accelerating [93]. In other words, the center of mass of a system of interacting bodies is at rest or in uniform motion for Newton's laws of motion to be applicable. In true sense, there is no such location that is non-accelerating, unless the center of the universe is considered to be one. Also, the inertial frame is chosen for convenience to address a particular problem. For events that span over a billion years, a frame fixed at the center of the universe is an appropriate choice. For events that span under a million years, the center of the galaxy is a decent choice to place the origin of an inertial frame. A mission scenario that spans over a few years, an inertial frame at the center of the solar system is a sufficient choice. For the kinematics problems, one that span over a few seconds, the Earth itself is considered non-accelerating. Depending on the time-span of the problem of interest, an inertial frame is

defined such that the effect of the Coriolis force is negligible, as the angular rate of rotation over the time-span is insignificant.

Space missions typically span for a few years and for such a time-span the center of the solar system is assumed to be non-accelerating. As a consequence, the motion of a spacecraft is captured using Newton's equations of motion expressed relative to an inertial frame defined with an origin at the center of the solar system. An accurate representation of the inertial frame is crucial for consistency and accuracy for representation of spacecraft motion among various researchers and organizations across the globe. Fundamentalkatalog (FK) is a series of six astrometric catalogues of high precision positional data for a small selection of stars that defines a celestial reference frame and offers a standard coordinate system for measuring positions of stars [94]. The fifth of the series update, FK5 J2000, calibrated relative to 1535 stars, is defined with the Earth mean equator and equinox of J2000.0 epoch (1 Jan 2000 12:00:00.000 TDB). FK5 J2000 model, or commonly J2000 model, use optical methods based on positional data of the stars to identify the reference frame. With more sophisticated calibration using interferometry, the International Celestial Reference Frame (ICRF) is more accurate than the FK5 J2000 model that is derived from optical calibration. Very-long-baseline interferometry (VLBI) approaches track extra-galactic quasars and offer more precise measurements, hence, supersedes the FK5 J2000.0 version. The orientation of the ICRF frame and the FK5 J2000 frame are fairly consistent and only differ by a few arc-radians. For implementing the Newton's relative equations of motion, the relative planetary positions are retrieved from Spice Kernals provided by NASA JPL. As per the Spice Kernals user guide, 'J2000' essentially denotes the updated ICRF frame [95].

2.5 Coordinate Frame Transformations

The circular restricted three-body problem is formulated in the coordinate frame that rotates along with the primaries. With respect to an inertial frame, such a frame appears to be rotating at a rate equal to the angular velocity of the primaries about its barycenter, hence, commonly denoted as the rotating frame. The motion of a spacecraft relative to the primaries is not easily perceived in the inertial frame. Furthermore, the ephemeris data is

expressed in the inertial coordinate frame. It is crucial to transform position and velocity states from one coordinate frame to the other, to visualize the motion of a spacecraft in each of the frames. The apparent motion in one frame may not reveal its behavior in the other frame, therefore, regardless of the frame in which the trajectory is computed, for visual understanding coordinate transformation of the states becomes necessary.

2.5.1 Correlating the Inertial and Rotating Coordinate Frames

A straight forward approach to correlate states in one frame to another is to use a transformation matrix that is multiplied directly to the states in one frame to get the states in the other frame. Figure 2.2 indicates the relation between the rotating frame and the inertial frame. The rotating coordinate frame, $\underline{\mathcal{R}}$, is labelled using unit vectors $\hat{x}, \hat{y}, \hat{z}$ (small letters) while the inertial coordinate frame, $\underline{\mathcal{I}}$, is labelled using unit vectors $\hat{X}, \hat{Y}, \hat{Z}$ (capital letters). The angle that relates frame $\underline{\mathcal{R}}$ to frame $\underline{\mathcal{I}}$ given by θ, that is a function of non-dimensional time, such that, $\theta = \dot{\theta}\tau = \tau$, as $\dot{\theta} = 1$ for CR3BP in non-dimensional units. The Direction Cosine Matrix (DCM) defined as ${}^{I}C^{R}$,

$$ {}^{I}C^{R} = \begin{bmatrix} cos(\theta) & -sin(\theta) & 0 \\ sin(\theta) & cos(\theta) & 0 \\ 0 & 0 & 1 \end{bmatrix} \tag{2.110} $$

that transforms the position states in the rotating frame to the inertial frame as

$$ \begin{bmatrix} r_X \\ r_Y \\ r_Z \end{bmatrix} = {}^{I}C^{R} \begin{bmatrix} r_x \\ r_y \\ r_z \end{bmatrix} \tag{2.111} $$

where the superscript R in ${}^{I}C^{R}$ indicates that the column vector of the states in the rotating frame is multiplied to the DCM. Similarly, a direction cosine matrix ${}^{R}C^{I}$ is used to convert the states in inertial frame to rotating frame where ${}^{R}C^{I} = \left[{}^{I}C^{R}\right]^{-1}$.

Since velocity components are derivatives of position with respect to time the conversion from inertial frame to rotating frame requires an additional consideration. Either using the equation (2.16) or by taking the derivative of equation (2.111) with respect to non-dimensional time, the velocity between the two frames is related as

$$\begin{bmatrix} v_X \\ v_Y \\ v_Z \end{bmatrix} = {}^{I}\dot{C}^{R} \begin{bmatrix} r_x \\ r_y \\ r_z \end{bmatrix} + {}^{I}C^{R} \begin{bmatrix} v_x \\ v_y \\ v_z \end{bmatrix} \tag{2.112}$$

where ${}^{I}\dot{C}^{R}$ indicates derivative of each element of ${}^{I}C^{R}$ with respect to non-dimensional time. A combined, total transformation matrix is established that converts both the position and velocity states from the rotating frame to the inertial frame as

$$\begin{bmatrix} r_X \\ r_Y \\ r_Z \\ x_X \\ x_Y \\ x_Z \end{bmatrix} = \begin{bmatrix} {}^{I}C^{R} & O_{3x3} \\ {}^{I}\dot{C}^{R} & {}^{I}C^{R} \end{bmatrix} \begin{bmatrix} r_x \\ r_y \\ r_z \\ v_x \\ v_y \\ v_z \end{bmatrix} \tag{2.113}$$

where O_{3x3} is a 3×3 zero matrix. Similarly, full states from inertial frame is converted to the rotating frame using the inverse of 6×6 DCM used in equation (2.113).

2.5.2 Correlating the Inertial J2000 and Rotating Coordinate Frames

Transitioning from an Inertial J2000 frame to a rotating frame is comparable to the transformation in section 2.5.1 except that the planetary ephemerides information is also incorporated to enable the transformation. Since the barycenter of the two main primary bodies P_1 and P_2 is not inertially fixed, it is not possible to introduce the rotation matrix with respect to the barycenter. Instead, it is convenient to convert to a primary centered ro-

tating frame centered at the main primary body P_1. The instantaneous position and velocity of the smaller primary with respect to the main primary obtained from DE421 ephemerides data is used to convert the frame.

The rotating frame is derived from the available relative positions of primaries from the ephemerides data. Let the vector

$$\bar{R} = \bar{r}_{12} = \begin{bmatrix} r_X \\ r_Y \\ r_Z \end{bmatrix} \tag{2.114}$$

be the instantaneous position of smaller primary with respect to the main primary obtained from DE421 Ephemerides in the primary centered inertial frame. In the rotating frame the smaller primary is always directed along the positive x-axis of the rotating frame while z-axis corresponds to the direction of the angular momentum and y-axis completes the dextral coordinate system. Using the same principle, the instantaneous rotating frame is defined as

$$\hat{x} = \frac{\bar{R}}{||\bar{R}||} \tag{2.115}$$

$$\hat{z} = \frac{\bar{R} \times \bar{V}}{||\bar{R} \times \bar{V}||} \tag{2.116}$$

$$\hat{y} = \hat{z} \times \hat{x} \tag{2.117}$$

where $\bar{R}$ and $\bar{V}$ are the instantaneous position and velocity vectors of smaller primary body P_2 with respect to the main primary P_1, expressed in the primary centered inertial J2000

frame. The instantaneous transformation matrix to convert position in primary centered rotating frame to inertial J2000 frame is given by

$$ {}^{I}C^{R} = \begin{bmatrix} \hat{x} & \hat{y} & \hat{z} \end{bmatrix} = \begin{bmatrix} C_{11} & C_{12} & C_{13} \\ C_{21} & C_{22} & C_{23} \\ C_{31} & C_{32} & C_{33} \end{bmatrix} \tag{2.118} $$

where each C_{ij} represents the (i,j)-th term of the transformation matrix ${}^{I}C^{R}$. The DCM, ${}^{I}C^{R}$, transforms the position of a body represented in the primary centered rotational frame to the primary centered inertial J2000 frame as

$$ \begin{bmatrix} X_{PC} \\ Y_{PC} \\ Z_{PC} \end{bmatrix} = {}^{I}C^{R} \begin{bmatrix} x_{PC} \\ y_{PC} \\ z_{PC} \end{bmatrix} \tag{2.119} $$

such that, the subscript PC denotes that the vectors in rotating and inertial frame of reference are with respect to primary center.

Contradictory to the circular restricted three-body problem, the angular velocity in an ephemeris model is not constant, instead, it is a time variant function. The instantaneous angular velocity defined as

$$ \dot{\theta} = \frac{h}{||\bar{R}||^2} = \frac{\bar{R} \times \bar{V}}{||\bar{R}||^2} \tag{2.120} $$

is used to relate the velocity of the body of interest in the primary centered rotating frame to the primary centered inertial J2000 frame.

The Basic Kinematic Equation (BKE) is used to correlate the velocity of the body of interest P_3 in the primary centered rotating frame to the velocity in the primary centered inertial frame. It is mathematically expressed as

$$\frac{{}^{I}d\bar{r}_{13}}{d\tau} = \frac{{}^{R}d\bar{r}_{13}}{d\tau} + {}^{I}\omega^{R} \times \bar{r}_{13} \tag{2.121}$$

where subscript 1 denotes the primary body. For simplicity, this is denoted in the primary centered system where all measurements of the spacecraft are taken with respect to this primary body, hence, $\bar{r}_{PC} = \bar{r}_{13}$. Therefore, the Basic Kinematic equation is expressed alternatively as

$$\frac{{}^{I}d\bar{r}_{PC}}{d\tau} = \frac{{}^{R}d\bar{r}_{PC}}{d\tau} + {}^{I}\omega^{R} \times \bar{r}_{PC} \tag{2.122}$$

$$\frac{{}^{I}d\bar{r}_{PC}}{d\tau} = (\dot{x}_{PC} - \dot{\theta}y_{PC})\hat{x} + (\dot{y}_{PC} + \dot{\theta}x_{PC})\hat{y} + \dot{z}_{PC}\hat{z} \tag{2.123}$$

where ${}^{I}\omega^{R} = \dot{\theta}\hat{z}$ represents the angular velocity of the instantaneous primary centered rotating frame to the primary centered inertial J2000 frame. Equation (2.123) is used to correlate velocity in the inertial frame to the position and velocity states in the primary centered rotational frame. When expressed in the matrix form, equation (2.123) becomes

$$\begin{bmatrix} \dot{X}_{PC} \\ \dot{Y}_{PC} \\ \dot{Z}_{PC} \end{bmatrix} = \begin{bmatrix} \dot{\theta}C_{12} & -\dot{\theta}C_{11} & 0 & C_{11} & C_{12} & C_{13} \\ \dot{\theta}C_{22} & -\dot{\theta}C_{21} & 0 & C_{12} & C_{22} & C_{23} \\ \dot{\theta}C_{32} & -\dot{\theta}C_{31} & 0 & C_{13} & C_{32} & C_{33} \end{bmatrix} \begin{bmatrix} x_{PC} \\ y_{PC} \\ z_{PC} \\ \dot{x}_{PC} \\ \dot{y}_{PC} \\ \dot{z}_{PC} \end{bmatrix} \tag{2.124}$$

where velocity states in the inertial frame are now a function of both position and velocity states in the rotating frame. Combining equations (2.119) and (2.124) provides a 6×6 transformation matrix that converts the three position and three velocity states of the body of interest in the primary centered rotational frame to the primary centered inertial J2000 frame in a single step, i.e.,

$$\begin{bmatrix} X_{PC} \\ Y_{PC} \\ Z_{PC} \\ \dot{X}_{PC} \\ \dot{Y}_{PC} \\ \dot{Z}_{PC} \end{bmatrix} = \begin{bmatrix} C_{11} & C_{12} & C_{13} & 0 & 0 & 0 \\ C_{12} & C_{22} & C_{23} & 0 & 0 & 0 \\ C_{13} & C_{32} & C_{33} & 0 & 0 & 0 \\ \dot{\theta}C_{12} & -\dot{\theta}C_{11} & 0 & C_{11} & C_{12} & C_{13} \\ \dot{\theta}C_{22} & -\dot{\theta}C_{21} & 0 & C_{12} & C_{22} & C_{23} \\ \dot{\theta}C_{32} & -\dot{\theta}C_{31} & 0 & C_{13} & C_{32} & C_{33} \end{bmatrix} \begin{bmatrix} x_{PC} \\ y_{PC} \\ z_{PC} \\ \dot{x}_{PC} \\ \dot{y}_{PC} \\ \dot{z}_{PC} \end{bmatrix} \tag{2.125}$$

where the transformation matrix is a function of C_{ij} obtained from equation (2.118) and $\dot{\theta}$ obtained from equation (2.120). Since the bottom left 3×3 matrix is dimensional due to the presence of $\dot{\theta}$ that is measured in rad/s, the entire transformation is done in the dimensional units. Once transformed, the vectors is non-dimensionalized for convenience. Similar to the transformation procedure in the circular restricted model, the states in the primary centered J2000 inertial frame is converted to the primary centered rotating frame by taking the inverse of the transformation matrix, as required.

3. DYNAMICAL SYSTEMS THEORY

From the mission perspective, it is vital to deduce an initial condition that drives the spacecraft to the desired final states. The nonlinear equations of motion of the Circular Restricted Three Body Problem does not provide the observability to estimate the initial state to reach a particular target. The desired final state may be close to observed final state along any baseline trajectory. The initial conditions can be modified in infinite ways out of which only one true initial condition would drive to the target, thus it is highly unlikely that a chosen starting condition drives to the desired end. The Dynamical Systems theory provides intuitive schemes to predict the right conditions that leads to the desired final states.

3.1 State Transition Matrix

The *State Transition Matrix (STM)* is a linear operator that correlates the initial variation about the baseline solution to the variation at the end. It is a fundamental tool that predicts the changes in states at the final time due to certain minute changes in initial condition contemplated in the linear sense. Similar to linearizing the nonlinear equations of motions of CR3BP about its equilibria, linearization is exercised along a fixed baseline/reference trajectory using Taylor series expansion to develop the State Transition Matrix.

The State Transition Matrix is formulated by considering the flow of a trajectory nearby a reference trajectory. Let the reference trajectory be represented by the asterisks(*) symbol, the initial initial state vector $\bar{x}_0^*$ is propagated for time, t, to a final state $\bar{x}^*(t)$. Let a nearby varied trajectory, with isochronous correspondence, be obtained by perturbing the initial states of the reference trajectory and propagating for the same time, t, as demonstrated in Figure 3.1. Let the initial condition of the perturbed solution be denoted by

$$\bar{x}_0 = \bar{x}_0^* + \delta\bar{x}_0 \tag{3.1}$$

where $\delta\bar{x}_0$ is the small perturbation applied at the initial time. The new initial condition drives the solution to a new final state $\bar{x}(\bar{x}_0, t)$ such that,

$$\bar{x}(\bar{x}_0, t) = \bar{x}^*(\bar{x}_0^*, t) + \delta\bar{x}(t) \tag{3.2}$$

where $\delta\bar{x}(t)$ is the small variation about the reference solution at time, t, while the elements within the brackets, $(\bar{x}_0, t)$ and $(\bar{x}_0^*, t)$ are the initial state vector they were propagated from, and the time of propagation. Since $\bar{x}_0 = \bar{x}_0^* + \delta\bar{x}_0$, equation (3.2) becomes,

$$\bar{x}(\bar{x}_0^* + \delta\bar{x}_0, t) = \bar{x}^*(\bar{x}_0^*, t) + \delta\bar{x}(t) \tag{3.3}$$

where all the vectors are presented purely in terms of states of the nearby reference solution and the corresponding perturbation at anytime t. First order Taylor expansion applied to equation (3.3) as

$$\bar{x}^*(\bar{x}_0^*, t) + \frac{\partial\bar{x}}{\partial\bar{x}_0}\delta\bar{x}_0 + H.O.T.s = \bar{x}^*(\bar{x}_0^*, t) + \delta\bar{x}(t) \tag{3.4}$$

to compute the linear State transition Matrix. Since approximation only up to first oder is required, the higher order terms $H.O.T.s$ are neglected to yield

$$\frac{\partial\bar{x}}{\partial\bar{x}_0}\delta\bar{x}_0 \approx \delta\bar{x}(t) \tag{3.5}$$

where the partial $\dfrac{\partial\bar{x}}{\partial\bar{x}_0}$ is the $n \times n$ sensitivity matrix or the State Transition Matrix which is a linear correlation between the initial variation to the variation at the final time computed along some baseline trajectory. The perturbation vectors $\delta\bar{x}_0$ and $\delta\bar{x}(t)$ are $n \times 1$ matrices that relates to the variation in the n states measured along the reference trajectory at initial time t_0 and final time t respectively.

Specifically for the circular restricted three-body problem where there are 6 states inclusive of 3 position and 3 velocity states, the State Transition Matrix is of the size 6×6.

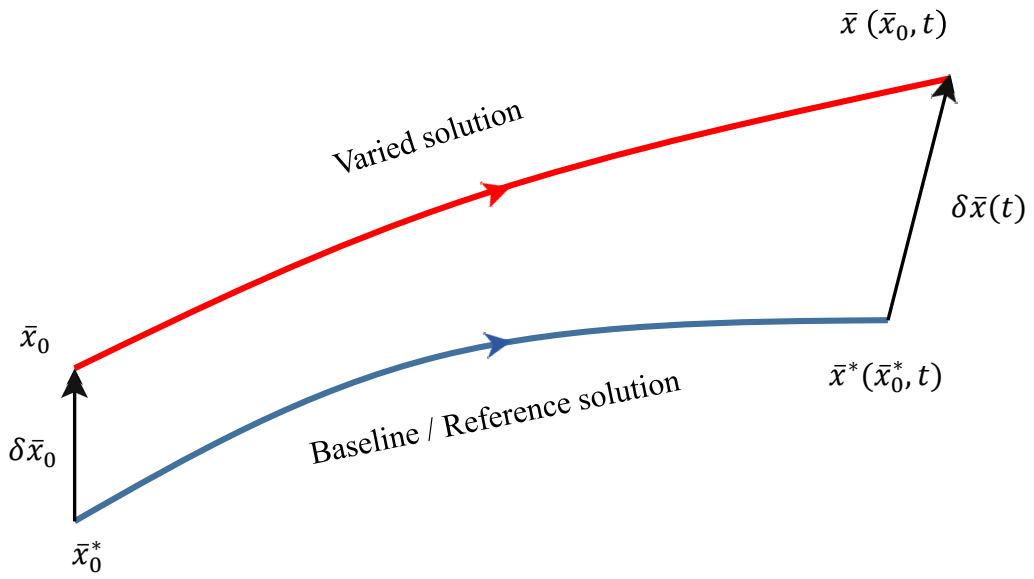

Figure 3.1. Baseline/Reference solution and isochronous variations.

The partials in the STM is calculated by propagating the states along the reference orbit for time, t, as

$$\phi(t,t_0) = \frac{\partial \bar{x}(t)}{\partial \bar{x}_0} = \begin{bmatrix} \frac{\partial x}{\partial x_0} & \frac{\partial x}{\partial y_0} & \frac{\partial x}{\partial z_0} & \frac{\partial x}{\partial \dot{x}_0} & \frac{\partial x}{\partial \dot{y}_0} & \frac{\partial x}{\partial \dot{z}_0} \\ \frac{\partial y}{\partial x_0} & \frac{\partial y}{\partial y_0} & \frac{\partial y}{\partial z_0} & \frac{\partial y}{\partial \dot{x}_0} & \frac{\partial y}{\partial \dot{y}_0} & \frac{\partial y}{\partial \dot{z}_0} \\ \frac{\partial z}{\partial x_0} & \frac{\partial z}{\partial y_0} & \frac{\partial z}{\partial z_0} & \frac{\partial z}{\partial \dot{x}_0} & \frac{\partial z}{\partial \dot{y}_0} & \frac{\partial z}{\partial \dot{z}_0} \\ \frac{\partial \dot{x}}{\partial x_0} & \frac{\partial \dot{x}}{\partial y_0} & \frac{\partial \dot{x}}{\partial z_0} & \frac{\partial \dot{x}}{\partial \dot{x}_0} & \frac{\partial \dot{x}}{\partial \dot{y}_0} & \frac{\partial \dot{x}}{\partial \dot{z}_0} \\ \frac{\partial \dot{y}}{\partial x_0} & \frac{\partial \dot{y}}{\partial y_0} & \frac{\partial \dot{y}}{\partial z_0} & \frac{\partial \dot{y}}{\partial \dot{x}_0} & \frac{\partial \dot{y}}{\partial \dot{y}_0} & \frac{\partial \dot{y}}{\partial \dot{z}_0} \\ \frac{\partial \dot{z}}{\partial x_0} & \frac{\partial \dot{z}}{\partial y_0} & \frac{\partial \dot{z}}{\partial z_0} & \frac{\partial \dot{z}}{\partial \dot{x}_0} & \frac{\partial \dot{z}}{\partial \dot{y}_0} & \frac{\partial \dot{z}}{\partial \dot{z}_0} \end{bmatrix} \tag{3.6}$$

where $[x, y, z, \dot{x}, \dot{y}, \dot{z}]^T$ are the final states along the reference orbit propagated using initial conditions, $[x_0, y_0, z_0, \dot{x}_0, \dot{y}_0, \dot{z}_0]^T$. At time $t = t_0$, since the initial and final states along the reference trajectory is the same, the STM $\phi(t_0, t_0) = I_{6\times6}$, a six-dimensional identity matrix, mathematically this describes the derivative of the initial states with respect to itself. The 6×6 STM can be written in a more compact form, by collectively representing the position states r and velocity states v as

$$\phi(t, t_0) = \begin{bmatrix} \phi_{rr} & \phi_{rv} \\ \phi_{vr} & \phi_{vv} \end{bmatrix} \tag{3.7}$$

where ϕ_{rr} is the partial of final position states to initial position states, ϕ_{rv} relates final velocity states to initial position states, ϕ_{vr} relates final position states to initial velocity states and finally ϕ_{vv} is the partial of final velocity states to initial velocity states.

To perform certain conditions, state correction process is performed with the help of STM information. The partials of the state transition matrix is also integrated numerically along with the equations of motion in the CR3BP model, and in higher fidelity model. The differential equations that govern the partials of the STM are

$$\dot{\phi}(t, t_0) = \frac{d}{dt}\frac{\partial \bar{x}}{\partial \bar{x}_0} = \frac{\partial \dot{\bar{x}}}{\partial \bar{x}_0} \tag{3.8}$$

that is essentially the partials of the derivative of the final states with respect to the initial states. From equation (2.50), $\dot{\bar{x}} = A(t)\bar{x}$, hence equation (3.8) is reduced to

$$\dot{\phi}(t, t_0) = \frac{\partial A(t)\bar{x}}{\partial \bar{x}_0} = A(t)\frac{\partial \bar{x}}{\partial \bar{x}_0} \tag{3.9}$$

$$\dot{\phi}(t, t_0) = A(t)\phi(t, t_0) \tag{3.10}$$

that produces a 6×6 matrix $\dot{\phi}(t, t_0)$, producing 36 scalar partial differential equations. Combined with the 6 equations of motion, a total of 42 partial differential equations are numerically propagated to get the time history of the actual states and the partials of the final states with respect to the initial states.

The State Transition matrix being a linear operator, the accuracy substantially depends on the initial variation, that is expected to be small. A large initial variation may amplify the error in the final solution as the linear STM may no longer be capable of accurately predicting the flow. In general, when predicting the desired initial or final states, the baseline

trajectory is updated continuously to minimize variation every successive step. The accuracy of the STM increases as variation diminishes. The same principal concept is applied in the Differential Correction process

3.2 Differential Correction Process

Targeting a desired state is one of the most sought after tasks especially for trajectory design and optimization. Differential correction process is a scheme that facilitates targeting certain final conditions. Since STM is a linear operator that estimates the final variation due to some initial variation about a baseline solution, Differential Correction process involving the State Transition Matrix is exploited to target the required end conditions for trajectory design in the CR3BP. Finally, an iterative process is applied till demanded tolerance is reached.

Several schemes are available for implementing the Differential Correction Process. The method of free variables and constraints as carried out by many other researchers have been used throughout this investigation[96], [97], [98]. The method employs the Newton-Raphson approximation technique which uses the truncated Taylor expansion to the first order [99]. The method is formulated by considering a design variable vector $\bar{X}$ with n free variables which are subjected to updates. Vector $\bar{X}$ is defined as a column vector,

$$\bar{X} = \begin{bmatrix} X_1 \\ X_2 \\ \vdots \\ X_n \end{bmatrix} \tag{3.11}$$

where X_1, X_2, ... , X_n may be position states, velocity states, time and/or any other relevant design variables. The constraint vector $\bar{F}(\bar{X})$ defined as a column vector

$$\bar{F}(\bar{X}) = \begin{bmatrix} F_1(\bar{X}) \\ F_2(\bar{X}) \\ \vdots \\ F_m(\bar{X}) \end{bmatrix} \tag{3.12}$$

is subjected to m different constraints $F_1(\bar{X})$, $F_2(\bar{X})$ through $F_m(\bar{X})$ which may be combination of continuity constraints, altitude constraints, energy constraint or any other user defined constraint that are a function of the defined state variables $\bar{X}$. Taylor series expansion of $\bar{F}(\bar{X})$ with free variable at initial time $\bar{X}_0$ results in

$$\bar{F}(\bar{X}) = \bar{F}(\bar{X}_0) + D\bar{F}(\bar{X}_0)\left(\bar{X} - \bar{X}_0\right) + H.O.T.s \tag{3.13}$$

where the higher order terms, $H.O.T.s$, are neglected as Newton-Raphson method truncates the Taylor series expansion to only the first order term. Additionally, the aim of this method is to update the free design variable till $\bar{X}$ drives the constraint vector $\bar{F}(\bar{X}) = 0$. Hence equation (3.13) reduces to

$$\bar{0} \approx \bar{F}(\bar{X}_0) + D\bar{F}(\bar{X}_0)\left(\bar{X} - \bar{X}_0\right) \tag{3.14}$$

where $D\bar{F}(\bar{X}_0)$ is the Jacobian matrix of size $m \times n$ as

$$D\bar{F}(\bar{X}_0) = \frac{\partial \bar{F}(\bar{X}_0)}{\partial \bar{X}_0)} = \begin{bmatrix} \frac{\partial F_1}{\partial X_1} & \cdots & \frac{\partial F_1}{\partial X_n} \\ \vdots & \ddots & \vdots \\ \frac{\partial F_m}{\partial X_1} & \cdots & \frac{\partial F_m}{\partial X_n} \end{bmatrix} \tag{3.15}$$

that consists of the first order partials of each of the constraint vector F_{i} with respect to each of the state variables X_{j}, such that $\mathrm{i} \in \{1, ..., m\}$ and $\mathrm{j} \in \{1, ..., n\}$.

For a linear problem, a single step is sufficient for Differential correction process to update the free design vector that drives the constraint vector to zero, however, for a nonlinear problem, iterative approach is applied to drive the constraint vector below the specified tolerance level. The updated design variable after every successive iteration is used as the new initial condition for the baseline solution upon which the Newton's method is applied again. To incorporate the iterative strategy equation (3.14) is modified to

$$\bar{F}(\bar{X}_{\mathrm{j}}) + D\bar{F}(\bar{X}_{\mathrm{j}}) \left(\bar{X}_{\mathrm{j+1}} - \bar{X}_{\mathrm{j}}\right) = \bar{0} \tag{3.16}$$

where j is the number of iterations performed and $\bar{X}_{\mathrm{j+1}}$ is the updated free variable after j-th iteration that serves as the initial condition for the updated baseline solution. If the number of design variables n and number of constraints m are equal i.e $n = m$, then a unique solution exists for $\bar{X}_{\mathrm{j+1}}$,

$$\bar{X}_{\mathrm{j+1}} = \bar{X}_{\mathrm{j}} - \left[D\bar{F}(\bar{X}_{\mathrm{j}})\right]^{-1} \bar{F}(\bar{X}_{\mathrm{j}}) \tag{3.17}$$

such that, $\left[D\bar{F}(\bar{X}_{\mathrm{j}})\right]^{-1}$ is perfectly invertible. If there are more design variables than the number of constraints i.e. $n > m$ the system is under-determined, infinitely many solutions exits. A potential solution,

$$\bar{X}_{\mathrm{j+1}} = \bar{X}_{\mathrm{j}} - D\bar{F}(\bar{X}_{\mathrm{j}})^T \left[D\bar{F}(\bar{X}_{\mathrm{j}})\ D\bar{F}(\bar{X}_{\mathrm{j}})^T\right]^{-1} \bar{F}(\bar{X}_{\mathrm{j}}) \tag{3.18}$$

is computed using minimum norm solution. On the contrary, if there are less design variables than the number of constraints i.e. $n < m$ the system is over-determined, no solutions exits. Using the least squares approach, a conceivable solution is computed as

$$\bar{X}_{\mathrm{j+1}} = \bar{X}_{\mathrm{j}} - \left[D\bar{F}(\bar{X}_{\mathrm{j}})^T\ D\bar{F}(\bar{X}_{\mathrm{j}})\right]^{-1} D\bar{F}(\bar{X}_{\mathrm{j}})^T \bar{F}(\bar{X}_{\mathrm{j}}) \tag{3.19}$$

that produces the minimum error. Least squares approach is used in several other places such as curve fitting and optimization where errors are to be minimized. Using the Newton's method, the solutions are likely to converge every successive iteration and is continued till required tolerance is achieved.

3.3 Single Shooting

The state transition matrix is utilized to achieve various end conditions in the CR3BP. As its name suggests, Single shooting technique implies correcting a single reference transfer arc to target a predefined end condition. Since the STM is not self-starting, a baseline solution is generated upon some initial conditions over which the STM is computed and single shooting algorithm is applied. The technique is illustrated in detail involving a fixed time target and a variable time target scheme.

3.3.1 Fixed Time Position Target

The most common application of Single shooting technique involving the STM in CR3BP is to target a desired position from an initial location. As in Figure 3.2, let the initial position be defined as $\bar{r}_0$ and the predefined target position be $\bar{r}_d$. The initial velocity $\bar{v}_{old}$ drives the reference trajectory to final position $\bar{x}$ at time T. Since this is a fixed time position target, the desired trajectory should take exactly 'T' time to travel from $\bar{r}_0$ to $\bar{r}_d$ with no constraint on the arrival velocity at the target location. The initial position $\bar{r}_0$ being fixed, the aim is to determine the required change in velocity components i.e. Δv maneuver required to achieve $\bar{r}_d$ at time T.

To apply the Differential Correction scheme, free variables and constraints have to be defined distinctly. Let the free design variables be expressed as the three initial velocity components i.e.

$$\bar{X} = \begin{bmatrix} \dot{x}_0 \\ \dot{y}_0 \\ \dot{z}_0 \end{bmatrix} \tag{3.20}$$

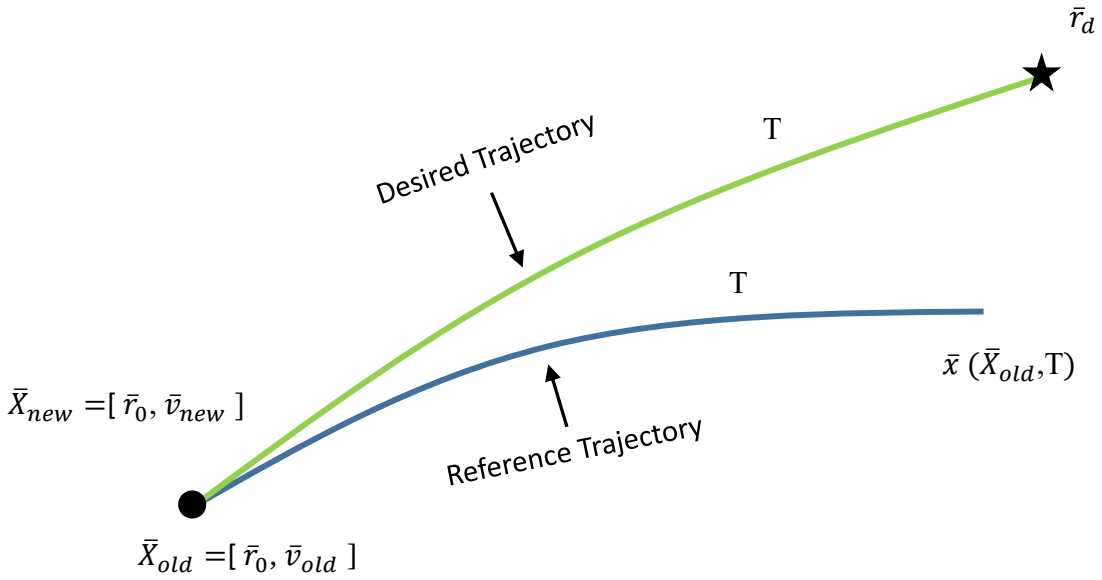

Figure 3.2. Single shooting technique with fixed time position target.

that is updated every iteration till it drives to desired state $\bar{r}_d$ at time T with some tolerance. Here, $\bar{r}_d = [x_d, y_d, z_d]^T$. Similarly, the constraint vector $\bar{F}(\bar{X})$,

$$\bar{F}(\bar{X}) = \begin{bmatrix} x(T) - x_d \\ y(T) - y_d \\ z(T) - z_d \end{bmatrix} \tag{3.21}$$

is defined as the difference between the positions at the end of the reference trajectory and the desired state. As the solution approaches the desired solution, $\bar{F}(\bar{X})$ tends to zero. The corresponding Jacobian matrix for the fixed time position target is

$$D\bar{F}(\bar{X}) = \begin{bmatrix} \frac{\partial F_1}{\partial X_1} & \frac{\partial F_1}{\partial X_2} & \frac{\partial F_1}{\partial X_3} \\ \frac{\partial F_2}{\partial X_1} & \frac{\partial F_2}{\partial X_2} & \frac{\partial F_2}{\partial X_3} \\ \frac{\partial F_3}{\partial X_1} & \frac{\partial F_3}{\partial X_2} & \frac{\partial F_3}{\partial X_3} \end{bmatrix} = \begin{bmatrix} \frac{\partial x(T)}{\partial \dot{x}_0} & \frac{\partial x(T)}{\partial \dot{y}_0} & \frac{\partial x(T)}{\partial \dot{z}_0} \\ \frac{\partial y(T)}{\partial \dot{x}_0} & \frac{\partial y(T)}{\partial \dot{y}_0} & \frac{\partial y(T)}{\partial \dot{z}_0} \\ \frac{\partial z(T)}{\partial \dot{x}_0} & \frac{\partial z(T)}{\partial \dot{y}_0} & \frac{\partial z(T)}{\partial \dot{z}_0} \end{bmatrix} \tag{3.22}$$

where the partials for $D\bar{F}(\bar{X})$ constitute the STM defined in equation (3.6), therefore

$$D\bar{F}(\bar{X}) = \begin{bmatrix} \phi_{14} & \phi_{15} & \phi_{16} \\ \phi_{24} & \phi_{25} & \phi_{26} \\ \phi_{34} & \phi_{26} & \phi_{36} \end{bmatrix} \tag{3.23}$$

where each ϕ_{ij} corresponds to the element in the ith row and jth column of the 6×6 STM. Here, $D\bar{F}(\bar{X})$ is same as the ϕ_{vr} matrix defined in equation (3.7). Once the free design vector $\bar{X}$, constraint vector $\bar{F}(\bar{X})$ and the Jacobian matrix $D\bar{F}(\bar{X})$ is defined, the Newton's equation is applied to find the required update. In this case, the number of variables and the number of constraints are equal hence a unique solution exists. The appropriate update to the reference solution is computed as $\delta\bar{X}$,

$$\delta\bar{X} = -[D\bar{F}(\bar{X})]^{-1}\bar{F}(\bar{X}) \tag{3.24}$$

from equation (3.17). After every successive iteration, the reference solution is updated as

$$\bar{X}_{\text{j+1}} = \bar{X}_{\text{j}} + \delta\bar{X} \tag{3.25}$$

till the desired tolerance level is attained. The Differential Correction process computes variation using linear approximation while CR3BP is a nonlinear problem, therefore no matter how many iterations are performed, the reference trajectory will never be exactly equal to the desired solution. With every successful iteration, constraint vector $\bar{F}(\bar{X})$ diminishes hence the numerical process can be terminated once the norm $||\bar{F}(\bar{X})||$ is within the permissible tolerance.

3.3.2 Variable Time Position Target

Unlike for fixed time position target, as shown in Figure 3.3, the time of flight from the initial position to the desired position is not constrained to be the same as the time

of flight of the reference trajectory, hence this is a variable time position target problem. The method only tries to find one possible trajectory that satisfies both the initial and final position states.

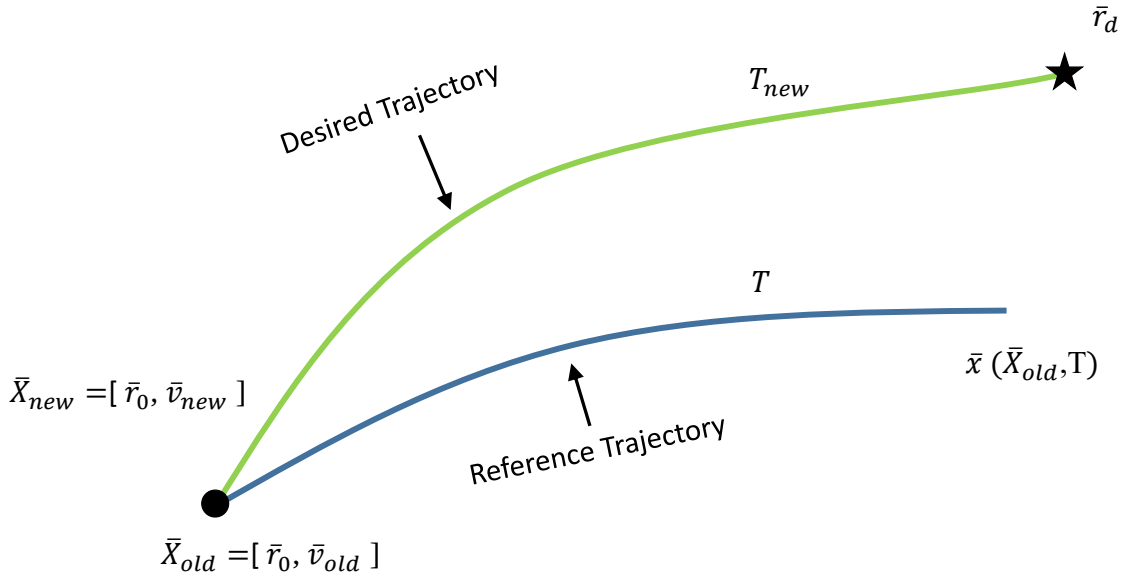

Figure 3.3. Single shooting technique with variable time position target.

For any targeting scheme, free variables and constraints are to be defined appropriately. The time of flight T becomes an additional design variable hence,

$$\bar{X} = \begin{bmatrix} \dot{x}_0 \\ \dot{y}_0 \\ \dot{z}_0 \\ T \end{bmatrix} \tag{3.26}$$

is defined as the new free variable vector. The goal is only to achieve the predefined position states at the end hence the end conditions still remains the same. As a result there is

no modifications to the constraint vector $\bar{F}(\bar{X})$. Nonetheless, $D\bar{F}(\bar{X})$ is altered due to a different design vector $\bar{X}$, thus

$$D\bar{F}(\bar{X}) = \begin{bmatrix} \frac{\partial x(T)}{\partial \dot{x}_0} & \frac{\partial x(T)}{\partial \dot{y}_0} & \frac{\partial x(T)}{\partial \dot{z}_0} & \frac{\partial x(T)}{\partial T} \\ \frac{\partial y(T)}{\partial \dot{x}_0} & \frac{\partial y(T)}{\partial \dot{y}_0} & \frac{\partial y(T)}{\partial \dot{z}_0} & \frac{\partial y(T)}{\partial T} \\ \frac{\partial z(T)}{\partial \dot{x}_0} & \frac{\partial z(T)}{\partial \dot{y}_0} & \frac{\partial z(T)}{\partial \dot{z}_0} & \frac{\partial z(T)}{\partial T} \end{bmatrix} = \begin{bmatrix} \phi_{14} & \phi_{15} & \phi_{16} & \dot{x}(T) \\ \phi_{24} & \phi_{25} & \phi_{26} & \dot{y}(T) \\ \phi_{34} & \phi_{26} & \phi_{36} & \dot{z}(T) \end{bmatrix} \tag{3.27}$$

where an additional column of the derivative of the position states with respect to time are also included. $D\bar{F}(\bar{X})$ is no longer a square matrix. There are more design variables than the number of constraints, hence, infinitely many solutions exists. One such solution can be found using the minimum norm approach. The update to the reference can be computed to be,

$$\delta\bar{X} = -D\bar{F}(\bar{X})^T \left[D\bar{F}(\bar{X}) \;\; D\bar{F}(\bar{X})^T \right]^{-1} \bar{F}(\bar{X}) \tag{3.28}$$

as mentioned in equation (3.18). The iterative process is continued till acceptable tolerance is reached.

The single shooting technique is illustrated using position target scheme. The application is not limited to just position target. The design vector, the constraint vector and the corresponding Jacobian matrix can be modified to target any combinations of position, velocity and/or any other relevant quantity. The technique is although restricted to only single target vector. To target multiple conditions, more robust methods like multiple shooting technique is applied.

3.4 Multiple Shooting

A single shooting technique has vast applications, however, when the trajectory passes through regions of higher sensitivities, this technique struggles to converge. In such cases, few intermediate patch points are incorporated through which the trajectories should traverse before reaching the desired end condition. Multiple shooting is a strategy to cumulatively use single shooting technique to target two adjacent patch points forming a sub-arc as described

in Figure 3.4. The process is continued till a transfer trajectory is created from the initial location to the final state that is continuous in position and velocity at each of the updated patch points within some acceptable tolerance. The patch points are free to move around in any directions in the phase space. Similar to single shooting technique, the final state can be achieved either through a fixed time target strategy or a variable time target strategy.

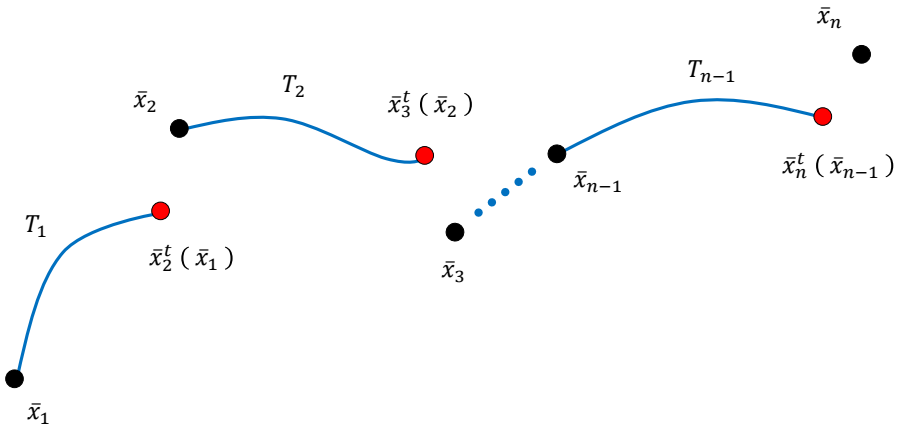

(a) Intermediate Sub-arcs

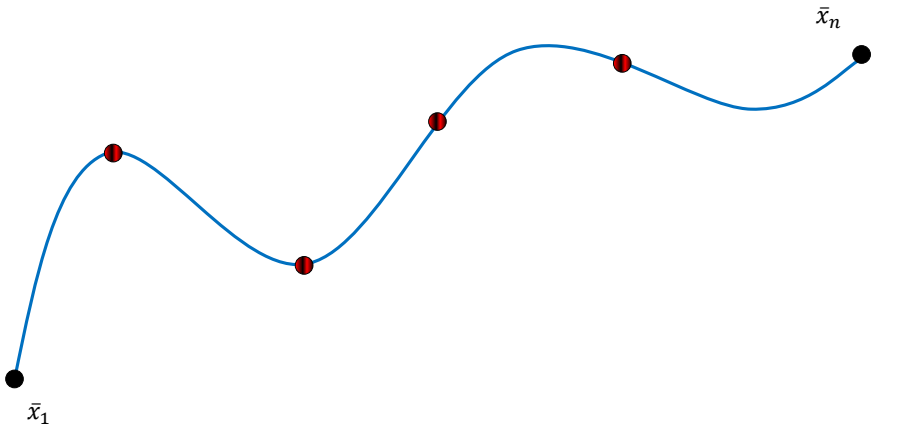

(b) Final Converged Trajectory

Figure 3.4. Concept of multiple shooting target algorithm.

3.4.1 Fixed Time Multiple Shooting

Similar to a fixed time single shooting process where the time between the starting point and the end point is fixed, in fixed time multiple shooting the time of flight between any two

successive patch points is fixed. Identical to formulating the single shooting technique, free design variables and constraints are to be defined for the multiple shooting target algorithm. The free design variables at all the defined patch points are accumulated into one stacked vector. It is considered that the states at each of the patch points are free to be updated every iteration i.e. $\bar{x}_{\mathrm{i}}$ according to Figure 3.4(a). The design variable $\bar{X}$ is therefore a $6n$ sized vector,

$$\bar{X} = \begin{bmatrix} \bar{x}_1 \\ \bar{x}_2 \\ \vdots \\ \bar{x}_n \end{bmatrix} \tag{3.29}$$

where each $\bar{x}_{\mathrm{i}}$ is a column vector with position and velocity states at that patch point. The sub-arcs have to be continuous in position and time at the intermediate patch points in order to achieve a smooth trajectory between the initial and final point as the solution converges. Hence the constraint vector $\bar{F}(\bar{X})$ is defined as

$$\bar{F}(\bar{X}) = \begin{bmatrix} \bar{x}_2^t(\bar{x}_1) - \bar{x}_2 \\ \bar{x}_3^t(\bar{x}_2) - \bar{x}_3 \\ \vdots \\ \bar{x}_n^t(\bar{x}_{n-1}) - \bar{x}_n \end{bmatrix} \tag{3.30}$$

where each $\bar{x}_{\mathrm{j}+1}^t(\bar{x}_{\mathrm{j}})$ are the states achieved by propagating state vector $\bar{x}_{\mathrm{j}}$ as the initial condition for fixed predefined time. Since the trajectory originates at the initial point there is no constraint at $\bar{x}_1$, so the length of the constraint vector is $6(n-1)$. The corresponding Jacobian Matrix becomes

$$D\bar{F}(\bar{X}) = \begin{bmatrix} \left(\frac{\partial \bar{x}_2^t}{\partial \bar{x}_1} - \frac{\partial \bar{x}_2^t}{\partial \bar{x}_1}\right) & \left(\frac{\partial \bar{x}_2^t}{\partial \bar{x}_2} - \frac{\partial \bar{x}_2^t}{\partial \bar{x}_2}\right) & & \\ & \ddots & \ddots & \\ & & \left(\frac{\partial \bar{x}_n^t}{\partial \bar{x}_{n-1}} - \frac{\partial \bar{x}_n^t}{\partial \bar{x}_{n-1}}\right) & \left(\frac{\partial \bar{x}_n^t}{\partial \bar{x}_n} - \frac{\partial \bar{x}_n^t}{\partial \bar{x}_n}\right) \end{bmatrix} \tag{3.31}$$

that is reduced to more revealing form by correlating the partials to the STM, as

$$D\bar{F}(\bar{X}) = \begin{bmatrix} \phi_{2,1} & -I_{6\times 6} & & \\ & \ddots & \ddots & \\ & & \phi_{n,n-1} & -I_{6\times 6} \end{bmatrix} \tag{3.32}$$

where each $\phi_{\mathrm{i}+1,\mathrm{i}}$, is the 6×6 State transition Matrix computed between ith patch point to $(\mathrm{i}+1)$th patch point. Newton's method is used to update position and velocity states the patch points and iterated till acceptable level of accuracy is obtained.

3.4.2 Variable Time Multiple Shooting with Additional Constraints

Alike variable time single shooting process, where the time between initial time and the desired final state is not constrained, in variable time multiple shooting, the time of flight between two successive patch points is not constrained. To consider a time variable multiple shooting technique, let the time of flight between each patch points be T_{i} as in Figure 3.4(a), that can be considered as a design variable additional to its position and velocity states. Hence a total of $7n-1$ design variable exists for this case i.e.

$$\bar{X} = \begin{bmatrix} \bar{x}_1 \\ \bar{x}_2 \\ \vdots \\ \bar{x}_n \\ T_1 \\ \vdots \\ T_{n-1} \end{bmatrix} \tag{3.33}$$

where each T_{i} represents the time of flight between ith patch point and $(\mathrm{i}+1)$th patch point. To represent a more specific problem, like a trajectory with predefined Jacobi constant, or

trajectory with fixed starting point and/or fixed end point or any other criterion, Multiple shooting technique provides the leverage to add additional constraints to represent the same. Let '$\mathcal{C}$' denote any additional constraint besides the ones defined for fixed time multiple shooting, such that upon convergence $\mathcal{C} = 0$. Hence, the constraint vector $\bar{F}(\bar{X})$ becomes

$$\bar{F}(\bar{X}) = \begin{bmatrix} \bar{x}_2^t(\bar{x}_1) - \bar{x}_2 \\ \bar{x}_3^t(\bar{x}_2) - \bar{x}_3 \\ \vdots \\ \bar{x}_n^t(\bar{x}_{n-1}) - \bar{x}_n \\ \mathcal{C} \end{bmatrix} \tag{3.34}$$

where $\mathcal{C}$ is an added constraint that is a function of the state variables at any one or more patch points. The Jacobian matrix in this variable time multiple shooting method with added constraints defined as $D\bar{F}(\bar{X})$,

$$D\bar{F}(\bar{X}) = \left[\begin{array}{cccc|ccc} \phi_{1,2} & -I_{6\times6} & & & \dot{\bar{x}}_2^t & & \\ & \ddots & \ddots & & & \ddots & \\ & & \phi_{n-1,n} & -I_{6\times6} & & & \dot{\bar{x}}_n^t \\ \hline \frac{\partial \mathcal{C}}{\partial \bar{x}_1} & \cdots & \cdots & \frac{\partial \mathcal{C}}{\partial \bar{x}_n} & \frac{\partial \mathcal{C}}{\partial T_1} & \cdots & \frac{\partial \mathcal{C}}{\partial T_{n-1}} \end{array}\right] \tag{3.35}$$

contains additional partials that represents time derivatives with respect to free variables as well as partials of '$\mathcal{C}$' with the states at all patch points and corresponding time of flights. The additional partials that $\dot{\bar{x}}_{\mathrm{i}}^t$ represents the time derivative of $\bar{x}_{\mathrm{i}}$ with respect to the time of flight from $(\mathrm{i}-1)$-th to i-th patch point i.e. $\dot{\bar{x}}_{\mathrm{i}}^t = \partial \bar{x}_{\mathrm{i}} / \partial T_{\mathrm{i}-1}$. For every iteration, the update can be computed by taking direct inverse or minimum norm depending on the dimensions of the Jacobian Matrix.

4. ORBIT MAINTENANCE OPERATIONS

A spacecraft is expected to traverse along a nominal path that is designed to satisfy various mission requirements. Due to unmodeled perturbations the spacecraft deviates away from the reference path, besides the unstable nature of certain libration point orbits amplifies the deviation in both position and velocity states with time. An impulsive stationkeeping strategy is introduced to deliver regular orbit maintenance maneuvers that secures the spacecraft within an acceptable region near the reference path. The stationkeeping algorithm computes an impulsive maneuver that potentially sustains the spacecraft in the neighborhood of the reference path throughout the mission duration. Minimizing the propellant usage required for stationkeeping maneuvers is a priority for increased life of the space mission.

4.1 Representation of Reference Orbit

A known precise nominal path is convenient to simulate a mission scenario. Prior studies have illustrated ways to compute precise halo orbits in the circular restricted three-body problem [18]–[20], [100], [101]. The orbits are determined by propagating the nonlinear equations of motion and corrected using differential correction schemes [19]. Computing Lissajous orbits and quasi-halo orbits in the vicinity of the libration points is challenging as they are not precisely periodic. Howell and Pernicka [20] use a two-level patching algorithm to patch trajectories of arbitrary duration to form a continuous trajectory that form the quasi-periodic orbits. Pavlak and Howell [45] use a multiple-shooting technique to generate a continuous trajectory by patching intermediate trajectory segments. The application of these strategies are extended in the higher-fidelity ephemeris model as well.

To simulate a real mission scenario, a precise periodic, like a halo orbit in CR3BP, may not be ideal, primarily due to other perturbing forces in space that is non-periodic. A more accurate trajectory that resembles a real nominal path is generated by numerically converging a continuous trajectory in the higher fidelity ephemeris model, and serves as a baseline trajectory for stationkeeping operations.

Halo orbits are a type of family of 3-dimensional periodic trajectories that exist near the L1 and L2 libration points in the circular restricted three-body problem [19]. Within the Earth-Moon system, the L1 and L2 halo orbits are explored as potential destinations for a long-term facility in cislunar space. Specifically for the Gateway mission, a southern L2 halo orbit is the current focus. The family of the L1 and L2 southern halo orbits in the Earth-Moon system are plotted in Figure 4.1. Some members of the L1 and L2 halo families with close lunar passage and high out-of-plane amplitudes are stable or nearly stable based on a variational linear stability analysis [3]. Define the stability index to measure the stability characteristics of a periodic orbit such that

$$\nu_{\mathrm{i}} = \frac{1}{2}\left(\lambda_{\mathrm{i}} + \frac{1}{\lambda_{\mathrm{i}}}\right) \tag{4.1}$$

where λ_{i} are the eigenvalues from the monodromy matrix, i.e., the state transition matrix over precisely one orbital period. Here, ν_{i} is defined in the form of Joukowski transformation (also referred as Zhukovsky transformation) of λ_{i} [102]. Figures 4.2(a) and 4.2(b) describes the evolution of the stability indices as a function of perilune radii for members of the L1 and L2 halo orbits, respectively. For stable orbits, the absolute value of stability index is less than or equal to one, i.e., $|\nu_{\mathrm{i}}| \leq 1$. The Near Rectilinear Halo Orbits (NRHOs) are a subset of the halo orbit family that are stable or nearly stable orbits, as measured using the stability index, the range of which is marked in Figure 4.2. Within Figure 4.1 the orbits colored in red are the NRHOs in both the L1 and the L2 families. Only the halo orbits that do not intersect the Moon's surface are plotted in the configuration space. The periods of the NRHOs range across a block of values such that some of these orbits exhibit different resonance properties. For the stationkeeping analysis, orbits are selected with different perilune radius distances including those that demonstrates simple resonance ratios.

The cislunar orbits in the CR3BP are modeled based on the gravitational forces due to the Earth and the Moon at a fixed relative distance from each other, expressed relative to their mutual barycenter. However, the time-variant relative distance between the Earth and the Moon as well as effects of other bodies not considered in the CR3BP affect the motion

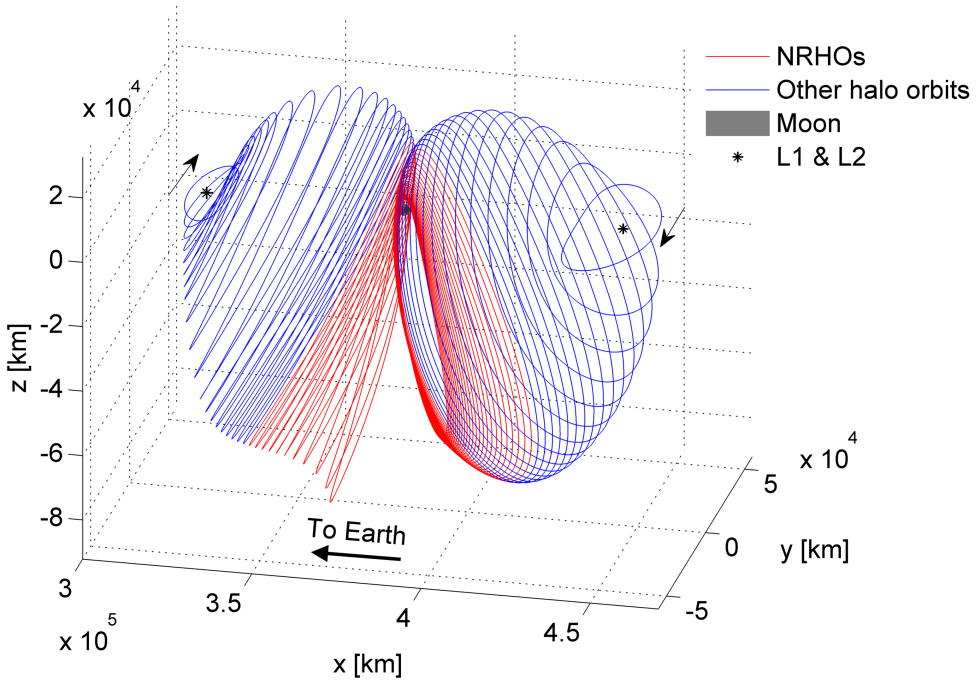

Figure 4.1. L1 and L2 halo orbits in the Earth-Moon system.

of the spacecraft substantially. The initial conditions of an orbit in the CR3BP when propagated in the higher fidelity model does not result in a closed orbit, due to perturbations caused by unmodeled forces including gravitational force of other celestial bodies. Figure 4.3 illustrates the net perturbing accelerating acting along the 9:2 synodic resonant southern L2 NRHO and the 3:1 L2 synodic resonant southern L2 NRHO, due to the effects from a number of celestial bodies, relative to an observer at the Earth-Moon barycenter. Clearly for both the orbits, the gravitational forces due to the Earth, the Moon and the Sun are the most dominant, which is followed by the Solar Radiation Pressure (SRP). Here Solar Radiation Pressure is calculated based on an assumed cannonball model for the spacecraft with mass 25848 kg, a projected area of 50 sq.m. and a perfectly reflective surface with coefficient of reflectivity $C_r = 2$; such values are consistent with the dimensions of the Gateway spacecraft in literature [4], [58]. Similar effects are observed on a range of halo orbits. The effect of the J2 perturbing accelerating due to the Moon increases briefly during an orbit, especially when the spacecraft is close to the periapsis, however it is insignificant for most duration along the orbit. In addition, the effect of Moon's J2 perturbing acceleration is

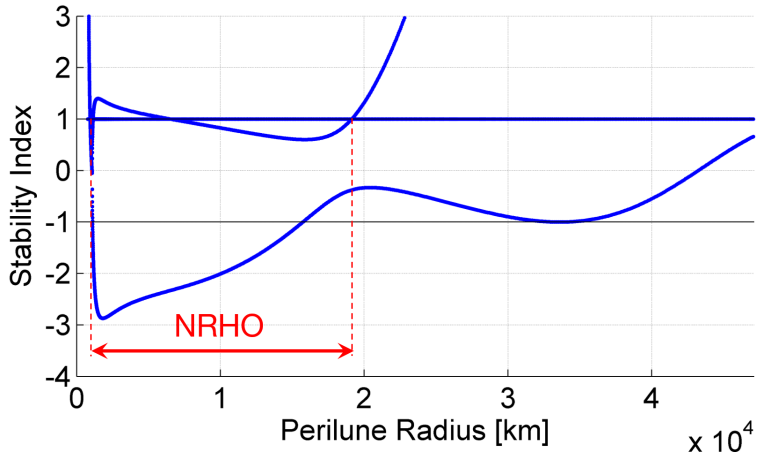

(a) L1 halo family

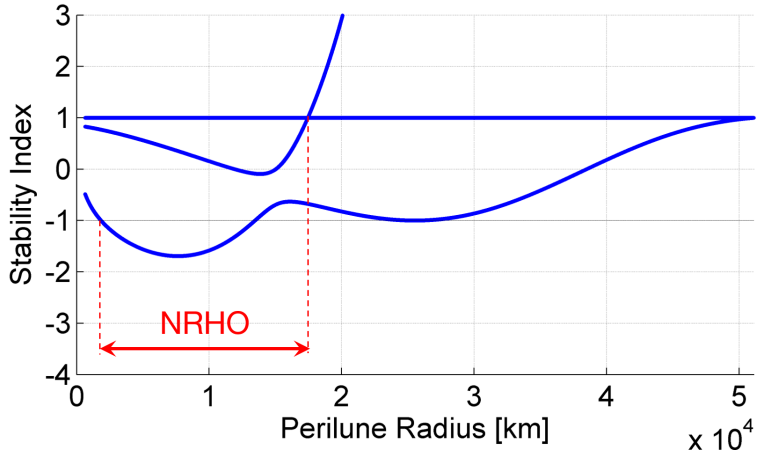

(b) L2 halo family

Figure 4.2. Stability indices for different halo orbits in the Earth-Moon system.

more significant along the 9:2 synodic resonant southern L2 NRHO with a smaller perilune radius of 3200 km while considerably lower in the case of the 3:1 synodic resonant southern L2 NRHO with a larger perilune radius of 15000 km. Due to the large variations in the effect of J2 perturbing accelerations due to the Moon along different reference orbits, i.e., notable for some orbits while insignificant for the others, it is omitted while generating the reference trajectory. However, any state perturbations caused due to the effects of J2 perturbing acceleration is compensated by running simulations with larger uncertainties in state measurements. The fidelity of the model is enhanced by adding the effect of a large number of celestial bodies but too many additional bodies is computationally intensive and may

be nontrivial, especially when simulations that incorporates additional orbit determination errors. Based on the order of magnitude of different net perturbing accelerations as well as prior investigations in the literature, gravitational forces due to the Earth, the Moon and the Sun, as well as Solar Radiation Pressure (SRP) are the most dominant forces on the Earth-Moon halo orbits in the L1 and L2 region and considered sufficient for this analysis [61]. The effect of any additional forces are minimal, however, consistent with other stationkeeping literature, gravitational force due to Jupiter is also included [4], [57]. Ephemeris data is incorporated using the DE421 model. Once the significant perturbing forces are determined in the higher-fidelity ephemeris model, multiple revolutions of the CR3BP orbit are stacked and corrected using a multiple shooting algorithm for position and velocity continuity [103]. The iterative procedure produces a quasi-periodic trajectory in the higher-fidelity model that resembles the geometry of the corresponding orbit defined in the CR3BP. The natural trajectory in the ephemeris model offers a virtual reference solution that serves as an anchor for stationkeeping operations; the entire virtual reference is updated over time as appropriate. To accommodate the updated reference, infrequent long horizon orbit correction maneuvers are easily incorporated as a part of the stationkeeping algorithm. A virtual reference trajectory generated in the higher-fidelity ephemeris model by incorporating the dominant forces for the L2 southern NRHO with perilune radius 3200 km, that serves as the baseline for the Gateway mission is plotted in Figure 4.4, in three different views, including the rotating frame of view, $\underline{\mathcal{R}}$, the Moon-centered inertial view as well as the Earth-centered inertial view.

The patch points from the CR3BP halo orbit is used as an initial guess to converge a continuous trajectory in the higher fidelity ephemeris model that serves as a baseline for performing stationkeeping operations. The baseline trajectories for the southern L1 and L2 NRHOs, including the 9:2 synodic resonant L2 NRHO that is the current choice for the Gateway mission, are constructed for about 1 year duration. The length of the trajectory roughly corresponds to 40-50 orbit periods and is sufficient for simulating mission duration with additional target horizon times. The epoch date at the halo orbit injection (HOI) is assumed to be January 13, 2023 UT1: 00:00:00.0 (Julian Date: 2459957.5). The transition halo orbits, with perilune radii roughly between 10,000 to 22,000 km, are constructed for

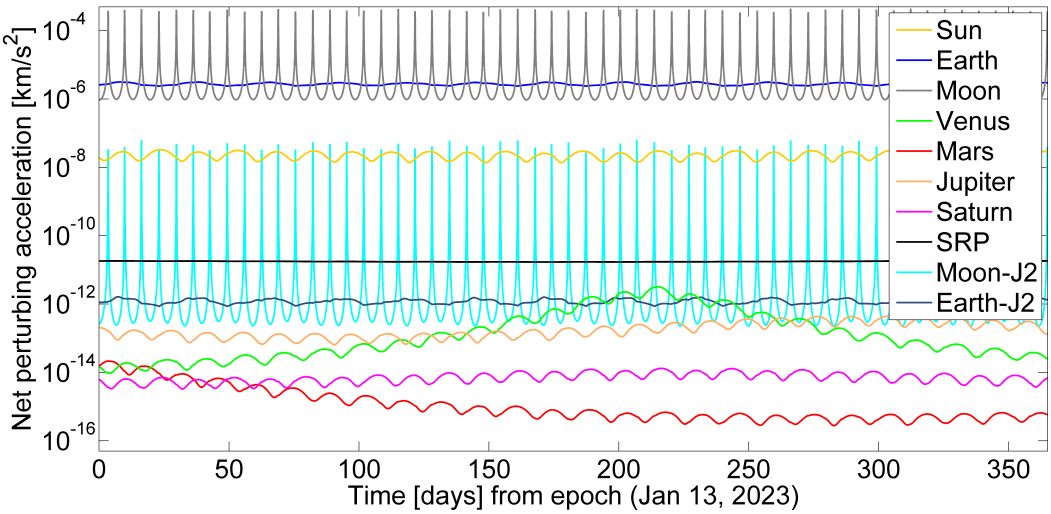

(a) 9:2 synodic resonant southern L2 NRHO with a perilune radius 3200 km.

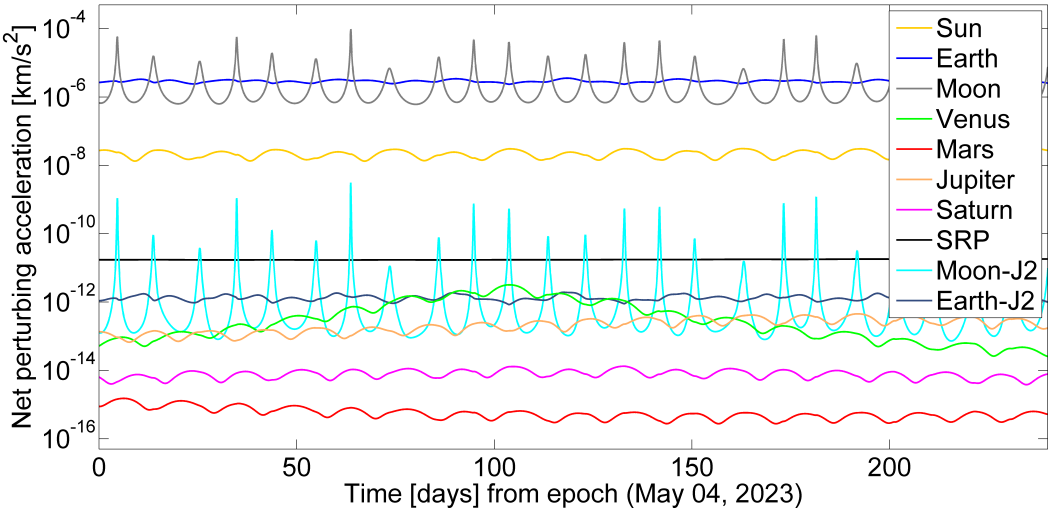

(b) 3:1 synodic resonant southern L2 NRHO with a perilune radius 15000 km.

Figure 4.3. Net perturbing acceleration along different NRHO expressed relative to the Earth-Moon barycenter.

duration about 0.5 years. Each of the transition halo orbit baseline trajectories are generated with variable epoch dates at the halo orbit injection (HOI) to investigate the effect of epoch dates on stationkeeping.

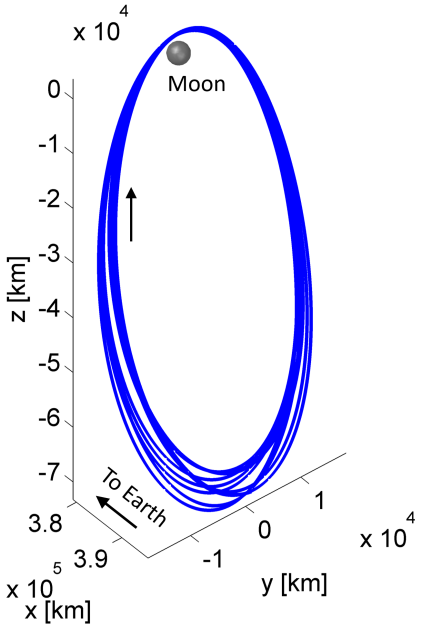

(a) Rotating frame of view

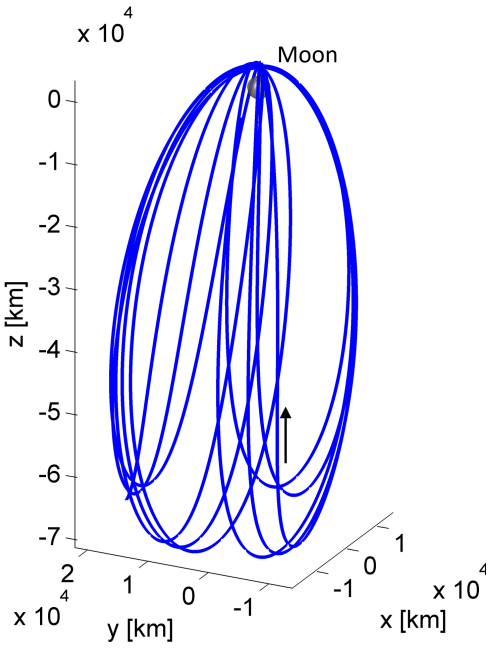

(b) Moon-centered inertial view

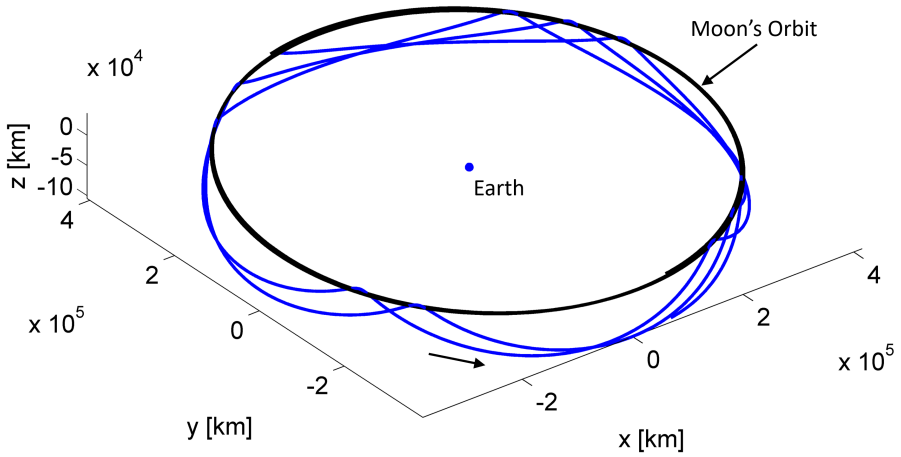

(c) Earth-centered inertial view

Figure 4.4. L2 NRHO with perilune radius 3200 km in the higher-fidelity ephemeris model.

As the spacecraft advances with time it may drift away from the nominal path due to unmodeled forces and uncertainties. It is crucial to continuously assess the spacecraft states relative to the virtual reference path, that is obtained from converging in the higher fidelity system, in form of tabular listings of time, position and velocity states. It is computationally expensive to store large data sets as well retrieve the large data every time to compare the true spacecraft states to the reference. Howell and Pernicka [30], [31] stored data points spaced within 1.1 days for the Sun-Earth libration point orbits. There has been substantial literature on the type of curve that is used to retrieve interpolated data accurately. Richardson [18] uses a complete 13^{th} order analytical Fourier series representation of the halo orbit. Howell and Pernicka [30], [31] use Akima cubic spline interpolation while Howell and Gordon [46], [47] analyze different interpolating schemes and conclude that cubic splines especially Akima cubic splines gave smoother representation. Within the Earth-Moon halo orbits under investigation here, states and times are stored as data points placed at an interval of 5 minutes. Since the data points are placed in a mere 5 minutes interval, cubic spline interpolation offers fairly accurate results with errors well within the uncertainties in orbit determination. The accuracy of linear interpolation is also observed to be satisfactory near the apoapsis region. Nevertheless, to not compromise on the accuracy of state estimation in sensitive regions, a cubic spline interpolation technique is employed throughout this investigation. For consistency, the constants or parameters used throughout this investigation are retrieved from Adaptive Trajectory Design (ATD) software, while spacecraft characteristics are retrieved from literature [4], [57]. The values are summarized in table 4.1.

4.2 Orbit Determination

Uncertainty in navigation is a major contributor to the stationkeeping cost. The magnitude of uncertainty impacts the stationkeeping cost proportionally. For many missions in the cislunar vicinity the spacecraft position and velocity are tracked by Earth-based stations, that generally measure range and range rate (also known as Doppler) quantities [104]–[110]. Of course the tracking stations on the Earth take measurements angular displacement, rate of angular displacement, relative astronomical quantities, etc., to precisely determine the states of the spacecraft. In addition, spacecraft-based sensors are also capable of orbit de-

Table 4.1. Constants used for stationkeeping applications.

Standard Gravitational Parameter $\tilde{\mu} = \tilde{G}M$, km^3/s^2	
Sun	132712197035.766
Earth	398600.432896939280908555
Moon	4902.800582147764544061
Jupiter	126686535.0

Characteristic quantities Earth-Moon system	
μ $[ndim]$	0.012150585609624
l^* [km]	385692.50
t^* [s]	3770841.526670390

Spacecraft characteristics	
Mass	25848 kg
Proj. Area	50 sq.m
C_r	2

termination. For this investigation, however, range and range rate quantities are considered to measure uncertainty in state estimation.

The Earth-based stations record multiple observations of each quantities, range and range rate of the spacecraft, at different time intervals. The uncertainty covariance derived from the range and range rate measurements offer insight into the uncertainty in each of the position and velocity quantities. A batch least squares filter and a sequential Kalman filter are two of the commonly used signal-processing filters for orbit determination. It is assumed that there are no uncertainty in the measurements of the latitude and longitude coordinates of the Earth-based tracking station, therefore the range and range rate measurements expressed with respect to the center of the Earth offer the same uncertainty covariance as that wih respect to the ground station. Further, the mass of the celestial bodies, gravitational constant, etc are regarded as consider parameters.

Kalman filter has been used for orbit estimation, as early as the Apollo mission [111], [112]. The batch least squares filter and the sequential Kalman filter have been widely applied in the orbit determination problem ever since, and shown comparable results, as documented in literature [46], [113]. In recent times, batch least squares filter and Kalman filter techniques have been applied for orbit determination on the ARTEMIS mission in the Earth-Moon L1 and L2 libration point orbits. Batch least squares technique require relatively lower number of observations as opposed to a sequential Kalman filter in reducing the uncertainty covariance. A batch least squares approach, however, requires storage of all the prior observations to compute the covariance, resulting in larger memory usage in comparison to a sequential Kalman filter. For this investigation, a sequential Kalman filter is implemented considering the benefit of not having to store prior observations.

The spacecraft motion along a trajectory is defined by the six states, $\bar{\mathbf{x}} = [x, y, z, \dot{x}, \dot{y}, \dot{z}]^{\mathrm{T}}$. A Kalman filter is modeled to correlate observations, range and range rate, to state change. The system is modeled as

$$\delta\bar{\mathbf{x}}_{k+1} = \mathbf{A}_k \delta\bar{\mathbf{x}}_k + \mathbf{w}_k \tag{4.2}$$

$$\delta\bar{\mathbf{y}}_k = \mathbf{H}_k \delta\bar{\mathbf{x}}_k + \epsilon_k \tag{4.3}$$

where $\mathbf{A}_k = \phi(t_{k+1}, t)$, while $\delta\bar{\mathbf{y}}_k$ is the measurement residue vector, $\delta\bar{\mathbf{y}}_k = [\delta\mathbf{R}, \delta\dot{\mathbf{R}}]^{\mathrm{T}}$, where measurements are in range $\mathbf{R}$ and range rate, $\dot{\mathbf{R}}$. Any linear change in the states is represented as $\delta\bar{\mathbf{x}} = [\delta x, \delta y, \delta z, \delta\dot{x}, \delta\dot{y}, \delta\dot{z}]^{\mathrm{T}}$. The quantity $\mathbf{w}_k$ is the process noise such that $E[\mathbf{w}_k] = 0$ and $E[\mathbf{w}_k \mathbf{w}_k^{\mathrm{T}}] = \mathbb{Q}$. The matrix $\mathbf{H}_k$ is known as the measurement matrix and ϵ_k is the measurement noise. Since it is assumed that there are no uncertainties in the location of the tracking station, the measurements relative to the center of the Earth yield the same covariance. The range and range rate values are determined to be,

$$\mathbf{R} = \sqrt{(x+\mu)^2 + y^2 + z^2} \tag{4.4}$$

$$\dot{\mathbf{R}} = \frac{(x+\mu)\dot{x} + y\dot{y} + z\dot{z}}{\mathbf{R}} \tag{4.5}$$

as a result, the measurement matrix, $\mathbf{H}_k$, is the Jacobian, $\mathbf{H}_k(\mathrm{i},\mathrm{j}) = \frac{\partial \bar{\mathbf{y}}_\mathrm{i}}{\partial \bar{\mathbf{x}}_\mathrm{j}}$. The measurement noise, ϵ_k, is assumed to be white, with mean, $E[\epsilon_k] = 0$, and variance , $E[\epsilon_k \epsilon_k^\mathrm{T}] = \mathbb{R}$. The covariance in state estimation is given by

$$\mathbb{P}_{k|k-1} = E[(\bar{\mathbf{x}}_k - \hat{\bar{x}}_k)(\bar{\mathbf{x}}_k - \hat{\bar{x}}_k)^\mathrm{T}] \tag{4.6}$$

where, $\hat{\bar{x}}_k$ is the estimate of $\bar{\mathbf{x}}_k$ prior to the k-th observation, but after $k-1$ observations are recorded. Also,

$$\mathbb{P}_{k|k} = E[(\bar{\mathbf{x}}_k - \tilde{\bar{x}}_k)(\bar{\mathbf{x}}_k - \tilde{\bar{x}}_k)^\mathrm{T}] \tag{4.7}$$

is defined such that, $\mathbb{P}_{k|k}$ covariance in state estimation after k-th observation is made. The quantity $\tilde{\bar{x}}_k$ is the estimate of $\bar{\mathbf{x}}_k$ after the k-th observation is available. The covariance matrix is propagated as

$$\mathbb{P}_{k|k-1} = \mathbf{A}_{k-1}\mathbb{P}_{k-1|k-1}\mathbf{A}_{k-1}^\mathrm{T} + \mathbb{Q} \tag{4.8}$$

along with the system dynamics. With an additional observation,

$$\mathbb{P}_{k|k} = (\mathbb{P}_{k|k-1} + \mathbf{H}_k^\mathrm{T}\mathbb{R}^{-1}\mathbf{H}_k)^{-1} \tag{4.9}$$

the state covariance is updated, incorporating the measurement covariance. With no *a priori* information, $\mathbb{P}_{k|k-1}$ is initialized with a very large value.

The linear state transition matrix is accepted to be fairly accurate when propagated over short time duration. In a typical orbit determination problem, observations are recorded in short time intervals, hence, for the simplicity of the problem, it is assumed that there is no process noise, i.e, $E[\mathbf{w}_k \mathbf{w}_k^\mathrm{T}] = \mathbb{Q} = 0$. Tracking precision in terms of range and range rate uncertainty has improved over the years. The uncertainty in range and range rate measurements for some past missions are listed in Table 4.2. With modern sophisticated technology 1σ error in range measurements lower than 10 m is achievable. Similarly, 1σ error in range rate or Doppler measurement under 1 mm/s is common for recent missions. A conservative 1σ error in range and range rate error of 10 m and 1 mm/s respectively is considered for this investigation.

Table 4.2. Tracking errors for various missions.

Sl. No.	Range (1σ)	Range rate (1σ)	Mission Type	Year	Reference
1	15.24 m	15.24 cm/s	Apollo	1963	[104]
2	1 km	1 mm/s	Voyager	1983	[114]*
3	15 m	3 mm/s	SOHO	1992	[46]
4	0.6 m	0.3 mm/s	TOPEX/POSEIDON	1994	[115]**
5	3 m	0.3 mm/s	Low Lunar Orbit	1997	[105]
6	2-5 m	0.1 mm/s	Interplanetary (ESA)	2004	[116]
7	1-2 m	0.1 mm/s	Interplanetary (ESA)	2004	[116]
8	5 m	1 mm/s	SELENE satellites	2011	[106]
9	10 m	1 mm/s	LRO	2012	[107]
10	10 m	3 mm/s at USN 1 mm/s at DSN	LRO	2014	[108]
11	1 m	1 mm/s	CE-5T1	2018	[110]
12	3 m	1 cm/s	Chang'E-4	2019	[109]
13	10 m	1 mm/s			Here

*Measurements taken near Jupiter
**Measurements through Tracking and Data Relay Satellite System (TDRSS)

The orbit of interest for the Gateway mission is the 9:2 synodic resonant NRHO with perilune radius approximately 3200 km. The uncertainty in state estimation for a spacecraft along the Gateway is considered here. Without loss of generality, it is assumed that the spacecraft is injected on the NRHO at the apoapsis. With no *a priori* information, the state covariance is initialized as $\mathbb{P}_{1|0} \to \infty$, or some very large number, at the apoapsis. In cases where an *a priori* covariance is known, then $\mathbb{P}_{1|0}$ can be initialized to that *a priori* covariance value. A few observations are allowed before the state covariance, $\mathbb{P}_{k|k}$, becomes a meaningful quantity. Certainly, most of the orbit determination process yields a covariance matrix with non-zero correlation coefficient, where change in one state quantity influences the other, however, for simplicity, consider, $\sigma_x = \sqrt{\mathbb{P}_{k|k}(1,1)}$, $\sigma_y = \sqrt{\mathbb{P}_{k|k}(2,2)}$ and so on. To collectively measure position uncertainty and velocity uncertainty as a whole, define root mean square (RMS) quantity, $\sigma_{RMS-position} = \sqrt{\sigma_x^2 + \sigma_y^2 + \sigma_z^2}$ and $\sigma_{RMS-velocity} = \sqrt{\sigma_{\dot{x}^2} + \sigma_{\dot{y}^2} + \sigma_{\dot{z}^2}}$. The plot in Figure 4.5 describes the derived position and velocity uncertainties along each of the

x, y and z directions for a spacecraft along the 9:2 synodic southern NRHO with tracking data collected at an interval of 4 hours. The simulation is continued till the spacecraft has traversed at least half of the time period of the orbit, roughly 3.5 days, to yield a meaningful covariance. Not surprisingly, since the position states along the x direction does not change as widely as along the y and z directions, the error levels in position along the x direction is significantly lower than the y and z directions. Further, based on the dynamics along the orbit, the spacecraft traverses more gradually closer to the apoapsis region than the periapsis region, therefore, more observations are recorded near the apoapsis region resulting in lower uncertainty in position and velocity states. Similarly, sparse observations near the periapsis region increases the uncertainty level.

Tracking interval affects the uncertainty level significantly. Shorter intervals yield more observations spaced closer to each other resulting in relatively lower uncertainty in state measurements, however, taking too many observations is not always feasible. There exists a trade-off between the uncertainty level and the number of observations. Figure 4.6 demonstrates the uncertainly in along the position and velocity states, expressed in root mean square quantity, for different tracking intervals ranging from 1 observation per hour to observations spaced at 24 hours interval. As discussed, uncertainty is lower in the apoapsis region, where most of the stationkeeping maneuvers are likely. The observations spaced at 1 hour interval yields a smoother curve for uncertainty levels along the orbit, while the curve corresponding to observations spaced 24 hours apart is coarse. For the range of tracking intervals tested for the 9:2 synodic NRHO, a 1σ position uncertainty less than 0.3 km and a 1σ velocity uncertainty less than 0.3 cm/s is achievable. Of course, additional observations reduce the uncertainty values and may be recorded for operational reasons. For this investigation, a conservative 3σ uncertainty in position ranging from 1 km to 10 km is considered. Similarly, a conservative 3σ uncertainty in velocity is chosen between 1 cm/s to 10 cm/s.

4.3 Unmodeled Orbit Determination Errors

A spacecraft experiences perturbations persisting from its launch, due to several factors like atmospheric drag, limitations of the measuring apparatus, additional gravitational

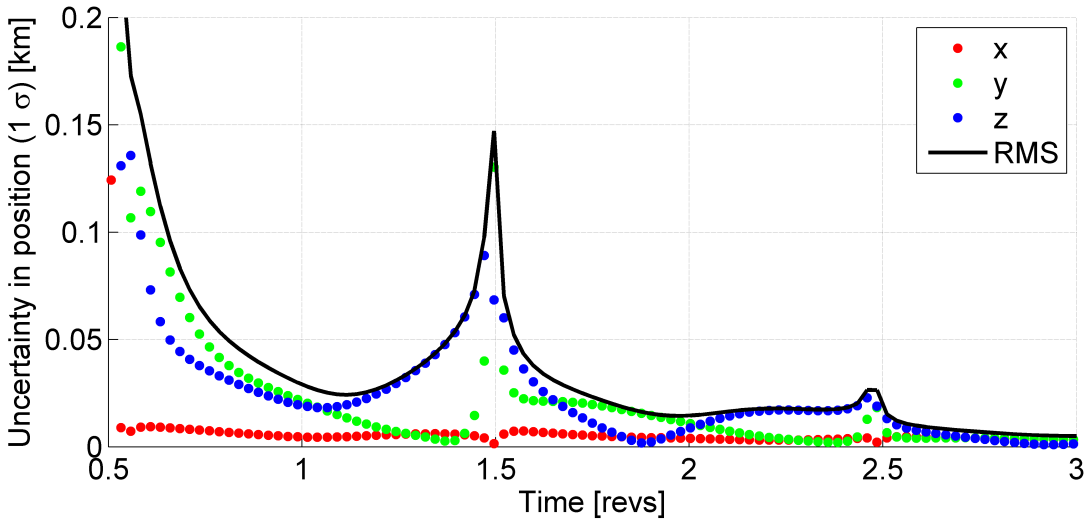

(a) Position uncertainty (1σ)

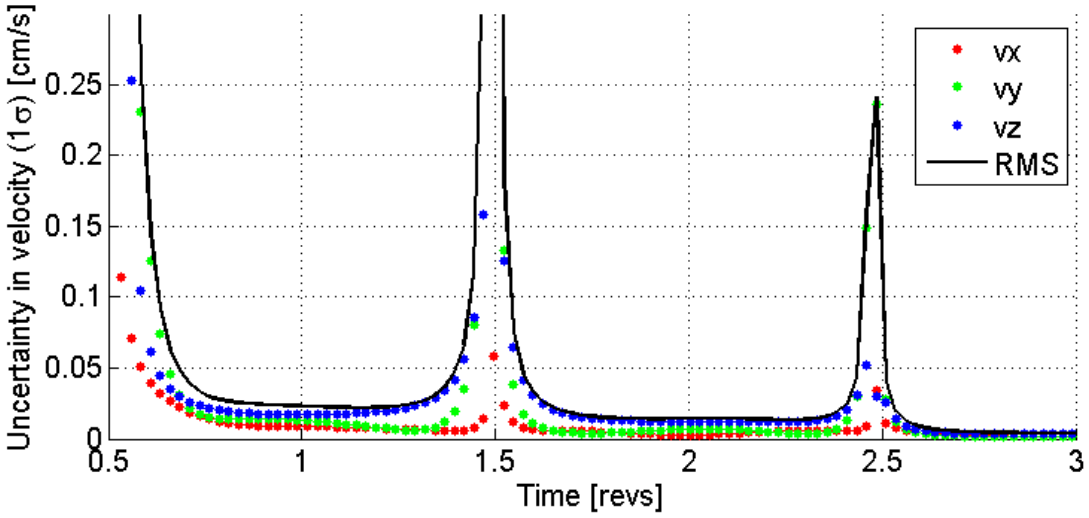

(b) Velocity uncertainty (1σ)

Figure 4.5. Position and velocity uncertainty derived from range and range rate measurements taken at 4 hours intervals, along the 9:2 synodic resonant southern L2 NRHO.

bodies, magnetic field of earth, charged particles, solar radiation pressure, etc. Besides, modeling errors also result in the spacecraft's true path being different from the reference path. Despite all these potential challenges, the primary focus of a stationkeeping process is to sustain the spacecraft near the reference trajectory beyond the orbit injection phase. Any uncertainty in the measurement of the position and the velocity states of the spacecraft

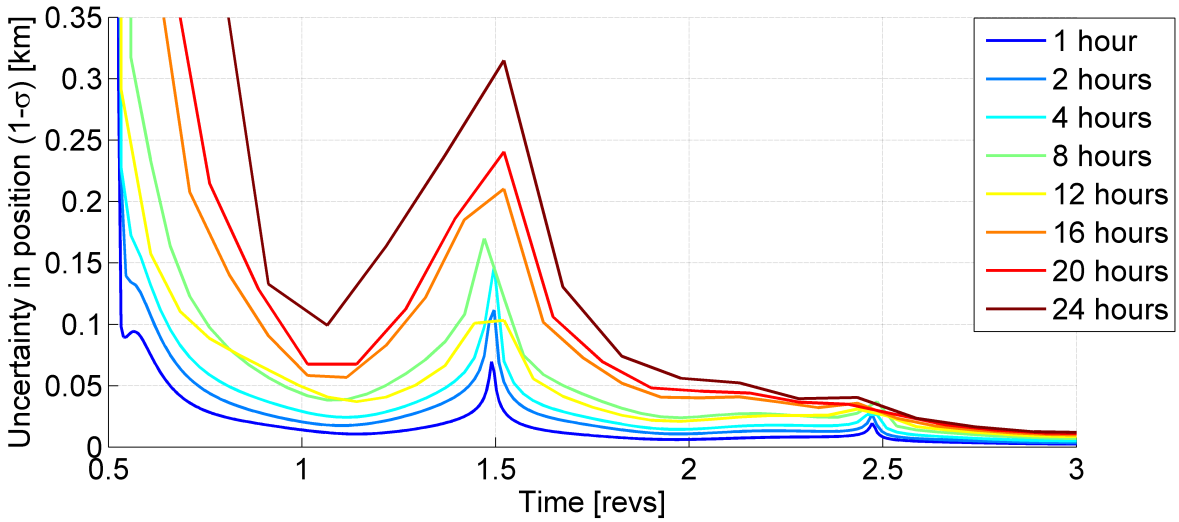

(a) Position uncertainty (1σ)

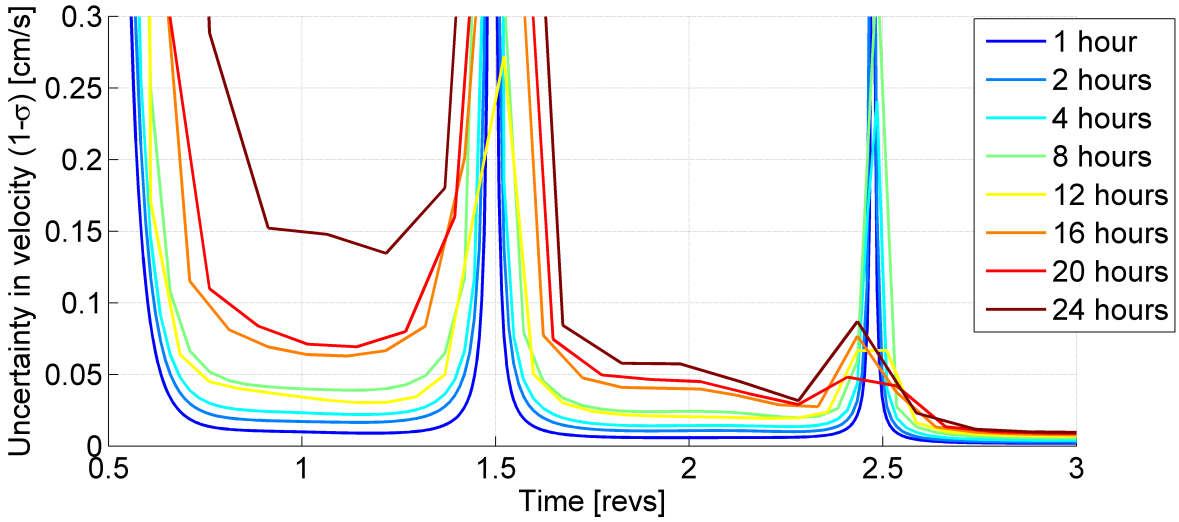

(b) Velocity uncertainty (1σ)

Figure 4.6. Position and velocity uncertainty derived from range and range rate measurements taken at various time intervals, along the 9:2 synodic resonant southern L2 NRHO.

is called orbit determination errors. Orbit injection error, tracking or navigation errors and maneuver execution error are the significant contributors to uncertainty in state measurements, and considered in this investigation. These errors are inevitable due to limitations in the orbit determination equipment and thrusting abilities. The magnitude of these errors are controllable by using better quality and sophisticated instruments, but cannot be

completely eradicated. If not addressed, these errors potentially destabilizes the motion of a spacecraft. These errors are stochastic in nature, thus cannot be modeled into the system. However, for simulating a stationkeeping operation these stochastic errors are incorporated as state perturbations, and a maneuver is delivered to overcome such quantities. Based on the evolution of these stochastic orbit determination errors are broadly classified into the three types.

4.3.1 Orbit Injection Errors

For convenience, the orbit injection is considered as the starting of the stationkeeping process. As the spacecraft approaches the end of the transfer trajectory an orbit injection maneuver is applied to inject the spacecraft into a long-horizon reference orbit. Undoubtedly, the injection is not accurate due to limitations in the thruster performance and tracking instruments that measures the spacecraft states. Consequently, the resulting position and velocity states immediately after the orbit injection is considered perturbed from the reference states.

To incorporate the orbit injection/insertion error, the reference position and velocity states are perturbed by a fixed magnitude in an arbitrary direction. A Gaussian random number generator is used to perturb the magnitude of position and velocity states. The mean of the magnitude of perturbation is considered zero while the standard deviation is chosen based on the knowledge of the existing hardware. Similarly, a Gaussian random number identifies an arbitrary direction. The perturbed position and velocity states are propagated as the actual trajectory or the true path of the spacecraft, along which maneuvers are delivered. Of course, there are multiple ways of generating perturbed position and velocity states for simulation, and may offer comparable results.

4.3.2 Tracking or Navigation Errors

As the spacecraft traverses along the orbit, the earth based tracking stations derive the position and velocity states of the spacecraft at discrete intervals, better known as tracking

intervals. Due to limitations in the orbit determination process, the states are never known to absolute precision. A stationkeeping strategy is expected to deliver a reasonable maneuver to maintain the spacecraft in the neighborhood of the virtual reference solution despite of the tracking errors.

To simulate the tracking error, position and velocity states along the true propagated path are perturbed by a fixed magnitude in an arbitrary direction, similar to the orbit insertion error. Again, the perturbed position and velocity states are propagated as the actual trajectory or the true path of the spacecraft. Similar to orbit injection errors, tracking or navigation errors may be incorporated in multiple ways, and likely offer comparable results.

4.3.3 Maneuver Execution Errors

The stationkeeping algorithm computes a corrective maneuver at regular intervals to maintain the spacecraft near a close proximity to the virtual reference solution. However, the computed maneuver and the implemented maneuver is never exact, typically due to limitations in thrusting. To incorporate this inaccuracy, the computed maneuver is perturbed by a fixed magnitude in an arbitrary direction.

A summary of various state estimation errors used within this investigation to simulate stationkeeping operations are given in Table 4.3. Two different error levels are considered for orbit insertion and navigation. The range of uncertainties considered are consistent with the quantities determined in section 4.2, derived through signal processing using Kalman filter where uncertainties in measurement quantities in form of range and range rate data are converted to state uncertainties.

4.4 Solar Radiation Pressure Errors

Solar radiation pressure (SRP) is introduced into the model to simulate the spacecraft motion, however, the exact orientation of the spacecraft is unknown, hence SRP errors

Table 4.3. State estimation errors.

Uncertainty Type	Low Error	High Error
Orbit Injection	Mean : 0 km, 0 cm/s 3σ : 1 km, 1 cm/s	Mean : 0 km, 0 cm/s 3σ : 10 km, 10 cm/s
Navigation	Mean : 0 km, 0 cm/s 3σ : 1 km, 1 cm/s	Mean : 0 km, 0 cm/s 3σ : 10 km, 10 cm/s
Maneuver Execution	0.03 cm/s (fixed)	

are introduced to simulate a perturbing force. Uncertainties in the projected area of the spacecraft facing the Sun and the coefficient of relfectivity C_r are consistent with literature [4], [57]. The approach of considering SRP as perturbing term may inflate the stationkeeping cost, but gives an upper bound to the propellant consumption. In fact, if the fidelity of the model is improved by considering exact attitude dynamics for solar radiation pressure in the model the annual stationkeeping cost is expected to deflate.

Table 4.4. Solar Radiation Pressure errors.

Uncertainty Type	Error Level
Proj. Area	Mean : 0 km, 1σ : 5%
C_r	Mean : 0 km, 1σ : 10%

4.5 Stationkeeping Algorithm

A mission has several phases that roughly encompasses launch, parking orbit, transfer trajectory, stationkeeping and departure. For simplicity, a stationkeeping phase is assumed to commence as soon as the spacecraft is injected in to the desired orbit. In the stationkeeping phase regular orbit maintenance maneuvers are delivered to sustain a spacecraft near the desired orbit for a relatively long duration. The spacecraft deviates away from the reference path due to unmodelled dynamics and limitations in orbit determination. To simulate a real mission stationkeeping scenario, various errors are introduced on purpose. The halo orbits

have gained a lot of focus for upcoming missions, in such cases, the halo orbit injection (HOI) is assumed to be the starting point for the stationkeeping process. Based on the understanding of the thrusters, orbit injection error is introduced with a certain standard deviation. The position and the velocity magnitudes are perturbed with a random number generated using Gaussian probability distribution corresponding to standard deviation of orbit injection error, in any arbitrary direction. The spacecraft naturally deviates from the desired orbit due to the errors in the states, requiring frequent stationkeeping maneuvers to maintain the spacecraft within a specific bounds near the nominal path. The exact states of the spacecraft are never known to 100% precision due to limitations in orbit determination, hence at every maneuver locations the states are deliberately perturbed corresponding to the orbit determination error levels. Various stationkeeping algorithms exists that determines the corrective maneuver to ensure the spacecraft is in close vicinity to the nominal path. In this investigation, an x-axis crossing control approach determines the magnitude and the direction of the corrective maneuver. Additional maneuver execution errors are introduced and the states are updated and propagated. In the higher-fidelity ephemeris model the additional solar radiation pressure errors are also Incorporated while propagating the dynamical equations of motion. The states are propagated till the subsequent maneuver location and the process is repeated till the end of the mission duration. After simulating till the end of mission duration, the magnitude of all implemented maneuvers within the mission duration are tallied to estimate the stationkeeping costs. For a stochastic process, multiple Monte Carlo simulations are conducted to estimate the mean and standard deviation of the annual stationkeeping costs.

For stationkeeping algorithm used throughout this investigation, if the spacecraft drifts unacceptably far from the reference, 10000 km for this investigation, the simulation is ceased immediately and the computed costs for that particular iteration is ignored. A 10000 km drift in position quantity is a reasonable choice along the NRHO that is comparable to departure estimated by Momentum Integral [4], [57]. A new seed for the random numbers are introduced and the simulations are continued. Throughout this investigation, two different levels of orbit determination errors are used, as detailed in Table 4.3.

4.6 Monte Carlo Simulation

Stationkeeping algorithm uses random sampling errors to represent uncertainties in orbit determination and maneuver execution that is then propagated in a nonlinear regime. Estimating the mean maneuver cost is not possible using an analytical approach. Due to the stochastic nature, it is convenient to use Monte Carlo simulations to determine the probabilistic mean. The quality of the solution obtained using the Monte Carlo process is assessed by the closeness of the observed solution to the true solution. When the true mean to a problem is known, the sample sizes are adjusted to meet the desired accuracy of the observed mean. In the case of a stochastic stationkeeping process, the true solution itself is unknown. It is therefore challenging to decipher the appropriate sample size required to estimate a mean value that is close enough to the true value. A sample size about 20 or 30 is generally too small to get a solution with reasonable confidence level for comparison. On the other hand, having too many simulations, adds very little information at high computational expense, one that is ineffective. An appropriate sample size is desired that provides substantially high confidence level making comparison effective.

Many authors in the past have used about 50, 100, 300, 500 or even 1000 Monte Carlo runs depending on their problems. Some researchers do offer a qualitative reasoning on the appropriate number of Monte Carlo runs or specify the standard deviation at the end of the simulation [25], [46]–[50]. Sample size determination is vital for Monte Carlo simulations. Muralidharan [117] elaborates the process of determining the right sample size based on the accepted confidence intervals. The strategy had been adopted by Gordon [47] for his station-keeping application. For a trial that produces observations $\varkappa_1$, $\varkappa_2$, ..., $\varkappa_n$, the mean, $\bar{\varkappa}$ and the standard deviation, $S_\varkappa$, of the samples can be computed by

$$\bar{\varkappa} = \frac{1}{n}\sum_{\mathrm{i}=1}^{n} \varkappa_{\mathrm{i}} \tag{4.10}$$

$$S_\varkappa^2 = \frac{1}{n-1}\sum_{\mathrm{i}=1}^{n} (\varkappa_{\mathrm{i}} - \bar{\varkappa})^2 \tag{4.11}$$

where n is the sample size. The mean computed from the samples may not be exactly equal to the true mean, therefore, the variance of the computed mean, $\sigma^2_{\bar{\varkappa}}$, is defined as

$$\sigma^2_{\bar{\varkappa}} = \frac{S^2_{\varkappa}}{n} \tag{4.12}$$

that is a function of the variance of the samples $S^2_{\varkappa}$. A superior quality Monte Carlo simulation estimates the computed mean, $\bar{\varkappa}$, close to the true mean, $\mu_{\varkappa}$. The confidence level of the computed mean provides the probability that the true mean lies within a certain bounded region about the computed mean. As demonstrated in Figure 4.7, let the *lower control limit* and the *upper control limit* of the bounded region be denoted as LCL and UCL respectively. Mathematically, LCL and UCL are defined as

$$[LCL,\, UCL] \;=\; \bar{\varkappa} \pm \tilde{t}_{n-1}\sigma_{\bar{\varkappa}} \;\approx\; \bar{\varkappa} \pm z_c\sigma_{\bar{\varkappa}} \;\approx\; \bar{\varkappa} \pm z_c\frac{S_{\varkappa}}{\sqrt{n}} \tag{4.13}$$

where $\tilde{t}_{n-1}$ and z_c are quantities that defines the percentage confidence levels. Since the true distribution is unknown, the observations are in form of a Student's T-distribution, where $\tilde{t}_{n-1}$ is the corresponding t-score for degrees of freedom, $n-1$, in a two-sided T-test. As the sample size $n \to -infty$, the Student's T-distribution tends to a Normal distribution , i.e., $\tilde{t}_{n-1} \to z_c$. The relation between percentage confidence level and the corresponding sigma limit is provided in table 4.5 [117]. As the sample size increases, the gap between LCL and UCL becomes narrower, consequently, the computed mean approaches the true mean. The half width, h, between LCL and UCL, also referred to as 'precision' by some researchers, is a deciding factor on the number of Monte Carlo runs. The precision or half width is defined as

$$h = \frac{UCL - LCL}{2} = z_c\frac{S_{\varkappa}}{\sqrt{n}} \tag{4.14}$$

that inversely depends on the number of iterations. Large number of iterations will produce a more precise result at the cost of immense computational time. The number of simulations actually required is in fact a function of the preferred precision level. The precision or the half width, h, desired may be an absolute parameter or a relative parameter in comparison to the mean. The number of Monte Carlo runs are estimated as follows:

- Absolute Precision

  Assuming that the precision of the required solution is given in terms of the permissible absolute error, α. In other words, for the chosen confidence level, true mean should be within $\bar{\varkappa} \pm \alpha$, thus

$$h = \alpha = z_c \frac{S_\varkappa}{\sqrt{n}} \quad \rightarrow \quad n = \left(\frac{z_c S_\varkappa}{\alpha} \right)^2 \tag{4.15}$$

- Relative Precision

  If the precision of the required solution is given in terms of the permissible relative error ($\alpha\%$). In other words, for the chosen confidence level, true mean should be within $\bar{\varkappa} \pm (\alpha/100)\bar{\varkappa}$, thus

$$h = \frac{\alpha}{100}\bar{\varkappa} = z_c \frac{S_\varkappa}{\sqrt{n}} \quad \rightarrow \quad n = \left(100 \frac{z_c S_\varkappa}{\alpha \bar{\varkappa}} \right)^2 \tag{4.16}$$

Either of equations (4.15) or (4.16) can be used to compute the required number of Monte Carlo simulations that yields computed mean that would be close to the true mean within the accepted confidence level. The sample size, n, depends on the accepted sigma limit, z_c, the permissible absolute or relative error, α, the present computed mean, $\bar{\varkappa}$ and standard deviation of the samples tested, $S_\varkappa$.

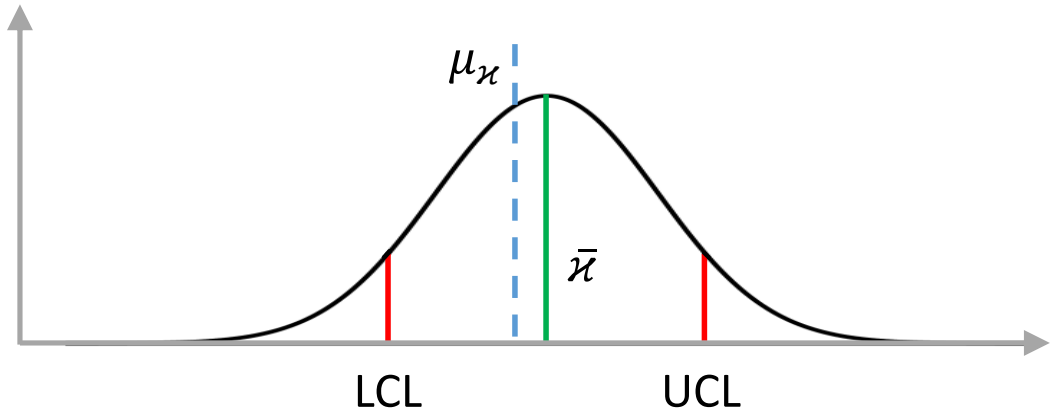

Figure 4.7. Precision in a stochastic process.

Table 4.5. Percentage confidence level and corresponding sigma limits and T-score.

Confidence Level (%)	Z-score / Sigma Limit (z_c)	$\tilde{t}_{100-1}$	$\tilde{t}_{1000-1}$
68.26	1	1.005	1.000
95	1.96	1.984	1.962
95.45	2	2.025	2.003
99	2.58	2.626	2.581
99.73	3	3.078	3.008
99.99	3.89	4.055	3.906

Estimating the appropriate sample size for the Monte Carlo runs is challenging. It is observed that at least 30 runs are required to stabilize the variance in a Monte Carlo process for stationkeeping applications. Monte Carlo method is a probabilistic mean computation technique based on stochastic sampling hence no fixed number of runs or value of precision is defined. The termination of a Monte Carlo process is based on the precision demanded by the user to evaluate the data appropriately. Either based on a predefined precision level, the sample size is estimated using the procedures discussed, or, the standard deviation of the estimated mean be specified along with the computed mean to provide the essence of the actual distribution.

5. IMPULSIVE STATIONKEEPING STRATEGY

Any type of spacecraft mission requires regular orbit maintenance operations for long-term sustainability. The orbits in this investigation are particularly subject to sensitive dynamics that perturb spacecraft from the desired path. In this investigation, stationkeeping operations maintain the spacecraft in the vicinity of a long horizon virtual reference solution that is generated incorporating science constraints as well as phase constraints such as eclipse avoidance [4], [57]. The virtual reference is updated over time as appropriate. Several stationkeeping techniques are evaluated on the Earth-Moon L1 and L2 orbits, i.e., Lyapunov and halo orbits, both stable and unstable [4], [57], [59]–[61], [64], [103], [118]. Since the Gateway mission is planned for launch in the early 2020s and expected to operate in the 9:2 synodic resonant NRHO, with a radius of periapsis approximately 3200 km from the Moon, it serves as a baseline trajectory to test the efficiency of a control strategy for stationkeeping on NRHOs. Of course, the control strategy must also be applicable to other low perilune radius NRHOs. This investigation focuses on leveraging the underlying dynamics to improve the control algorithm and parameter selection process, as well as determine the annual cost for stationkeeping, thereby estimate the propellant requirement for a desired mission duration.

5.1 Overview of x-axis Crossing Control Approach

Recent analyses have focused on the x-axis crossing control algorithm and a formulation that is applied for a number of successful missions [60], [118]. It is also currently employed for analysis in support of the Gateway mission [4], [57], [119]. The x-axis control strategy generally relies on the symmetry of the NRHOs across the xz plane in the rotating frame of reference. In the CR3BP, the rotating $\dot{x}$ value along the orbit at the xz plane crossing is zero. The notion of a zero value for the rotating $\dot{x}$ velocity component at the xz plane crossing is exploited for orbit maintenance operations. Due to complex dynamics in the higher-fidelity ephemeris model, the natural trajectory that resembles the NRHO does not possess a precise value of $\dot{x} = 0$ at the xz plane crossing, hence, it is further constrained that the rotating $\dot{x}$ value along the actual trajectory matches the $\dot{x}$ value along a long horizon virtual reference path at the xz plane crossing that is within an acceptable tolerance.

The stationkeeping operation is a sequential process. A baseline trajectory is introduced that acts as a long horizon virtual reference solution. From previous investigations [4], [57], it is seen that targeting xz plane crossings near the periapsis region yields low stationkeeping costs. The algorithm also targets the rotating $\dot{x}$ value at subsequent xz plane crossings along the evolving path. The $\dot{x}$ values at each of the xz plane crossings near the periapsis on the long horizon virtual reference solution are initially recorded. The spacecraft state is originally introduced at the halo orbit injection epoch and additional white noise in both position and velocity states, and with specified mean and variance is subsequently incorporated. In the ephemeris model, additional uncertainty in solar radiation pressure is introduced with errors in the coefficient of reflection C_r and the surface area of the spacecraft model. The perturbed states are propagated to a predetermined maneuver location, generally closer to the apoapsis region, and a maneuver $\Delta\bar{v}$ is computed to meet the goal of achieving the $\dot{x}$ value along the virtual baseline at a specified downstream xz plane crossing, within some predefined tolerance, that is, 0.45 m/s, consistent with the literature [4]. The target xz plane crossing may be the 1^{st}, 2^{nd}, ..., n^{th} crossing, increasing further downstream along the propagated trajectory. If the targeting process fails to compute a successful maneuver that meets the goal for a specified target, the target horizon time is reduced and the process is repeated again until a successful maneuver is computed. In this investigation, however, target horizon is fixed to analyze the impact of a fixed target horizon on the maneuver magnitude and direction. Additional white noise modelled as maneuver execution error is incorporated into the maneuver and implemented. Along the subsequent path, the states are updated and further perturbed with navigational errors and solar radiation pressure errors and the procedure is continued till the end of the mission duration or some specified duration. In contrast, if none of the target horizon times delivers a successful maneuver, the particular simulation is considered as failed. The simulation is also tagged as failed if the spacecraft deviates more than 10000 km from the virtual reference solution at any time. Additional tuning parameters is introduced such as minimum value of $|\Delta\bar{v}|$ that is deliverable and minimum deviation to compute a maneuver. The total sum of the maneuvers $|\Delta\bar{v}|$ over each run is recorded. Since white noise is generated randomly, a Monte Carlo simulation is performed over 100 runs and the mean cost is estimated [103]. With a sample size of 100, a sufficient

level of precision is achieved while estimating the mean, i.e., the 95% confidence intervals for the mean are the same order of magnitude as the orbit determination errors. Such precision is sufficient for this analysis [46], [50]. The total cost is then linearly extrapolated over one year to estimate an annual maintenance cost. In certain sample cases, the virtual reference solution is updated incorporating infrequent orbit correction maneuvers, also known as long-horizon stationkeeping maneuvers. The long-horizon stationkeeping maneuvers are application specific. The costs to update the long horizon orbit may be added to the annual stationkeeping cost estimate.

5.2 Principal Stretching Directions

A linear mapping of state perturbations near a reference trajectory is reliable to design appropriate control algorithms, as well as to leverage the characteristic dynamical behavior in the vicinity of the reference path. The Cauchy-Green tensor (CGT) is a function of the state transition matrix (STM) and yields valuable information concerning the linearized variational dynamical flow in the vicinity of a reference solution [81], [120]. While the STM, ϕ, relates the variation of each individual state over time such that $\phi(t, t_0) = \frac{\partial \bar{\mathbf{x}}(t)}{\partial \bar{\mathbf{x}}_0}$, the CGT relates the evolution of the perturbations represented as a material volume over time. The STM evaluated along a reference trajectory, $\bar{\mathbf{x}}^*(t)$, maps the initial perturbation, $\delta\bar{\mathbf{x}}_0$, to the final perturbed states, $\delta\bar{\mathbf{x}}_f$, as a linear correlation, i.e.,

$$\delta\bar{\mathbf{x}}_f = \phi(t_f, t_0)\delta\bar{\mathbf{x}}_0 \tag{5.1}$$

where, t_0 and t_f are the initial and final epochs. The isochronous perturbations are measured relative to this reference path as $\delta\bar{\mathbf{x}}(t) = \bar{\mathbf{x}}(t) - \bar{\mathbf{x}}^*(t)$. The CGT, or simply '$\mathbb{C}$' is evaluated as

$$\mathbb{C}(t_f, t_0) = \phi(t_f, t_0)^{\mathrm{T}}\phi(t_f, t_0) \tag{5.2}$$

and defines the deformation, as a product of the transpose (superscript T) of the state transition matrix, ϕ, with itself. Physically, CGT renders the square of the magnitude of the final deformation to the initial deformation as

$$||\delta\bar{\mathbf{x}}_f||^2 = \delta\bar{\mathbf{x}}_f^{\mathrm{T}}\delta\bar{\mathbf{x}}_f = \delta\bar{\mathbf{x}}_0^{\mathrm{T}}\phi(t_f,t_0)^{\mathrm{T}}\phi(t_f,t_0)\delta\bar{\mathbf{x}}_0 = \delta\bar{\mathbf{x}}_0^{\mathrm{T}}\mathbb{C}(t_f,t_0)\delta\bar{\mathbf{x}}_0. \tag{5.3}$$

The growth or decay of the quantity $||\delta\bar{\mathbf{x}}_f||^2$ describes the sensitivity of the trajectory to the initial perturbation, $\delta\bar{\mathbf{x}}_0$, however, when the size of an initial perturbation is undefined, the sensitivity information is directly extracted from CGT. The eigen-decomposition of the CGT, or the singular value decomposition of the STM, yields details about directions and magnitudes for the stretching of the flow.

In a dynamical system, the flow as emulated in terms of a material volume, is characterized primarily by the elongation and orientation of the volume. The flow for any volume is visualized either using the eigen-decomposition or the singular value decomposition of the corresponding matrices. The eigen-decomposition of the CGT yields the eigenvalues λ_{i} and the eigenvectors $\mathbb{V}_{\mathrm{i}}$. For a linear system, the contraction or expansion of the local phase space is captured by σ_{i} corresponding to the directions in $\mathbb{V}_{\mathrm{i}}$. Note that σ_{i} equals $\sqrt{\lambda_{\mathrm{i}}}$. The singular value decomposition (SVD) of the STM, reveals the same critical details about the flow in the phase space but with additional directional information in $\mathbb{U}_{\mathrm{i}}$. Mathematically, the STM is decomposed into the matrices, $\mathbb{U}$, Σ and $\mathbb{V}$, such that,

$$\mathbb{U}\Sigma\mathbb{V}^* = \phi(t_f,t_0) \tag{5.4}$$

where, the columns of $\mathbb{U}$ yield the stretching directions at the final epoch. For a square matrix, ϕ, there is associated a diagonal matrix, Σ, with the magnitude of the stretching along different directions in descending order, i.e.,

$$\Sigma = \begin{bmatrix} \sigma_1 & & & \\ & \sigma_2 & & \\ & & \ddots & \\ & & & \sigma_n \end{bmatrix} \tag{5.5}$$

such that, $\sigma_1 > \sigma_2 > \ldots > \sigma_n$. The matrix $\mathbb{V}$ then provides the principal stretching di-

rections at the initial time along the propagated arc. The matrices Σ and $\mathbb{V}$ essentially supply the same details, acquired using an eigenvalue decomposition of $\mathbb{C}$, while $\mathbb{U}$ offers additional information captured from singular value decomposition, also derivable from the Cauchy-Green tensor. The matrices $\mathbb{U}$ and $\mathbb{V}$ are mutually orthogonal. Figure 5.1 illustrates the contraction or expansion along different flow directions with the example of a two-dimensional system transitioned through the SVD or the CGT. Consider a unit circle in the phase space near a point along an initial reference path that undergoes deformation and evolves into a stretched ellipse. The evolution of this unit circle into an ellipse is a combination of translation and rotation. The matrices $\mathbb{U}$ and $\mathbb{V}$ supply the rotation information while the matrix Σ yields information concerning linear translation. The columns of the matrix $\mathbb{V}$ represented by $\mathbb{V}_i$ indicate the principal directions at the initial time that evolve into $\mathbb{U}_i$ (the columns of matrix $\mathbb{U}$). The diagonal elements of the matrix Σ, or σ_i, indicate the stretching along corresponding principal directions. The Cauchy-Green tensor and the singular value decomposition fundamentally provides the same information, therefore, used to linearly approximate the attainable region in the vicinity of a reference trajectory. Precise applications of the principal stretching directions are discussed for two contrasting applications in this investigation. Effect of principal stretching directions on stationkeeping maneuvers are discussed in subsection 5.3.1, while chapter 6 discusses leveraging stretching directions for orbit departure and trajectory design applications.

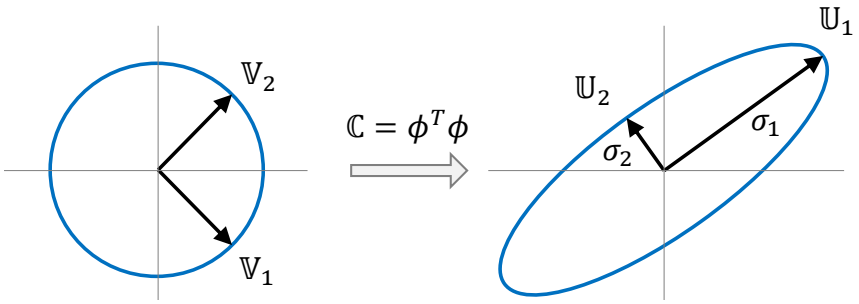

Figure 5.1. Principal stretching directions.

5.3 Stationkeeping Parameters

The stationkeeping algorithm depends on various parameters that influence the annual cost and the boundedness of a spacecraft trajectory near the virtual reference solution. The stationkeeping parameters that are user-defined impact its performance. For orbit maintenance using the x-axis control approach, three factors that impact the overall cost and deviation from reference path are explored in this investigation. The selection of these parameters offer a basis to understand the evolution of the underlying dynamical flow near the NRHO that enables the x axis crossing control strategy to succeed.

- Coast duration

  Currently, the stationkeeping process is based on impulsive maneuvers and, hence, between two successive maneuvers the spacecraft coasts under the natural dynamics. The minimum time duration between two successive maneuvers is defined as the coast duration. It is generally expected that, for a stable orbit, maneuvers with wider spacing are effective in reducing costs, in contrast to an unstable orbit that may require maneuvers spaced more closely for effective orbit maintenance. In addition, NRHOs frequently possess close lunar passages, a nonlinear effect that influences the dynamical flow near the reference orbit over time.

- Maneuver location

  Not all locations around the orbit offer the same characteristic properties. Some locations are notably more sensitive depending on the proximity to different gravitational bodies. These sensitive locations may offer maximum benefits if stationkeeping maneuvers are implemented accurately [121]. However, the primary function of a stationkeeping maneuver is to overcome error build-ups due to limitations in the orbit determination process and errors due to modeling and prior maneuvers. These sensitive locations often increase the measurement uncertainty, therefore, precise maneuvers are impossible in practice. These drawbacks, coupled with errors in maneuver execution, results in these sensitive regions being inferior maneuver locations as errors in the sensitive regions amplify rapidly over time. Identifying such regions in advance is particularly helpful for NRHO stationkeeping.

- Target horizon

  The length of time between the maneuver location and the targeted xz plane crossing near the periapsis region is denoted the target horizon. Since the target horizon is user defined, the target is placed at the first xz plane crossing near the periapsis, or any subsequent crossing near the next periapsis downstream. Since the target location is an xz plane crossing, the target horizon is labelled in terms of the number of revolutions downstream from the maneuever location. A precise maneuver is generated by targeting the rotating $\dot{x}$ value at the specified xz plane crossing using a single shooting process. It is generally reliable to target a sensitive region, e.g., the periapsis region, to yield the most economic maneuver. Guzzetti et al. suggest the same principle based on their results by targeting the xz plane crossings near the periapsis [4]. A longer target horizon, i.e., targeting further downstream, is expected to produce lower maneuver magnitudes, however, mission requirements or constraints may necessitate shorter target horizons.

The inter-dependency of the parameters, i.e., coast duration, maneuver location and target horizon, is illustrated in the flowchart in Figure 5.2. The simultaneous interactions between the flow evolving from one maneuver location to the next along a coast arc and the flow evolution from the maneuver location to the target determines the performance of the maneuver.

5.3.1 Effect of maneuver location and coast duration

The spacecraft coasts under the natural dynamics between two successive impulsive maneuver locations, and the time interval is termed the coast duration. The flow between the maneuver locations then determines the impact of the deviations in the initial states that are propagated downstream to the end states where the subsequent maneuver is generated. The dynamics of the flow in the circular restricted three-body problem as well as in the ephemeris model are complex, however, for small perturbations in a linear model that are reflective of the unmodelled forces and errors in the orbit determination process, predictions of the flow variations in the vicinity of a reference trajectory using the state transition matrix

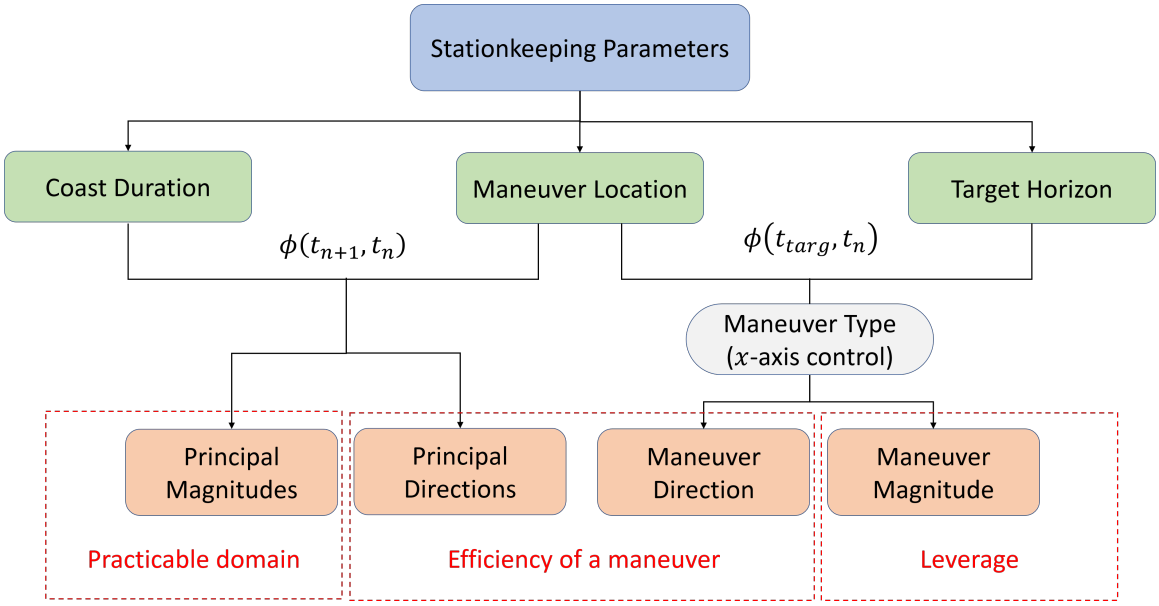

Figure 5.2. Stationkeeping parameter effects flowchart.

is generally reliable for these NRHOs. The Cauchy-Green tensor (CGT) is a function of the STM and aids in visualizing linear flow by decomposing it into different mutually orthogonal directions, along which components of perturbations grow independent of the other. The linear flow is typically visualized using eigen-decomposition or Cauchy-Green tensor. Since the primary trajectory of interest is the NRHO in the Earth-Moon system that are almost stable, the Cauchy-green tensor decomposition is used to monitor the growth in magnitude of perturbations in different orthogonal flow directions, thereby overcomes the shortcomings of the Eigen-structure to explain the flow in regions that lack definitive manifold structures. Since maneuvers are allowed anywhere along the orbit (multiple maneuvers per orbit or multiple orbits between maneuvers) the understanding of the mutual impact of the maneuver location and coast duration is critical. The Cauchy-Green tensor decomposes the flow into different orthogonal stretching directions providing necessary information about the growth of perturbations in each of the decomposed, mutually independent, orthogonal directions.

A maneuver is potentially delivered anywhere along a range of locations on the orbit, hence, identifying precise maneuver locations is a key input for the analysis. Maneuver locations and trajectory segment lengths are, thus, denoted in terms of a mean anomaly

and an osculating true anomaly. The quantities, mean anomaly and true anomaly, are used to represent locations along conic orbits in the two-body problem, however, a similar form in the CR3BP are reliable to uniquely identify locations along an orbit. Since the NRHO is a closed orbit in the CR3BP, the mean anomaly is defined as a fraction of an orbit the spacecraft has traversed since the most recent periapsis, i.e.,

$$\theta_{MA} = 2\pi\frac{t}{\wp}rad = 360\frac{t}{\wp}deg \tag{5.6}$$

where $\wp$ is the time period for the selected orbit while t is the time of propagation beyond the most recent instantaneous periapsis location (i.e., closest passage at the Moon) as defined in the circular restricted three-body problem. The quantity $2\pi/\wp$ is called the mean motion. Since the NRHO is not a Keplerian orbit, an osculating true anomaly, θ_{TA}, is only a mathematical representation defined with respect to a central body, i.e., the Moon [122]. The mean anomaly quantifies the relative locations in terms of the actual time of propagation while true anomaly offers the geometric interpretation of locations as noted in Figure 5.3. Since NRHOs are highly eccentric, i.e., NRHOs have significantly larger apolune radius than perilune radius, measurements using mean anomaly makes it convenient to express locations on the orbit of different sizes as a direct function of the actual time of propagation while osculating true anomaly provides a geometric interpretation as shown in Figure 5.3. In the case of NRHOs apoapsis occurs at 180 degrees and periapsis at 0 and 360 degrees respectively in both mean anomaly and osculating true anomaly scales. The coast duration is also defined in similar manner as the change in the mean anomaly or the osculating true anomaly past the maneuver location. In mean anomaly, for example, 180 degree coast arc signifies that the spacecraft states are propagated for 0.5 time period past the maneuver location.

The flow between the n^{th} and $(n+1)^{\text{th}}$ impulsive maneuvers, at time t_n and t_{n+1} respectively, is measured by the state transition matrix evaluated along the coast segment, i.e., φ_C, such that $\varphi_C = \phi(t_{n+1}, t_n)$. Without loss of generality, assume, $t_n = t_0$, the initial time at which the maneuver is implemented, and $t_{n+1} = t_f$, as the final time along the propagated

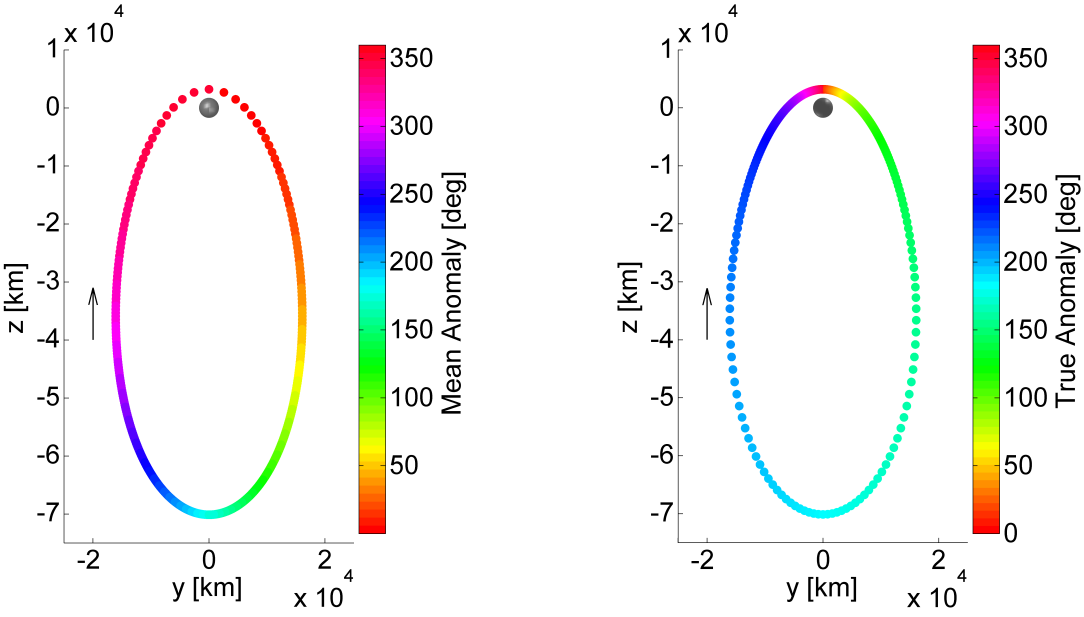

(a) Mean Anomaly (b) Osculating True Anomaly

Figure 5.3. Definition of locations along NRHO.

natural trajectory segment. In the stationkeeping problem, however, only the initial velocity terms are controllable, hence tracking the flow generated by the 6×6 state transition matrix φ_C is inconsequential. Specific submatrices of φ_C defined by

$$\varphi_C = \begin{bmatrix} \varphi_{C,r,r} & \varphi_{C,r,v} \\ \varphi_{C,v,r} & \varphi_{C,v,v} \end{bmatrix} = \begin{bmatrix} \frac{\partial \bar{r}_f}{\partial \bar{r}_0} & \frac{\partial \bar{r}_f}{\partial \bar{v}_0} \\ \frac{\partial \bar{v}_f}{\partial \bar{r}_0} & \frac{\partial \bar{v}_f}{\partial \bar{v}_0} \end{bmatrix} \tag{5.7}$$

yield more relevant characteristics. For example, the 3×3 dimensional submatrix, $\varphi_{C,r,v}$, maps the initial velocity perturbation, $\delta\bar{v}_0$, to the final position change, $\delta\bar{r}_f$, and the 3×3 dimensional submatrix, $\varphi_{C,v,v}$, maps the initial velocity perturbation, $\delta\bar{v}_0$, to the final velocity change, $\delta\bar{v}_f$. Also, combined, the 6×3 dimensional submatrix $\varphi_{C,rv,v}$, that is constructed as

$$\varphi_{C,rv,v} = \begin{bmatrix} \varphi_{C,r,v} \\ \varphi_{C,v,v} \end{bmatrix} \tag{5.8}$$

and maps the initial velocity perturbation, $\delta\bar{v}_0$, to the final position and velocity state change,

$\delta\bar{r}_f$ and $\delta\bar{v}_f$. This matrix yields significant characteristics, as only the initial velocity states, $\delta\bar{v}_0$, are subject to change. The sensitivity of the orbit states to initial velocity changes is measured by monitoring the magnitude of maximum stretching, σ_1, corresponding to each of the $\varphi_{C,r,v}$, $\varphi_{C,v,v}$ and $\varphi_{C,rv,v}$ submatrices. The values of the largest stretching magnitude, σ_1, corresponding to each of the $\varphi_{C,r,v}$, $\varphi_{C,v,v}$ and $\varphi_{C,rv,v}$ submatrices for various combinations of maneuver locations and coast durations along the 9:2 synodic resonant orbit with perilune radius 3200 km is plotted in Figure 5.4. Not surprisingly, the maximum stretching magnitudes corresponding to $\varphi_{C,v,v}$ and $\varphi_{C,rv,v}$, the submatrices that include velocity perturbations at the final time, are significantly larger than the maximum stretching magnitudes corresponding to $\varphi_{C,r,v}$, suggesting that the velocity changes generally require tight control. Due to such behavior, the flow described by the $\varphi_{C,v,v}$ and $\varphi_{C,rv,v}$ submatrices offer measurements to identify sensitive regions along the orbit. Since the stationkeeping algorithm is required to reduce the successive maneuver magnitudes, the stretching direction from the $\varphi_{C,v,v}$ submatrix, that monitors the final velocity change, is incorporated throughout this investigation. Further, as is evident from Figure 5.4, trajectory segments that terminate close to or originate near the periapsis regions are highly sensitive to perturbations, i.e., hotter shades in the map, hence, maneuvers are generally avoided in such regions. The cooler shades in the map, highlight the likely regions suitable for defining the maneuver locations.

Of course, not all components of the maneuver lie along the largest stretching direction, however, the magnitude of largest stretching provides the maximum magnitude of state change that could result from any maneuver of a given magnitude. In addition to the maneuver, any error in maneuver execution also amplifies in the same manner. The lighter regions in the schematic, as in Figure 5.4 indicates a larger stretching compared to the darker regions. For a particular orbit, the L2 southern NRHO with perilune radius 3200 km, a sharp light-colored contour is visible across the figures corresponding to measurements in mean anomaly. These contours represent the trajectory segments that originates or terminates close to the periapsis region, for example, a trajectory segment that originates at a maneuver location at 180 degree θ_{MA} or θ_{TA}, i.e. the apoapsis, when propagated for a coast duration of 180 degrees approaches the periapsis region that is highly sensitive. Any small perturbations

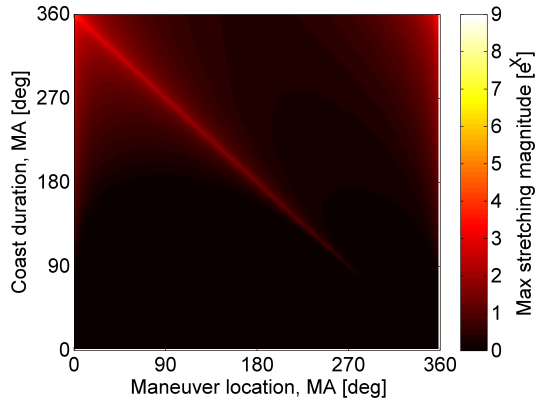

(a) Maximum stretching along $\varphi_{C,r,v}$ for measurements in mean anomaly

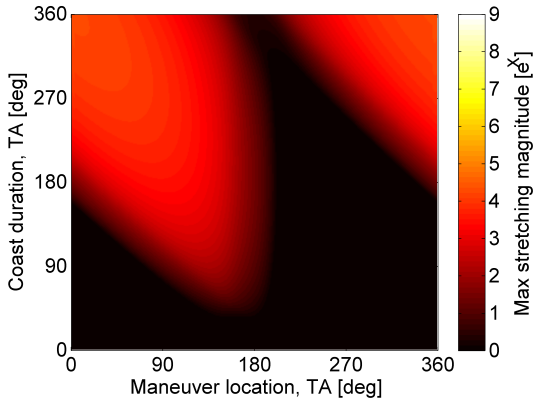

(b) Maximum stretching along $\varphi_{C,r,v}$ for measurements in osculating true anomaly

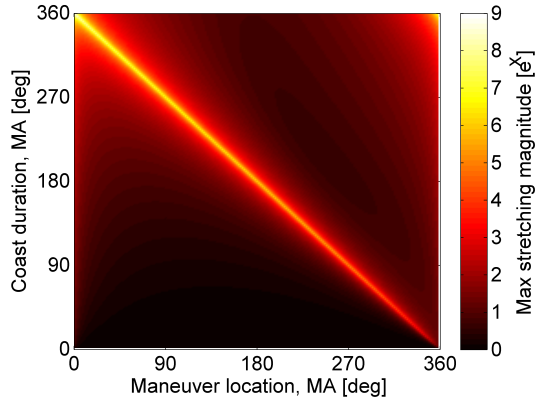

(c) Maximum stretching along $\varphi_{C,v,v}$ for measurements in mean anomaly

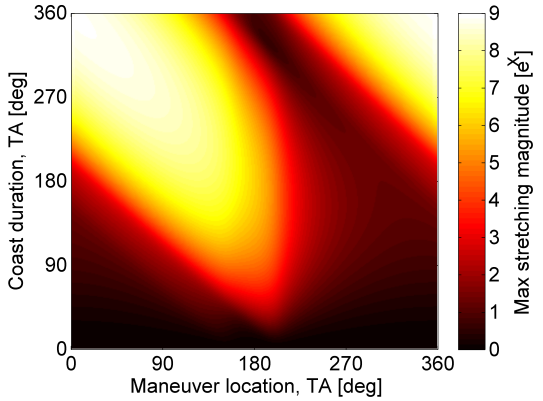

(d) Maximum stretching along $\varphi_{C,v,v}$ for measurements in osculating true anomaly

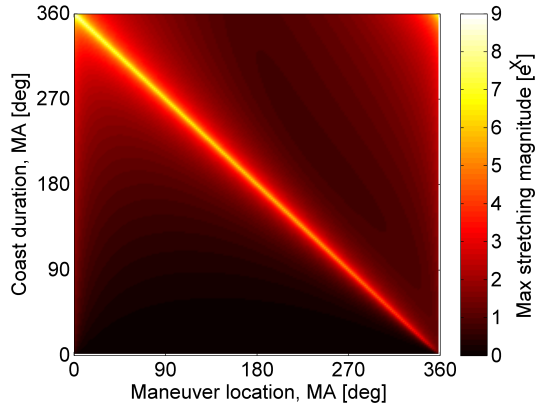

(e) Maximum stretching along $\varphi_{C,rv,v}$ for measurements in mean anomaly

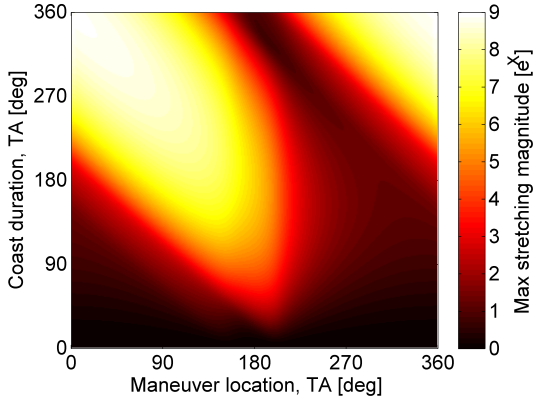

(f) Maximum stretching along $\varphi_{C,rv,v}$ for measurements in osculating true anomaly

Figure 5.4. Maximum stretching magnitude along different submatrices of the state transition matrix, φ_C, on L2 NRHO with perilune radius 3200 km.

along the trajectory segment amplifies as much as e^8 times, if it were to be aligned along the largest stretching direction, on the contrary, a trajectory segment originating at the same maneuver location when propagated for 360 degrees, i.e. the spacecraft approaches the following apoapsis, the error amplification is low indicated by the darker regions in Figure 5.4. The trend is similar along any NRHO that has close lunar passage. For unstable halo orbits, that are farther away from the primary body, a more gradual change is observed, if a map similar to Figure 5.4 is generated. It is preferred to apply a maneuver at a location indicated by darker regions in the map, to ensure that the spacecraft remains in tight vicinity to the reference trajectory when propagated downstream for the specified coast duration. The darker regions on the map therefore establishes the practicable regions for maneuver placements.

5.3.2 Effect of maneuver location and target horizon

In an effective stationkeeping strategy, the flow between the maneuver location and the target determines the maneuver characteristics. As previously introduced, for an x-axis control strategy, the rotating $\dot{x}$ value at different downstream xz plane crossings near the periapsis region serves as a target parameter. The stationkeeping control effort is based on the idea that a 3-dimensional maneuver is implemented at the current time that satisfies the required target conditions. Mathematically, this is then represented by

$$\Delta\dot{x}_f = \begin{bmatrix} \varphi_{T,44} & \varphi_{T,45} & \varphi_{T,46} \end{bmatrix} \Delta\bar{v}_0 = \begin{bmatrix} \varphi_{T,44} & \varphi_{T,45} & \varphi_{T,46} \end{bmatrix} \begin{bmatrix} \Delta\dot{x}_0 \\ \Delta\dot{y}_0 \\ \Delta\dot{z}_0 \end{bmatrix} \tag{5.9}$$

where, $\Delta\dot{x}_f$ is the change in the rotational $\dot{x}$ value at the target xz-plane crossing and $\Delta\bar{v}_0 = [\Delta\dot{x}_0,\ \Delta\dot{y}_0,\ \Delta\dot{z}_0]^{\mathrm{T}}$ defines a column vector with three scalar independent control variables that comprise the impulsive maneuver. Finally, $[\varphi_{T,44}\ \varphi_{T,45}\ \varphi_{T,46}]$ is the appropriate submatrix of the 6×6 state transition matrix, φ_T. The subscripts, i and j, in $\varphi_{T,\mathrm{ij}}$, indicate the element in φ_T in the i^{th} row and j^{th} column. Moreover, φ_T is the state transition matrix from the maneuver location to the target, i.e., $\varphi_T = \phi(t_{Target}, t_0)$. The time difference between

t_0 and t_{Target} is the target horizon time. Define $\bar{M} = [\varphi_{T,44}\ \varphi_{T,45}\ \varphi_{T,46}]^{\mathrm{T}}$ as a 3×1 column vector and, therefore, $\Delta\dot{x}_f = \bar{M}^{\mathrm{T}}\Delta\bar{v}_0$. One of the most useful options for the stationkeeping process is minimizing the propellant costs, hence, a minimum norm solution that delivers the smallest maneuver is generally an appropriate choice for this problem. Since the control equation $\Delta\dot{x}_f = \bar{M}^{\mathrm{T}}\Delta\bar{v}_0$ is equivalent to the dot product between $\bar{M}$ and the $\Delta\bar{v}_0$ vector, the maneuver magnitude is deduced as

$$|\Delta\dot{x}_f| = |\bar{M}||\Delta\bar{v}_0|\ cos\vartheta \quad \longrightarrow \quad |\Delta\bar{v}_0| = \frac{|\Delta\dot{x}_f|}{|\bar{M}|\ cos\vartheta} \tag{5.10}$$

where $cos\vartheta$ is the angle between $\bar{M}$ and the $\Delta\bar{v}_0$ vectors. Of course, $\bar{M}$ includes components of the state transition matrix φ_T but $\Delta\bar{v}_0$ and ϑ are variables. In any case, the smallest maneuver $|\Delta\bar{v}_0|$ is generated only if $cos\vartheta = 1$, i.e., $\vartheta = 0^o$ or $\Delta\bar{v}_0$ vector is aligned in the direction of $\bar{M}$. Therefore, a minimum norm solution for stationkeeping renders a maneuver magnitude of

$$|\Delta\bar{v}_0|_{min-norm} = \frac{|\Delta\dot{x}_f|}{|\bar{M}|} \tag{5.11}$$

in the direction of $\bar{M}$. The maneuver magnitude that is generated depends on the change in the rotational velocity $\Delta\dot{x}_f$, which varies with time, however, the maneuver magnitude as a function of the initial perturbation is a better metric, i.e.,

$$|\Delta\bar{v}_0|_{min-norm} = \frac{|\bar{B}^{\mathrm{T}}\Delta\bar{\mathbf{x}}_0|}{|\bar{M}|} \leq \frac{|\bar{B}^{\mathrm{T}}||\Delta\bar{\mathbf{x}}_0|}{|\bar{M}|} \tag{5.12}$$

where $\Delta\dot{x}_f = \bar{B}^{\mathrm{T}}\Delta\bar{\mathbf{x}}_0$ with $\bar{B} = [\varphi_{T,41}\ \varphi_{T,42}\ \varphi_{T,43}\ \varphi_{T,44}\ \varphi_{T,45}\ \varphi_{T,46}]^{\mathrm{T}}$ as the submatrix of φ_T that relates the initial state perturbation that delivers a final $\dot{x}$ change. Define an initial perturbed state, $\Delta\bar{\mathbf{x}}_0 = [\Delta x_0,\ \Delta y_0,\ \Delta z_0,\ \Delta\dot{x}_0,\ \Delta\dot{y}_0,\ \Delta\dot{z}_0]^{\mathrm{T}}$, as a result of position and velocity errors in the orbit determination process as well as modeling errors. The inequality in equation (5.12), is then represented in the standardized form as

$$\frac{|\Delta\bar{v}_0|_{min-norm}}{|\Delta\bar{\mathbf{x}}_0|} \leq \frac{|\bar{B}|}{|\bar{M}|} \tag{5.13}$$

and offers an upper bound on the magnitude of the stationkeeping maneuver required to overcome any unit initial perturbation at specific target horizons in a linear sense. A plot of $\frac{|\bar{B}|}{|\bar{M}|}$ for different targets, i.e., 1$^{\text{st}}$, 2$^{\text{nd}}$ and 7$^{\text{th}}$ xz plane crossings near the periapsis region is represented in Figure 5.5 for an L2 NRHO with perilune radius 3200 km. The value of $|\bar{B}|/|\bar{M}|$ for combinations of maneuver locations along the orbit and coast durations are plotted as a colormap (in a logarithmic scale) for a number of target horizons, and range from $e^{0.5}$ to e^{2}. For different target horizons, maneuver locations along the orbit offer distinct characteristics. A lower value of $\frac{|\bar{B}|}{|\bar{M}|}$ suggests that the executed maneuver requires a smaller magnitude maneuver in that region. From Figures 5.5(e) and 5.5(f), it is evident that when targeting the 7$^{\text{th}}$ xz plane crossing, there exists a wide range of maneuver locations, i.e., the dark blue regions, that result in low maneuver magnitudes compared to targeting the rotating $\dot{x}$ at the 1$^{\text{st}}$ or 2$^{\text{nd}}$ xz plane crossings as in Figures 5.5(a), 5.5(b), 5.5(c) and 5.5(d).

The ratio $|\bar{B}|/|\bar{M}|$ offers the upper bound on the value of the maneuver magnitude that is required given a specified initial perturbation, however, the direction of the maneuver is governed by the direction of the $\hat{M}$ vector. The direction of the maneuver is an important parameter that supplies an assessment for the efficiency of the maneuver in maintaining the spacecraft in the vicinity of the reference path. The stretching directions for the submatrices of the STM along the coast segment, φ_C, are available; such a quantity offers insight for predicting a maneuver that likely results in the spacecraft deviating from the reference trajectory. Geometrically, if the maneuver direction $\hat{M}$ is aligned in the most stretching direction $\mathbb{V}_1$, with $\sigma_1 > 1$, then the executed maneuver produces the maximum change in the state by the time corresponding to the following maneuver location thereby increasing the spacecraft deviation from the reference. In contrast, the maneuver direction $\hat{M}$ that is aligned perpendicular to the most stretching direction, $\mathbb{V}_1$, reduces the deviation at the following maneuver location. If the stretching along the directions associated with σ_2 and σ_3 are less than a nondimensional value of 1, then the plane represented by the $\mathbb{V}_2 - \mathbb{V}_3$ vectors defines a restoring plane. If only $\sigma_3 < 1$, then the direction along the $\mathbb{V}_3$ vector is a restoring direction. The restoring plane or the restoring direction is vital as deviations at the end of the propagated arc diminish in comparison to deviations at the beginning. The maneuvers,

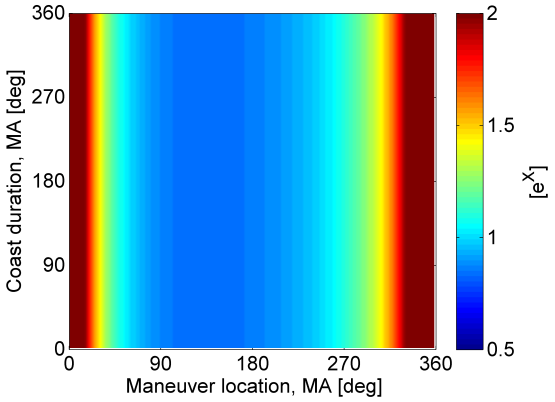

(a) Target: 1st xz plane crossing near periapsis. Measurement: Mean anomaly.

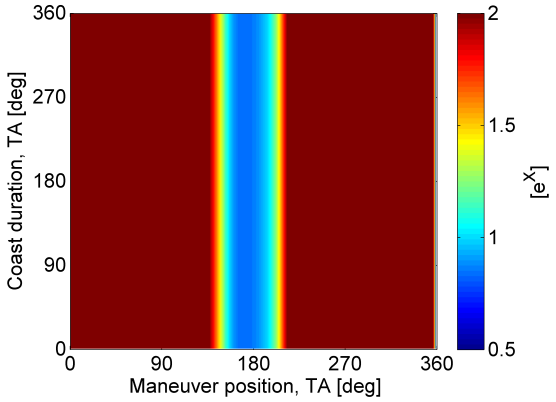

(b) Target: 1st xz plane crossing near periapsis. Measurement: Osculating true anomaly.

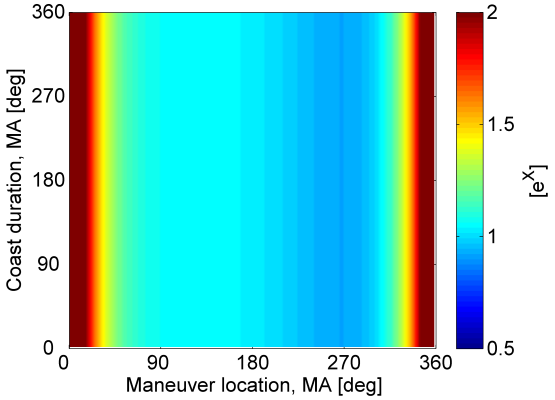

(c) Target: 2nd xz plane crossing near periapsis. Measurement: Mean anomaly.

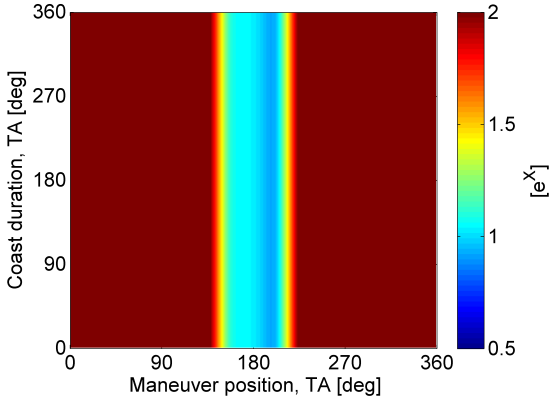

(d) Target: 2nd xz plane crossing near periapsis. Measurement: Osculating true anomaly.

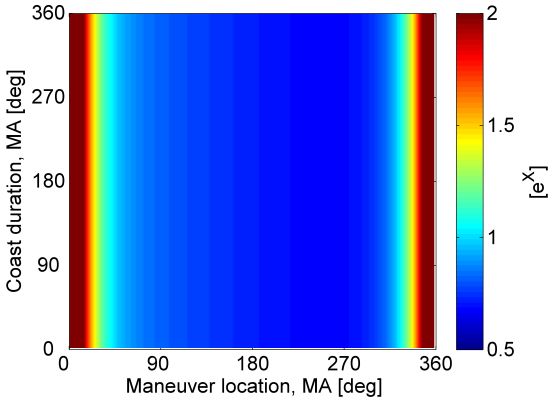

(e) Target: 7th xz plane crossing near periapsis. Measurement: Mean anomaly.

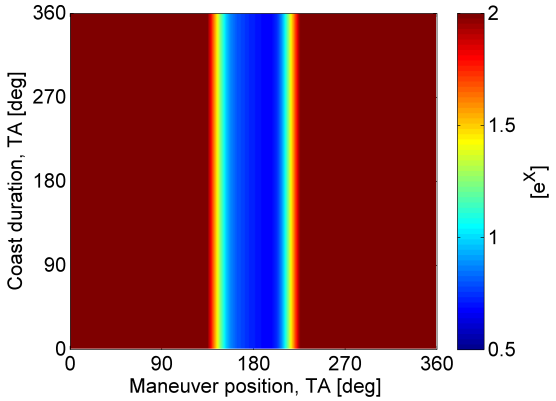

(f) Target: 7th xz plane crossing near periapsis. Measurement: Osculating true anomaly.

Figure 5.5. Ratio of maximum maneuver magnitude per magnitude of the initial state deviation, $|\bar{B}|/|\bar{M}|$, for different target horizons. Reference orbit: L2 NRHO with perilune radius 3200 km.

when executed in the restoring plane or along the restoring direction, reduces the spacecraft deviation at the downstream locations, thereby maintaining the spacecraft boundedness. A map for the direction between the maneuver and the most stretching direction for different combination of maneuver location and coast duration for three different target horizons is presented in Figure 5.6, for an L2 NRHO with perilune radius 3200 km. Regions such that the maneuver and the most stretching direction are almost perpendicular facilitate efficient maneuvers.

It is sometimes intuitive to deliver a maneuver along the most stretching direction, however, such is the case where the subsequent maneuver location and the target are the same. A small change in the velocity components at the initial time and in the largest stretching direction result in the largest change at the final time. Thus, a small maneuver is required to satisfy the target condition. So, when the target and the subsequent maneuver location are the same, satisfying the target conditions is equivalent to reducing state errors at the subsequent maneuver location. However, in the x-axis crossing control approach, the target is the rotating xz plane near the periapsis region, while the maneuver locations are closer to apoapsis. The flow between two successive maneuver locations that defines the stretching directions evolves independently from the flow between the maneuver location and the selected target. Subsequently, a maneuver (that meets the $\dot{x} = \dot{x}_{ref}$ constraint at the target xz plane crossing within some predefined tolerance) is calculated independently of the dynamical flow until the following maneuver location. In case, the computed maneuver aligns with the maximum stretching direction, the state change at the following maneuver location is amplified.

In this investigation, the maneuver directions are identified from the context of an x-axis control strategy, one that targets only one state (i.e., the rotating x velocity) of the three position and three velocity states. For such a strategy the maneuver direction, $\hat{M}$, is predicted in a straightforward manner that consists of elements of the state transition matrix, without much impact of the initial state perturbations. It is possible to isolate the maneuver directions for a similar approach, one that targets the rotating y-velocity, as

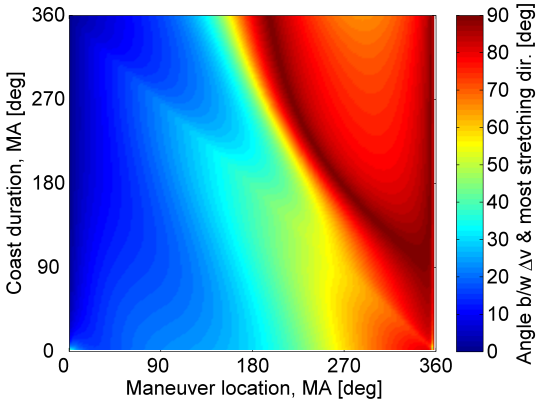

(a) Target: 1st xz plane crossing near periapsis. Measurement: Mean anomaly.

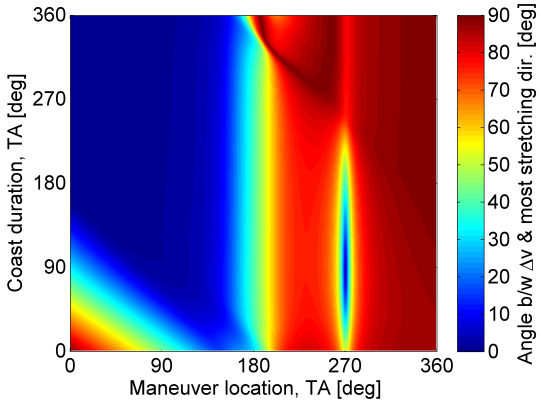

(b) Target: 1st xz plane crossing near periapsis. Measurement: Osculating true anomaly.

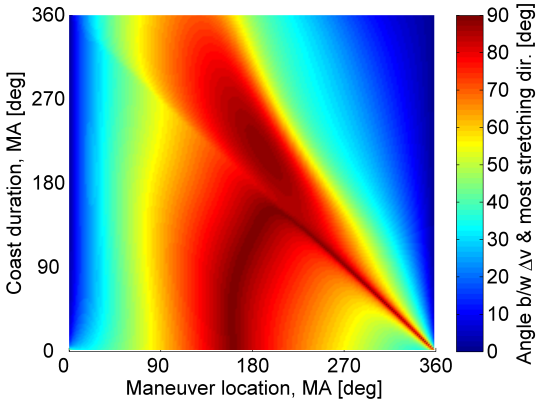

(c) Target: 2nd xz plane crossing near periapsis. Measurement: Mean anomaly.

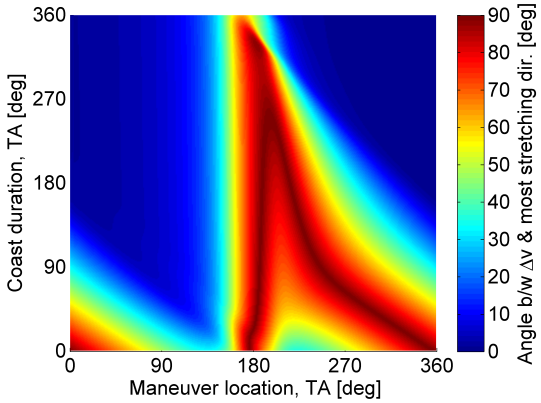

(d) Target: 2nd xz plane crossing near periapsis. Measurement: Osculating true anomaly.

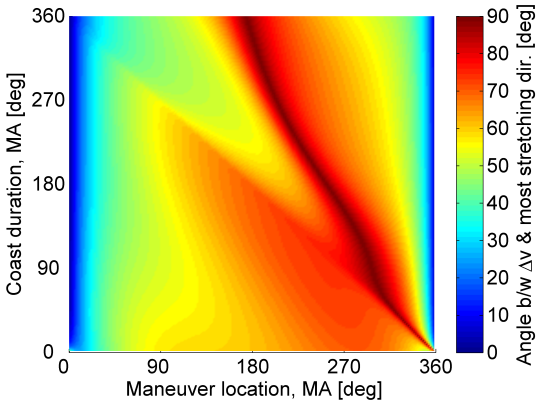

(e) Target: 7th xz plane crossing near periapsis. Measurement: Mean anomaly.

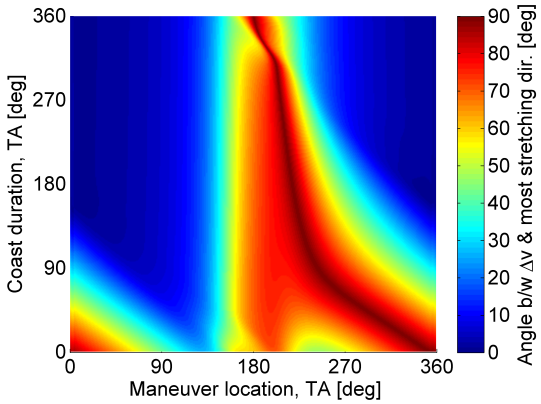

(f) Target: 7th xz plane crossing near periapsis. Measurement: Osculating true anomaly.

Figure 5.6. Estimated angle between maneuver direction and the most stretching direction $\mathbb{V}_1(\varphi_{C,v,v})$ for different target horizons. Reference orbit: L2 NRHO with perilune radius 3200 km.

demonstrated in section 5.6.2, as well as a modified version of the x-axis crossing control strategy with direction constrained maneuvers, as described in section 5.6.3. The ability to identify the maneuver directions just based on the dynamics along the orbit, without much impact of the initial state perturbations, enables a comparison with the stretching directions to investigate the impact of the maneuver downstream without performing Monte Carlo simulations. If two or more conditions (in position and velocity) are targeted the resulting maneuver magnitude and direction cannot be predicted without *a priori* information on initial position and velocity perturbations unlike using equation 5.10. For such a case, the analyses is more complex and modifications to the process described in this investigation may be required.

5.4 L2 Near Rectilinear Halo Orbits

With a focus on expanding the human presence in the region, NASA's Gateway mission, formerly the Deep Space Gateway (DSG) or Lunar Orbital Platform-Gateway (LOP-G) mission, delivers a hub-like facility that is currently planned to move along a Near Rectilinear Halo Orbit (NRHO) near the L2 region in the Earth-Moon system [1], [2]. Besides, the NRHO is close to the L2 portal and offers uninterrupted relay communications to any potential lunar landing sites on the side farther from the Earth. Halo orbits near the L2 portal also facilitates departures for any interplanetary missions. With several scientific opportunities, NRHOs in the L2 region of the Earth-Moon system remain a popular choice. A systematic and straightforward approach to sustain spacecraft along the L2 NRHOs is desired.

5.4.1 Conventional approach: Maneuvers at apoapsis

For orbit maintenance operations as simulated in the ephemeris model by Davis et al. [57] as well as Guzzetti et al. [4] for Earth-Moon L2 NRHOs, maneuvers are implemented once per revolution, generally at (or near) the apoapsis. Since the period of the NRHO is approximately one week, implementing maneuvers only in the apoapsis region provides ample time for orbit determination. The annual stationkeeping costs estimated by targeting the rotating $\dot{x}$ value at the xz plane crossing 6.5 revolutions ahead (i.e., the target horizon) pro-

duces the most efficient result, for various orbit determination error levels, both in position and velocity. A similar result is observed for simulations in the CR3BP model. Of course, larger orbit determination errors resulted in larger orbit maintenance cost. The intuition that a longer target horizon consistently produces a lower maneuver cost, is not necessarily true for all the L2 NRHO, however. For the L2 NRHO with a radius of periapsis 3200 km, the current baseline for the Gateway, the target horizon at 1.5 revolutions results in several failed set of Monte Carlo trials or a high maintenance costs, irrespective of the magnitude of the ODE errors and the model, CR3BP or ephemeris model. Contrary to targeting a 1.5 rev target horizon, other target horizons produce successful cases, particularly a target horizon of 6.5 revs downstream. The results from Davis et al. [57] and Guzzetti et al. [4] are analogous to this observation.

In the conventional x-axis control approach, once the maneuvers are executed at (or near) the apoapsis, the spacecraft is allowed to coast till the subsequent apoapsis where the next maneuver is generated and, and most often implemented. Since maneuvers induce a change in the state at the apoapsis, the effect of an implemented maneuver at the following apoapsis is vital. If the maneuver is implemented in the most stretching direction, the spacecraft experiences a larger deviation when it reaches the subsequent apoapsis and the phenomenon continues till the deviation is sufficiently magnified and the spacecraft is escaping. The flow defined by the Cauchy-Green tensor provides the magnitude and direction of the stretching, as available from the components of the monodromy matrix between two consecutive apoapses computed along a virtual reference orbit. For the L2 NRHOs, orbits with perilune radius between 2000-9000 km and with one maneuver per orbit, executed at the apoapsis, i.e., maneuver location at $\theta_{MA} = 180^o$ and a coast arc of 360^o (1 time period), there exists one stretching direction and two non-stretching directions forming a restoring plane as demonstrated by [82]. The plot in Figure 5.7 summarizes the stretching as computed from the monodromy matrix for certain members of the NRHO family. For the orbit of interest, the 9:2 synodic L2 resonant orbit with perilune radius 3200 km, the current baseline for the Gateway mission, and with maneuvers at apoapsis ($\theta_{TA} = \theta_{MA} = 180^o$ and coast arc of 360^o), the three stretching directions possess magnitudes of stretching such that

$\sigma_1 = 2.34$, $\sigma_2 = 0.78$ and $\sigma_3 = 0.25$. Since $\sigma_1 > 0$, the directions deduced from $\mathbb{V}_1$ and $\mathbb{U}_1$ correspond to direction of the perturbation growth at the initial and final times, respectively. In contrast, $\sigma_2, \sigma_3 < 1$, therefore directions $\mathbb{V}_2$, $\mathbb{V}_3$ at the initial time and $\mathbb{U}_2$, $\mathbb{U}_3$ at the final time are restoring directions where the magnitude of the perturbation diminishes over the propagated time. It is to be noted that the directions $\mathbb{V}_1$, $\mathbb{V}_2$ and $\mathbb{V}_3$ are perpendicular. For the L2 NRHO orbits with perilune radius between 2000-9000 km and with one maneuver per revolution, near apoapsis, there exists a stretching direction and a restoring plane, therefore, ensuring maneuvers that are perpendicular to the stretching direction that establishes the stability of the maneuvers.

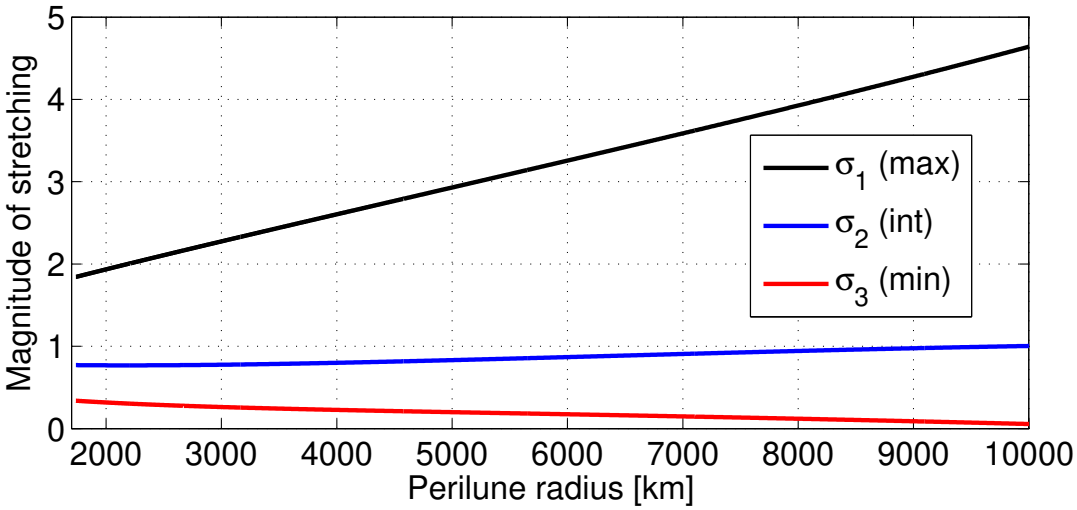

Figure 5.7. Magnitude of stretching, σ_i, along different $\mathbb{U}_i$ directions for various NRHOs in the L2 region.

The maneuver direction as compared to the stretching and restoring directions play an important role in determining the efficiency of the stationkeeping scheme. If successive maneuvers are implemented that are aligned closely to the $\mathbb{V}_1$ direction, the magnitude of change in the state increases over time. On the contrary, any maneuvers that are aligned perpendicular to the $\mathbb{V}_1$ direction, in the restoring $\mathbb{V}_2 - \mathbb{V}_3$ plane, the magnitude of the perturbation does not grow significantly over the propagated time, hence, a better success rate for stationkeeping is achieved. When targeting different xz plane crossings near the periap-

sis region, i.e., downstream at 0.5 rev, 1.5 rev, and subsequent target horizons, a different maneuver direction, $\hat{M}$, is computed. The angle between the direction of the maneuver $\hat{M}$ and the most stretching direction of $\varphi_{C,v,v}$ for different target horizons, are summarized for an L2 NRHO with perilune radius 3200 km in Figure 5.8. A curve is also included for the angle between the direction of the maneuver $\hat{M}$ and the most stretching direction of $\varphi_{C,rv,v}$. Both these curves demonstrate a similar pattern, but as noted previously, comparing with $\varphi_{C,v,v}$ is useful for halo orbits that are notably sensitive to velocity perturbations. When targeting 1.5 revs ahead, the angle between the maneuver and the most stretching direction for $\varphi_{C,v,v}$ is approximately 50 degrees, while for the 6.5 rev target horizon the angle is nearly 90 degrees. For target horizons where the angle is almost perpendicular to the most stretching direction, i.e., aligned with the restoring plane, the state variations at the initial time do not induce a large final variation, hence, the spacecraft remains bounded closer to the reference trajectory. In contrast, at the 1.5 rev target horizon, the maneuver possesses a significant component in the most stretching direction that results in amplification of the state variation at the final time for a specific initial state perturbation. In such a case, the deviation size and the maneuver size continuously increase with time and, eventually, divergence from the virtual reference trajectory occurs.

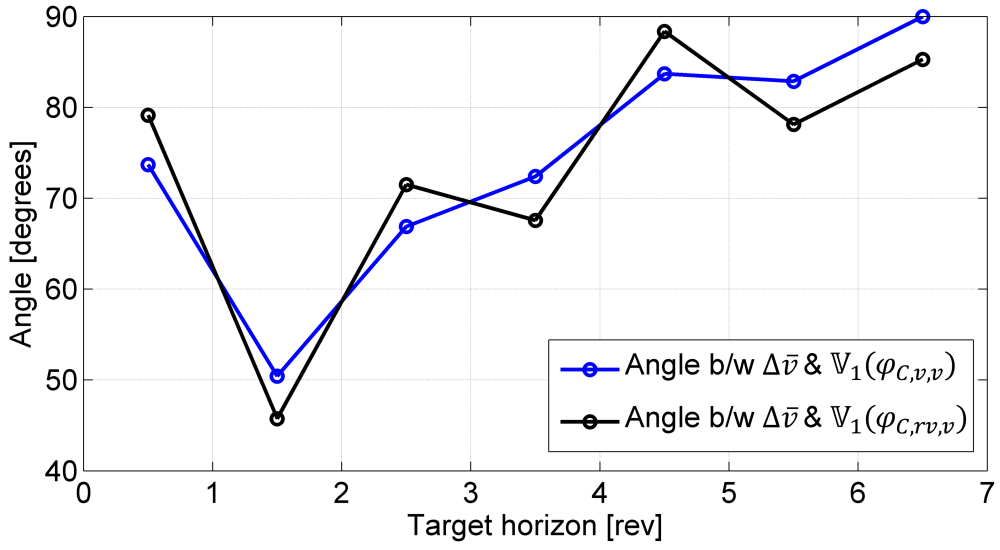

Figure 5.8. Angle between maneuver and most stretching direction for the 9:2 synodic resonant NRHO with perilune radius 3200km.

The maneuver direction, $\hat{M}$, is determined from the elements of the state transition matrix (φ_T) that reflect the flow from the maneuver location to the target such that $\bar{M}(t) = [\varphi_{T,44}\ \varphi_{T,45}\ \varphi_{T,46}]^{\mathrm{T}}$. Any location that is situated some time past the maneuver location is a potential target. For such a target, the maneuver direction is computed from the elements of φ_T that is a continuous function of time. For the 9:2 synodic resonant L2 NRHO and the case where the maneuvers are located only at apoapsis locations, the direction between the most stretching direction and any potential target along the orbit may be represented as a continuous function of time as illustrated in Figure 5.9. The conventional x-axis algorithm, however, targets only specific xz plane crossings that are periapsis locations in the CR3BP. Such locations are marked at discrete intervals of 0.5 rev, 1.5 rev and so on. Since dynamics near periapsis change rapidly the curves appear in form of spikes but they are continuous curves. Besides, the angle between measurement is restricted between $0^o - 90^o$, i.e., value of 95^o and 85^o are equivalent (they just switch the direction). As a consequence, the continuous curve appears to bounce of the 90^o limit. Although the angle between the most stretching direction and the maneuver generated by targeting the 1.5 rev target (approximately 50^o) appear distinct from other target horizons typically used for stationkeeping, each value are a result of the discretization along a continuous curve.

The maneuvers are based, of course, on the states along the actual trajectory nearby the baseline path and may not precisely align with the angles in Figure 5.8, therefore, the angle between the actual maneuvers as compared to the most stretching direction that result from Monte Carlo simulations are plotted in Figures 5.10 and 5.11 for both the CR3BP as well as the ephemeris model, with low and high orbit determination errors respectively. For each of the target horizons, i.e., 0.5 rev, 1.5 rev and subsequently, the angle between the actual maneuvers and the most stretching direction $\mathbb{V}_1$ are well estimated in Figure 5.8. For the ephemeris case, due to the complex dynamics, the angles do not precisely coincide with the estimated values, but do follow the underlying pattern. The maneuvers as viewed in configuration space in Figure 5.12 for both the CR3BP and the ephemeris case, demonstrate distinctly different directions for the 1.5 rev target horizon and the 6.5 rev target horizon. Not surprisingly, a larger variance is observed for maneuvers in the ephemeris model as compared

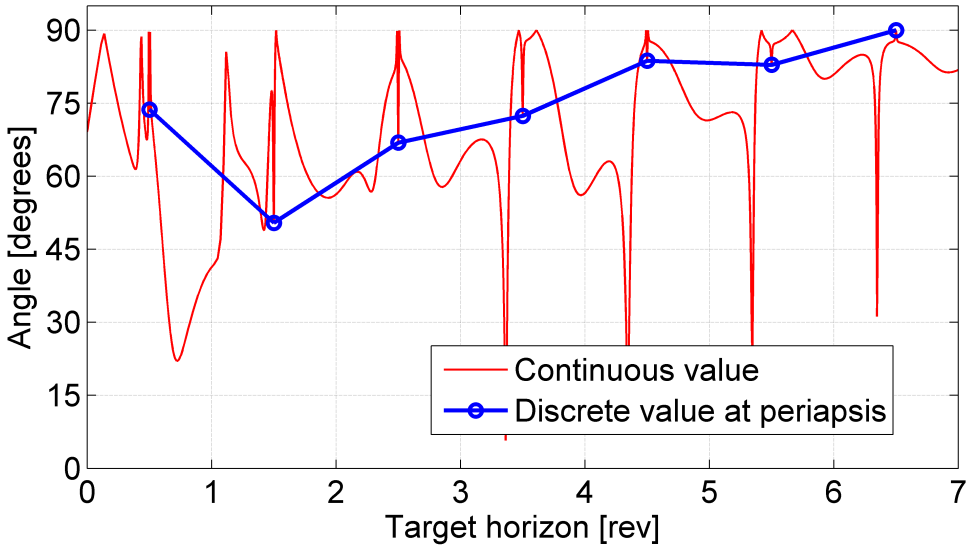

Figure 5.9. Angle between most stretching direction and $\hat{M}(t)$ as a continuous function of time for the 9:2 synodic resonant NRHO with perilune radius 3200km. Here $\bar{M}(t) = [\varphi_{T,44}\ \varphi_{T,45}\ \varphi_{T,46}]^{\mathrm{T}}$.

to the CR3BP model. In addition, the stretching direction as well as the restoring plane that are estimated using the underlying CR3BP dynamics are plotted in Figure 5.12(a), for the L2 NRHO with 3200 km perilune radius. Clearly, the direction of the maneuvers computed for different target horizons influences the performance of the stationkeeping algorithm. Not surprisingly, the characteristics of the flow along the orbit delivers a poor performance for the 1.5 rev target horizon, as the maneuvers include a significant component in the most stretching direction. In contrast, the 6.5 rev target horizon proves superior for the L2 NRHO with perilune radius 3200 km, as maneuvers are closely aligned with the restoring plane.

The same type of analyses applied to other L2 NRHOs. In the conventional x-axis control approach, the status of the target condition determines the effectiveness of the maneuvers to maintain the spacecraft within the close vicinity of a virtual reference trajectory over time. The flow from the maneuver location to the target determines the direction and the magnitude of the maneuvers. As noted, although the maneuver magnitude depends on the initial error, the ratio of the maximum maneuver magnitude for an unit initial perturbation is deterministic in the linear sense. Similarly, the direction of the maneuver with respect

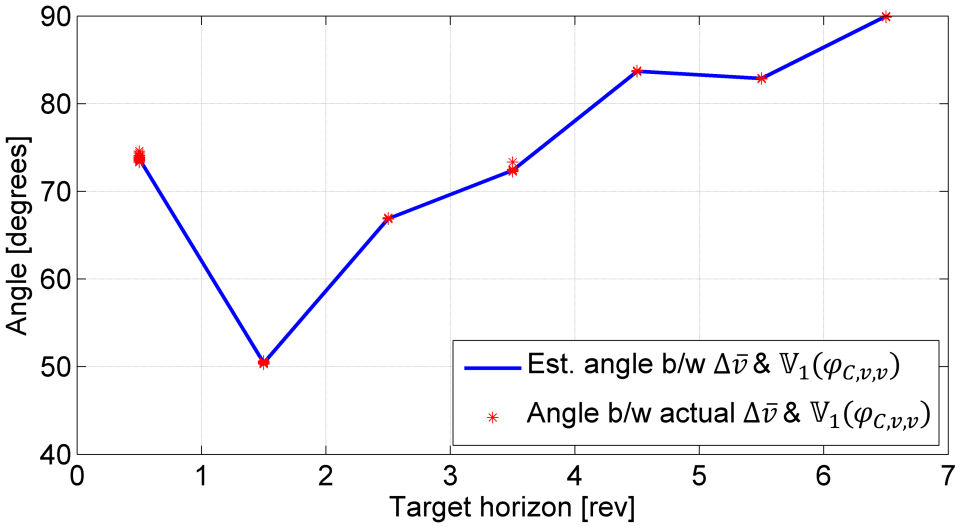

(a) CR3BP model

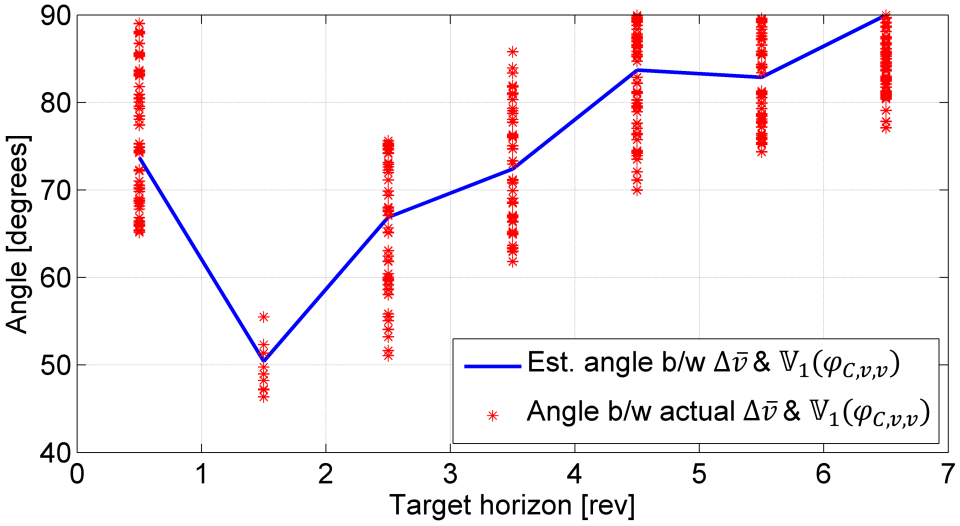

(b) Ephemeris model

Figure 5.10. Angle between the actual maneuver and the most stretching direction $\mathbb{V}_1(\varphi_{C,v,v})$ for the 9:2 synodic resonant L2 NRHO with perilune radius 3200 km. Low orbit determination error (3σ: 1 km and 1 cm/s) case.

to the most stretching direction is available for any NRHO under investigation. The maneuver magnitude and direction offers a control metric, that reflects the effectiveness of the maneuver and assists in an informed selection for the target horizon. The angle between the estimated maneuver and the most stretching direction appears in Figure 5.13(a) across various NRHOs. Clearly, for the range of NRHOs under investigation, the 1.5 rev target horizon

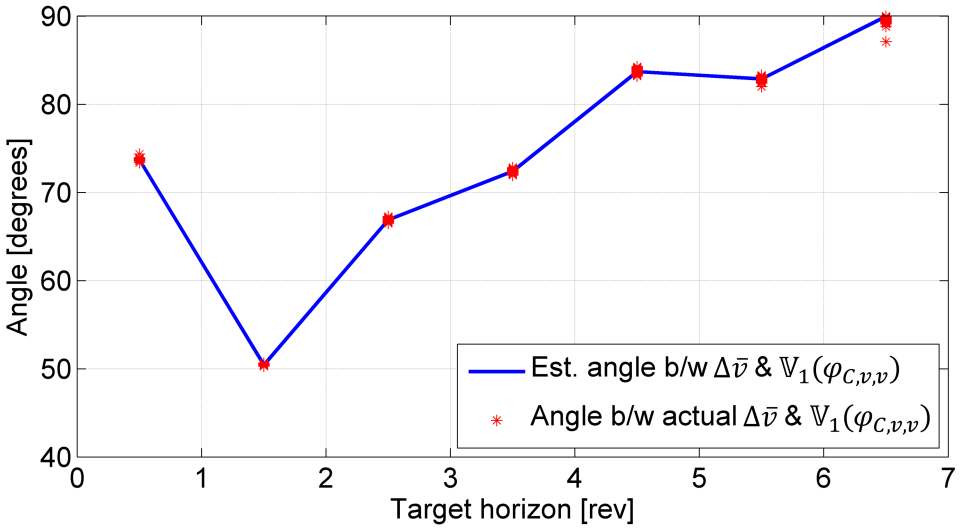

(a) CR3BP model

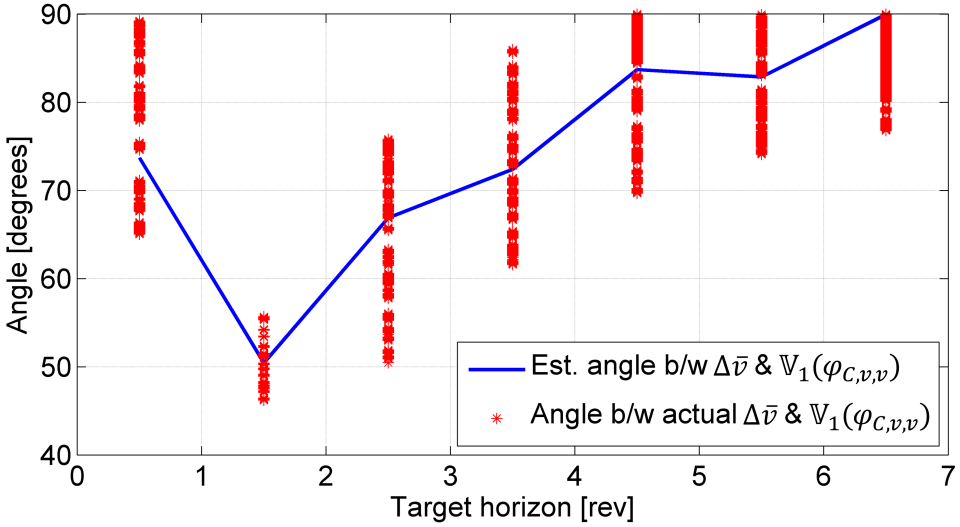

(b) Ephemeris model

Figure 5.11. Angle between the actual maneuver and the most stretching direction $\mathbb{V}_1(\varphi_{C,v,v})$ for the 9:2 synodic resonant L2 NRHO with perilune radius 3200 km. High orbit determination error (3σ: 10 km and 10 cm/s) case.

is not recommended, as maneuvers (as typically computed) possess a significant component in the most stretching direction that deviates away from the virtual reference trajectory over time. Depending on the orbit of interest, selecting 6.5 rev, 4.5 rev and 2.5 rev target horizons offer good performance. Similarly, the map in Figure 5.13(b) indicates that targeting the 1.5 rev horizon offers lower leverage in terms of the maneuver magnitude required to overcome

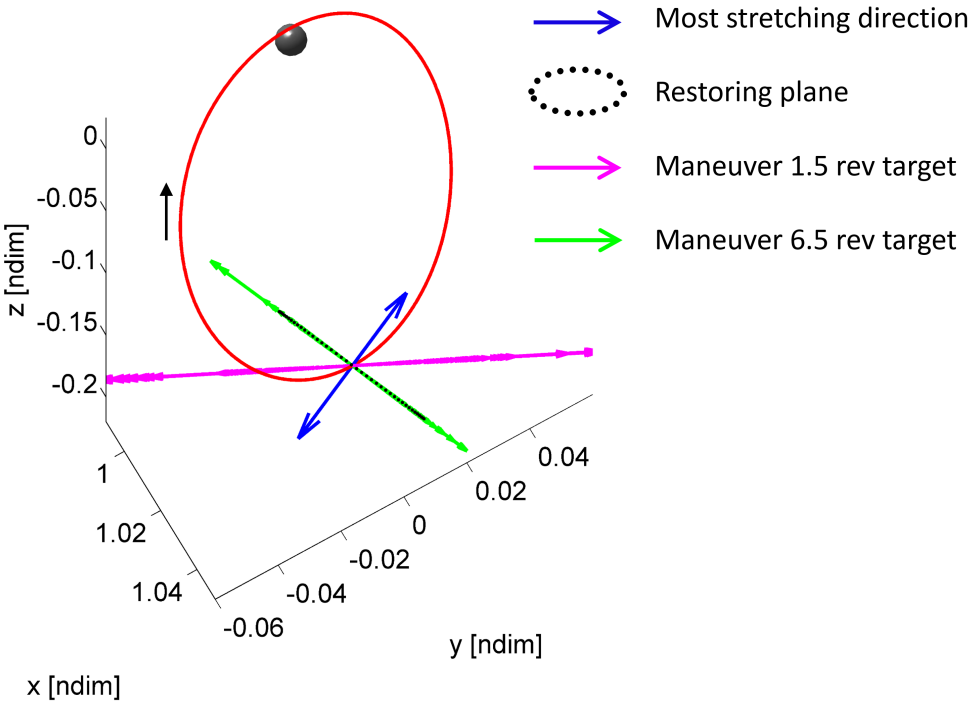

(a) CR3BP

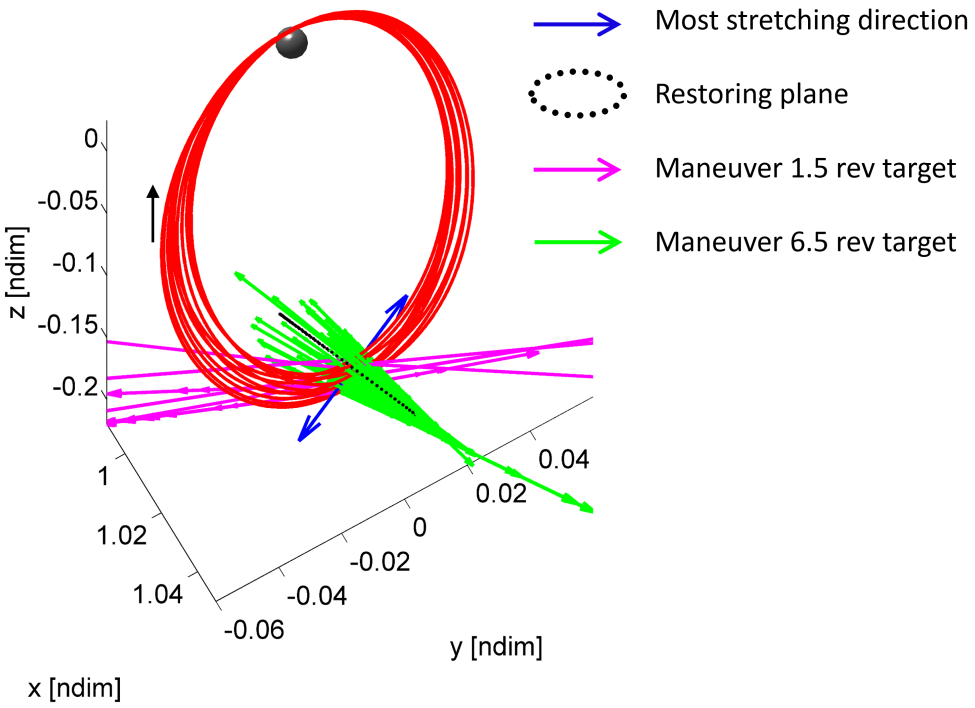

(b) Ephemeris

Figure 5.12. Maneuvers in configuration space for L2 NRHO with perilune radius 3200 km. Low orbit determination error (3σ: 1 km and 1 cm/s) case.

unit initial perturbations thereby resulting in larger maneuvers costs. Again, target horizons other than 1.5 rev, for NRHOs with perilune radius 3000 km or larger, offers good leverage, i.e., relatively smaller maneuver magnitude required to overcome unit initial perturbations. Targeting further downstream beyond 6.5 rev horizon is computationally intensive and does not necessarily yield any substantial improvements in stationkeeping costs. Other NRHOs, independently evaluated, may offer flow patterns that differ from the 9:2 synodic resonant NRHO in the L2 region, and different target horizons may yield a different performance.

The spacecraft is maintained along the orbit at the expense of propellant cost used for delivering impulsive maneuvers, also known as stationkeeping cost. The annual stationkeeping cost is estimated by running Monte Carlo runs with a different seed for orbit determination errors and maneuvers execution errors that are assumed to be a Gaussian distribution. The annual cost generated from individual Monte Carlo runs may not be resemble a Gaussian distributed, nevertheless, the mean of the distribution, i.e., the estimate of the annual stationkeeping cost, is still Gaussian under the central limit theorem [123]. With about 100 Monte Carlo runs, the standard error of the mean is reduced to 10% of the standard errors of the observations. Additionally, with sample size 100, the Student-T distribution and Normal (Gaussian) distribution are comparable, hence,

$$\sigma_{\bar{\varkappa}} = \frac{S_{\varkappa}}{\sqrt{100}} = \frac{S_{\varkappa}}{10} \tag{5.14}$$

where, $\sigma_{\bar{\varkappa}}$ is the standard error of the estimated mean. The annual stationkeeping cost along the L2 NRHO with 3200 km perilune radius for different Monte Carlo runs are plotted in Figure 5.14 for high orbit determination error. Target horizon of 6.5 rev is considered for the measurements. The black asterisk (*) corresponds to the sample cost generated for a particular Monte Carlo run, while bold blue line corresponds to the running mean annual cost. Dotted red and green lines corresponds to $+1.96\sigma_{\bar{\varkappa}}$ and $-1.96\sigma_{\bar{\varkappa}}$ values respectively. The interval between the red and green dotted lines corresponds to the 95% confidence interval of the estimated mean. The range of 95% confidence intervals for the mean are the

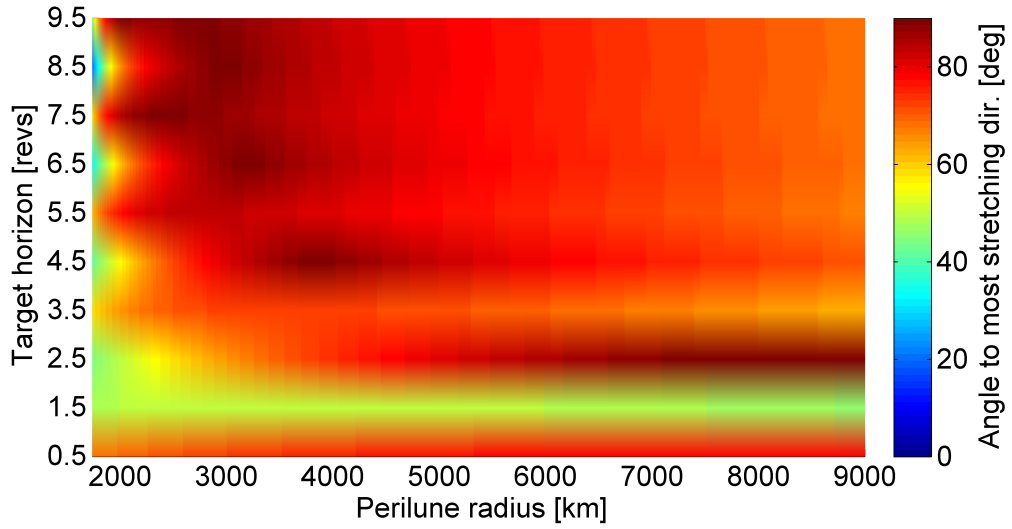

(a) Angle between maneuver and most stretching direction

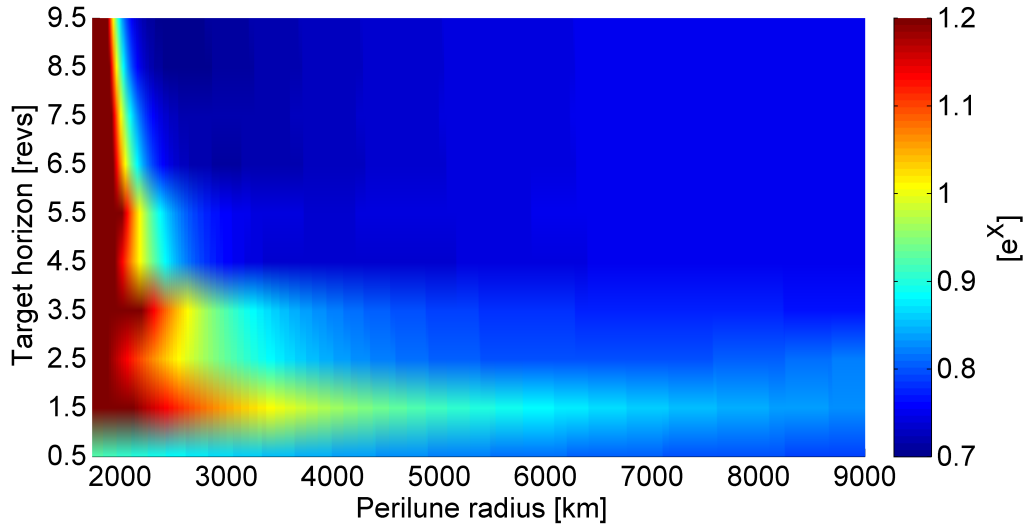

(b) Maximum maneuver magnitude per unit initial deviation (max value capped at 1.2)

Figure 5.13. Maneuver effectiveness for different target horizon for different NRHOs in the L2 region.

same order of magnitude as the orbit determination errors. Such a precision is sufficient for the analysis.

The x-axis approach is a loose control strategy that targets only two of the seven states (including time), i.e., the rotating $\dot{x}$ component at $y = 0$, thus providing low cost station-

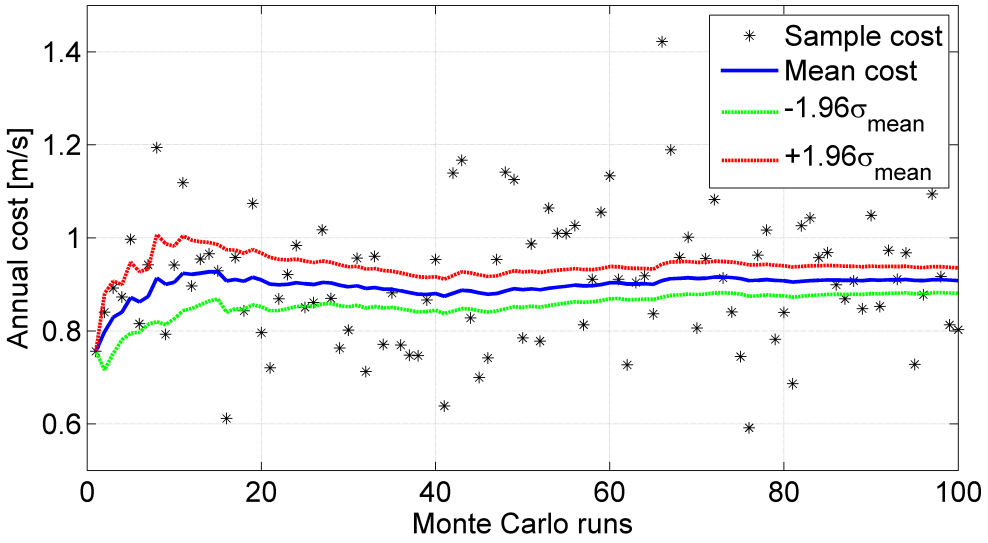

Figure 5.14. Annual stationkeeping cost with 95% confidence interval ($\pm 1.96\sigma_{mean}$) estimated using Monte Carlo runs. Example: L2 NRHO with perilune radius 3200 km, with 6.5 rev target horizon.

keeping solutions. For different NRHOs, the annual orbit maintenance costs are computed for both low (3σ: 1 km and 1 cm/s) and high (3σ: 10 km and 10 cm/s) orbit determination error levels in Tables 5.1 and 5.2, respectively. Annual costs are estimated from the Monte Carlo simulations, each trials involving propagation of trajectories for duration of approximately 240 days. Certain cases, specific to the baseline orbit for the Gateway mission are propagated for a duration of 300 days. It is evident that increased uncertainty in orbit determination increases the orbit maintenance costs. For a particular orbit, irrespective of the orbit determination error levels, the annual stationkeeping costs generated by targeting relatively longer horizon times, i.e., 4.5, 5.5 and 6.5 revs, are not significantly different. For the very short target horizon of 0.5 rev, a significantly higher cost of operation is observed in contrast to targeting a longer time horizon. As noted earlier, no Monte Carlo runs yield successful maneuvers for a target horizon of 1.5 rev.

5.5 L1 Near Rectilinear Halo Orbits

Near rectilinear halo orbits that originate in the L1 region are also potential candidates for space exploration missions. Although the NRHOs in the L1 region demonstrate stability

Table 5.1. Annual orbit maintenance cost, $\bar{\varkappa}$, and 95% confidence interval, $\pm 1.96\sigma_{\bar{\varkappa}}$, in [m/s] with low orbit determination error level (3σ: 1 km and 1 cm/s).

Perilune radius [km]	Target horizon [rev]						
	0.5	1.5	2.5	3.5	4.5	5.5	6.5
3200	0.28 ± 0.02	DNC	0.18 ± 0.01	0.13 ± 0.00	0.14 ± 0.00	0.15 ± 0.00	0.16 ± 0.00
4000	0.29 ± 0.02	DNC	0.18 ± 0.01	0.13 ± 0.00	0.14 ± 0.00	0.15 ± 0.00	0.15 ± 0.00
4800	0.32 ± 0.02	DNC	0.16 ± 0.01	0.13 ± 0.00	0.15 ± 0.00	0.15 ± 0.00	0.15 ± 0.00
5645	0.45 ± 0.03	DNC	0.16 ± 0.01	0.13 ± 0.00	0.15 ± 0.00	0.14 ± 0.00	0.15 ± 0.00
6400	0.58 ± 0.05	DNC	0.17 ± 0.01	0.13 ± 0.00	0.15 ± 0.00	0.15 ± 0.00	0.16 ± 0.00
7200	0.72 ± 0.12	DNC	0.18 ± 0.01	0.13 ± 0.00	0.16 ± 0.00	0.15 ± 0.00	0.15 ± 0.00

* DNC - Did not converge

characteristics similar to the L2 NRHOs, at least in terms of the linear variational flow. They do not, however, mirror all the properties of L2 NRHOs. In the L2 NRHOs, as perilune radius decreases, the apolune radius also decreases, however, as the perilune radius of L1 NRHOs decrease, the apolune radius initially decreases and then increases rapidly, forming high out-of-plane amplitudes [3]. Stationkeeping maneuvers to maintain spacecraft in the neighborhood of a virtual reference solution depend on the maneuver locations and the target horizon times, rather than the stability index. The interaction between flow evolving between one maneuver to the other and the flow evolution from maneuver location to target are different across the NRHOs in the L1 family in comparison to the L2 family. Observations and results obtained for L2 NRHOs are not always preserved for the L1 family.

A Cauchy-Green tensor assists in visualizing the flow of the magnitude of the state vectors in the neighborhood of a virtual reference trajectory by again decomposing the evolution of the variations into different stretching directions that are orthogonal to each

Table 5.2. Annual orbit maintenance cost, $\bar{\varkappa}$, and 95% confidence interval, $\pm 1.96\sigma_{\bar{\varkappa}}$, in [m/s] with high orbit determination error level (3σ: 10 km and 10 cm/s).

Perilune radius [km]	Target horizon [rev]						
	0.5	1.5	2.5	3.5	4.5	5.5	6.5
3200	5.84 ± 0.32	DNC	1.81 ± 0.12	1.02 ± 0.04	0.96 ± 0.03	0.90 ± 0.03	0.91 ± 0.03
4000	3.78 ± 0.41	DNC	1.86 ± 0.18	0.92 ± 0.03	0.90 ± 0.03	0.89 ± 0.03	0.91 ± 0.03
4800	3.73 ± 0.47	DNC	1.58 ± 0.15	0.93 ± 0.04	0.86 ± 0.03	0.85 ± 0.03	0.82 ± 0.03
5645	4.53 ± 0.58	DNC	1.43 ± 0.11	0.86 ± 0.03	0.85 ± 0.03	0.82 ± 0.03	0.86 ± 0.10
6400	7.16 ± 0.93	DNC	1.42 ± 0.12	0.88 ± 0.03	0.80 ± 0.03	0.81 ± 0.03	0.83 ± 0.19
7200	7.45 ± 0.92	DNC	1.66 ± 0.14	0.88 ± 0.04	0.81 ± 0.03	0.78 ± 0.03	0.78 ± 0.07

* DNC - Did not converge

other, such that, the flow along each of the decomposed directions evolves independent of the other. The number of directions with a magnitude of stretching, $\sigma_{\mathrm{i}} > 1$, is labelled as the stretching subspace. For a 3-dimensional flow, the number of stretching subspace varies between 0 and 3. A 0-dimensional stretching subspace is a characteristic of regions where the magnitude of perturbation always diminishes along a propagated arc, irrespective of the direction of maneuver. If the dimensions of stretching subspace is 1, there exists a single direction along which perturbations grow while a restoring plane exists where perturbations diminish downstream. Similarly, a 2-dimensional stretching subspace indicates a plane along which perturbations expand and then one restoring direction. Finally, all directions in a 3-dimensional stretching subspace amplify perturbations, certainly causing a larger variations downstream. Any maneuvers in the region with a 3-dimensional stretching subspace must be avoided. Figure 5.15 offers maps that correspond to the dimensions of the stretching subspace for flow originating and terminating at different locations along the orbit, computed for a perilune radius 3200 km (L2 NRHO) and a perilune radius 4000 km (L1 NRHO), respectively.

The maps are plotted in both mean anomaly as well as the osculating true anomaly. The characteristics of the other L1 and L2 NRHOs are similar to the members plotted in Figure 5.15. Clearly, there is a distinct difference in the number of stretching subspaces over different maneuver locations, described in terms of mean anomaly, for the L1 NRHO as compared to L2 NRHO. These subtle differences cause variations in the stationkeeping performance between the L1 NRHO family versus the L2 NRHO family. Note that, the number of stretching subspaces for a combination of maneuver location and coast durations affect the performance of stationkeeping maneuvers. The x-axis control stationkeeping strategy in the conventional form as applied for the L2 NRHOs is inadequate for the L1 NRHOs. It is therefore, an option to place one or more maneuvers along an orbit, at locations along the orbit that maybe symmetric or asymmetric across the line joining the apsides.

5.5.1 Symmetric one-maneuver location per orbit

Implementing a single maneuver along an orbit, on an axis of symmetry, i.e., at apoapsis ($\theta_{MA} = \theta_{TA} = 180^o$), is convenient for stationkeeping. From the map in Figure 5.15, there exists only a 1-dimensional stretching subspace for an L2 NRHO with perilune radius 3200 km, corresponding to maneuver at 180^o mean anomaly and a coast duration of 360^o. Hence, a maneuver away from the most stretching direction is likely to offer long-term stability. Other low perilune L2 NRHOs also possess similar characteristics. In contrast, the magnitudes of stretching, σ_{i}, along different L1 NRHOs, are plotted in Figure 5.16 for flow between two successive apoapses. Unlike the L2 NRHOs with a 1-dimensional subspace for flow between two successive apoapsis, there exists a 2-dimensional stretching subspace for L1 NRHOs with low perilune radii. Therefore, ensuring a maneuver away from the most stretching direction is not sufficient for long-term stability. A maneuver is effective if it is perfectly aligned in the restoring direction, i.e., mutually perpendicular to both the elongating directions, the maximum stretching direction and the intermediate stretching direction. However, targeting the xz plane crossing near the periapsis regions does not deliver maneuvers precisely along the restoring direction. Further, if the magnitude of stretching in the intermediate stretching direction is not significantly larger than 1, maneuvers perpendicular to the most stretching direction are still unlikely to maintain the spacecraft near the virtual reference solution

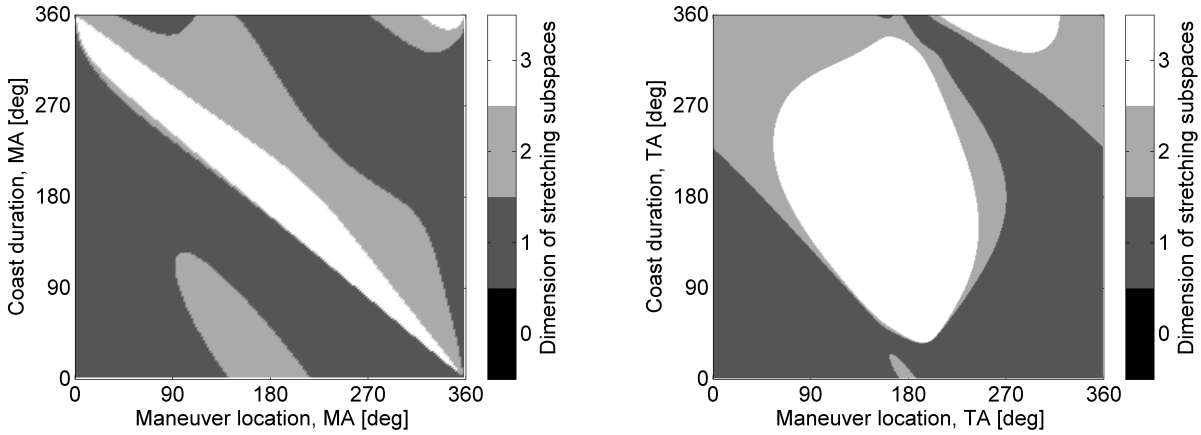

(a) Rp 3200 L2 NRHO (Mean Anomaly)

(b) Rp 3200 L2 NRHO (True Anomaly)

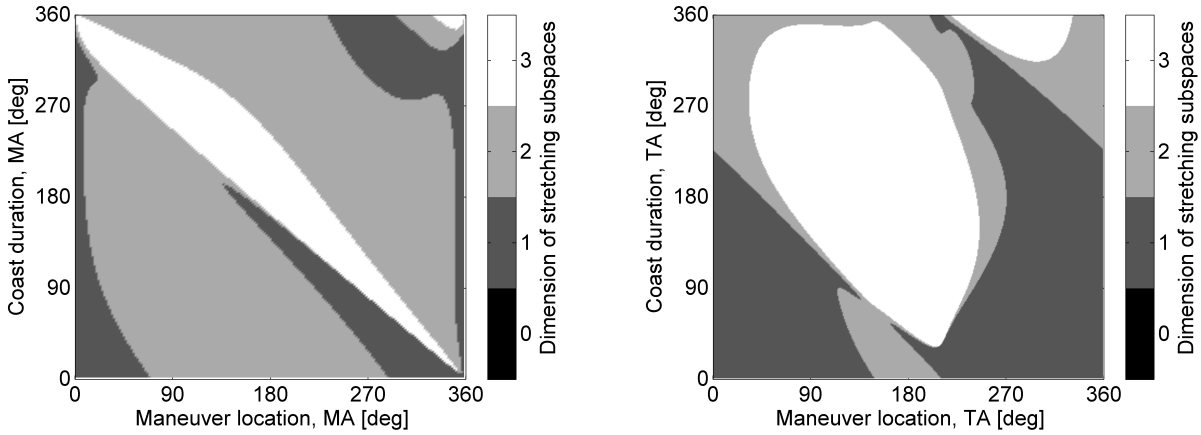

(c) Rp 4000 L1 NRHO (Mean Anomaly)

(d) Rp 4000 L1 NRHO (True Anomaly)

Figure 5.15. Number of stretching subspaces for different combinations of maneuver locations and coast durations.

for a sufficiently long time as variations increase gradually over time. Perhaps, maintaining spacecraft for a shorter duration may still be possible. Nevertheless, as seen in Figure 5.16, for L1 NRHOs with magnitude of $\sigma_2 > 1$, which is significant, any component of maneuvers along the intermediate stretching direction amplifies over time substantially, causing divergence from the baseline trajectory. A single maneuver implemented per orbit at the apoapsis is not generally an efficient choice for the L1 NRHOs. Maintaining a spacecraft along a sufficiently long horizon reference trajectory with stationkeeping maneuvers delivered at apoapsis is an effective choice for the L2 NRHOs but not so effective for the L1 NRHOs.

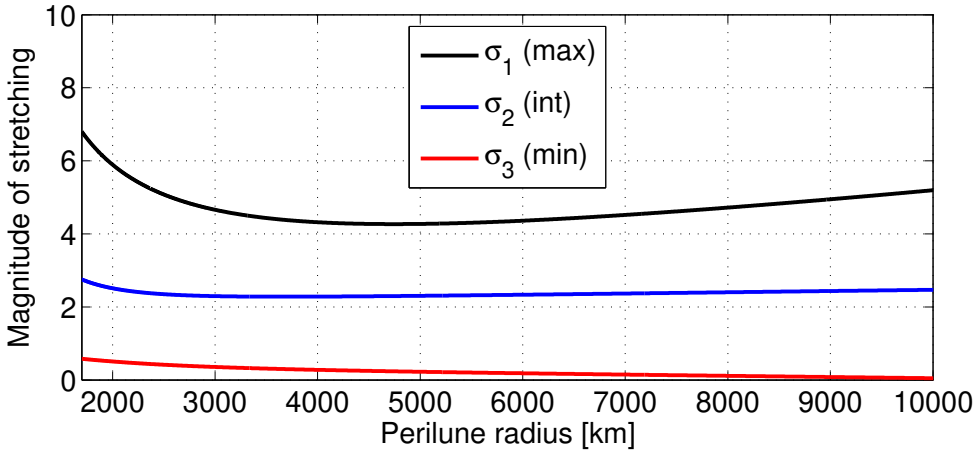

Figure 5.16. Magnitude of stretching, σ_{i}, along different $\mathbb{U}_{\mathrm{i}}$ direction for various L1 NRHOs.

5.5.2 Symmetric two-maneuver locations per orbit

A maneuver executed at the apoapsis on an L1 NRHO may not be efficient, however, implementing two maneuvers per orbit offer more possibilities. An option is to deliver the two maneuvers at locations that are symmetric about the apoapsis. Figure 5.17(b) corresponds to the map for several combinations of maneuver location and coast duration, as well as the associated angle from the most stretching direction, for the L1 NRHO with perilune radius 4000 km described in terms of osculating true anomaly. The map is generated by targeting the 1$^{\mathrm{st}}$ xz plane crossing near the periapsis. Of course, several combinations may exist, but an effective strategy introduces both maneuvers, or at least one with an almost 90^o angle between the most stretching direction and the maneuver direction. One such combination is denoted with white dots in Figure 5.17(b), represented osculating true anomaly. In this case, maneuvers are selected at 150^o and 210^o values of osculating true anomaly, corresponding to the x-coordinate of the white dots. Note that the maneuver locations are symmetrically located 30^o in osculating true anomaly before and after the apoapsis. The y-coordinate of each of the white dots corresponds to the coast duration till the subsequent maneuver location. For visual simplicity, the angle swept by the spacecraft along the orbit as a result of the selected maneuvers are represented in terms of white dotted lines. The maneuver at 210^o is aligned almost perpendicularly to the most stretching direction, and

offers the most useful choice. Since maneuvers are symmetric about apoapsis, the maneuver location at 150^o osculating true anomaly (TA) is complementary and there are no degrees of freedom for its selection. The maneuver at 150^o TA possess a significant component in the stretching directions but since the propagated trajectory traverses through the apoapsis region, the resulting instability is limited. The short horizon maneuvers generated at 150^o and 210^o are a plausible combination. Figure 5.17(a) is complimentary to Figure 5.17(b) but plotted in mean anomaly scale for reference. The symmetric two-maneuver locations for an L1 NRHO with a perilune radius 4000 km in the configuration space is plotted in Figure 5.18 along a long-horizon reference trajectory in the CR3BP and the ephemeris model. Not surprisingly, the maneuver locations at a specified osculating true anomaly is more dispersed in the ephemeris model but they resemble the geometry of the maneuver locations in the CR3BP. Since maneuvers may include a component in the intermediate stretching direction (eg., the maneuver at 210^o osculating true anomaly) with a stretching magnitude marginally greater than 1, perturbations do grow, but at a very low rate. Some long-term simulations result in trajectories deviating from the virtual reference solution as the corrective stationkeeping maneuvers with a component in the intermediate stretching direction does amplify the variations; an occasional long horizon manuever overcomes such predictable behavior. For the L1 NRHO with 4000 km perilune radius, maps similar to Figure 5.17 for longer target horizons may not necessarily offer suitable combinations for two-maneuver locations symmetric about the apoapsis that are conducive for stationkeeping. Application to different NRHOs and different target horizons yield different maps, for which feasible solutions employing a strategy for symmetric two-maneuver per orbit may or may not exist, hence cannot be generalized. The analyses are based on the dynamics along an orbit in the CR3BP model and therefore may not precisely reflect the behavior in the ephemeris model, however, the CR3BP offers a fairly reliable initial guess.

5.5.3 Symmetric three-maneuvers per orbit

Due to the existence of more than one stretching directions for a number of combinations of maneuver locations and coast durations in the case for L1 NRHOs as described in Figure 5.15(c), finding maneuver combinations suitable for stationkeeping in L1 NRHOs are more

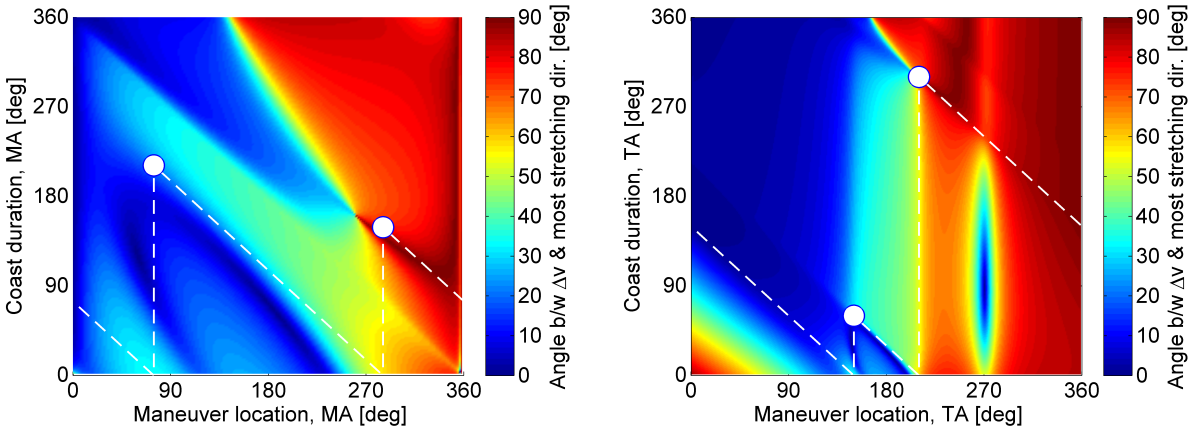

(a) Mean Anomaly (b) True Anomaly

Figure 5.17. Symmetric two-maneuvers per orbit locations for L1 NRHO with perilune radius 4000 km. Maneuvers at 74.46^o and 285.54^o Mean Anomaly or 150^o and 210^o osculating True Anomaly. Map generated by targeting rotating x-velocity at 1^{st} xz plane crossing.

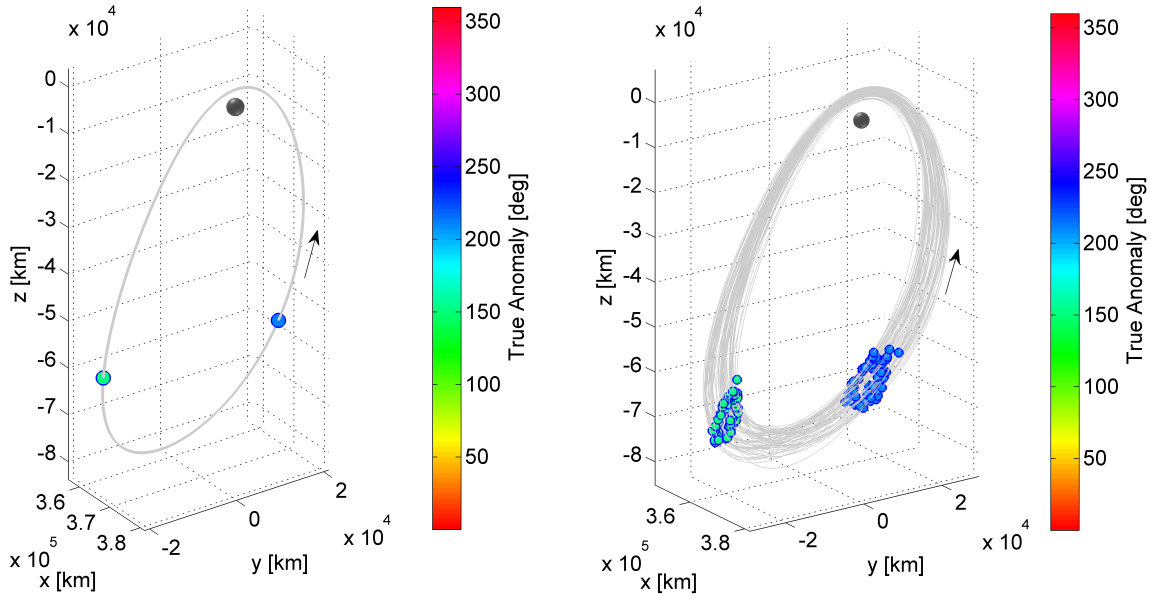

(a) CR3BP (b) Ephemeris

Figure 5.18. Symmetric two-maneuver locations for an L1 NRHO with perilune radius 4000 km placed at 150^o and 210^o osculating True Anomaly in the configuration space along a long-horizon reference orbit in the CR3BP and the ephemeris model.

challenging than the L2 NRHOs. A three-maneuver combination is an attempt to further exploit the region within the map in Figure 5.17. A combination of three-maneuvers per orbit that are symmetric about the apoapsis is an extended version of the case with two-maneuvers per orbit that are located symmetric about the apoapsis. This case is equivalent to selecting a two-maneuver combinations located symmetric across the apoapsis, along with an additional maneuver exactly at the apoapsis. Figure 5.19 corresponds to a three-maneuver combination noting the maneuver locations and coast durations, as well as the associated angle described in terms of osculating true anomaly from the most stretching direction, for the L1 NRHO with perilune radius 4000 km. The map is presented in both mean anomaly as well as in osculating true anomaly scale. The map is generated by targeting the 1^{st} xz plane crossing near the periapsis. In comparison to the symmetric two-maneuver per orbit case in Figure 5.17(b), the time duration for propagation after the maneuver at 150^o is essentially halved (from 4.610 days to 2.305 days) to accommodate a maneuver at the apoapsis, as in the case of symmetric three-maneuver per orbit case in Figure 5.19(b). A three-maneuver combination decreases the time of propagation after the maneuver at 150^o TA to the subsequent maneuver at 180^o TA. The reduction in the time post maneuver, one with a significant component in the stretching direction, is essentially a trade-off between an added maneuver at 180^o TA and reducing deviation. A symmetric three-maneuver locations at 150^o, 180^o and 210^o osculating true anomaly for an L1 NRHO with a perilune radius 4000 km in the configuration space is plotted in Figure 5.20 along a long-horizon reference trajectory in the CR3BP and the ephemeris model. Again, feasibility is not generalized as the maps are a reflective of a particular NRHO, as well as the maneuver location, coast duration and the target horizon time.

The number of maneuvers per orbit is a design choice and hence, more than three maneuvers per orbit is also an option. As noted previously, several combinations of maneuver locations is straightforwardly generated through different maps for different halo orbits and different target horizon times. Some maps offer feasible combinations for a greater number of maneuvers per orbit. Nevertheless, too many maneuvers along a nearly stable NRHO may be redundant. Further, maneuvers placed closer to each other may not provide ample time

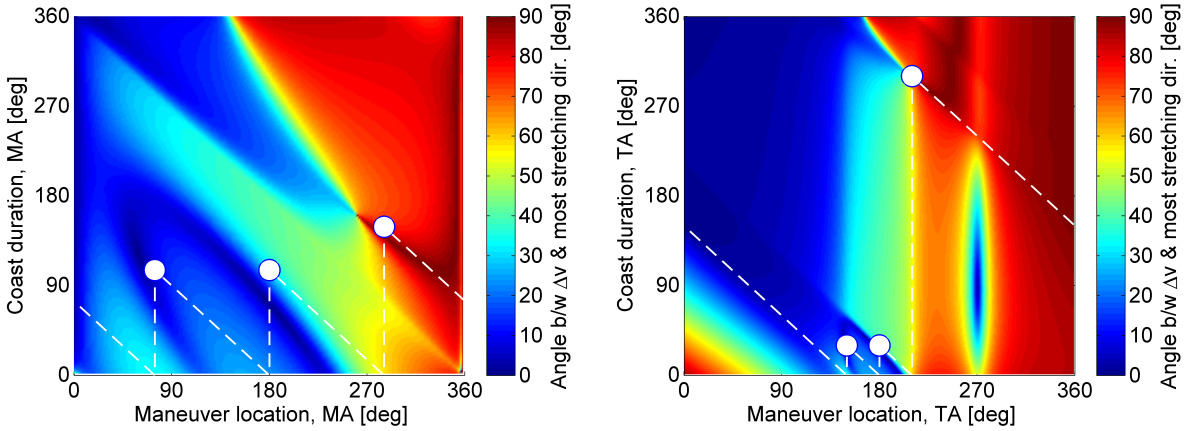

(a) Mean Anomaly (b) True Anomaly

Figure 5.19. Symmetric three-maneuvers per orbit locations for L1 NRHO with perilune radius 4000 km. Maneuvers at 74.46^o, 180^o and 285.54^o Mean Anomaly or 150^o, 180^o and 210^o osculating True Anomaly. Map generated by targeting rotating x-velocity at 1^{st} xz plane crossing.

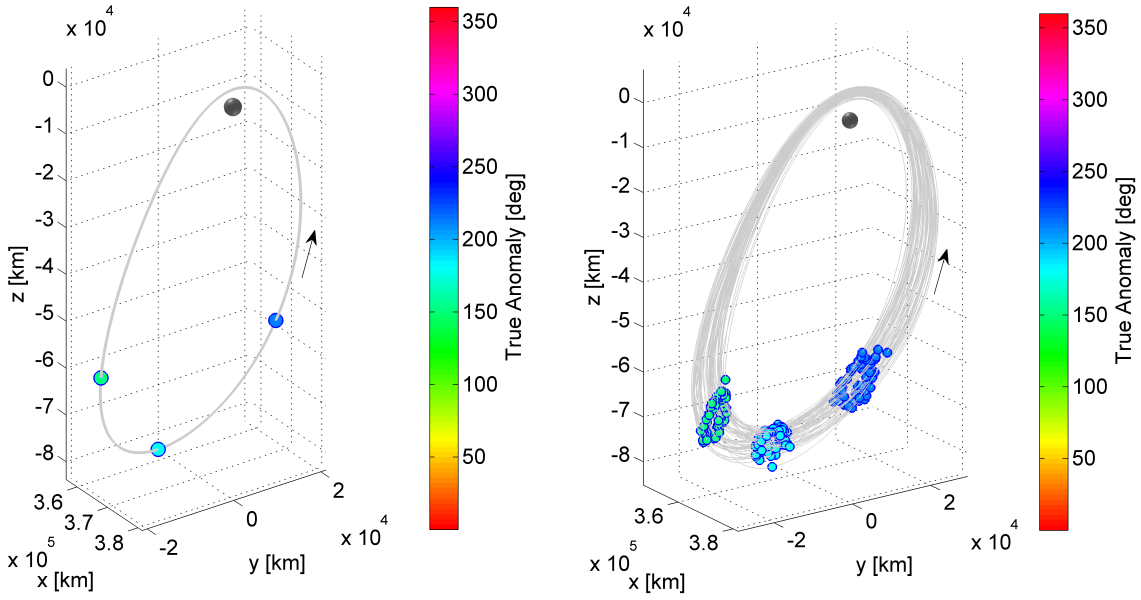

(a) CR3BP (b) Ephemeris

Figure 5.20. Symmetric three-maneuver locations for an L1 NRHO with perilune radius 4000 km placed at 150^o, 180^o and 210^o osculating True Anomaly in the configuration space along a long-horizon reference orbit in the CR3BP and the ephemeris model.

for orbit determination. In theory, the strategy as discussed is applicable for cases with a higher number of maneuvers per orbit as well, but they are not explored here.

5.5.4 Asymmetric one-maneuver location per orbit

Asymmetric placement of maneuver locations offer a larger trade-space for feasible solutions than the symmetric counterpart, due to more flexibility in exploring regions of the map. If only one maneuver is implemented every orbit and not placed at the apoapsis, the placement is asymmetric. In such a case, the coast duration must be 360^o, repeating the location in configuration space over every revolution, hence, the region to explore on the map is restricted to a line along the y-coordinate for 360^o coast duration. It is then straightforward to identify a maneuver location where a maneuver is aligned perpendicular to the maximum stretching direction. For example, Figure 5.21 corresponds to an asymmetric single maneuver location for the L1 NRHO with perilune radius 8000 km placed at 150^o osculating TA. The maps are described in terms of both mean anomaly and osculating true anomaly. The map is generated by targeting the 2^{nd} xz plane crossing near the periapsis. In this case, at 150^o osculating TA, a maneuver is aligned perpendicular to the most stretching direction, hence, offering a reasonable maneuver location. An asymmetric one-maneuver location at 150^o osculating true anomaly for an L1 NRHO with a perilune radius 8000 km in the configuration space is plotted in Figure 5.22 along a long-horizon reference trajectory in the CR3BP and the ephemeris model. Again, maps are a reflective of the NRHO and the target horizon time; as a result, they may or may not be conducive to single maneuver per orbit cases.

5.5.5 Asymmetric two-maneuvers per orbit

A larger degree of freedom exists in selecting asymmetric maneuver locations on an NRHO, that likely results in effective maneuvers. The maneuver locations are complementary, i.e., the sum of their coast durations must add to 360^o, for maneuvers that are expected to repeat every revolution. With higher flexibility, multiple combinations of maneuver locations are possible on the same map. Figures 5.23, 5.25 and 5.27 correspond to three different

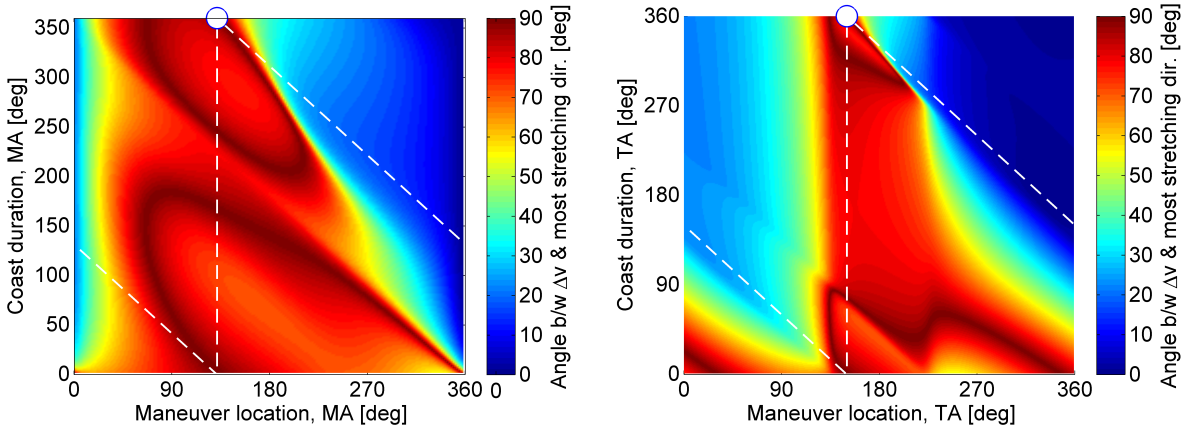

(a) Mean Anomaly (b) True Anomaly

Figure 5.21. Asymmetric one-maneuver per orbit location for L1 NRHO with perilune radius 8000 km. Maneuver at 131.61^o Mean Anomaly or 150^o osculating True Anomaly. Map generated by targeting rotating x-velocity at 2$^{\text{nd}}$ xz plane crossing.

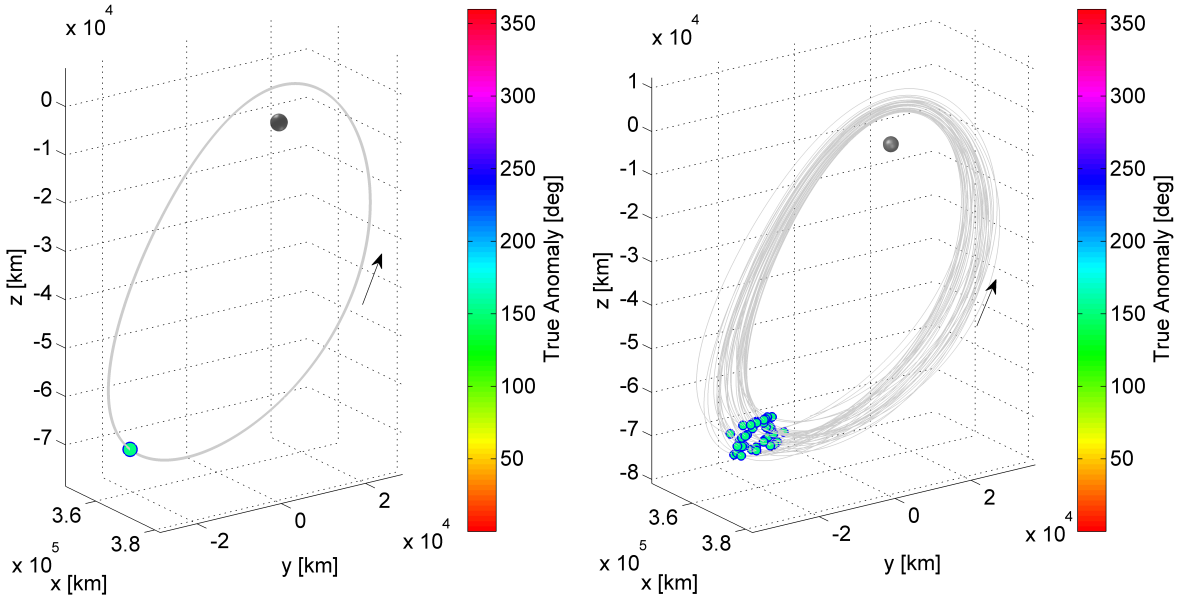

(a) CR3BP (b) Ephemeris

Figure 5.22. Asymmetric one-maneuver location for an L1 NRHO with perilune radius 8000 km placed at 150^o osculating True Anomaly in the configuration space along a long-horizon reference orbit in the CR3BP and the ephemeris model.

cases of asymmetric two-maneuver combinations for the L1 NRHO with perilune radius 8000 km described in terms of osculating true anomaly. Again, the maps are plotted in both mean aanomaly and osculating true anomaly. The map is generated by targeting the 2$^{\text{nd}}$ xz plane crossing near the periapsis, and favorable to illustrate an asymmetric two-maneuver combination. Not all target horizon times offer maps conducive to two-maneuver combinations. Figure 5.23 offers plausible maneuver locations at 142^o and 180^o in osculating true anomaly values, while Figure 5.25 introduces maneuver locations at 139^o and 194^o true anomalies, and finally, Figure 5.27 reciprocates maneuver locations at 133^o and 201^o true anomalies. Each of these combinations for an asymmetric two-maneuver locations for an L1 NRHO with a perilune radius 8000 km in the configuration space is plotted in Figures 5.24, 5.26 and 5.28 along a long-horizon reference trajectory in the CR3BP and the ephemeris model. These are only three distinct sample cases that are selected from the map, however, many such combinations are possible. Once again, despite a larger flexibility in the selection of the maneuver locations, feasibility of maneuver combinations depend on the individual maps that are generated for an NRHO and a target horizon time and are not easily generalized.

For the L2 NRHOs there exists a greater number of combinations of maneuver locations and coast durations that have only one dimension stretching subspace as described in Figure 5.15(a). One such combination suitable for stationkeeping is to implement maneuvers once every orbit, at the apoapsis, away from the most stretching direction. Furthermore, targeting significantly downstream is favorable. However, for the range of L1 NRHOs, a maneuver every revolution delivered at the apoapsis does not necessarily maintain the spacecraft near the reference trajectory as the maneuver may have a component in the intermediate stretching direction, that amplifies with time. Depending on the L1 NRHO of interest and a different target horizons, a map for the angle between the maneuver and the most stretching direction is generated. One or more combinations of maneuver locations from the map are identified, that may or may not be symmetric across the apoapsis. Table 5.3 lists the estimated annual stationkeeping costs for various L1 NRHOs, for different maneuver locations, coast durations and target horizon time. The values are estimated by propagating a trajectory for duration of 180 days. For an NRHO, for example, L1 NRHO with 5000 km perilune radius,

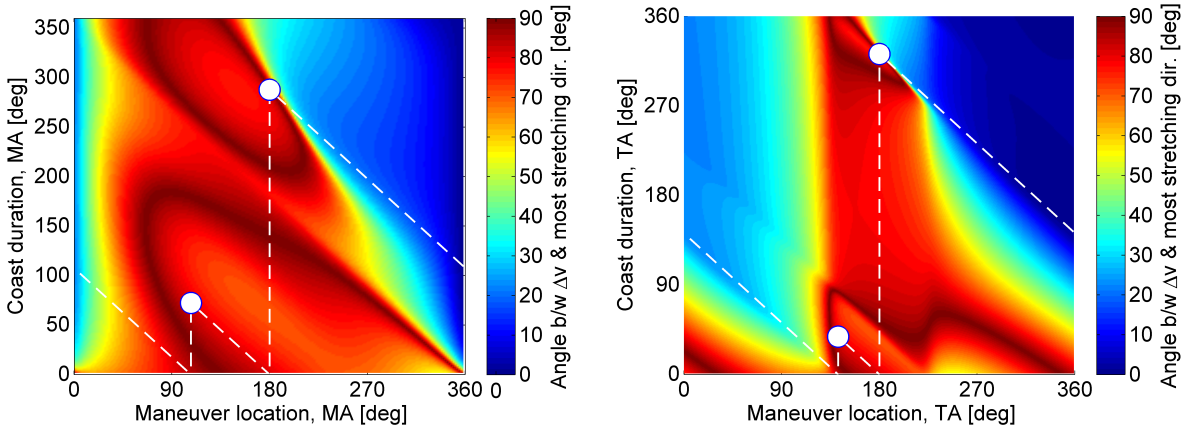

(a) Mean Anomaly (b) True Anomaly

Figure 5.23. Asymmetric two-maneuvers per orbit locations for L1 NRHO with perilune radius 8000 km. Case with maneuvers at 107.66^o and 180^o Mean Anomaly or 142^o and 180^o osculating True Anomaly. Map generated by targeting rotating x-velocity at 2^{nd} xz plane crossing.

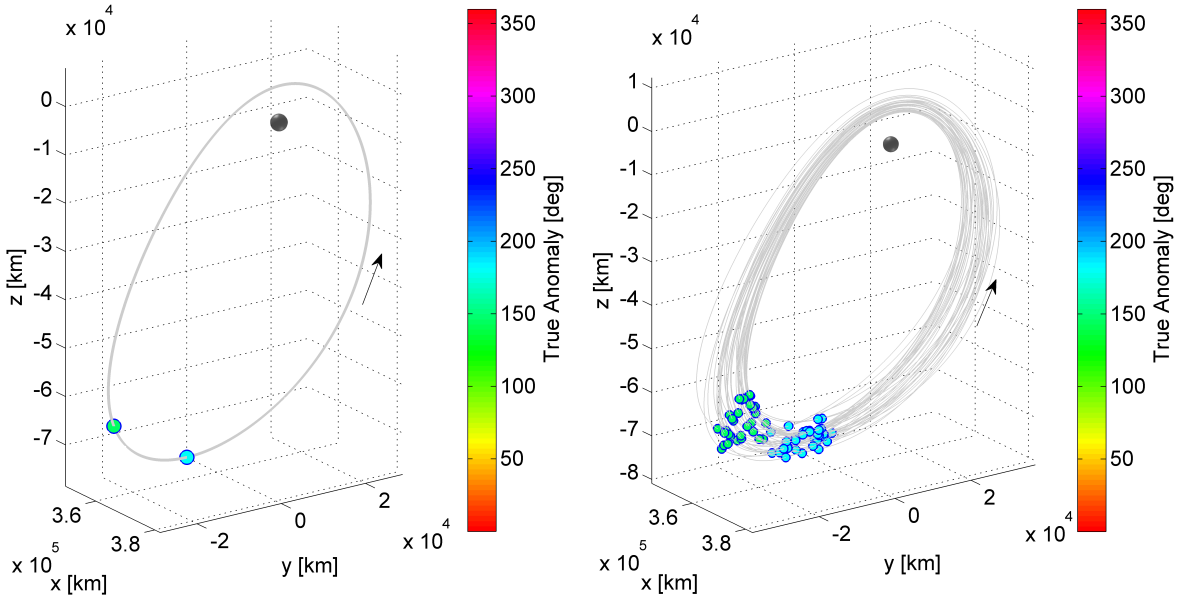

(a) CR3BP (b) Ephemeris

Figure 5.24. Asymmetric two-maneuver location for an L1 NRHO with perilune radius 8000 km placed at 142^o and 180^o osculating True Anomaly in the configuration space along a long-horizon reference orbit in the CR3BP and the ephemeris model.

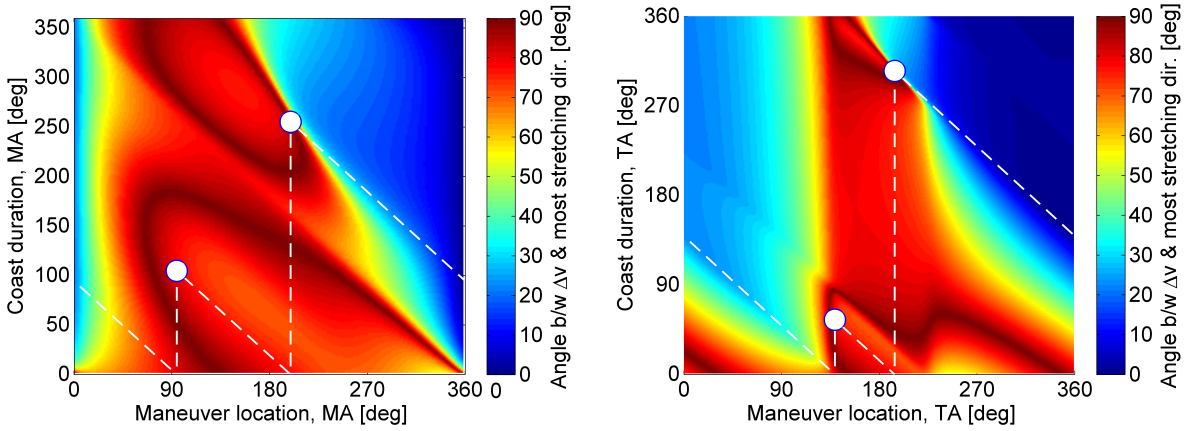

(a) Mean Anomaly (b) True Anomaly

Figure 5.25. Asymmetric two-maneuvers per orbit locations for L1 NRHO with perilune radius 8000 km. Case with maneuvers at 94.56^o and 199.32^o Mean Anomaly or 139^o and 194^o osculating True Anomaly. Map generated by targeting rotating x-velocity at 2^{nd} xz plane crossing.

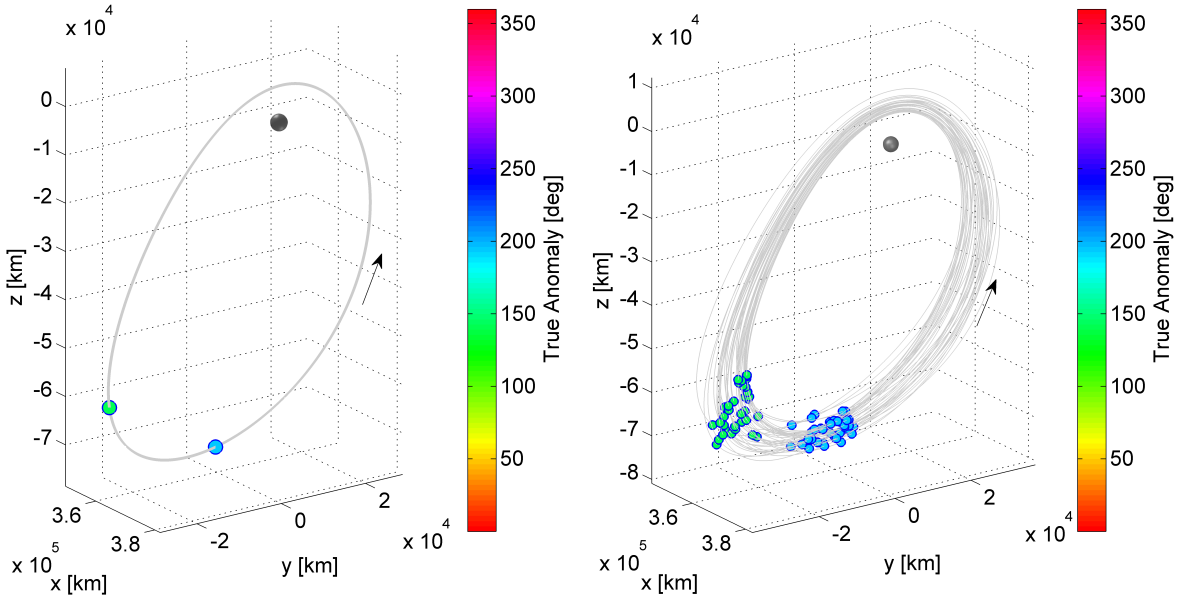

(a) CR3BP (b) Ephemeris

Figure 5.26. Asymmetric two-maneuver location for an L1 NRHO with perilune radius 8000 km placed at 139^o and 194^o osculating True Anomaly in the configuration space along a long-horizon reference orbit in the CR3BP and the ephemeris model.

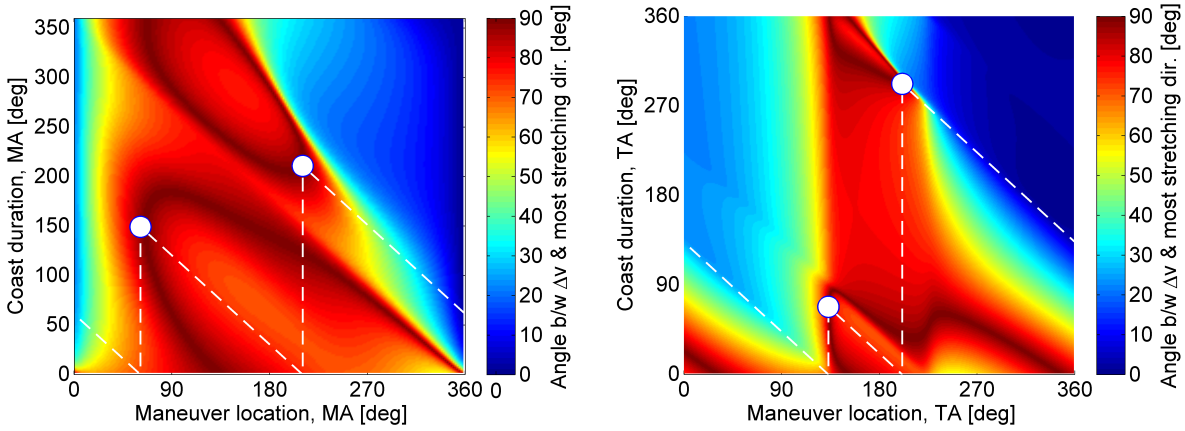

(a) Mean Anomaly (b) True Anomaly

Figure 5.27. Asymmetric two-maneuvers per orbit locations for L1 NRHO with perilune radius 8000 km. Case with maneuvers at 61.22^o and 210.43^o Mean Anomaly or 133^o and 201^o osculating True Anomaly. Map generated by targeting rotating x-velocity at 2^{nd} xz plane crossing.

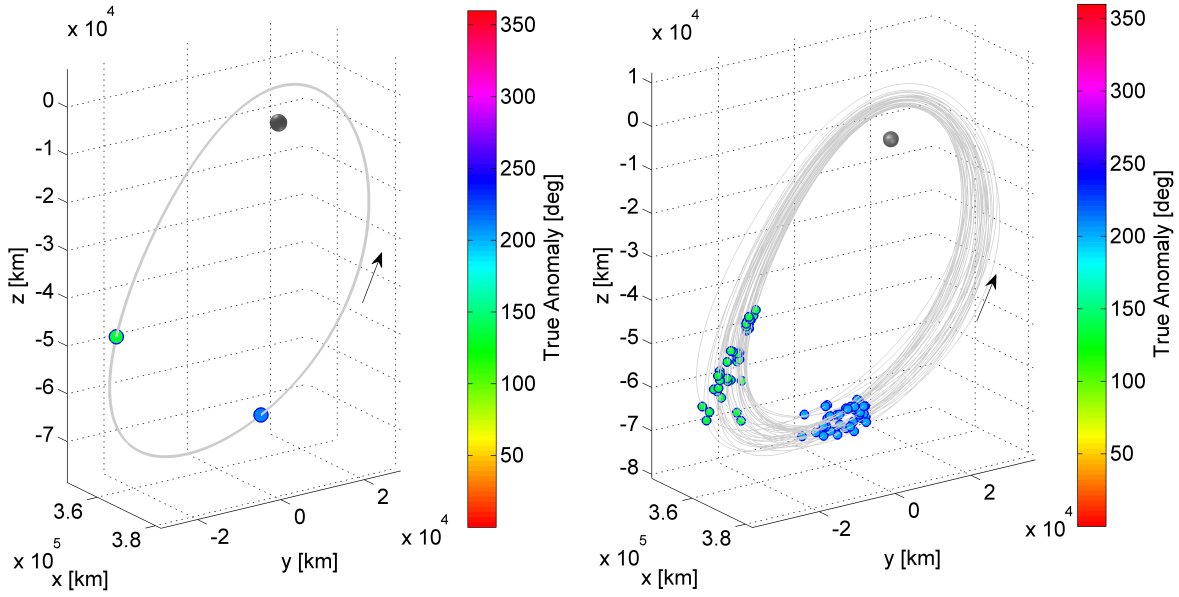

(a) CR3BP (b) Ephemeris

Figure 5.28. Asymmetric two-maneuver location for an L1 NRHO with perilune radius 8000 km placed at 133^o and 201^o osculating True Anomaly in the configuration space along a long-horizon reference orbit in the CR3BP and the ephemeris model.

there exists numerous combinations of target horizons and maneuver combinations that yield successful stationkeeping. The examples demonstrated for the L1 NRHO with 5000 km perilune radius include, symmetric and asymmetric placement of maneuver locations about the apoapsis, one or more maneuvers per orbit, and target horizons ranging from the first xz plane crossing to the fifth xz plane crossing. Similar combinations exists for other L1 NRHOs as well. Outcomes for the L1 NRHOs with perilune radius ranging from 4000 km to 8000 km are demonstrated in Table 5.3. Of course, as discussed, many several combinations of maneuver locations and target horizon time are possible for stationkeeping. Longer target horizons may offer maps conducive to some but not all the cases discussed (symmetric and asymmetric maneuver locations as well as one or more maneuvers every orbit).

Table 5.3. Annual stationkeeping cost [m/s] along L1 NHROs

Perilune radius [km]	Target xz-plane crossing #	Sym/Asym	# $\Delta\bar{v}$/rev	Maneuver Locations [TA]	Annual Cost [m/s]			
					Low ODE		High ODE	
					Mean $\bar{\varkappa}$	$1.96\sigma_{\bar{\varkappa}}$	Mean $\bar{\varkappa}$	$1.96\sigma_{\bar{\varkappa}}$
4000	1	Sym	2	150, 210	2.21	0.21	6.25	0.44
4000	1	Sym	3	150, 180, 210	1.19	0.12	7.79	0.47
4000	3	Asym	1	188	0.74	0.09	1.61	0.11
5000	1	Sym	2	145, 215	2.47	0.22	5.46	0.26
5000	1	Sym	3	145, 180, 215	1.18	0.11	6.83	0.31
5000	1	Sym	2	150, 210	1.88	0.18	6.30	0.44
5000	1	Sym	3	150, 180, 210	1.21	0.13	7.73	0.49
5000	2	Asym	1	164	0.46	0.02	2.11	0.23
5000	5	Sym	1	180	0.20	0.01	0.72	0.02
6000	1	Sym	2	145, 215	2.31	0.25	6.47	0.39
6000	1	Sym	3	145, 180, 215	1.11	0.08	7.63	0.48
6000	2	Asym	1	160	0.52	0.03	2.24	0.18
7000	2	Asym	1	156	0.56	0.02	1.91	0.15
7000	5	Asym	1	171	0.20	0.01	0.78	0.03
8000	2	Asym	1	150	0.65	0.03	1.86	0.13
8000	2	Asym	2	142, 180	0.40	0.02	2.89	0.12
8000	2	Asym	2	133, 201	0.41	0.02	2.85	0.14
8000	2	Asym	2	139, 194	0.46	0.02	2.92	0.17

5.6 Alternate Control Strategies and Constraints

5.6.1 Phase control approach

Precise orbit control is expensive and may be nontrivial. The conventional x-axis control approach is effective in maintaining the spacecraft in the vicinity of a virtual reference

solution at a relatively low cost. By only targeting two of the seven states, that is, the y and $\dot{x}$ quantities, ample flexibility in targeting results in the spacecraft remaining loosely bounded in the neighborhood of the virtual reference trajectory that is originally generated over a significantly longer duration, at a low cost. However, the low cost stationkeeping solutions generated by the conventional approach do not necessarily synchronize in phase space with the virtual reference trajectory, resulting in the actual trajectory lagging or leading the virtual reference in time space. Figure 5.30(a) illustrates the time difference between the actual trajectory and the virtual reference measured at periapsis over different Monte Carlo simulations, i.e., cases with different seeds for random errors to mimic an uncertainty in orbit determination. The phase difference between the actual trajectory and the virtual reference path increases either positively or negatively over time. If the baseline trajectory is generated to satisfy any eclipse avoidance properties or any other phase constraints, the phase shift between the actual and reference trajectories may impede the mission objectives. To overcome such a scenario, additional restrictions are imposed on the x-axis control algorithm to generate maneuvers that align with the appropriate phasing for the actual trajectory. For controlling phase shift, Davis et al. [119] target the rotating $\dot{x}$ value as well as the periapsis altitude simultaneously. With the updated strategy a decrease in the rate of phase shift is observed. For any cases, where the spacecraft states have deviated significantly, a long horizon orbit correction maneuver is implemented to drive the states to the virtual reference trajectory. An alternate approach with time shift feedback is explored here.

To maintain the correct phasing between the actual trajectory and the virtual reference path, a phase constraint is delivered either at periapsis, or apoapsis, or even the xz-plane crossing, as they are complimentary. Since the x-axis control approach targets a condition at the xz-plane crossing, additional phase control constraints at the xz-plane crossing satisfy the requirement. A fixed time targeting scheme is incorporated that targets conditions at the xz-plane crossing to occur at the same time, relative to the virtual reference, at the corresponding xz-plane crossing. All trajectories neighboring a reference solution that cross the xz plane crossings at the same time as the reference trajectory are considered to be in-phase. In contrast, certain neighboring trajectories when propagated downstream for a fixed

time duration equivalent to the time evolved along the reference trajectory at the xz plane crossing, are either leading or lagging as described in Figure 5.29. The leading or the lagging trajectories are identified by a positive or a negative change in the y_f position relative to the reference trajectory, i.e., the Δy_f component. A maneuver that compensates for the Δy_f quantity ensures appropriate phasing between the virtual reference solution and the actual trajectory, one that incorporates regular stationkeeping maneuvers. As formulated by [82], a feedback constraint is formulated as

$$\Delta y_f - \dot{y}_f \Delta t_0 = \begin{bmatrix} \varphi_{T,24} & \varphi_{T,25} & \varphi_{T,26} \end{bmatrix} \Delta \bar{v}_0 = \begin{bmatrix} \varphi_{T,24} & \varphi_{T,25} & \varphi_{T,26} \end{bmatrix} \begin{bmatrix} \Delta \dot{x}_0 \\ \Delta \dot{y}_0 \\ \Delta \dot{z}_0 \end{bmatrix} \tag{5.15}$$

and is solved along with the control equation as in equation (5.9) to compute the required maneuver. Here, the final time of propagation, $t_f = t_{Target} = t^*_{xz}$ is the time along the virtual reference trajectory at the appropriate xz plane crossing. The term $\dot{y}_f \Delta t_0$ in equation (5.15) is a feedback term to compensate for the adjustment in the phase difference detected at the apoapsis where the maneuver is implemented. Additionally, Δy_f corresponds to the difference in y position between the actual and the reference trajectory at the end of the propagated arc. For a trajectory with no phase difference, $\Delta t_0 = 0$ and $\Delta y_f = 0$. With an iterative process, the states are updated to drive the left side of equation (5.15) to zero. The maneuver generated with an additional phase constraint bounds the spacecraft motion in the vicinity of the virtual reference trajectory in the time states as well.

Using a phase control approach, the phase shift between the actual trajectory and the virtual reference is minimized. Since the virtual reference is generated satisfying any added eclipse or phase constraint, the actual trajectory does not violate any phase constraint, to within a few seconds tolerance. Figure 5.30(b) demonstrates the efficacy of the phase control approach to minimize the time shift at periapsis for 100 Monte Carlo trials completed on the L2 NRHO with perilune radius 3200 km. The time difference, measured at the periapsis

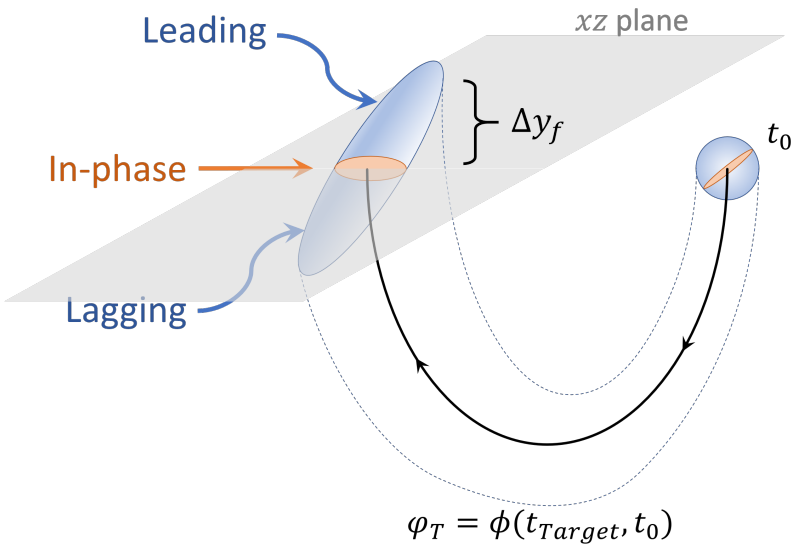

Figure 5.29. Phase control approach formulation.

location is low, in contrast to Figure 5.30(a) using the conventional x-axis control approach.

The annual orbit maintenance cost for stationkeeping with active phase control approach is higher than the conventional approach as flexibility is reduced. Not surprisingly, an additional constraint equation that is solved simultaneously with the control equation decreases the range of the solution space and results in a higher cost for operations. The phase control approach is notably efficient when the target horizon is sufficiently long. The approach produces favorable solutions for the 9:2 synodic resonant L2 NRHO when targeting 6.5 rev, 5.5 rev, 4.5 rev and 2.5 rev downstream. Although considerably better phasing than the conventional approach, diminishing returns are observed at 3.5 rev target horizon time. For short target horizons, i.e., 0.5 rev and 1.5 rev, the stiffer targeting conditions using a phase control approach do not generate satisfactory results. Due to an additional constraint, an increase in the annual maintenance cost is detected. The costs for various L2 NRHOs under consideration are listed in Tables 5.4 and 5.5 for low and high orbit determination errors, respectively. Marginal increases in costs are apparent as the perilune radius of the NRHOs increase.

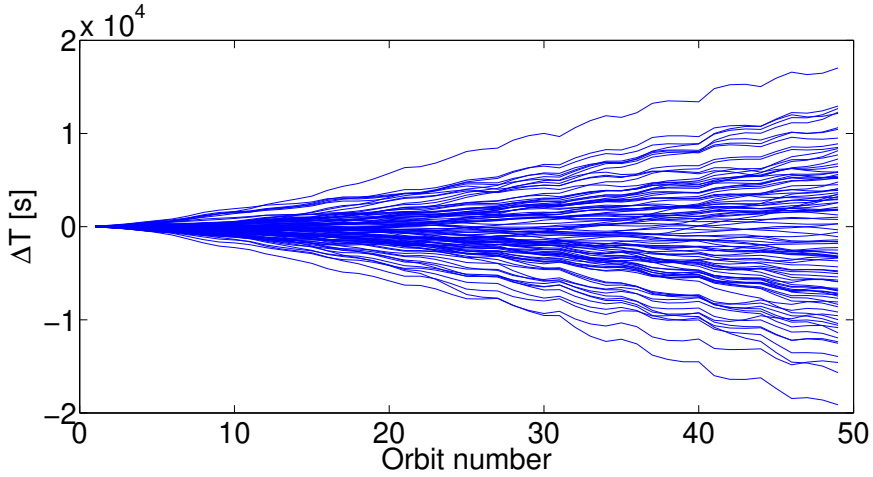

(a) Conventional approach

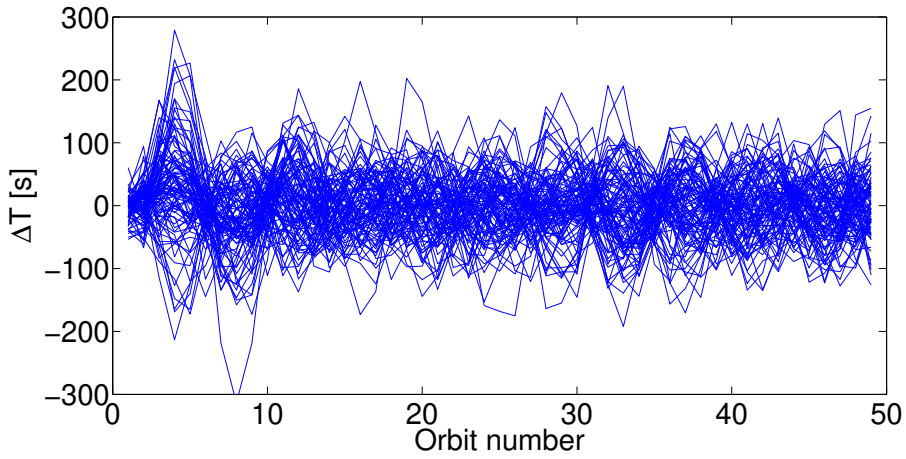

(b) Phase control approach

Figure 5.30. Phase shift measured at periapsis with and without phase control for L2 NRHO with perilune radius 3200 km. Target horizon: 6.5 rev. Case with high ODE level (3σ: 10 km and 10 cm/s).

The conventional x-axis control approach for the L1 NRHOs is not observed to be as effective as the L2 NRHOs, primarily due to the multiple stretching subspaces between the two successive maneuver locations along an L1 NRHO. As a result, combination of one or more maneuvers along every orbit, placed either symmetrically or asymmetrically across the apoapsis have shown to be effective for stationkeeping. Phasing errors still exists for cases with one or more maneuvers along the orbit, and irrespective of their locations on the orbit. The phasing control constraints, as discussed previously, are effective for many of the L1

Table 5.4. Annual orbit maintenance cost, $\bar{\varkappa}$, and 95% confidence interval, $\pm 1.96\sigma_{\bar{\varkappa}}$, in [m/s] with low ODE level (3σ: 1 km and 1 cm/s) and phase constraints

Perilune radius [km]	Target horizon [rev]						
	0.5	1.5	2.5	3.5	4.5	5.5	6.5
3200	DNC	DNC	0.24 ± 0.01	0.33 ± 0.02	0.26 ± 0.01	0.30 ± 0.01	0.31 ± 0.01
4000	DNC	DNC	0.24 ± 0.01	0.27 ± 0.01	0.29 ± 0.01	0.34 ± 0.01	0.33 ± 0.01
4800	DNC	DNC	0.23 ± 0.00	0.27 ± 0.01	0.33 ± 0.01	0.37 ± 0.01	0.34 ± 0.01
5645	DNC	DNC	0.24 ± 0.01	0.32 ± 0.01	0.39 ± 0.01	0.41 ± 0.01	0.36 ± 0.01
6400	DNC	DNC	0.26 ± 0.01	0.42 ± 0.02	0.51 ± 0.01	0.50 ± 0.02	0.39 ± 0.01
7200	DNC	DNC	0.33 ± 0.01	0.57 ± 0.06	0.61 ± 0.02	0.52 ± 0.02	0.38 ± 0.01

* DNC - Did not converge

NRHOs that include maneuvers at one or more maneuver locations along the orbit that may or may not be symmetric across the apoapsis. The annual stationkeeping costs with active phase control are estimated for the L1 NRHOs, for both low and high orbit determination errors, and listed in Table 5.6. Of course, a longer target horizon is certainly beneficial for the phase control approach as it provides ample flexibility for trajectory corrections rather than a shorter target horizon. In some cases with an active phase control, the spacecraft motion remained bounded in the vicinity of the reference solution more tightly in contrasts to simulations without any phase constraints. Inclusion of phase constraints are illustrated for one or more maneuvers every orbit, and those that may or may not be located symmetric across the apoapsis. Nevertheless, for the L1 NRHOs, performing maneuvers once every revolution at the apoapsis with an active phase control may still be an effective option despite the conventional algorithm without phase constraints not delivering promising results. The case is however not simulated here.

Table 5.5. Annual orbit maintenance cost, $\bar{\varkappa}$, and 95% confidence interval, $\pm 1.96\sigma_{\bar{\varkappa}}$, in [m/s] with high ODE level (3σ: 10 km and 10 cm/s) and phase constraints.

Perilune radius [km]	Target horizon [rev]						
	0.5	1.5	2.5	3.5	4.5	5.5	6.5
3200	DNC	DNC	2.02 ± 0.06	2.51 ± 0.18	1.98 ± 0.05	2.28 ± 0.07	2.62 ± 0.07
4000	DNC	DNC	1.91 ± 0.05	2.00 ± 0.07	2.06 ± 0.06	2.23 ± 0.07	2.13 ± 0.07
4800	DNC	DNC	1.80 ± 0.06	1.89 ± 0.09	2.03 ± 0.07	2.31 ± 0.11	2.09 ± 0.05
5645	DNC	DNC	1.77 ± 0.05	2.08 ± 0.12	2.19 ± 0.09	2.33 ± 0.10	1.99 ± 0.07
6400	DNC	DNC	1.79 ± 0.06	2.46 ± 0.19	2.49 ± 0.16	2.31 ± 0.09	2.09 ± 0.10
7200	DNC	DNC	1.85 ± 0.08	2.84 ± 0.33	2.74 ± 0.20	2.47 ± 0.20	2.14 ± 0.08

* DNC - Did not converge

Table 5.6. Annual stationkeeping cost [m/s] along L1 NHROs with phase control.

Perilune radius [km]	Target xz-plane crossing #	Sym/Asym	# $\Delta\bar{v}$/rev	Maneuver Locations [TA]	Annual Cost [m/s]			
					Low ODE		High ODE	
					Mean $\bar{\varkappa}$	$1.96\sigma_{\bar{\varkappa}}$	Mean $\bar{\varkappa}$	$1.96\sigma_{\bar{\varkappa}}$
4000	1	Sym	2	150, 210	0.53	0.01	4.38	0.11
4000	1	Sym	3	150, 180, 210	0.69	0.02	6.16	0.14
4000	3	Asym	1	188	0.31	0.01	1.36	0.05
5000	1	Sym	2	145, 215	0.57	0.01	4.48	0.11
5000	1	Sym	3	145, 180, 215	0.65	0.01	5.93	0.14
5000	1	Sym	2	150, 210	0.54	0.01	4.55	0.13
5000	1	Sym	3	150, 180, 210	0.67	0.01	6.18	0.16
5000	2	Asym	1	164	1.26	0.15	5.70	0.62
5000	5	Sym	1	180	0.28	0.01	1.28	0.04
6000	1	Sym	2	145, 215	0.54	0.01	4.39	0.12
6000	1	Sym	3	145, 180, 215	0.66	0.02	6.01	0.15
6000	2	Asym	1	160	1.22	0.12	6.30	0.71
7000	2	Asym	1	156	1.43	0.15	6.39	0.57
7000	5	Asym	1	171	0.29	0.01	1.35	0.04
8000	2	Asym	1	150	1.30	0.12	7.58	0.73
8000	2	Asym	2	142, 180	2.03	0.22	8.89	0.77
8000	2	Asym	2	133, 201	2.62	0.27	9.13	0.59
8000	2	Asym	2	139, 194	2.06	0.18	9.94	0.56

5.6.2 Targeting rotating y velocity

The x-axis control offers a loose control strategy to maintain a spacecraft near the vicinity of a nominal baseline by targeting the rotating $\dot{x}$ component at some xz plane crossing downstream. However, targeting the $\dot{x}$ value is not a necessary condition for stationkeeping rather a user-defined choice. Targeting the $\dot{y}$ value is explored as an alternative, and synonymously labelled as a $\dot{y}$-control strategy. As discussed in section 5.3, the flow between the maneuver location over the coast duration does not define the maneuver characteristics, rather the flow the between the maneuver location to the target determines the maneuver characteristics. Consequently, the stretching directions that are identified for the flow between two successive maneuver location over the coast arc remains unchanged for different types of control strategy. Similar to targeting the $\dot{x}$ value in the x-axis control approach, different maps that demonstrate the evolution of the magnitude and direction of the maneuver delivered by the $\dot{y}$-control strategy offer reliable insight on its effectiveness.

The $\dot{y}$-control stationkeeping approach delivers a 3-dimensional maneuver that targets the rotating y-velocity value at the xz plane crossing downstream. Mathematically, this is represented by

$$\Delta\dot{y}_f = \begin{bmatrix} \varphi_{T,54} & \varphi_{T,55} & \varphi_{T,56} \end{bmatrix} \Delta\bar{v}_0 = \begin{bmatrix} \varphi_{T,44} & \varphi_{T,45} & \varphi_{T,46} \end{bmatrix} \begin{bmatrix} \Delta\dot{x}_0 \\ \Delta\dot{y}_0 \\ \Delta\dot{z}_0 \end{bmatrix} \tag{5.16}$$

where, $\Delta\dot{y}_f$ is the change in the rotating $\dot{y}$ value at the target xz-plane crossing and $\Delta\bar{v}_0 = [\Delta\dot{x}_0,\ \Delta\dot{y}_0,\ \Delta\dot{z}_0]^{\mathrm{T}}$ defines a column vector with three scalar independent control variables that comprise the impulsive maneuver. Moreover, $[\varphi_{T,54}\ \varphi_{T,55}\ \varphi_{T,56}]$ is the corresponding submatrix of the state transition matrix, φ_T. For convenience, define $\bar{M}_y = [\varphi_{T,54}\ \varphi_{T,55}\ \varphi_{T,56}]^{\mathrm{T}}$ as a 3×1 column vector and, therefore, $\Delta\dot{y}_f = \bar{M}_y^{\mathrm{T}}\Delta\bar{v}_0$. For the purpose of comparison, define, $\bar{M}_x = \bar{M}$, where $\bar{M}$ is as defined previously for the x-axis control algorithm that targets the rotating $\dot{x}$ value. Again, one of the goal for the stationkeeping process is reducing

the propellant costs, hence, a minimum norm solution that delivers the smallest maneuver is defined as

$$|\Delta\bar{v}_0|_{min-norm} = \frac{|\Delta\dot{y}_f|}{|\bar{M}_y|} \tag{5.17}$$

in the direction of $\bar{M}_y$. The maneuver magnitude as well as the maneuver direction, both reflect the quality of the maneuver. Each of the maneuver magnitude and the maneuver direction are analyzed, and eventually compared to the results from the conventional x-axis control approach.

The direction of maneuver estimated by the $\dot{y}$-control does not explicitly depend on the initial perturbation however the maneuver magnitude is a direct function of the initial state perturbation. The maneuver magnitude as a function of the initial perturbation is expressed as an inequality as,

$$|\Delta v_0|_{min-norm} = \frac{|\bar{B}_y^{\mathrm{T}}\Delta\bar{\mathbf{x}}_0|}{|\bar{M}_y|} \leq \frac{|\bar{B}^{\mathrm{T}}||\Delta\bar{\mathbf{x}}_0|}{|\bar{M}_y|} \tag{5.18}$$

where $\Delta\dot{y}_f = \bar{B}_y^{\mathrm{T}}\Delta\bar{\mathbf{x}}_0$ with $\bar{B}_y = [\varphi_{T,51}\ \varphi_{T,52}\ \varphi_{T,53}\ \varphi_{T,54}\ \varphi_{T,55}\ \varphi_{T,56}]^{\mathrm{T}}$ as the submatrix of φ_T. The inequality in equation (5.18) is represented in the normalized form as

$$\frac{|\Delta\bar{v}_0|_{min-norm}}{|\Delta\bar{\mathbf{x}}_0|} \leq \frac{|\bar{B}_y|}{|\bar{M}_y|} \tag{5.19}$$

such that the upper limit varies depending on the target horizon chosen for estimating the stationkeeping maneuver. The upper bound on the ratio of maneuver magnitude to the magnitude of initial state perturbation offers the leverage the maneuver generates. A smaller upper limit provides more leverage to the maneuver as a small maneuver magnitude is required to overcome a unit initial state perturbation. A plot of $\frac{|\bar{B}_y|}{|\bar{M}_y|}$ for different targets, i.e., 1^{st}, 2^{nd} and 7^{th} xz plane crossings near the periapsis region is represented in Figure 5.31 for an L2 NRHO with perilune radius 3200 km. For different target horizons, maneuver

locations along the orbit offer distinct characteristics. A lower value of $\frac{|\bar{B}_y|}{|\bar{M}_y|}$ suggests that the maneuver generated produces a smaller magnitude in that region. From Figures 5.31(e) and 5.31(f), it is evident that when targeting the 7^{th} xz plane crossing, there exists a wide range of maneuver locations that result in low maneuver magnitudes. In general, irrespective of the target horizon, the locations along the orbit close to the apoapsis regions offer deliver smaller maneuver magnitude to overcome a unit perturbation, hence appropriate for maneuver placement. Similar observation is observed in the conventional x-axis control approach as well.

The direction of the maneuver delivered by the $\dot{y}$-control algorithm is another important parameter that yields an assessment for the efficiency of the maneuver in maintaining the spacecraft in the vicinity of the reference path. The stretching directions for the submatrices of the STM along the coast segment, φ_C, are available. As noted previously, the maneuvers, when executed in the restoring plane or along the restoring direction, reduces the spacecraft deviation at the downstream locations, thereby maintaining the spacecraft boundedness. A map for the direction between the maneuver, $\hat{M}_y$, and the most stretching direction, $\mathbb{V}_1$, for different combination of maneuver location and coast duration for three different target horizons is presented in Figure 5.32, for an L2 NRHO with perilune radius 3200 km. Each of the maps offer distinct regions where the maneuver and the most stretching direction are almost perpendicular; such regions facilitate efficient maneuvers.

Without loss of generality, define, $\Delta\bar{v}_{(x)}$ as the maneuver delivered by the conventional x-axis control that is aligned in the direction $\bar{M}$ or $\bar{M}_x$, while, $\Delta\bar{v}_{(y)}$ is the maneuver delivered by the $\dot{y}$-control that is aligned in the direction $\bar{M}_y$. The direction of the maneuvers determines how states evolve along a propagated trajectory. The components of $\bar{M}_x$ and $\bar{M}_y$ vectors vary along the underlying state transition matrix, φ_T, that is a function of the target horizon time. Consequently, at different target horizon times, there is a change in the direction of the maneuver that targets the $\dot{x}$ value and the $\dot{y}$ value, given by the $\bar{M}_x$ and $\bar{M}_y$ vectors, respectively. If the angle between the $\Delta\bar{v}_{(x)}$ in comparison to $\Delta\bar{v}_{(y)}$ are aligned perpendicular to each other, i.e., mathematically in the null space of one another, a

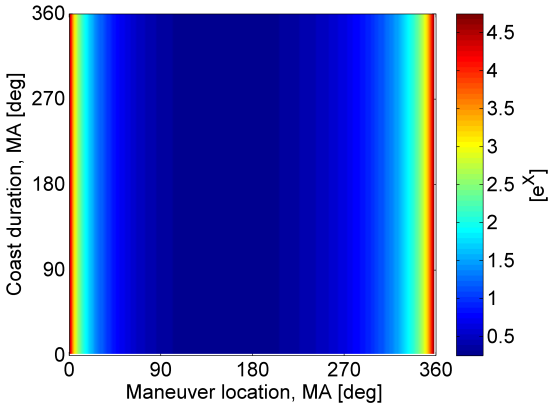

(a) Target: 1st xz plane crossing near periapsis. Measurement: Mean anomaly.

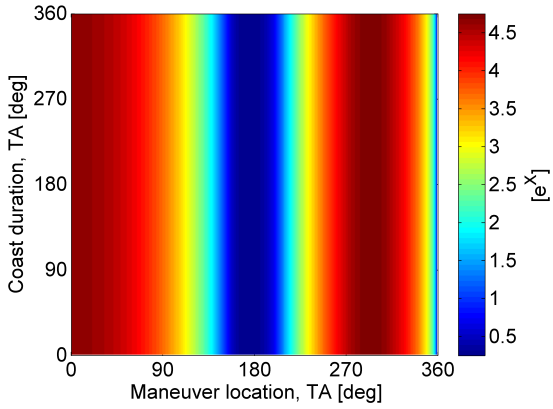

(b) Target: 1st xz plane crossing near periapsis. Measurement: Osculating true anomaly.

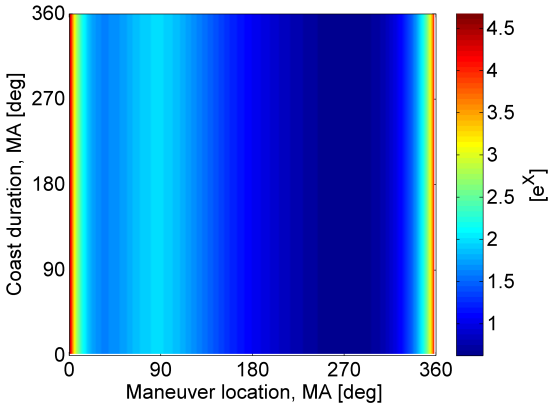

(c) Target: 2nd xz plane crossing near periapsis. Measurement: Mean anomaly.

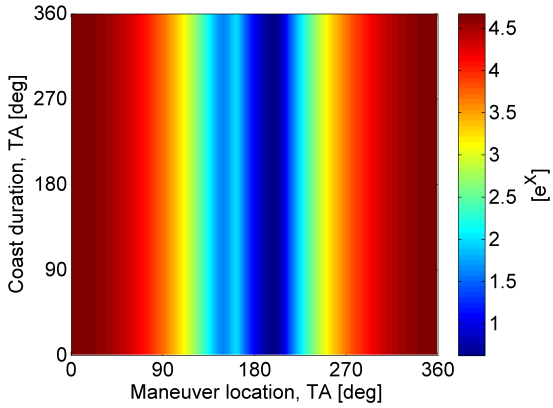

(d) Target: 2nd xz plane crossing near periapsis. Measurement: Osculating true anomaly.

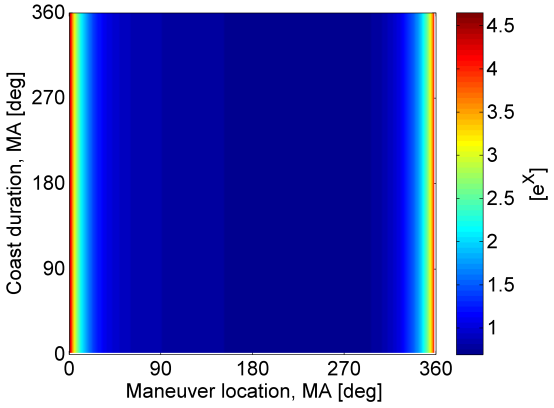

(e) Target: 7th xz plane crossing near periapsis. Measurement: Mean anomaly.

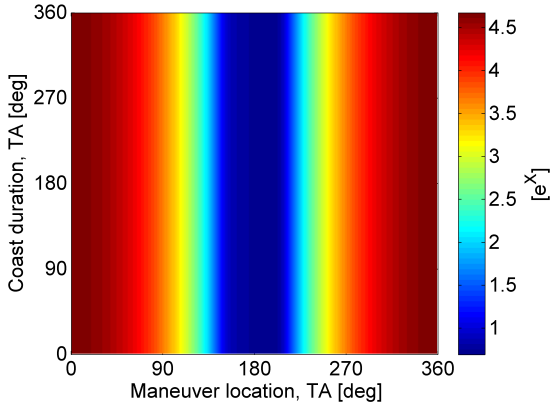

(f) Target: 7th xz plane crossing near periapsis. Measurement: Osculating true anomaly.

Figure 5.31. Ratio of maximum maneuver magnitude per magnitude of the initial state deviation, $|\bar{B}_y|/|\bar{M}_y|$, for different target horizons. Reference orbit: L2 NRHO with perilune radius 3200 km. Target: rotating $\dot{y}$ value.

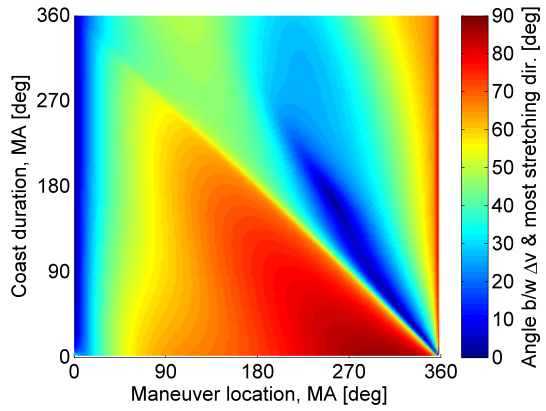

(a) Target: 1st xz plane crossing near periapsis. Measurement: Mean anomaly.

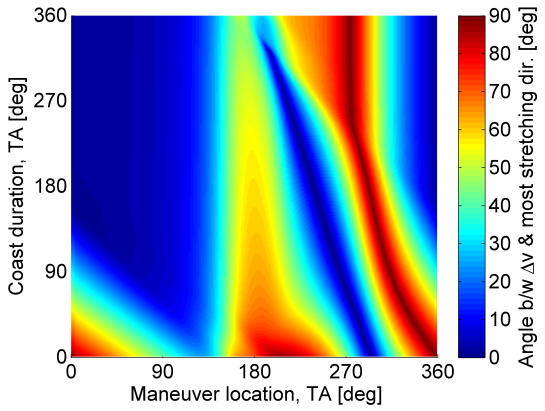

(b) Target: 1st xz plane crossing near periapsis. Measurement: Osculating true anomaly.

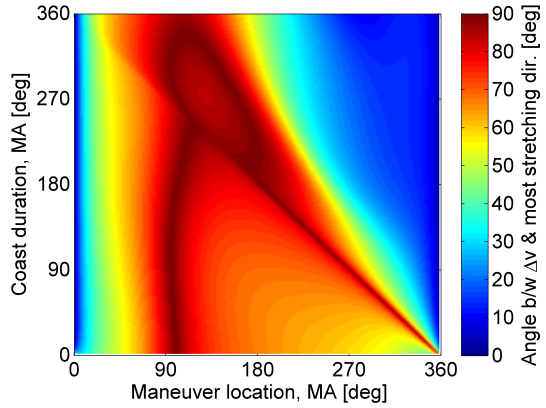

(c) Target: 2nd xz plane crossing near periapsis. Measurement: Mean anomaly.

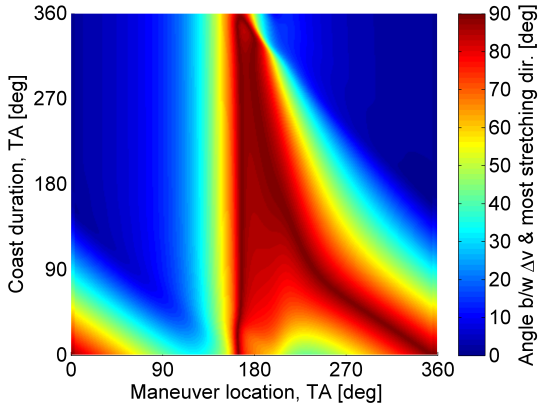

(d) Target: 2nd xz plane crossing near periapsis. Measurement: Osculating true anomaly.

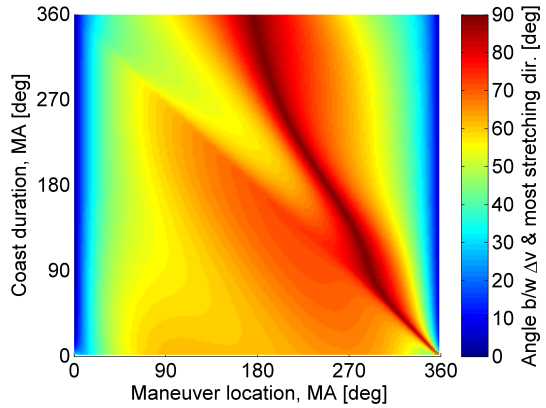

(e) Target: 7th xz plane crossing near periapsis. Measurement: Mean anomaly.

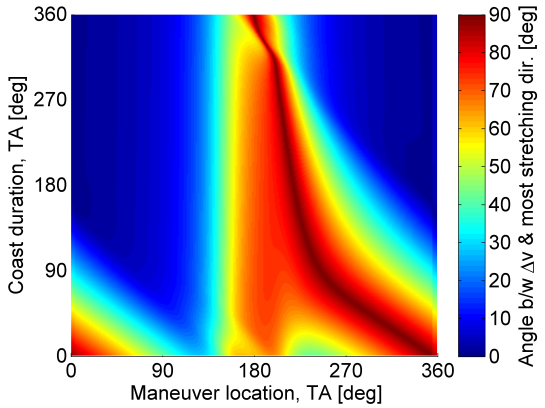

(f) Target: 7th xz plane crossing near periapsis. Measurement: Osculating true anomaly.

Figure 5.32. Estimated angle between maneuver direction, predicted by the $\dot{y}$-control, and the most stretching direction $\mathbb{V}_1(\varphi_{C,v,v})$ for different target horizons. Reference orbit: L2 NRHO with perilune radius 3200 km.

maneuver along the $\bar{M}_x$ direction does not compensate for any change in the $\dot{y}$ value, and vice versa. Depending on the type of the target condition, it is likely that the change in state measurements either in the $\dot{x}$ value or the $\dot{y}$ value increase over time, eventually the spacecraft deviates from virtual reference orbit. Alternatively, if the angle between the $\Delta\bar{v}_{(x)}$ maneuver in comparison to the $\Delta\bar{v}_{(y)}$ maneuver are aligned anti-parallel to each other, i.e., opposite to one another, correction of the $\dot{x}$ value aggravates the error in the $\dot{y}$ value, and vice versa. Such cases are not ideal for stationkeeping. Perhaps, if the angle between the maneuver that targets the $\dot{x}$ value and the $\dot{y}$ value are aligned parallel to each other, a maneuver that corrects any deviations along the $\dot{x}$ value, i.e., in the $\bar{M}_x$ direction, automatically tends to compensate for any change in the $\dot{y}$ value, and vice-versa. Such cases are suitable for stationkeeping. Figure 5.33 indicates the angle between the $\bar{M}_x$ and $\bar{M}_y$ vectors for various target horizon times, representing the angle between the maneuver that targets the $\dot{x}$ value and the $\dot{y}$ value, respectively. For shorter target horizon times, there is a larger angle between the $\bar{M}_x$ and $\bar{M}_y$ vectors, therefore the $\dot{y}$-control maneuvers does not substantially overcome the $\dot{x}$ value perturbations. Note that, in the CR3BP model, major gravitational accelerations are in the x direction, therefore perturbations along the $\dot{x}$ component increases rapidly with time if not corrected regularly. At target horizon times of 5.5 revs and 6.5 revs, the $\bar{M}_x$ and $\bar{M}_y$ vectors are almost aligned in the same direction, therefore, the $\dot{y}$-control maneuvers compensates for any $\dot{x}$ value perturbations at the xz plane crossing, making it a better option for stationkeeping.

The direction between the maneuvers $\Delta\bar{v}_{(x)}$ and $\Delta\bar{v}_{(y)}$ offers an insight into the effects of state perturbations at the target xz plane crossing, specifically, if the maneuver that targets the $\dot{y}$ value compensates for perturbation along the $\dot{x}$ values, and vice versa. However, the effect of state perturbations at the subsequent maneuver location is determined by the alignment between the maneuver direction and the stretching directions. In Figure 5.34, the angle between the maneuver computed using the $\dot{y}$-control approach, i.e., $\Delta\bar{v}_{(y)}$, with the most stretching direction is plotted for various target horizon times. For reference, the angle between the maneuver computed using the conventional x axis control algorithm, that targets the rotating $\dot{x}$ value, with the most stretching direction is also shown. For shorter

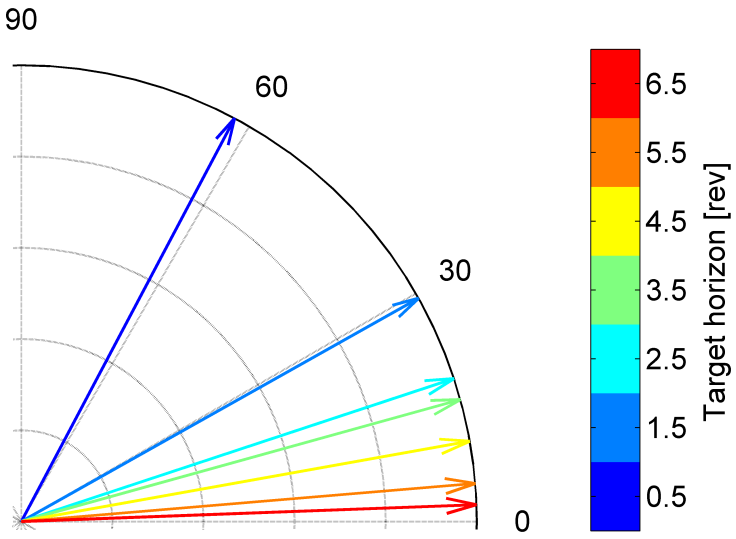

Figure 5.33. Angle between maneuver estimated by targeting the $\dot{x}$ value compared to targeting the $\dot{y}$ value for various target horizons.

target horizon such as 0.5 rev and 1.5 revs, there is a significant component of the maneuver, $\Delta\bar{v}_{(y)}$, in the most stretching direction causing growth in state perturbations over time. Shorter target horizons are not suitable for stationkeeping using the $\dot{y}$-control approach. Almost perpendicular alignment between $\Delta\bar{v}_{(y)}$ and $\mathbb{V}_1$ for longer target horizons are likely to offer better control of the spacecraft near the virtual reference trajectory, however, does not guarantee a success, rather effect of multiple parameters simultaneously affect the success of the control algorithm.

The dynamics in the CR3BP offer insight into the underlying dynamics that enables prediction of the effectiveness of a stationkeeping control strategy, however, actual simulations in the higher-fidelity ephemeris model yield actual stationkeeping performance. Red asterisks (*) in Figure 5.35 demonstrates the alignment of actual $\Delta\bar{v}_{(y)}$ with the most stretching direction in comparison to the angle predicted in the CR3BP. Of course, the figure also includes cases where the spacecraft diverged away from the reference trajectory, indicated by large dispersion from the predicted angle in the CR3BP. Nevertheless, the actual angle predicted in the higher-fidelity ephemeris model that includes orbit determination and model errors

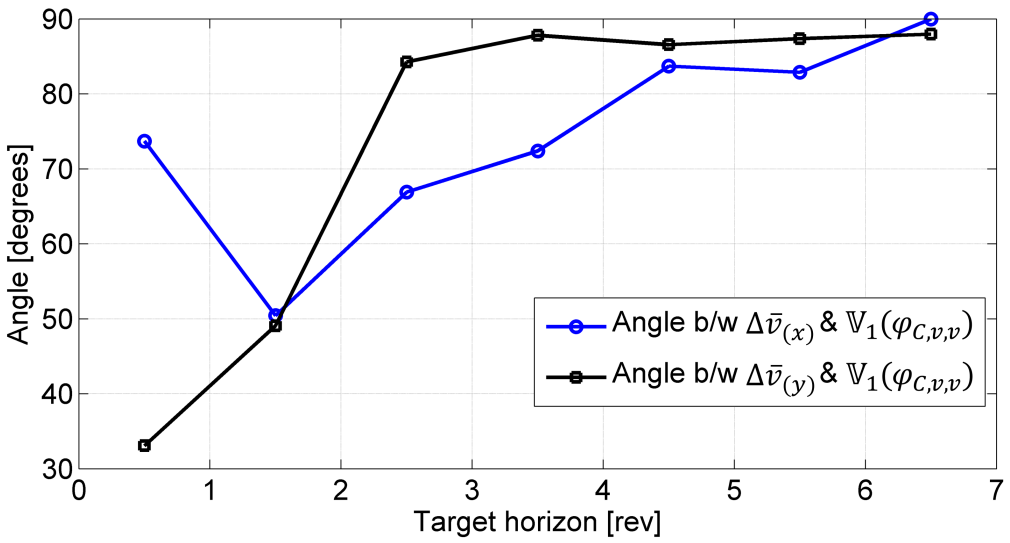

Figure 5.34. Angle between different estimated maneuvers ($\Delta\bar{v}_{(x)}$ and $\Delta\bar{v}_{(y)}$) and the most stretching direction in CR3BP for the 9:2 synodic resonant L2 NRHO with perilune radius 3200 km.

resembles the estimate in the CR3BP model. Figure 5.35 corresponds to the case with low orbit determination errors (3σ: 1 km and 1 cm/s). Similar trend is observed for high orbit determination errors (3σ: 10 km and 10 cm/s) as well, but with marginally larger dispersion and a few more diverged cases.

The annual stationkeeping costs delivered by an algorithm is a vital metric. The mean annual stationkeeping costs, $\bar{\varkappa}$, and the half width of a 95% confidence interval, $1.96\sigma_{\bar{\varkappa}}$, computed using the $\dot{y}$-control algorithm is listed in Table 5.7. A 95% confidence interval of the mean cost is thus given by $\bar{\varkappa} \pm 1.96\sigma_{\bar{\varkappa}}$. A 2.5 rev target horizon is effective for stationkeeping in cases with low ODE levels, however, does not generate enough successful trials for high ODE levels. Only if majority of the trials are successful in maintaining the spacecraft near the virtual reference solution over the simulated mission duration, it is considered a converged case. The 3.5 rev target horizon does not offer successful stationkeeping for either low ODE or high ODE. A larger $|\bar{B}_y|/|\bar{M}_y|$ ratio at the 3.5 rev target horizon in comparison to 2.5, 4.5, 5.5 and 6.5 rev may results in larger maneuver magnitude to overcome any initial perturbation and may likely cause poor stationkeeping performance. Targeting 4.5 rev xz

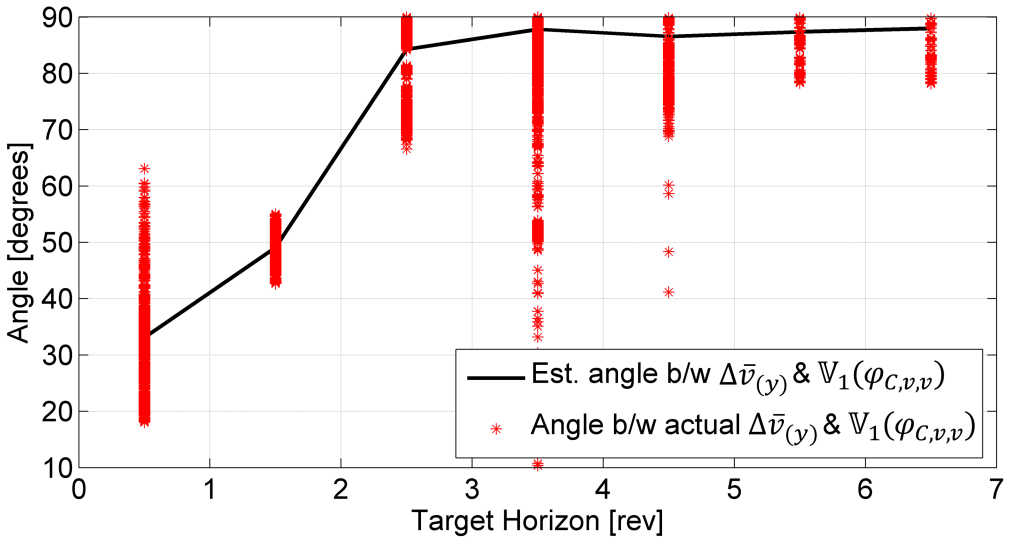

Figure 5.35. Angle between actual maneuvers, $\Delta\bar{v}_{(y)}$, and most stretching direction $\mathbb{V}_1(\varphi_{C,v,v})$ for the 9:2 synodic resonant L2 NRHO with perilune radius 3200 km. Low orbit determination error (3σ: 1 km and 1 cm/s) case.

plane crossing maintains the spacecraft near the virtual reference orbit at a higher annual cost. Stationkeeping using $\dot{y}$-control approach is effective for 5.5 revs and 6.5 revs target and offers comparable results to the conventional x axis crossing control algorithm for both low and high orbit determination error levels.

An effective stationkeeping strategy ensures that a consistent maneuver is generated over time and the spacecraft does not deviate rapidly from the baseline trajectory. The maneuver history for the $\dot{y}$-control algorithm, that targets the $\dot{y}$ value at the xz plane crossing, as well as the deviation history measured at the apoapsis location, for a target horizon time of 6.5 revs, are demonstrated in Figures 5.36(a) and 5.36(b), respectively. The maneuver history and the deviation history are represented in box plot, such that the upper limit the box corresponds to the 75^{th} percentile distribution. The width of the box corresponds to the intermediate 50% distribution. The maneuver magnitude is consistently under 1 cm/s for the range of simulated mission duration, for case with low ODE levels. The deviation history indicates that the spacecraft is well bounded near the virtual reference solution for the simulated duration. A similar trend in maneuver history and deviation history is measured

Table 5.7. Estimated mean annual orbit maintenance cost and half width of 95% confidence interval ($1.96\sigma_{\bar{\varkappa}}$) measured in [m/s] for both low and high orbit determination error levels. Algorithm: $\dot{y}$-control.

Target Horizon [rev]	Low ODE		High ODE	
	Mean, $\bar{\varkappa}$	$1.96\sigma_{\bar{\varkappa}}$	Mean, $\bar{\varkappa}$	$1.96\sigma_{\bar{\varkappa}}$
0.5	DNC	DNC	DNC	DNC
1.5	DNC	DNC	DNC	DNC
2.5	2.33	0.32	DNC	DNC
3.5	DNC	DNC	DNC	DNC
4.5	1.19	0.18	9.86	1.51
5.5	0.15	0.00	1.06	0.07
6.5	0.15	0.00	1.21	0.09

* DNC - Did not converge

for high ODE levels that target the 5.5 rev and 6.5 rev xz plane crossing.

A stationkeeping strategy that targets the $\dot{y}$ value at the xz plane crossing is demonstrated. Certain target horizons are conducive to stationkeeping. It is observed that at 5.5 rev and 6.5 rev target horizon, the direction of the $\dot{y}$-control approach is aligned with the maneuver computed using the conventional x axis crossing control approach. Due to such correlation, the maneuver that targets the $\dot{y}$ value automatically compensates for the $\dot{x}$ value, and vice versa. The success of the conventional x axis control at 6.5 rev target horizon is also attributed to the correlation with the $\dot{y}$-control algorithm, as the maneuver compensates for the $\dot{y}$ along with targeting the rotating $\dot{x}$ value.

5.6.3 Direction-constrained maneuvers

Mission specifications and spacecraft attitude configurations may require maneuvers to be delivered along a certain direction. These direction-constrained stationkeeping maneuvers meet the same targeting conditions downstream similar to the conventional algorithm. In this investigation, stationkeeping maneuvers computed by targeting the rotating $\dot{x}$ value at various xz plane crossings are constrained to exist in a specific direction given by unit

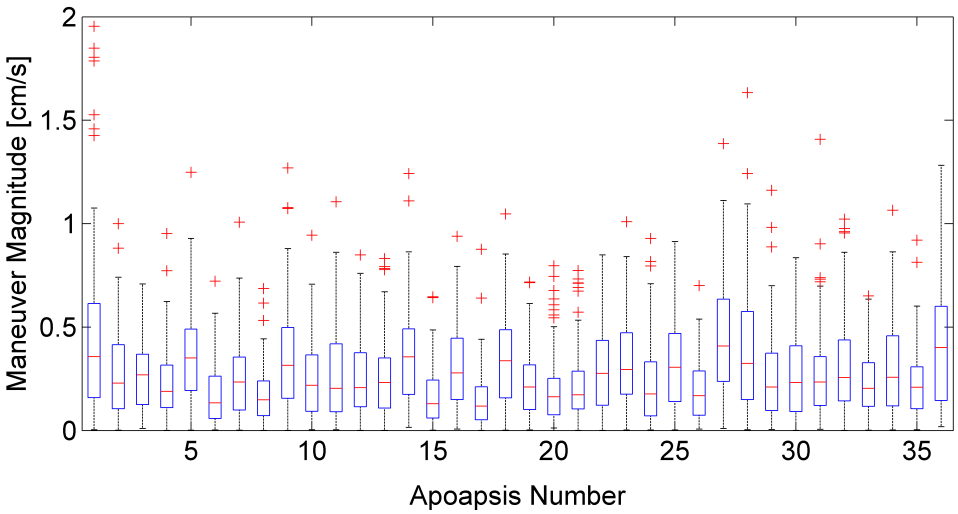

(a) Maneuver history.

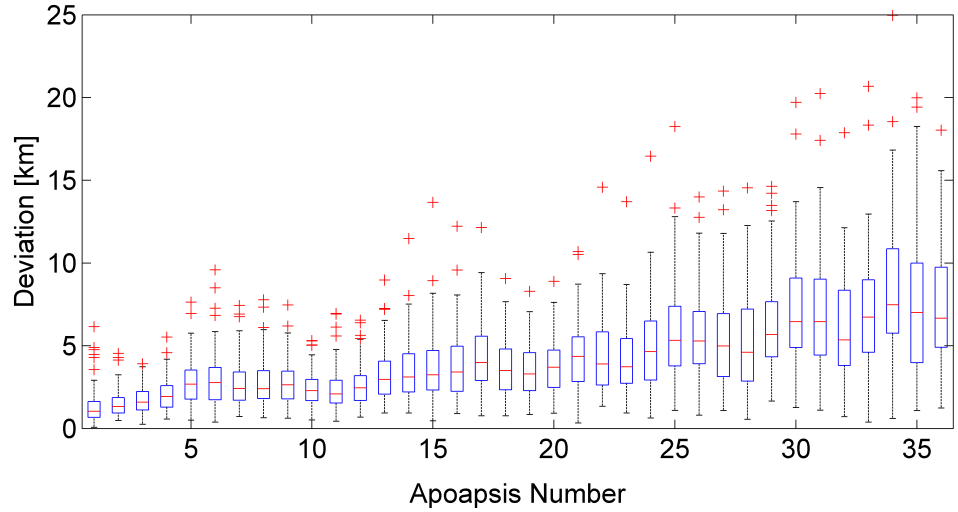

(b) Deviation history.

Figure 5.36. Stationkeeping performance using $\dot{y}$-control approach that targets the 6.5 rev xz plane crossing. Reference orbit: L2 NRHO with perilune radius 3200 km.

vector $\hat{K}$. For convenience, the direction-constrained maneuvers are labelled as $\Delta\bar{v}_{[\hat{K}]}$ that are parallel or anti-parallel to the direction $\hat{K}$. Here, unit vector $\hat{K}$ represents some specific directions that may be either of the rotating co-ordinate frame directions, $\hat{x}$, $\hat{y}$, or $\hat{z}$, Vehicle Local Coordinate Axes in the velocity $\hat{V}$, normal $\hat{N}$, or co-normal $\hat{C}$ directions, or any other

mission specific directions. The direction-constrained maneuvers are computed from the x-axis control approach by modifying the target equation (5.9), such as

$$\Delta\dot{x}_f = \begin{bmatrix} \varphi_{T,44} & \varphi_{T,45} & \varphi_{T,46} \end{bmatrix} \Delta\bar{v}_0 = \begin{bmatrix} \varphi_{T,44} & \varphi_{T,45} & \varphi_{T,46} \end{bmatrix} \begin{bmatrix} \Delta\dot{x}_0 \\ \Delta\dot{y}_0 \\ \Delta\dot{z}_0 \end{bmatrix} \tag{5.20}$$

where $\Delta\bar{v}_0$ is aligned along any $\hat{K}$-direction, i.e., $\Delta\bar{v}_0 \Leftrightarrow \Delta\bar{v}_{[\hat{K}]}$. By incorporating different direction constraints the corresponding maneuver directions and magnitudes are modified, some of which are detailed. Maneuvers that may be aligned in either of the rotating coordinate directions are computed directly from the corresponding elements of the state transition matrix, φ_T, such that

- $\hat{x}$-direction maneuvers

$$\Delta\dot{x}_f = \begin{bmatrix} \varphi_{T,44} \end{bmatrix} \begin{bmatrix} \Delta\dot{x}_0 \end{bmatrix}, \quad \Delta\dot{y}_0 = 0, \quad \Delta\dot{z}_0 = 0 \tag{5.21}$$

- $\hat{y}$-direction maneuvers

$$\Delta\dot{x}_0 = 0, \quad \Delta\dot{x}_f = \begin{bmatrix} \varphi_{T,45} \end{bmatrix} \begin{bmatrix} \Delta\dot{y}_0 \end{bmatrix}, \quad \Delta\dot{z}_0 = 0 \tag{5.22}$$

- $\hat{z}$-direction maneuvers

$$\Delta\dot{x}_0 = 0, \quad \Delta\dot{y}_0 = 0, \quad \Delta\dot{x}_f = \begin{bmatrix} \varphi_{T,46} \end{bmatrix} \begin{bmatrix} \Delta\dot{z}_0 \end{bmatrix} \tag{5.23}$$

Similarly, Vehicle Local Coordinate Axes defined by the Velocity Normal Co-normal (VNC) Frame may also offer an appropriate choice for delivering stationkeeping maneuvers. The directions in the VNC frame are derived quantities that require transitioning from the rotating coordinate frame. Since the NRHOs have close proximity to the Moon, the local dynamics represented in the Vehicle Local Coordinate Axes is measured relative to the Moon as the

central observing body. The coordinate frame transformation between the rotating frame and the VNC frame is given by the following equations,

$$\hat{V} = \frac{\bar{v}_0}{||\bar{v}_0||} \tag{5.24}$$

$$\hat{\Upsilon} = \frac{\bar{r}_0 - \bar{r}_{Moon}}{||\bar{r}_0 - \bar{r}_{Moon}||} \tag{5.25}$$

$$\hat{N} = \hat{V} \times \hat{\Upsilon} \tag{5.26}$$

$$\hat{C} = \hat{V} \times \hat{N} \tag{5.27}$$

where $\bar{r}_{Moon} = [1-\mu, 0, 0]^{\mathrm{T}}$ is the translational quantity in non-dimensional units. Here, $\bar{r}_0$ and $\bar{v}_0$ are position and velocity vectors of the spacecraft along the NRHO in the rotating coordinate frame centered at the Earth-Moon barycenter. Of course, the VNC frame changes its orientation continuously along the NRHO, however, for maneuvers delivered at the apoapsis, the orientation of the VNC frame relative to the rotational frame at the apoapsis as described in Figure 5.37 offers insight. Figure 5.37 corresponds to the 9:2 synodic resonant southern L2 NRHO, that is the current baseline for NASA's Gateway mission. For ease of understanding, the vectors that almost point in the same directions are colored in pairs, i.e., $\hat{V}$-direction and $\hat{y}$-direction are anti-parallel and thus colored in red, $\hat{C}$-direction and $\hat{z}$-direction colored in green, and finally, $\hat{N}$-direction and $\hat{x}$-direction are similar and thus colored in black. The dotted axes represents the VNC frame while solid bold lines represents vectors in the rotating coordinate frame. A maneuver in either of $\hat{V}\hat{N}\hat{C}$ directions is perpendicular to the other two directions, as a result dot product with the two orthogonal directions are zero. The concept is leveraged to compute maneuvers along a specific VNC frame direction in the following equations,

- $\hat{V}$-direction maneuvers

$$\begin{bmatrix} \Delta\dot{x}_f \\ 0 \\ 0 \end{bmatrix} = \begin{bmatrix} \varphi_{T,44} & \varphi_{T,45} & \varphi_{T,46} \\ & \hat{N}^{\mathrm{T}} & \\ & \hat{C}^{\mathrm{T}} & \end{bmatrix} \Delta\bar{v}_0 = \begin{bmatrix} \varphi_{T,44} & \varphi_{T,45} & \varphi_{T,46} \\ & \hat{N}^{\mathrm{T}} & \\ & \hat{C}^{\mathrm{T}} & \end{bmatrix} \begin{bmatrix} \Delta\dot{x}_0 \\ \Delta\dot{y}_0 \\ \Delta\dot{z}_0 \end{bmatrix} \tag{5.28}$$

- $\hat{N}$-direction maneuvers

$$\begin{bmatrix} \Delta\dot{x}_f \\ 0 \\ 0 \end{bmatrix} = \begin{bmatrix} \varphi_{T,44} & \varphi_{T,45} & \varphi_{T,46} \\ & \hat{V}^{\mathrm{T}} & \\ & \hat{C}^{\mathrm{T}} & \end{bmatrix} \Delta\bar{v}_0 = \begin{bmatrix} \varphi_{T,44} & \varphi_{T,45} & \varphi_{T,46} \\ & \hat{V}^{\mathrm{T}} & \\ & \hat{C}^{\mathrm{T}} & \end{bmatrix} \begin{bmatrix} \Delta\dot{x}_0 \\ \Delta\dot{y}_0 \\ \Delta\dot{z}_0 \end{bmatrix} \tag{5.29}$$

- $\hat{C}$-direction maneuvers

$$\begin{bmatrix} \Delta\dot{x}_f \\ 0 \\ 0 \end{bmatrix} = \begin{bmatrix} \varphi_{T,44} & \varphi_{T,45} & \varphi_{T,46} \\ & \hat{V}^{\mathrm{T}} & \\ & \hat{N}^{\mathrm{T}} & \end{bmatrix} \Delta\bar{v}_0 = \begin{bmatrix} \varphi_{T,44} & \varphi_{T,45} & \varphi_{T,46} \\ & \hat{V}^{\mathrm{T}} & \\ & \hat{N}^{\mathrm{T}} & \end{bmatrix} \begin{bmatrix} \Delta\dot{x}_0 \\ \Delta\dot{y}_0 \\ \Delta\dot{z}_0 \end{bmatrix} \tag{5.30}$$

Maneuvers along any of the $\hat{V}\hat{N}\hat{C}$ directions may be beneficial from the operations perspective. Mathematical considerations yield maneuvers that lie along the *restoring plane* and offer less rapid departure. Note that the restoring plane exists only if the dimension of the stretching subspace is one. The maneuvers in the restoring plane are likely to offer relatively better stationkeeping performance than the cases where the maneuvers have significant component in the most stretching directions. The maneuvers in the restoring plane directions are computed from a mathematical outlook and may not have any direct correlation to the operational point-of-view. The maneuver satisfies two equations simultaneously,

$$\begin{bmatrix} \Delta\dot{x}_f \\ 0 \end{bmatrix} = \begin{bmatrix} \varphi_{T,44} & \varphi_{T,45} & \varphi_{T,46} \\ & \mathbb{V}_1(\varphi_{C,v,v})^{\mathrm{T}} & \end{bmatrix} \Delta\bar{v}_0 = \begin{bmatrix} \varphi_{T,44} & \varphi_{T,45} & \varphi_{T,46} \\ & \mathbb{V}_1(\varphi_{C,v,v})^{\mathrm{T}} & \end{bmatrix} \begin{bmatrix} \Delta\dot{x}_0 \\ \Delta\dot{y}_0 \\ \Delta\dot{z}_0 \end{bmatrix} \tag{5.31}$$

one that targets the rotating $\dot{x}_f$ value and the other that meets the direction-constraints. The formulation considers that any maneuvers in the restoring plane are orthogonal to the maximum stretching direction. Fine tuning on the orientation between the maneuver and

the restoring directions, if they exists, are a choice. Define, α_2 and α_3 as scalar weights that influences the maneuvers to lie along a preferred direction, such that,

$$\Delta\bar{v}_0 = \alpha_2\mathbb{V}_2 + \alpha_3\mathbb{V}_3 \tag{5.32}$$

that is solved along the with conventional x-axis crossing control scheme, such as,

$$\begin{bmatrix} \Delta\dot{x}_f \\ \bar{0}_{3\times1} \end{bmatrix} = \begin{bmatrix} \varphi_{T,44} & \varphi_{T,45} & \varphi_{T,46} & 0 & 0 \\ & I_{3\times3} & & -\mathbb{V}_2 & -\mathbb{V}_3 \end{bmatrix} \begin{bmatrix} \Delta\bar{v}_0 \\ \alpha_2 \\ \alpha_3 \end{bmatrix} \tag{5.33}$$

$$= \begin{bmatrix} \varphi_{T,44} & \varphi_{T,45} & \varphi_{T,46} & 0 & 0 \\ & I_{3\times3} & & -\mathbb{V}_2 & -\mathbb{V}_3 \end{bmatrix} \begin{bmatrix} \Delta\dot{x}_0 \\ \Delta\dot{y}_0 \\ \Delta\dot{z}_0 \\ \alpha_2 \\ \alpha_3 \end{bmatrix} \tag{5.34}$$

where the two additional unknown quantities α_2 and α_3 are evaluated along with the three scalar components of the maneuver. The equations for direction-constrained maneuvers only offer a mathematical solution that may or may not be conducive for stationkeeping. Maneuvers may be constrained along any other directions as per the missions requisites, an alternate equation governs such a constraint and may be formulated in the same manner.

Stationkeeping maneuvers are computed by targeting the rotating $\dot{x}$ value at specific xz plane crossings downstream. As discussed, the flow from the maneuver location and the target determines the magnitude and direction of the maneuver. With no additional constraints, other than targeting the rotating $\dot{x}$ value and $y = 0$ at the xz plane crossing, by convention, a minimum norm approach yields a solution that minimizes the propellant cost. A minimum norm solution is effective for stationkeeping for several target horizon times. As the direction of the maneuvers are constrained, consequently the magnitude of the maneuvers

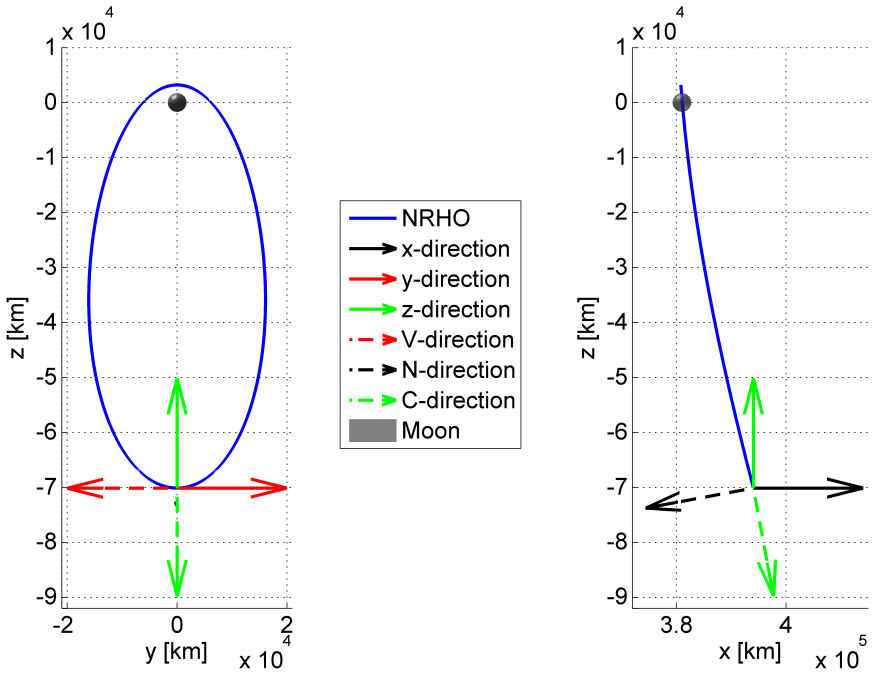

Figure 5.37. $\hat{V}\hat{N}\hat{C}$ directions and $\hat{x}\hat{y}\hat{z}$ directions along an NRHO, at apoapsis.

are altered to meet the target conditions. Let the direction of the maneuver be constrained in the direction $\hat{\mathcal{K}}$, representative of any of the $\hat{x}$, $\hat{y}$, $\hat{z}$, $\hat{V}$, $\hat{N}$, $\hat{C}$ directions and the restoring plane (the column space of vectors $\mathbb{V}_2 - \mathbb{V}_3$). The direction $\hat{\mathcal{K}}$ may also represent any other directions as required. Recall equation 5.10 that determines the magnitude of the maneuver for the x-axis control stationkeeping,

$$|\Delta\dot{x}_f| = |\bar{M}||\Delta\bar{v}_0|\ cos\vartheta \quad \longrightarrow \quad |\Delta\bar{v}_0| = \frac{|\Delta\dot{x}_f|}{|\bar{M}|\ cos\vartheta} \tag{5.35}$$

where the parameter $cos\vartheta$ is set to 1 to identify the maneuver with the smallest magnitude in the conventional approach, i.e., the minimum norm maneuver. Once the direction of the maneuver is fixed, the value of the parameter $cos\vartheta$ is no longer 1, and the change in the value of $cos\vartheta$ affects the maneuver magnitude. Consider the ratio of maneuver magnitude for the maneuver along the direction $\hat{\mathcal{K}}$ to the minimum norm solution as

$$\frac{|\Delta\bar{v}_0|_{\hat{\mathcal{K}}}}{|\Delta\bar{v}_0|_{min-norm}} = \frac{1}{cos\vartheta} \tag{5.36}$$

where, $|\Delta\bar{v}_0|_{\hat{\mathcal{K}}}$ is the magnitude for maneuver that is constrained along the $\hat{\mathcal{K}}$ direction. The angle ϑ is the measured between the $\hat{\mathcal{K}}$ direction and the $\hat{M}$ direction (the direction along minimum norm solution is computed). Figure 5.38 demonstrates the value of angle ϑ with respect to different directions along which maneuvers may be constrained. Certain directions, such as the $\hat{z}$ and $\hat{C}$ directions have a significant the angle to the minimum norm solution at multiple target horizons, while any maneuvers in the $\hat{x}$ and $\hat{N}$ directions have only small change in angle from a minimum norm maneuver especially at longer target horizons. More importantly, the value $1/cos\vartheta$ is the amplification in the maneuver magnitude that is constrained along the $\hat{\mathcal{K}}$ direction as opposed to the one that minimizes the propellant cost. Figure 5.39 illustrates the value $1/cos\vartheta$ for maneuvers along different directions. Not surprisingly, maneuver directions with smaller angle ϑ in Figure 5.38, results in little amplification in amplification in maneuver magnitude as in Figure 5.39. In contrast, maneuver along directions with very large angle ϑ, such as the maneuvers along the $\hat{y}$ and the $\hat{V}$ directions for 2.5 revs target horizon, generates a large maneuver magnitude compared to the minimum norm solution that targets hte same target horizon. Similarly, maneuvers along the $\hat{z}$ and the $\hat{C}$ directions consistently produce larger maneuver magnitudes, almost 5 to 10 times larger than their minimum norm counterpart. Figure 5.39 assists in identification of the effects of constraining the maneuver direction on the maneuver costs.

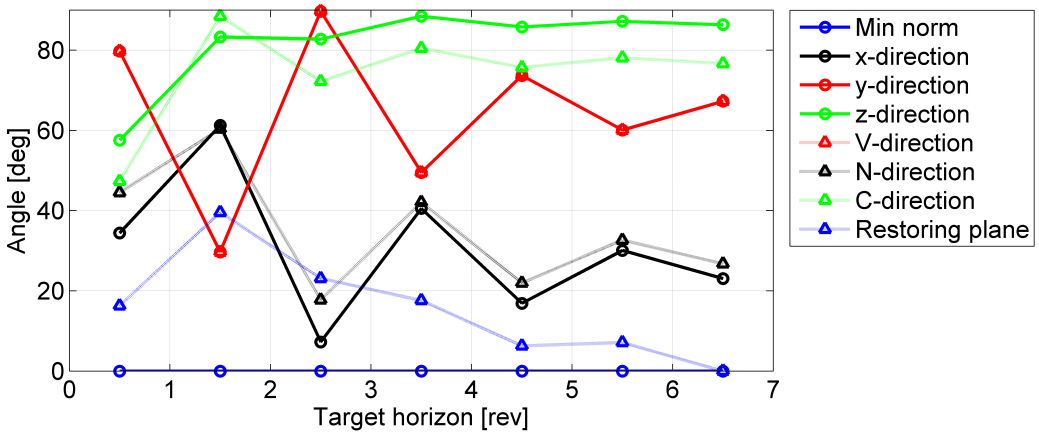

Figure 5.38. Angle between direction-constrained maneuvers and minimum norm maneuver.

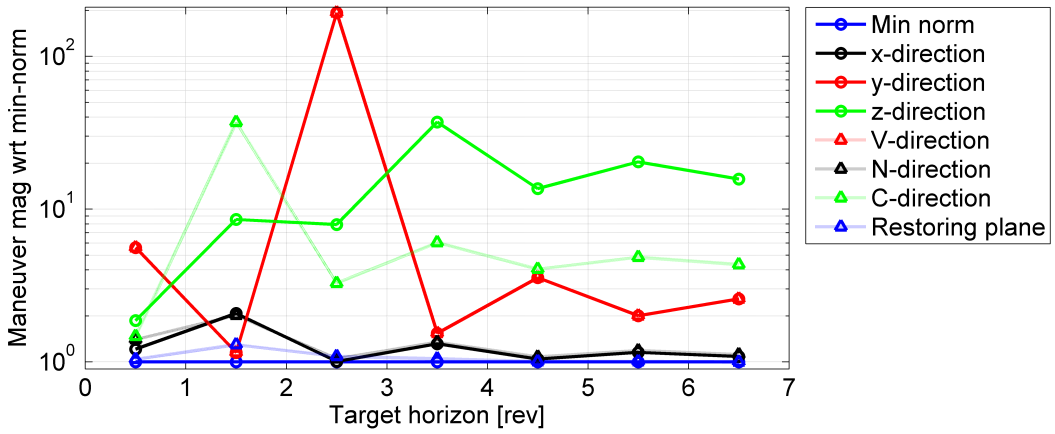

Figure 5.39. Direction-constrained maneuver magnitude relative to the minimum norm maneuver.

The effects of constraining maneuver directions on the stationkeeping maneuver costs are identified by inspecting the angle between the constrained maneuver direction to the direction of the minimum norm solution, i.e., the $\hat{M}$ direction (the components of the vector $\bar{M}$ are elements of the linear STM from the maneuver location to the target). The boundedness of the spacecraft near the reference orbit is also an important aspect of stationkeeping. Such effects are monitored by identifying the direction between the maneuver, $\hat{\mathcal{K}}$, and the maximum stretching direction, $\mathbb{V}_1$. Of course, this is applicable to maneuvers that are constrained along any $\hat{\mathcal{K}}$ direction. Figure 5.40 demonstrates the angle between various direction-constrained maneuvers and the maximum stretching direction. Not surprisingly, the maneuvers in the restoring plane are perpendicular to the maximum stretching direction. For maneuvers that are fixed along any $\hat{\mathcal{K}}$ direction, the angle between the maneuver and the maximum stretching direction remains a constant for any target horizon. Maneuvers along $\hat{x}$, $\hat{z}$, $\hat{N}$ and $\hat{C}$ directions have a significant component away from the maximum stretching direction in contrast to maneuvers along $\hat{y}$ and $\hat{V}$ directions.

Analyses in the CR3BP, along the dynamical flow near a reference NRHO offers significant information on the behavior of certain maneuver types. Figure 5.39 offers insight on the magnitude of direction-constrained maneuvers while Figure 5.40 reflects on the behavior of a trajectory in the vicinity of the reference orbit with maneuvers aligned in specific direc-

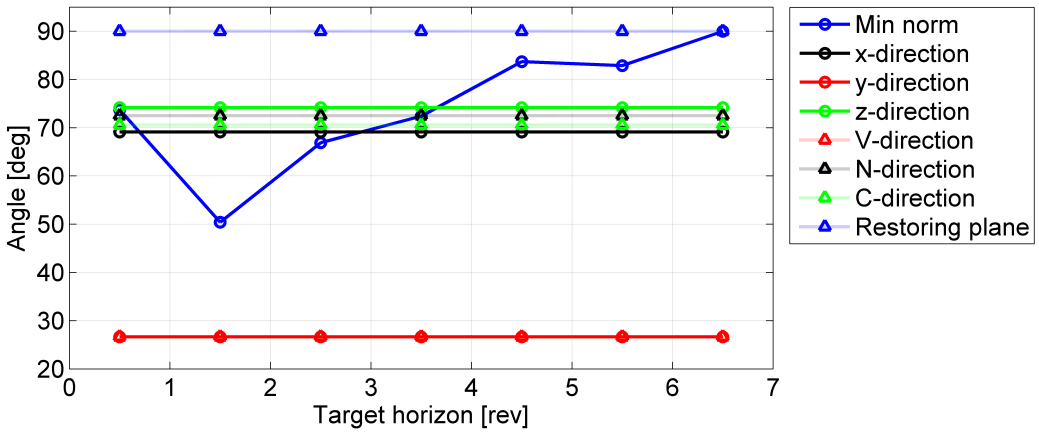

Figure 5.40. Angle between direction-constrained maneuvers and the maximum stretching direction.

tions. Of course, each of Figures 5.39 and 5.40 aid in understanding the dynamical flow in the CR3BP model, actual stationkeeping operations are performed in more complex environments with additional gravitational and non-gravitational forces. Figure 5.41 illustrates the alignment of the stationkeeping maneuvers that are constrained along each of the $\hat{V}\hat{N}\hat{C}$ directions in the higher-fidelity ephemeris model with respect to the maximum stretching directions, for a range of target horizons. Unlike in the CR3BP, the angle between the maneuver direction and the maximum stretching direction is no longer a constant, instead, a range of values are observed. Despite the dispersion in the angle between the maneuvers and the maximum stretching direction in the ephemeris model, the effects predicted in the CR3BP, as in Figure 5.40, still demonstrate the underlying dynamics. To further understand the behavior of the direction-constrained maneuvers, consider sample stationkeeping cases simulated for maneuvers constrained along each of the $\hat{V}\hat{N}\hat{C}$ directions for the 9:2 synodic resonant southern L2 NRHO. These sample cases are simulated for 6.5 rev target horizon. Figure 5.42 describes the orientation of the maneuvers in the configuration space. The maneuvers are scaled appropriately across each subplots for comparison. The magnitude of stationkeeping maneuvers constrained along each of the $\hat{V}\hat{N}\hat{C}$ directions are illustrated in Figure 5.43. The observations in Figure 5.43 are synonymous to the predictions in Figure 5.39. Maneuvers constrained in the normal $\hat{N}$ direction that is closely aligned with the minimum norm solution (maneuvers generated through minimum norm solution is along

the $\hat{M}$ direction) generates a smaller $\Delta\bar{v}$ in comparison to maneuvers constrained in the $\hat{V}$ and $\hat{C}$ directions. Again, maneuvers along the $\hat{V}$ directions are of relatively smaller magnitudes compared to maneuvers in the $\hat{C}$ directions. Such behavior observed in the plots in Figure 5.43 are reflected in Figure 5.39. Further, the effect of the direction-constrained maneuvers on the spacecraft boundedness near the reference trajectory are demonstrated in Figure 5.44 for maneuvers constrained along each of the $\hat{V}\hat{N}\hat{C}$ directions. Among the three cases, spacecraft experiences a larger deviation over time when maneuvers are constrained along the $\hat{V}$ direction. State changes along the $\hat{V}$ direction experiences larger stretching till the subsequent maneuver location due to close alignment of the maneuvers in the $\hat{V}$ direction with the maximum stretching direction, as reflected in Figure 5.40. The angle between each of the $\hat{N}$ and $\hat{C}$ direction, and the maximum stretching direction is comparable, consequently the actual spacecraft deviations for stationkeeping cases simulated are comparable. The Figures 5.43 and 5.44 are maneuver history and deviation history, respectively, recorded for stationkeeping simulations with low orbit determination errors, and follow the behavior predicted in the CR3BP as in Figures 5.39 and 5.40. As the orbit determination error levels are increased, behavior in the ephemeris model start to deviate away from the predictions in the CR3BP.

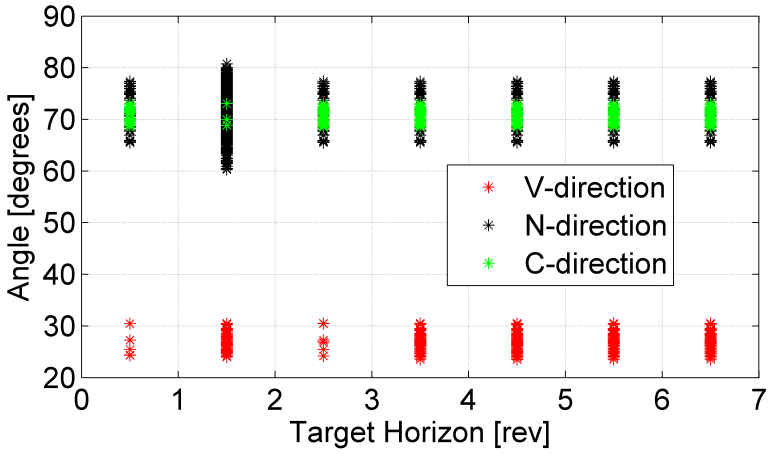

Figure 5.41. Actual angles between maneuvers along each of $\hat{V}\hat{N}\hat{C}$ directions and the maximum stretching directions along the 9:2 synodic resonant NRHO. Target horizon: 6.5 revs downstream. Low orbit determination error (3σ: 1 km and 1 cm/s) case.

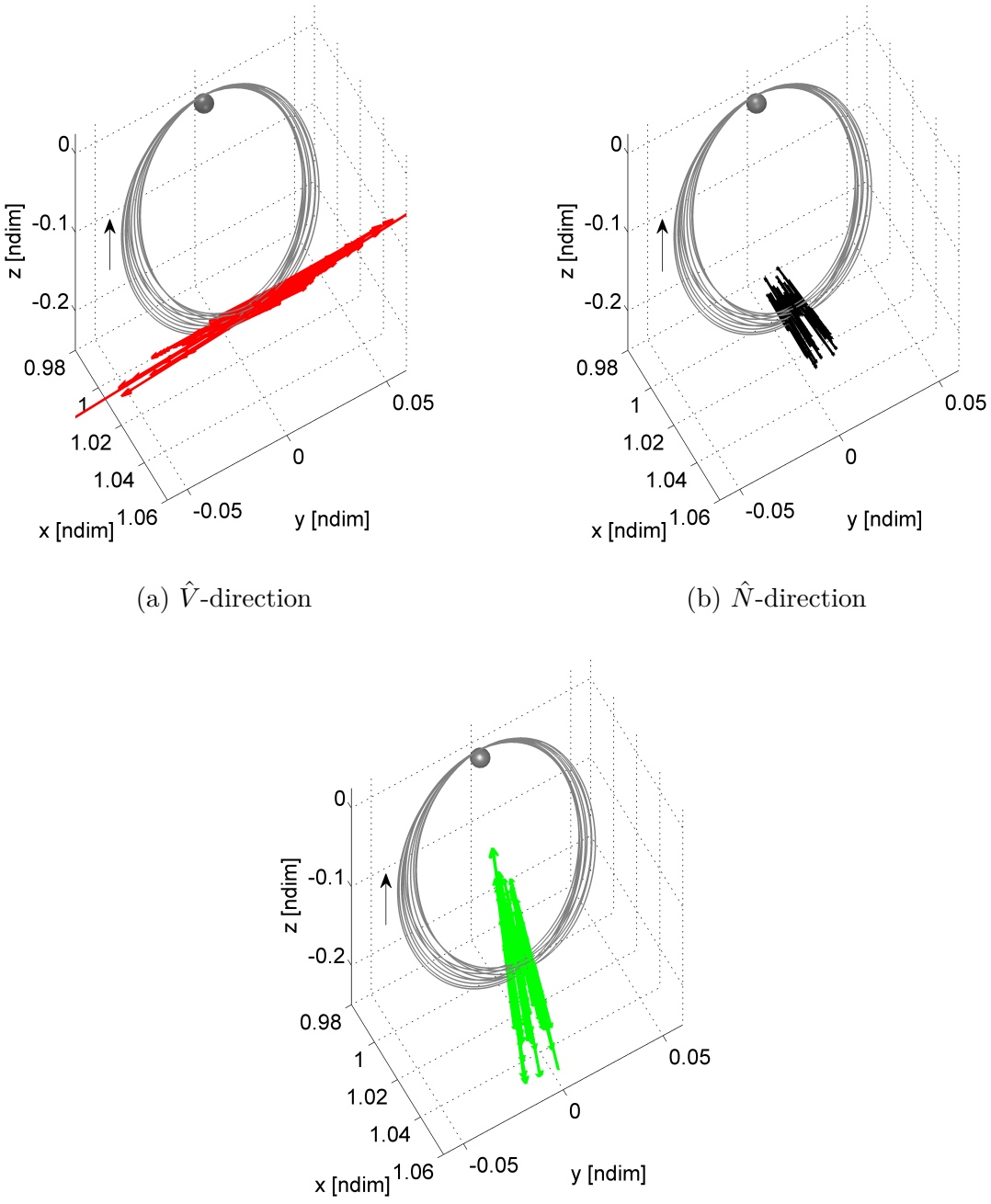

(a) $\hat{V}$-direction

(b) $\hat{N}$-direction

(c) $\hat{C}$-direction

Figure 5.42. Maneuvers along each of $\hat{V}\hat{N}\hat{C}$ directions in the configuration space. Target: 6.5 rev xz plane crossing. Reference orbit: L2 NRHO with perilune radius 3200 km. Low orbit determination error (3σ: 1 km and 1 cm/s) case.

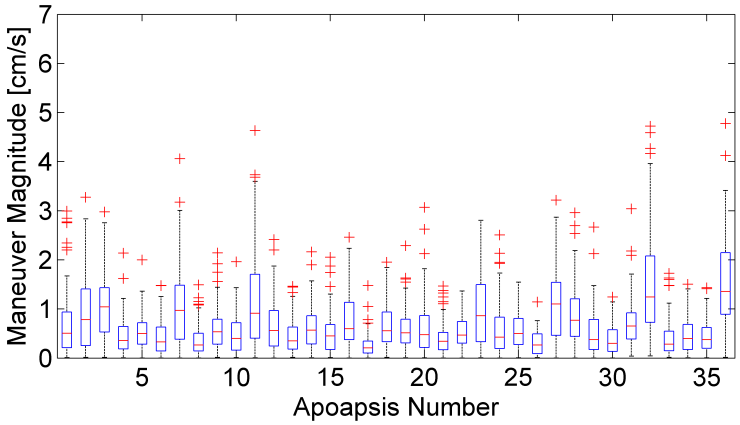

(a) Maneuvers along $\hat{V}$-direction

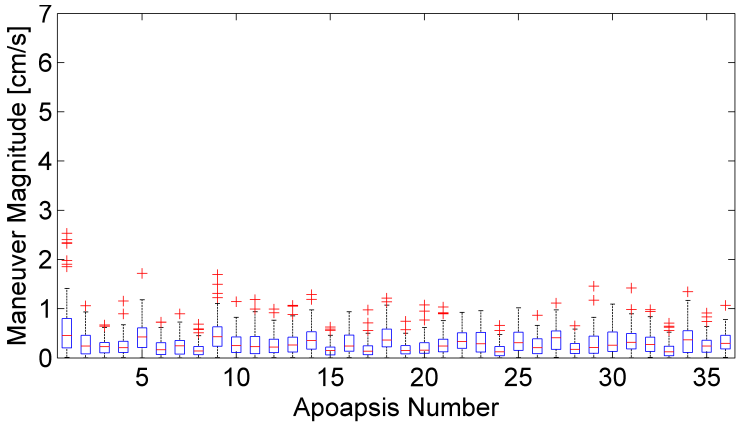

(b) Maneuvers along $\hat{N}$-direction

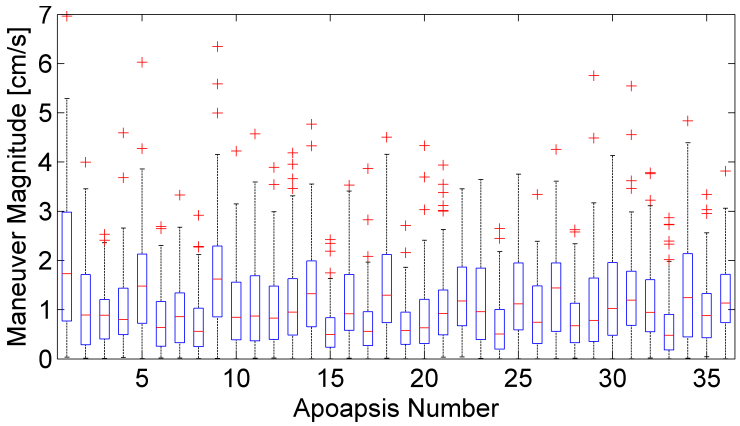

(c) Maneuvers along $\hat{C}$-direction

Figure 5.43. Stationkeeping maneuver history for direction constrained maneuvers along each of $\hat{V}\hat{N}\hat{C}$ directions that targets the 6.5 rev xz plane crossing. Reference orbit: L2 NRHO with perilune radius 3200 km. Low orbit determination error (3σ: 1 km and 1 cm/s) case.

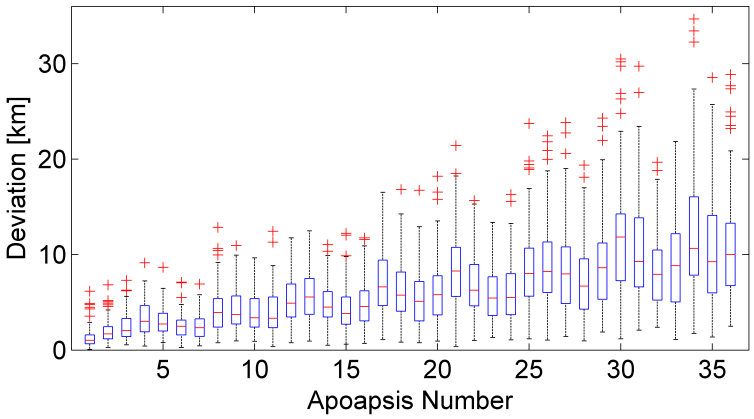

(a) Maneuvers along $\hat{V}$-direction

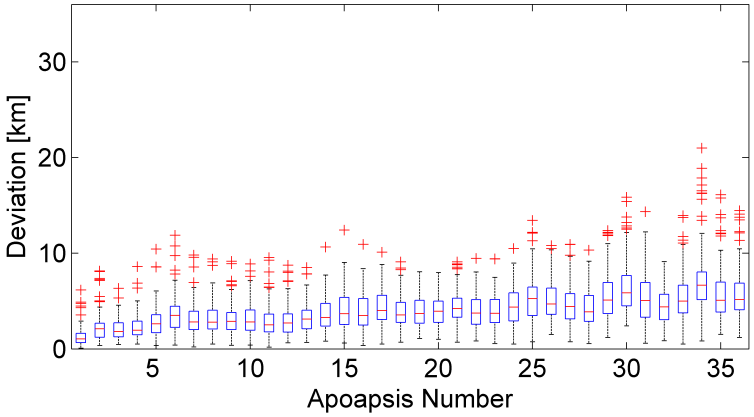

(b) Maneuvers along $\hat{N}$-direction

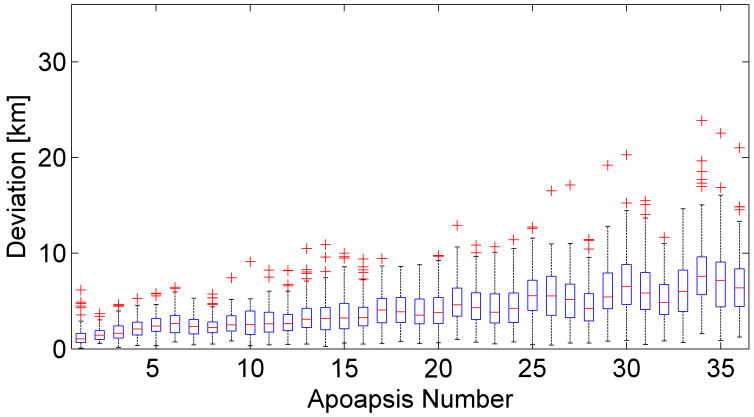

(c) Maneuvers along $\hat{C}$-direction

Figure 5.44. Deviation history for direction constrained maneuvers along each of $\hat{V}\hat{N}\hat{C}$ directions that targets the 6.5 rev xz plane crossing. Reference orbit: L2 NRHO with perilune radius 3200 km. Low orbit determination error (3σ: 1 km and 1 cm/s) case.

Direction-constrained maneuvers may or may not be conducive for stationkeeping. Certain directions that are closely aligned with the $\hat{M}$ direction (directions along the minimum norm solution) are likely to generate maneuvers of smaller magnitude to meet the target conditions. Similarly, maneuvers along certain directions that are closely aligned to the maximum stretching direction experience rapid departure from the reference trajectory over time. Any direction that is closely aligned with the $\hat{M}$ direction and orthogonal to the maximum stretching direction simultaneously is among the most suitable directions for stationkeeping maneuver. Such are the cases for maneuvers generated using the conventional minimum norm solutions at longer target horizons (2.5 revs to 6.5 revs), as well as maneuvers constrained along the $\hat{x}$ and/or $\hat{N}$ direction, again for longer target horizons (2.5 revs to 6.5 revs). In summary, stationkeeping costs for the 9:2 synodic resonant southern L2 NRHO simulated for various direction-constrained maneuvers with low and high orbit determination error levels are listed in Tables 5.8 and 5.9, respectively. As discussed, certain directions are conducive for stationkeeping and thus produce low stationkeeping costs while maintaining the spacecraft in the vicinity of the virtual reference solution. Spacecraft may experience continuous deviation from the reference trajectory as maneuvers are performed along specific directions, in such cases stationkeeping operations may not be successful as orbit determination error levels increase, as deviations amplify rapidly. Maneuvers along the $\hat{x}$ and/or $\hat{N}$ directions are effective for stationkeeping for a range of target horizons. A significantly large maneuver magnitude is required to meet the target conditions when constrained along the $\hat{y}$ and/or $\hat{V}$ directions. Moreover, state deviations along the $\hat{y}$ and $\hat{V}$ directions increase rapidly as they are aligned close to the maximum stretching direction. Stationkeeping maneuvers along the $\hat{y}$ and the $\hat{V}$ directions are effective only for very long target horizons and long term stationkeeping is less likely. A large maneuver magnitude is delivered along the $\hat{z}$ and the $\hat{C}$ directions to meet the target conditions, while being oriented significantly away from the most stretching direction. Performance of maneuvers aligned along either of the $\hat{z}$ and the $\hat{C}$ directions, thus are intermediate to that of the cases for $\hat{x}$ (also $\hat{N}$) directions and for the $\hat{y}$ (also $\hat{V}$) directions.

Table 5.8. Annual orbit maintenance cost, $\bar{\varkappa}$, and 95% confidence interval, $\pm 1.96\sigma_{\bar{\varkappa}}$, in [m/s] for direction constrained maneuvers with low ODE level (3σ: 1 km and 1 cm/s). Reference orbit: 9:2 synodic resonant southern L2 NRHO with 3200 km perilune radius.

Maneuver Direction	Target horizon [rev]						
	0.5	1.5	2.5	3.5	4.5	5.5	6.5
Min. Norm (Conventional)	0.28 ± 0.02		0.18 ± 0.02	0.13 ± 0.00	0.14 ± 0.00	0.15 ± 0.00	0.16 ± 0.00
$\hat{x}$	0.49 ± 0.01		0.19 ± 0.01	0.15 ± 0.00	0.15 ± 0.00	0.15 ± 0.00	0.15 ± 0.00
$\hat{y}$				0.31 ± 0.01	0.35 ± 0.01	0.32 ± 0.01	0.34 ± 0.01
$\hat{z}$			2.60 ± 0.13		2.23 ± 0.07	2.99 ± 0.15	2.41 ± 0.06
$\hat{V}$				0.31 ± 0.01		0.34 ± 0.01	0.37 ± 0.01
$\hat{N}$	0.75 ± 0.02		0.19 ± 0.01	0.17 ± 0.00	0.16 ± 0.01	0.16 ± 0.00	0.16 ± 0.00
$\hat{C}$			0.58 ± 0.02	0.74 ± 0.03	0.58 ± 0.02	0.59 ± 0.02	0.61 ± 0.01
Restoring Plane	0.25 ± 0.01	0.27 ± 0.01	0.16 ± 0.01	0.23 ± 0.02	0.14 ± 0.01	0.25 ± 0.03	0.19 ± 0.01

< empty cell > - Did not converge

Targeting conditions 1.5 rev downstream offers distinct behavior in comparison to other target horizon using the conventional scheme that employs a minimum norm solution. It is identified that such a behavior is a result of maneuver direction having a significant component in the most stretching direction. In contrast maneuvers restricted in the restoring-plane are likely to offer close boundedness of the trajectories near the reference orbit, as perturbations are not expected to grow rapidly along the restoring-plane. Figure 5.45 demonstrates the deviation history in the form of a box-plot for trajectories maintained using minimum norm approach and using maneuvers restricted in the restoring-plane direction that targets the 1.5 rev xz plane crossing downstream. Clearly, maneuvers restricted in the restoring-plane direction cause trajectories to be more closely maintained to the reference path in

Table 5.9. Annual orbit maintenance cost, $\bar{\varkappa}$, and 95% confidence interval, $\pm 1.96\sigma_{\bar{\varkappa}}$, in [m/s] for direction constrained maneuvers with high ODE level (3σ: 10 km and 10 cm/s). Reference orbit: 9:2 synodic resonant southern L2 NRHO with 3200 km perilune radius.

Maneuver Direction	Target horizon [rev]						
	0.5	1.5	2.5	3.5	4.5	5.5	6.5
Min. Norm (Conventional)	5.84 ± 0.32		1.81 ± 0.12	1.02 ± 0.04	0.96 ± 0.03	0.90 ± 0.03	0.91 ± 0.03
$\hat{x}$	4.23 ± 0.34		1.61 ± 0.11	1.04 ± 0.03	1.13 ± 0.05	1.05 ± 0.04	1.03 ± 0.04
$\hat{y}$					2.44 ± 0.09	2.15 ± 0.06	2.25 ± 0.07
$\hat{z}$					16.27 ± 0.54	25.75 ± 1.82	16.71 ± 0.51
$\hat{V}$						2.28 ± 0.07	2.43 ± 0.07
$\hat{N}$	4.53 ± 0.34		1.70 ± 0.10	1.07 ± 0.03	1.16 ± 0.05	1.06 ± 0.04	1.03 ± 0.04
$\hat{C}$			5.88 ± 0.34	6.65 ± 0.52	4.03 ± 0.13	4.16 ± 0.15	3.92 ± 0.13
Restoring Plane	2.03 ± 0.12	1.94 0.10	1.36 ± 0.09	1.92 ± 0.13	1.36 ± 0.10	1.61 ± 0.13	1.25 ± 0.07

< empty cell > - Did not converge

comparison to the maneuvers delivered using the minimum norm approach that is conventionally used for stationkeeping. In the ephemeris model, the maneuvers are constrained in the restoring-plane identified by the flow between two successive apoapsis computed instantaneously (the trajectory is not precisely a closed periodic trajectory). Figure 5.46 demonstrates the alignment of the maneuvers delivered by targeting the 1.5 rev xz plane crossing in the ephemeris model. For reference, the most stretching direction and the restoring-plane identified in the CR3BP are also plotted. Magnitude of any state change along the restoring plane do not amplify over time, however, any maneuver restricted in the restoring-plane is away from $\hat{M}$ direction (the direction of the minimum norm solution for 1.5 rev target horizon) hence a larger magnitude of velocity state change is intermittently introduced every

revolution, one that may continuously drive increasing velocity state change every revolution. Of course, targeting conditions 1.5 rev downstream does not deliver reliable stationkeeping if a minimum norm solution is calculated. An alternate approach that delivers a maneuver in a different direction, preferably away from the stretching direction that targets the 1.5 rev xz-plane crossing may still result in successful stationkeeping, an example is demonstrated using maneuvers restricted in the restoring-plane. Targeting an alternative condition at 1.5 rev xz-plane crossing may also yield a different maneuver magnitude and direction that is potentially suitable for stationkeeping, however, such a condition does not qualify as an x-axis control algorithm and therefore not explored in this investigation.

5.6.4 Uncorrelated position and velocity uncertainties

In a real mission scenario, the position and velocity state uncertainties are derived quantities based on observations that may be in the form of range and range rate measurements as described in section 4.2. Depending on the uncertainty in measurements and tracking intervals, the position and velocity uncertainties change subsequently. The position and velocity uncertainties are likely to be coupled as a result of the orbit determination process, however, a variable range of position and velocity uncertainties and its effects on stationkeeping offers a reliable information on the sensitivities along an orbit. Such an information may help decide the number of observations and the duration of tracking intervals that may be desired to meet the budgeted stationkeeping costs. Figure 5.47 offers an estimate of annual stationkeeping costs to maintain a spacecraft along the 9:2 synodic resonant southern L2 NRHO. The cases are simulated by targeting 6.5 rev horizon, considering variable position and velocity errors that are uncorrelated. The stationkeeping costs increase more rapidly with increasing velocity uncertainties rather than position uncertainties, and consistent with the sensitivity analysis measured using the maximum stretching directions as in Figure 5.4.

5.6.5 Minimum maneuver magnitude constraints

It may not be feasible to perform extremely small maneuvers, moreover, they may be redundant. The thrusters along a spacecraft may have a certain minimum $|\Delta\bar{v}|$ magnitude

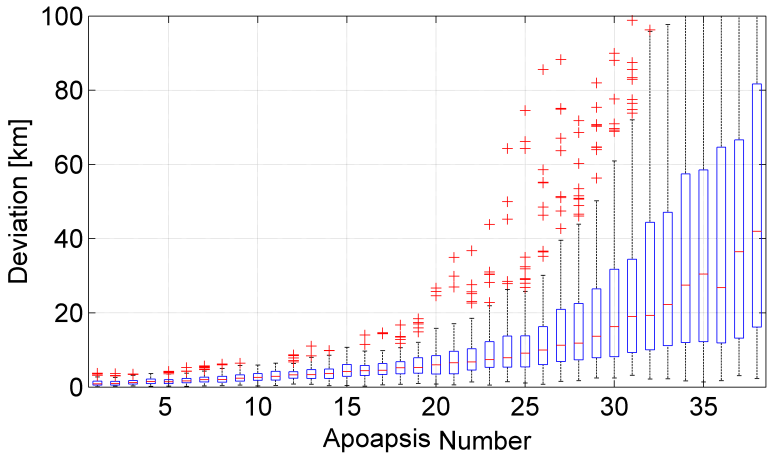

(a) Maneuvers using minimum norm approach

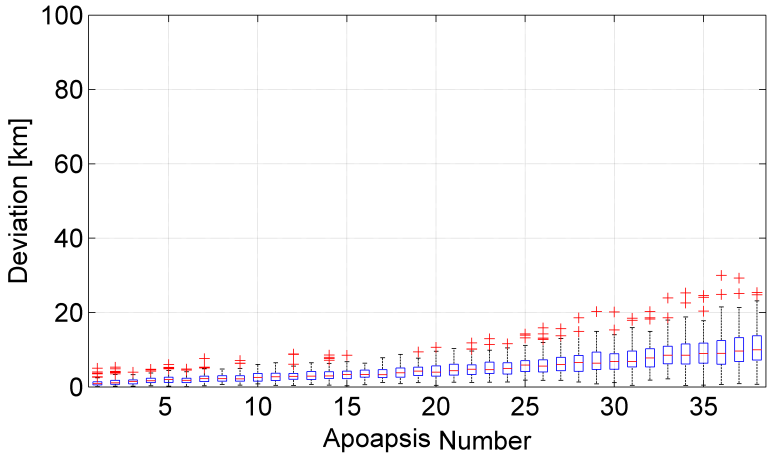

(b) Maneuvers in restoring-plane direction

Figure 5.45. Deviation history for trajectories maintained using maneuvers delivered using minimum norm solution and maneuvers restricted in the restoring-plane direction, each targets the 1.5 rev xz plane crossing in the CR3BP. Reference orbit: L2 NRHO with perilune radius 3200 km. Low orbit determination error (3σ: 1 km and 1 cm/s) case.

that is deliverable. A minimum $|\Delta\bar{v}|$ magnitude is incorporated into the stationkeeping algorithm, to estimate the performance of the stationkeeping process and investigate the impact on the annual stationkeeping costs and the length of each ballistic segments in the process. Figure 5.48 offers an estimate of the annual stationkeeping costs for cases with a range of minimum $|\Delta\bar{v}|$ magnitude constraints and state uncertainties in position and velocity. The values are estimated along a 9:2 synodic resonant southern L2 NRHO with an approximate perilune radius of 3200 km. For simplicity, position errors, quantified in

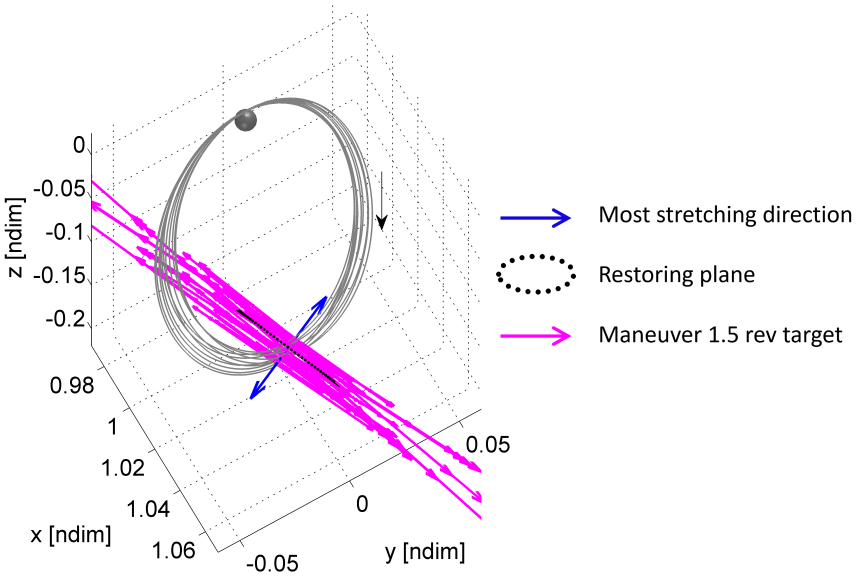

Figure 5.46. Stationkeeping maneuvers constrained in the restoring-plane delivered by targeting the 1.5 rev xz plane crossing for the 9:2 synodic resonant NRHO in the ephemeris model. Low orbit determination error (3σ: 1 km and 1 cm/s) case.

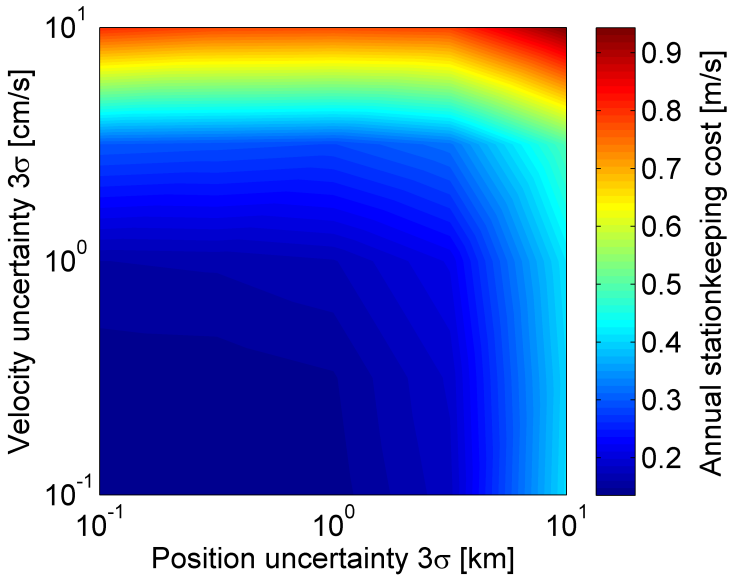

Figure 5.47. Annual stationkeeping cost for various uncorrelated combinations of position and velocity uncertainty on L2 NRHO with perilune radius 3200 km.

km, and velocity errors, quantified in cm/s, are considered to be coupled with the same order of magnitude. Figure 5.49 corresponds to the number of apoapsis where a maneuver is performed as a result of the $|\Delta\bar{v}|$ magnitude constraints, measured as a percentage of the total number of apoapsis along the trajectory. The annual stationkeeping costs increases with the minimum $|\Delta\bar{v}|$ magnitude constraints, and across increasing state uncertainties. Since a spacecraft is expected to remain fairly close to the reference orbit in cases with low state errors such as 3σ of 0.1 km and 0.1 cm/s, a minimum $|\Delta\bar{v}|$ magnitude constraints as high as 5 cm/s results in stationkeeping maneuvers performed at less than 20% of the apoapsis along the trajectory. Even at relatively high state errors such as 3σ of 10 km and 10 cm/s, a minimum $|\Delta\bar{v}|$ magnitude constraints as high as 5 cm/s results in stationkeeping maneuvers performed at less than 40% of the apoapsis along the trajectory, but consistently large maneuvers cause an increase in annual stationkeeping costs. Not surprisingly, a minimum $|\Delta\bar{v}| = 0$ case results in maneuvers being performed at all the apoapsis.

5.7 Nonlinear Effects

The periapsis region along an NRHO is very sensitive due to its close proximity to the Moon. As a consequence, targeting rotating x velocity component along an NHRO near the periapsis is susceptible to high nonlinear effects that may offset maneuver estimation that rely on linear state transition matrix. To visualize the nonlinear effects near the periapsis along the 9:2 synodic resonant L2 NRHO, velocity perturbations that are of the same order of magnitude as the orbit determination errors are introduced at the apoapsis and propagated for specific durations of 0.5 rev, 1.5 rev, and so on that corresponds to the periapsis location along the reference NRHO. Figures 5.50(a) and 5.50(b) describe the effects of velocity perturbation of sizes 1 cm/s, similar to 3σ levels for low ODE, and 10 cm/s, similar to 3σ levels for high ODE, introduced at the apoapsis and propagated for the specific durations. Clearly, the surface of perturbed states at final time are non-Gaussian and multimodal. For comparison, a linear STM is Gaussian and unimodal. Not surprisingly, the nonlinear effects are more dominant in Figure 5.50(b) that corresponds to larger perturbation size than in Figure 5.50(a). Besides, for both these cases, larger time horizon also contributes to the nonlinear effects being more prominent. The perturbation due to 6.5 rev of the NRHO is

more pronounced and overlays perturbations at other target horizons. In the stationkeeping algorithm, that targets states at time horizon as high as 6.5 revs, the effect of the nonlinear dynamical flow may restrict linear state transition matrix from accurately determining the

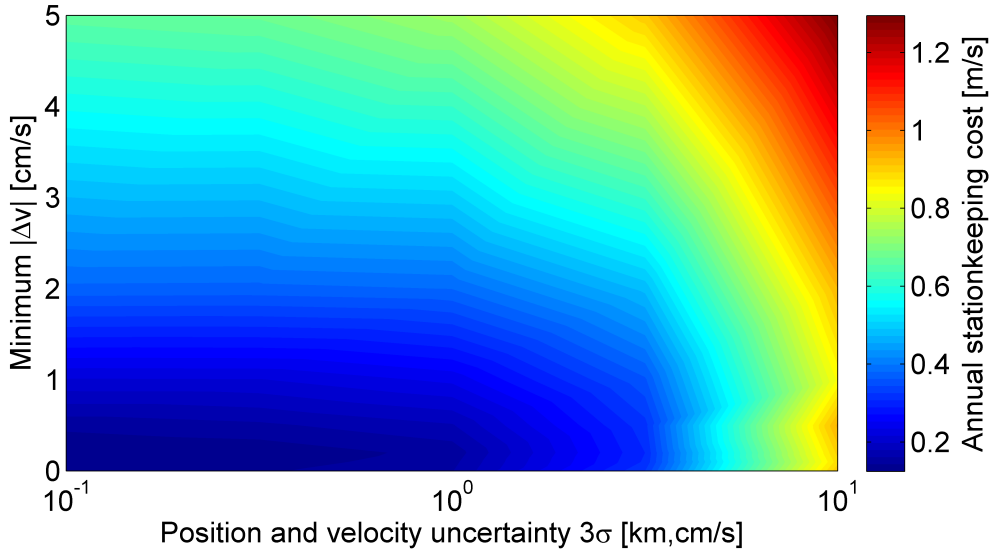

Figure 5.48. Annual stationkeeping cost for various minimum maneuver magnitude constraints and combinations of position and velocity uncertainty on L2 NRHO with perilune radius 3200 km.

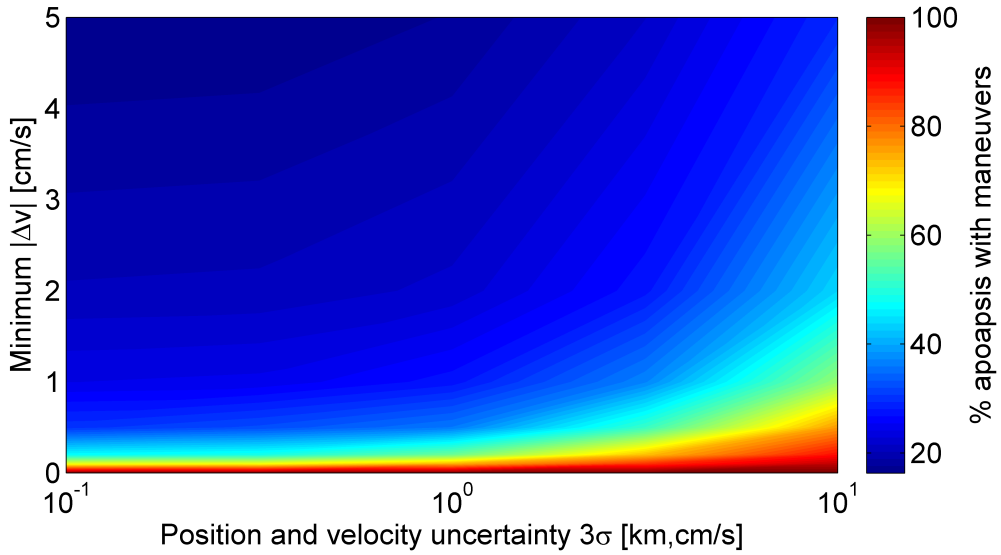

Figure 5.49. Percentage of apoapses where maneuvers are executed for various minimum maneuver magnitude constraints and combinations of position and velocity uncertainty on L2 NRHO with perilune radius 3200 km.

correction maneuvers. It is worth exploring the effectiveness of the entire differential corrections process in accurately determining the maneuvers despite the nonlinear effects.

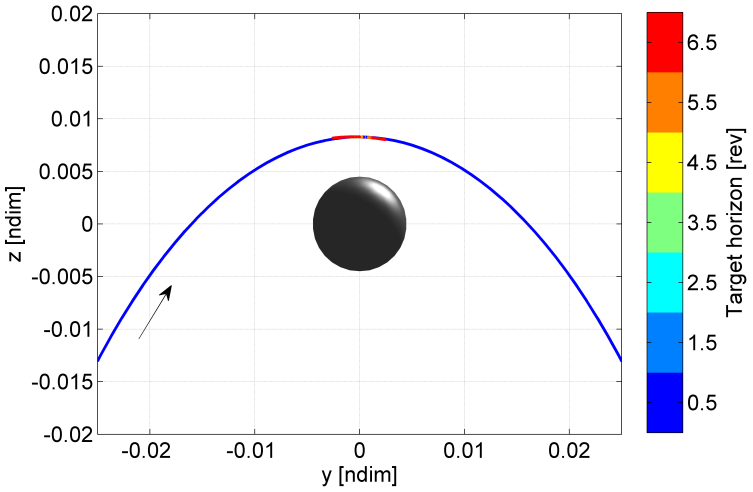

(a) Initial $|\Delta\bar{v}| = 1$ cm/s

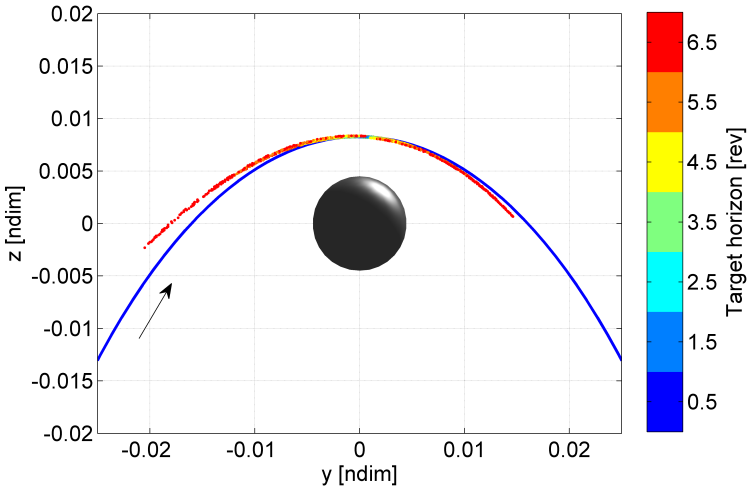

(b) Initial $|\Delta\bar{v}| = 10$ cm/s

Figure 5.50. End of trajectory segments that are propagated for different time horizons with initial velocity perturbations of a fixed magnitude in arbitrary directions, implemented at the apoapsis.

In the x-axis crossing control stationkeeping strategy, the time of propagation of a perturbed trajectory is not exactly equal to the time from the apoapsis to the corresponding target location along the reference orbit. Rather, all trajectories are allowed to propagate till

the xz plane crossing; an event that may or may not be in phase with the virtual reference trajectory. Figures 5.51 and 5.52 demonstrate the phase shift and the change in the rotating $\dot{x}$ value of the actual perturbed trajectories relative to the virtual reference trajectory, each recorded at the xz plane crossing at various target horizon times. Figure 5.51 corresponds to trajectories with an initial velocity perturbation of magnitude 1 cm/s while Figure 5.51 corresponds to trajectories with an initial velocity perturbation of magnitude 10 cm/s. In both these figures, a positive phase shift from the reference is analogous to a trajectory that takes more time to reach the xz plane crossing, or considered lagging relative to the reference solution. Similarly, a negative phase shift from the reference is equivalent to a trajectory that takes less time to reach the xz plane crossing, or considered leading relative to the reference solution. A correlation seems to exist between the phase shift experience by a perturbed trajectory and the change in the rotating $\dot{x}$ value at a particular xz plane crossing. Nonlinear effects are less profound for an initial velocity perturbation of magnitude 1 cm/s, comparable to low ODE levels, as in Figure 5.51, for the range of target horizons considered. A profound nonlinear correlation is observed for case with an initial velocity perturbation of magnitude 10 cm/s, comparable to high ODE levels, as in Figure 5.52, especially for the longer target horizons. The accuracy of a linear STM to deliver maneuver that targets the xz plane crossing 6.5 revs, subject to high ODE errors, serve as the limiting case to understand the underlying nonlinear effects. Cases with low velocity errors and shorter target horizon times adheres to the limiting case.

The angle between a maneuver and the maximum stretching direction governs the effectiveness of the strategy. The maximum stretching direction is computed along the coast arc, that is generally not longer than a period in length, a linear STM thus offers reliable measurements. It is the maneuver that is calculated along the arc propagated for a longer target horizon time, where nonlinear dynamics affects the maneuver calculation. It is observed in Figure 5.53 that for the case of 9:2 synodic resonant L2 NRHO, any perturbations along the maximum stretching directions are almost the extremas along the change in $\dot{x}$ values as well as the change in phase relative to the reference trajectory, in both the leading and lagging directions despite the non-Gaussian shape of the error correlation surface. As a consequence,

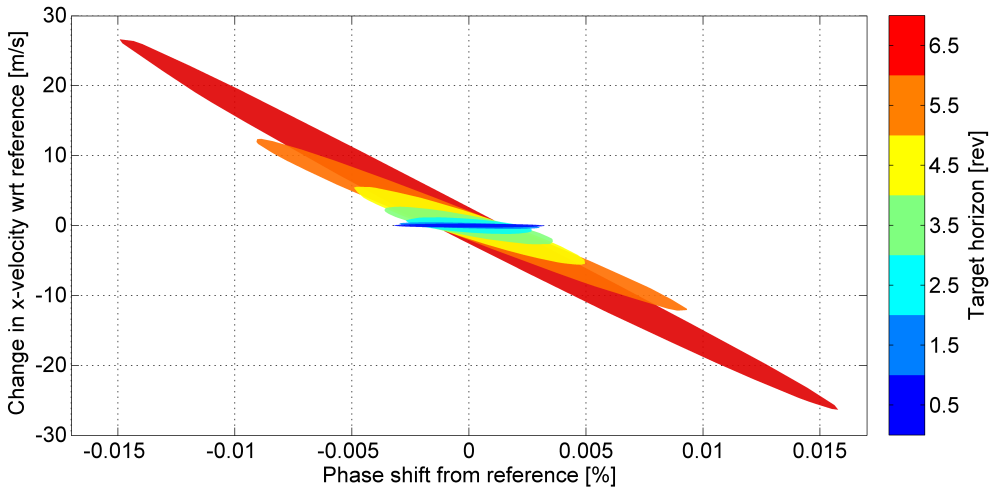

Figure 5.51. Correlation between phase shift and change in $\dot{x}$ value at various xz plane crossing, for trajectories propagated with initial velocity perturbations of a fixed 1 cm/s magnitude in arbitrary directions, implemented at the apoapsis.

a maneuver that targets any compensate errors that lie anywhere along the error correlation surface, is bounded by the information captured by the maximum stretching directions estimated in a linear sense. Consider a case, where the maximum stretching directions does not correspond to the extremas of the error correlation surface, there may exists cases where a maneuver delivered is away from the maximum stretching direction, that by intuition may restrict perturbation growth between two successive maneuver locations, but may have large offset in $\dot{x}$ values and/or phase shift relative to the reference trajectory measured at xz plane crossings further downstream. As a result, despite the maneuver being aligned away from the maximum stretching direction, the spacecraft eventually deviates away from the reference orbit due to large phase shift and/or large change in $\dot{x}$ value relative to the reference orbit that may be difficult to target.

The shape and orientation of the error correlation surface as in Figures 5.51 and 5.52 influence the phasing errors typically observed in the x-axis crossing control approach. In the conventional stationkeeping strategy, only the rotating $\dot{x}$ quantity is targeted, without actively controlling any phase shift. Independent of the orbit determination error levels,

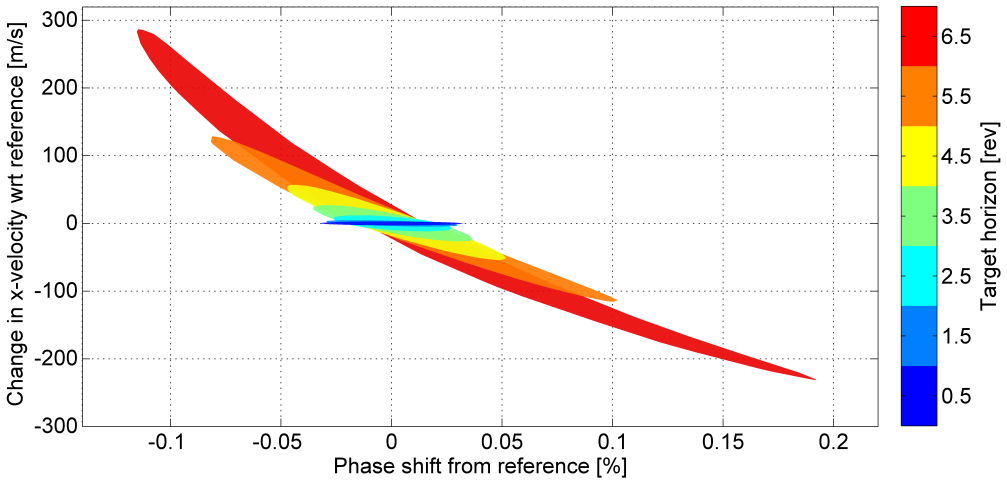

(a) Zoomed out view

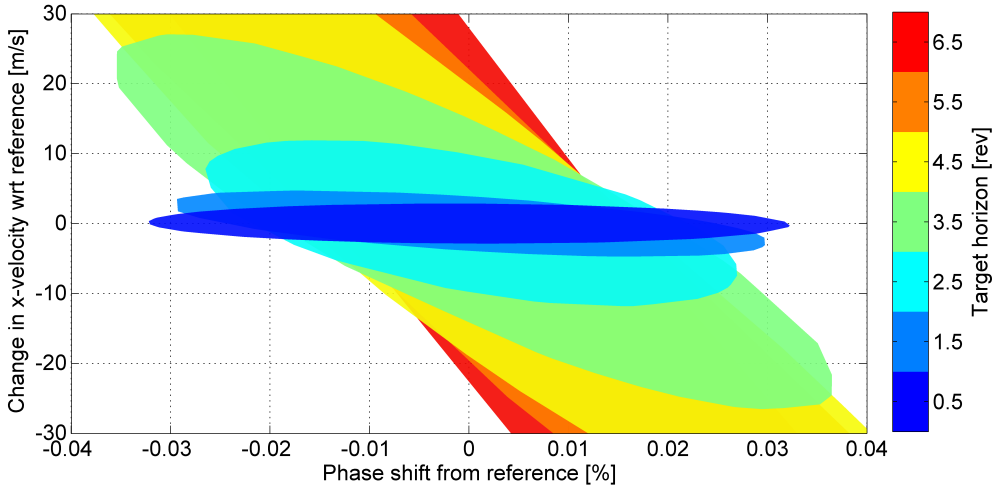

(b) Zoomed in view

Figure 5.52. Correlation between phase shift and change in $\dot{x}$ value at various xz plane crossing, for trajectories propagated with initial velocity perturbations of a fixed 10 cm/s magnitude in arbitrary directions, implemented at the apoapsis.

the elliptical shape of the error correlation surfaces as in Figures 5.51 and 5.52 for 0.5 rev and 1.5 rev target horizon times are almost horizontal, i.e., the semi-major axis is almost along the y = 0 line (x-axis) in these figures. Similarly, for longer target horizon times, the ellipses are oriented such that the semi-major axis is away from the y = 0 line (x-axis). For the error correlation surfaces that are almost horizontal ellipses, a maneuver that targets

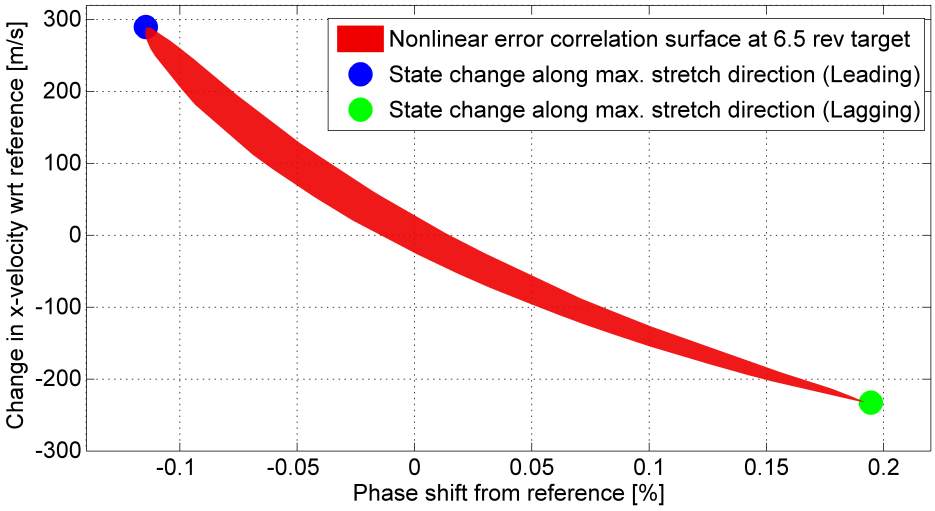

Figure 5.53. Nonlinear correlation between phase shift and change in $\dot{x}$ value at 6.5 rev xz plane crossing, along with crossings of trajectories propagated with initial velocity perturbations of fixed 10 cm/s magnitude in the maximum stretching directions.

the rotating $\dot{x}$ quantity, i.e., $\Delta\dot{x} \approx 0$, may have a large range of phase errors that are not compensated. Cases that target 0.5 rev and 1.5 revs are prone to larger phase errors than targeting the longer target horizons, where a corrective maneuver that compensates for the $\dot{x}$ value automatically compensates some component of the phase errors as well, i.e., for longer target horizon times $\Delta\dot{x} \approx 0$ line in Figures 5.51 and 5.52 have a smaller range of phase errors.

In general, it is expected that a single shooting technique to estimate the stationkeeping maneuver is less effective when targeting states that are significantly downstream, such as 6.5 rev, due to nonlinear effects resulting from close lunar passages along the path. In the x-axis crossing control approach, a maneuver is calculated using a single shooting technique that employs a Newton-Raphson iterative scheme, one that solves for linear state updates. Although the updates are based on a linear state transition matrix, the nonlinear equations of motion are propagated to ensure convergence criteria at the target are met. With small perturbations typical of a stationkeeping problem nearby a known reference trajectory, a Newton-Raphson scheme yields a quadratic convergence [99]. In cases with quadratic convergence, the first iteration formulated in terms of a linear STM that is the major up-

date, while the following iterations results in significantly smaller updates. From Figures 5.10(a) and 5.11(a), that are reflective of the CR3BP dynamics, it is evident that even for longer target horizon times such as 6.5 revs downstream, the angle estimated for the maneuver calculated from the linear STM (equivalent to the first update of the Newton-Raphson scheme), as denoted by the blue curve, reasonably captures the effect in comparison to the actual maneuvers noted by the red asterisks (*), that is, reflective of the nonlinear dynamics. Accordingly, the maps in Figures 5.8, 5.10 and 5.13 that offer linear predictions sufficiently capture the underlying dynamics over this range of target horizons.

5.8 L1 and L2 Transition Halo Orbits

Transition halo orbits are members of the halo orbit families in the L1 and L2 region, loosely identified with perilune radius between 10000 km to 22000 km that, when transitioned from CR3BP to a higher-fidelity ephemeris model exhibits large variation in apse angles [57], [75]. An apse angle is described as the shift in the periapsis or the apoapsis of the orbit in the higher-fidelity model in comparison to the orbit in the CR3BP [3]. The range of orbits that exhibit large variation in apse angles typically exists as the transition occurs from stable NRHOs with relatively low perilune radius to the unstable members of the halo orbit family with relatively larger perilune radius. Some of the transition halo orbit members exhibit a simple resonance with the Earth-Moon sidereal and synodic periods. In the L2 family, the NRHO with an approximately 15000 km perilune radius is labelled as the 3:1 synodic resonant orbit, i.e., three revolutions of the orbit corresponds to one synodic time period of the Moon around the Earth. Figure 5.54 illustrates the L2 NRHO with a 15000 km perilune radius transitioned from the CR3BP to an ephemeris model on different starting epoch dates in the month of May in 2023. Clearly, the natural trajectories corresponding to each epoch exhibit different geometry in configuration space, with large dispersion in apse angles, indicating the sensitivity of the orbit states as epoch time is varied. In particular, for the 3:1 synodic orbit, some similarity in geometry appears in 9-10 day intervals that roughly correspond to the time per revolution along the orbit in the CR3BP system [75]. Other transition orbits in the L1 and L2 family display similar characteristics. Clearly, alternative strategies are possible to transition such orbits. But, to assess the stationkeeping

challenges, assume sample ephemeris trajectories such as those in Figure 5.54. As a result of such sensitivity, stationkeeping along these transition halo orbits is challenging and requires modifications to the conventional impulsive stationkeeping algorithm.

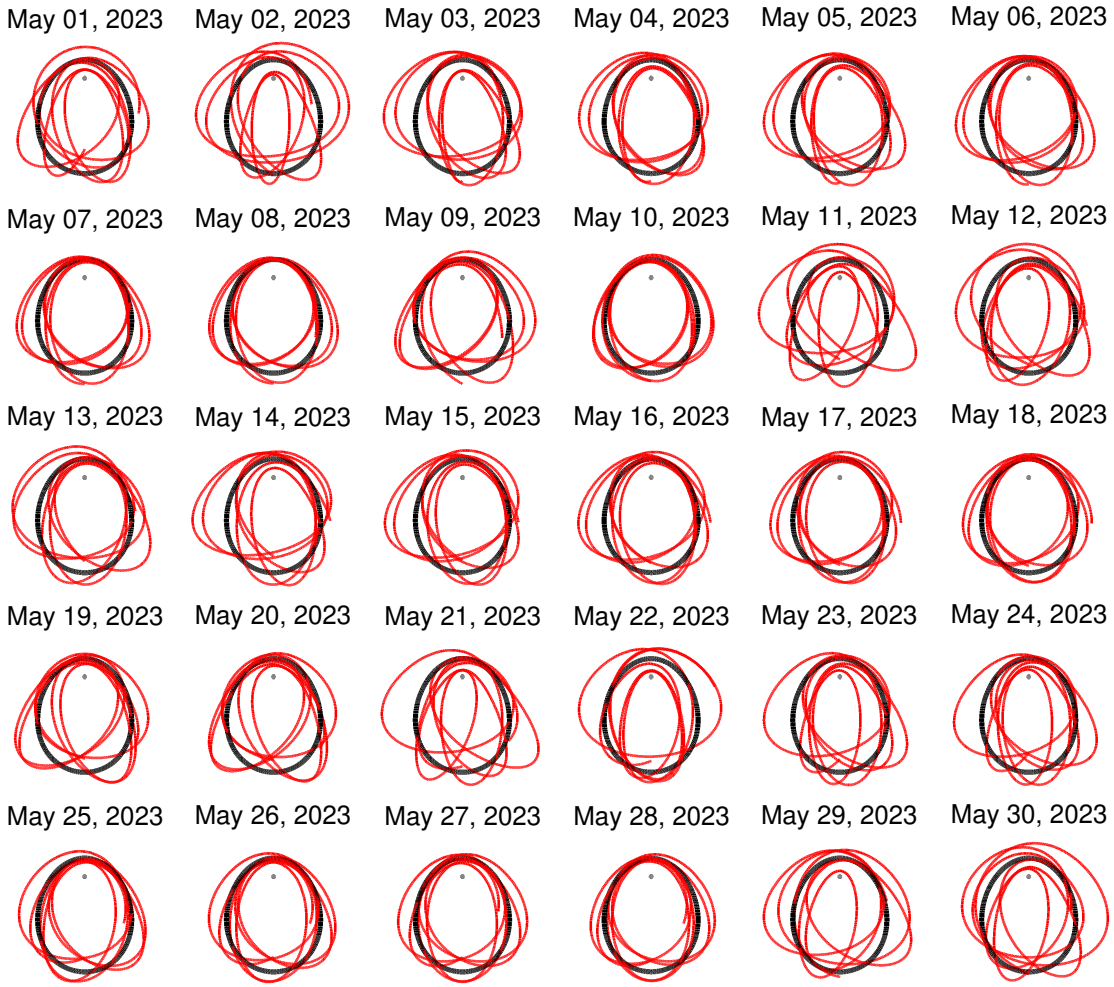

Figure 5.54. Dispersion in apse angle for L2 NRHO with perilune radius 15000 km in CR3BP (black) and higher-fidelity ephemeris model (red) converged for different starting epoch dates in May 2023. All projections are in yz view in the rotating frame; trajectory direction is clockwise.

To investigate the influence of the underlying reference trajectory on the x axis crossing control approach for stationkeeping, a sufficiently long reference trajectory is designed systematically and consistently. The generation of a natural trajectory in the higher-fidelity

ephemeris model is accomplished in a consistent manner, considering the sensitivity of the CR3BP states to the epoch time for transition halo orbits. A periodic orbit in the CR3BP is subdivided into 10 segments, equally spaced in time. The beginning node along each trajectory segment serves as a patch point for the multiple shooting process. To generate a natural trajectory approximately 12 time-periods in length, 12 revolutions of the orbit in the CR3BP are selected, and 'stacked' on top of each other, yielding a total of 121 patch points that serve as the initial conditions for the multiple shooting process. For consistency, the first patch point is selected at the apoapsis location in the CR3BP model. Further, it is constrained that the location of first patch point is in the xz-plane. Through a Newton-Raphson iterative process, as demonstrated in the literature, a natural trajectory is constructed that is continuous in position and velocity states, as well as in time [103]. Of course, the geometry of the natural trajectory varies with the epoch date corresponding to the first patch point, a case for the L2 NRHO with 15000 km is demonstrated in Figure 5.54. The length of the natural trajectory in the ephemeris model provides a sufficiently long duration to examine stationkeeping capabilities.

Davis et al. have investigated stationkeeping capabilities on the transition halo orbits using the conventional x-axis control approach, with a single maneuver per orbit near the apoapsis, one that targets the rotating $\dot{x}$ value at certain xz-plane crossings further downstream [57]. It is observed that, using this approach, only certain baseline solutions are conducive to long-term orbit maintenance. In addition, simulations for orbit determination errors larger than 3σ of 0.3 km and 0.3 cm/s, resulted in trajectories diverging from the virtual reference solution, and consequently produced fewer successful stationkeeping cases. Similar results are observed in this investigation as well. Upon careful observation, it is clear that the position and velocity states along the transition halo orbits are sensitive to epoch dates and, therefore, stationkeeping operations must also target the necessary timing conditions at the corresponding epochs, i.e., the actual trajectory must be in phase with the baseline trajectory.

In literature, it is observed that the phase difference between the actual spacecraft trajectory and the virtual baseline trajectory increases either positively or negatively over time, when maneuvers are implemented using the conventional x-axis control algorithm [82], [119]. For transition halo orbits that are sensitive to epoch time, any phase shift between the actual and reference trajectories may impede the stationkeeping operations. To overcome such sensitivities, additional phase constraints are introduced. Muralidharan and Howell have demonstrated that a phase control approach, as detailed in section 5.6.1, is effective for orbit maintenance in the transition halo orbits [83]. Again, in any case, if the spacecraft has deviated significantly from a virtual reference trajectory, an occasional long horizon orbit correction maneuver is implemented to shift the states to a new long horizon virtual reference trajectory.

A low-cost stationkeeping maneuver is generated typically by targeting further downstream to allow sufficient time to achieve the target conditions. The phase control approach applied on the 3:1 synodic resonant L2 NRHO with perilune radius 15000 km, a reference trajectory that falls within the transition halo orbit range, by targeting the 1^{st} xz-plane crossing near the periapsis is less effective in terms of cost and the number of successful cases compared to targeting the 2^{nd} xz-plane crossings near the periapsis, for both low and high orbit determination levels. Targeting the 2^{nd} xz-plane crossing is successful in maintaining the spacecraft near the virtual reference orbit even with high orbit determination errors (3σ of 10 km and 10 cm/s), which is a considerable improvement compared to the conventional x-axis control algorithm that is effective only for certain virtual reference orbits for very low orbit determination levels with 3σ of 0.3 km and 0.3 cm/s, in position and velocity respectively. Due to the sensitivity of the transition halo orbits, the perturbed initial states when propagated for a time duration equivalent to 6.5 revs of the reference orbit no longer adheres to the geometry of a halo orbit. A single shooting differential correction process faces a challenge with relatively longer target horizons, such as 6.5 rev downstream.

The sensitivity of the stationkeeping process on a reference orbit is measured by monitoring the stationkeeping performance along two reference orbits of the same NRHO with

the same epoch constructed using different approaches. A comparison of annual stationkeeping costs on two set of reference solutions is plotted in Figure 5.55 for the 3:1 synodic L2 NRHO with perilune radius 15000 km for different epoch dates in the month of May in 2023 described by the x-coordinate. The annual costs are estimated over 100 Monte Carlo simulations, consistent with the cases discussed previously. The set of reference orbits labelled as Sample 1, is generated by stacking 12 revolutions of the CR3BP orbit with 10 patch points along each orbit spaced equally in time, as detailed previously. In contrast, Sample 2 is generated by stacking 25 revolutions of the CR3BP orbit with 10 patch points along each orbit spaced equally in time. In both sample cases, the first node is constrained to be on the xz-plane. Not surprisingly, the stationkeeping cost is sensitive to the virtual reference trajectory. Hence, a direct cost comparison between trajectories constructed on two different epoch dates or using a different sequence of stacking operations, is not practical, as they are based on distinct natural baseline trajectories.

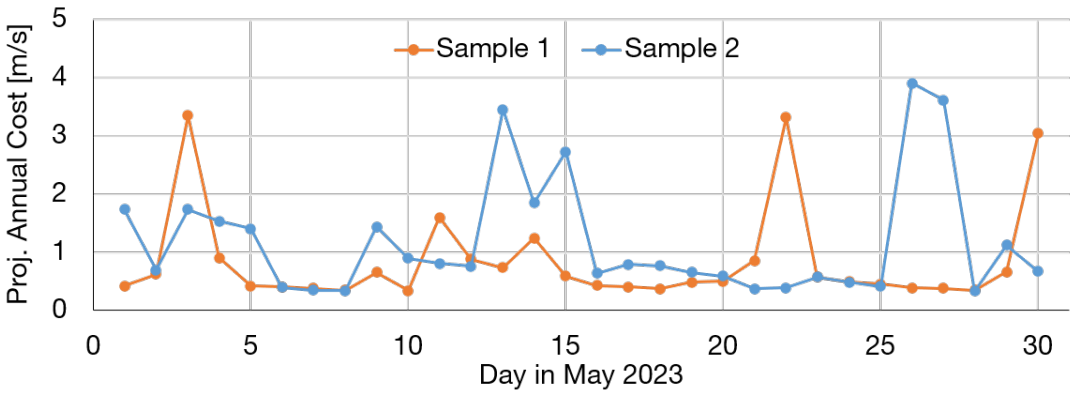

Figure 5.55. Annual stationkeeping cost comparison for reference orbits constructed on same epoch dates through different approaches. Case: 3:1 synodic resonant L2 NRHO with perilune radius 15000 km with low orbit determination error level (3σ: 1 km and 1 cm/s).

The stationkeeping costs estimated on the transition halo orbit is, of course, impacted by the underlying natural trajectory that serves as the virtual reference trajectory. Although, the mean estimated cost associated with the stationkeeping for a specific trajectory is not very useful, the range of mean stationkeeping costs associated with the same orbit con-

structed over different epoch dates may yield more relevant details. Figures 5.56(a) and 5.56(b) summarizes the projected annual orbit maintenance cost along different halo orbits in the transition region estimated by running 100 Monte Carlo simulations. Each curve represents a transition halo orbit in the L1 and L2 regions. The x-coordinate along these curve represents the epoch date at the halo orbit injection, i.e., the first node of the stacking sequence. The y-coordinate of the curve is the estimated mean stationkeeping costs computed for that epoch date. These simulations are conducted for a mission duration of 90 days. For low orbit determination errors, majority of the stationkeeping simulations across different orbits remains bounded near the virtual reference solutions, simulated over a range of epoch dates in the month of May 2023. A few trajectories do depart from the virtual reference solution. The worst performing case, L2 halo orbit with 21000 km on May 26, 2023, does include at least 80% simulations that remain bounded. In general, the annual stationkeeping cost across different halo orbits are generally in the range between 0.3 m/s and 5 m/s, for low orbit determination errors. In contrast, with higher orbit determination errors, the success rate is at least 60% successful Monte Carlo trials, across different orbits simulated over a range of epoch dates. The worst performing case for high orbit determination errors, the L1 halo orbit with 18000 km on May 13, 2023, includes only 16% Monte Carlo trials that successfully maintain the spacecraft near the virtual reference solution over the mission duration. Again, roughly, annual stationkeeping cost across different halo orbits are typically in the range of 1.5 m/s to 16 m/s, for high orbit determination errors. Stationkeeping performance are reflective of the underlying baseline orbit and a direct comparison between two different transition halo orbits and on different epoch dates is inconsequential, however, identification of the range of stationkeeping costs for various transition halo orbits are valuable.

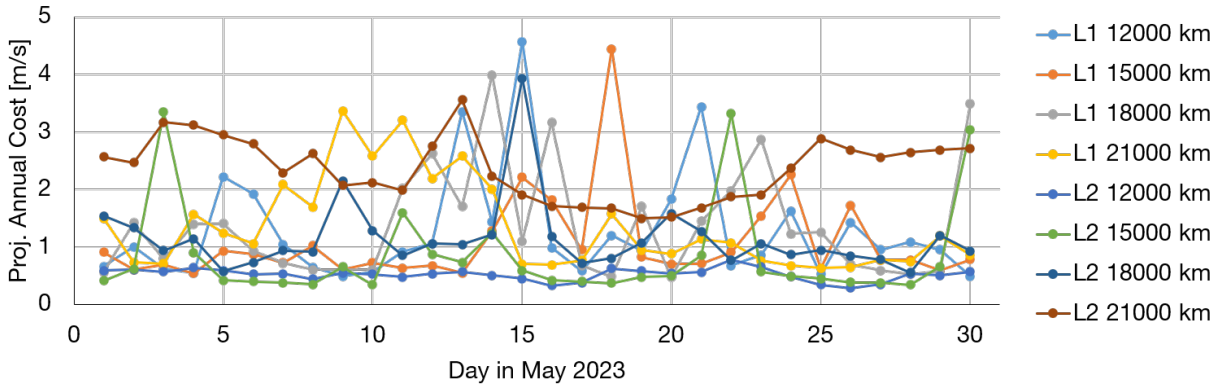

(a) Low orbit determination error (3σ: 1 km and 1 cm/s)

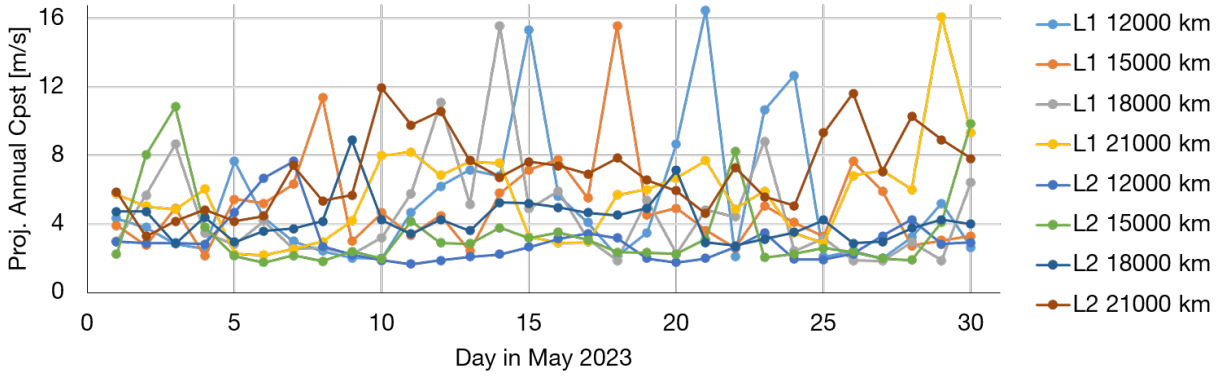

(b) High orbit determination error (3σ: 10 km and 10 cm/s)

Figure 5.56. Annual stationkeeping cost [m/s] for different transition halo orbits in the L1 and L2 families.

6. DEPARTURE AND TRANSFER TRAJECTORY DESIGN

With the long term potential of NASA's Lunar Gateway mission, there is a growing interest in accessing nearby stable cislunar orbits for various mission scenarios. Of course, the Near Rectilinear Halo Orbits (NRHOs) in the L1 and L2 regions of the Earth-Moon system offer potential candidates suitable for any long term presence. These NRHOs are stable or nearly stable as characterized by the linear variational flow in the circular restricted three-body problem (CR3BP) [3], [4], and offer distinct characteristics such as reasonably close lunar passages and large out-of-plane amplitudes relative to the Earth-Moon orbit plane, appropriate for investigating the polar regions of the Moon. Similar to the NRHOs, the Distant Retrograde Orbits (DRO) offer a range of stable orbits in the Earth-Moon system. The DROs are potential hosts for proposed propellant depot, that reduces costs for accessing various cislunar orbits and enable transfer options to interplanetary orbits [124], [125]. The Lunar Distant Retrograde Orbit (DRO) approximately 70,000 km from the Moon served as the baseline for the once proposed Asteroid Redirect Mission (ARM) [126]. The Lunar Orbits (LO) offer close coverage of the Lunar surface, crucial for various science missions.

With the increasing number of mission scenarios and with a potential human presence, an important capability is transfers between various locations of interest relatively quickly and cost efficiently. Disposal of logistic modules while avoiding any collisions is also a concern. Manifolds have been used extensively for orbit departure and trajectory design, however, the lack of well-distinguished stable and unstable manifold structures on orbits that are nearly stable is a challenge. Previous transfer trajectory design approaches between stable orbits exploit intermediate segments of known orbits, resonant arcs as well as manifolds of known unstable orbits [72], [73], [75]–[77], however, the most productive types of intermediate orbits are not known *a priori*. In this investigation, the dynamical flow is visualized using the principal stretching directions. An alternate strategy that offers reliable departure and arrival analysis from stable orbits are explored in this investigation, one that leverages the maximum stretching directions. An effective departure from the orbit serves as a preliminary step for the disposal problem as well as a basis for transfers to other spatial locations.

6.1 Orbit Departure

NASA's Gateway mission is to be maintained for a sufficiently long duration along the 9:2 synodic resonant orbit in the L2 southern NRHO family. The NRHO that is the current baseline is almost stable. While an almost stable orbit is suitable for reducing the station-keeping costs [4], [57], [82], [83], it is challenging to get the spacecraft and/or the discarded logistic modules away from the reference orbit [127]. Ability to depart from the vicinity of the baseline orbit is required for various reasons, including transfers to other orbits/regions of interest as well as discarding logistic modules away from the baseline orbit to avoid any potential collisions with the in-orbit spacecraft. This investigation focuses on leveraging the maximum stretching direction as a tool to depart the vicinity of a nearly stable NRHO, and provide an alternative to exploiting manifolds for departure. Manifolds offer a suitable highway architecture to access and depart the orbit, but for highly unstable orbits. As the stability of the orbit increases, the functionality of the manifolds reduces for such applications. The orbit departure problem considered in this investigation serves as the preliminary step to the disposal problem, and as a basis for transfers to other spatial locations.

6.1.1 Momentum Integral

Momentum integral is a parameter defined to identify the periodicity and boundedness of a trajectory [4]. Mathematically, it is the line integral of the position vector along a trajectory, i.e.,

$$\mathrm{MI}(t) = \int_{t_0}^{t} x(\tau)\dot{x}(\tau) + y(\tau)\dot{y}(\tau) + z(\tau)\dot{z}(\tau)d\tau \tag{6.1}$$

where, position vector is defined relative to the Earth-Moon barycenter in the CR3BP frame. For a time-invariant system like the higher-fidelity ephemeris model where states are not precisely periodic, momentum integral is not perfectly periodic, however, remains bounded along a trajectory that resembles the geometry of an orbit. Momentum integral evaluated along trajectories in the neighborhood of the reference trajectory provides a suitable measurement to assess their boundedness. Figure 6.1 demonstrates the behavior of a perturbed trajectory, colored as red, relative to the reference trajectory, colored as black, in the configuration space. Figure 6.2 quantifies the momentum integral evaluated along the trajectories shown

in Figure 6.1. Clearly, the evolution of momentum integral along the periodic reference path and the perturbed path are reflective of the motion in the configuration space. The reference trajectory is perfectly periodic, and the value of momentum integral corresponds to the same behavior. However, the perturbed trajectory, colored in red, undergoes motion similar to the reference trajectory for certain duration before departing significantly away from the reference motion. Consider, the reference trajectory represented by Γ, and the perturbed trajectory as $\tilde{\Gamma}$. A metric, defined as

$$\Delta \mathrm{MI}(t) = |\mathrm{MI}_{\tilde{\Gamma}}(t) - \mathrm{MI}_{\Gamma}(t)| \tag{6.2}$$

that is the absolute value of the difference between the momentum integral evaluated along the actual perturbed path and the reference path, serves well, to quantify the departure of the actual perturbed path relative to the reference path. Consistent with the previous literature [127], a spacecraft is considered to have departed the vicinity of the reference path as the value of ΔMI exceeds 10^{-1}, however, the specific value best suited for defining departure is dependent on each problem. For the current application, using 10^{-1} for the threshold is adequate. The departure of the perturbed trajectory, shown in Figure 6.1, is quantified relative to the reference trajectory in terms of ΔMI in Figure 6.3. Based on the threshold, the ΔMI at the end of the propagated segment is larger than 10^{-1}, hence considered to have departed the vicinity of the reference NRHO.

Stretching directions computed from various submatrices of the state transition matrix yield relevant information. As in the case of the stationkeeping problem, since only the initial velocity states, $\delta\bar{v}_0$, are subject to change, the submatrices that maps the impact of initial velocity are relevant. Besides, the NRHOs are sensitive to velocity state changes, hence, it is important to quantify final velocity state changes. The 3×3 dimensional submatrix, $\varphi_{C,v,v}$,

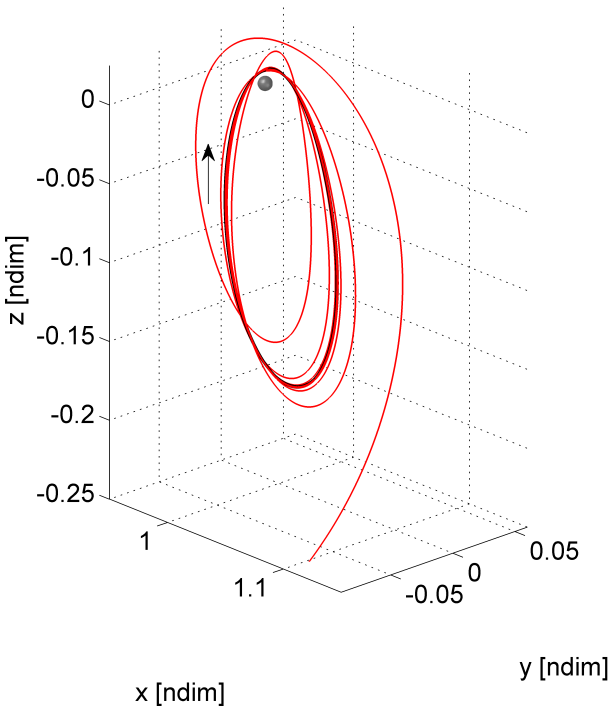

Figure 6.1. Trajectory deviating from the reference 9:2 synodic resonant L2 NRHO with a perilune radius 3200 km.

maps the initial velocity perturbation, $\delta\bar{v}_0$, to the final velocity change, $\delta\bar{v}_f$. Also, combined, the 6×3 dimensional submatrix $\varphi_{C,rv,v}$, where

$$\varphi_{C,rv,v} = \begin{bmatrix} \varphi_{C,r,v} \\ \\ \varphi_{C,v,v} \end{bmatrix} \tag{6.3}$$

that maps the initial velocity perturbation, $\delta\bar{v}_0$, to the final position and velocity state change, $\delta\bar{r}_f$ and $\delta\bar{v}_f$, yields significant characteristics. Figure 6.4(a) illustrates the maximum stretching direction, $\mathbb{V}_1$, corresponding to submatrix $\varphi_{C,v,v}$ while Figure 6.4(b) describes the maximum stretching direction, $\mathbb{V}_1$, that corresponds to submatrix $\varphi_{C,rv,v}$ in the configuration space. Clearly, the maximum stretching directions computed from either of the submatrices $\varphi_{C,v,v}$ or $\varphi_{C,rv,v}$ that include the final velocity state change are aligned in a similar direction. Since the submatrix $\varphi_{C,rv,v}$ offers information that includes both the final position and final

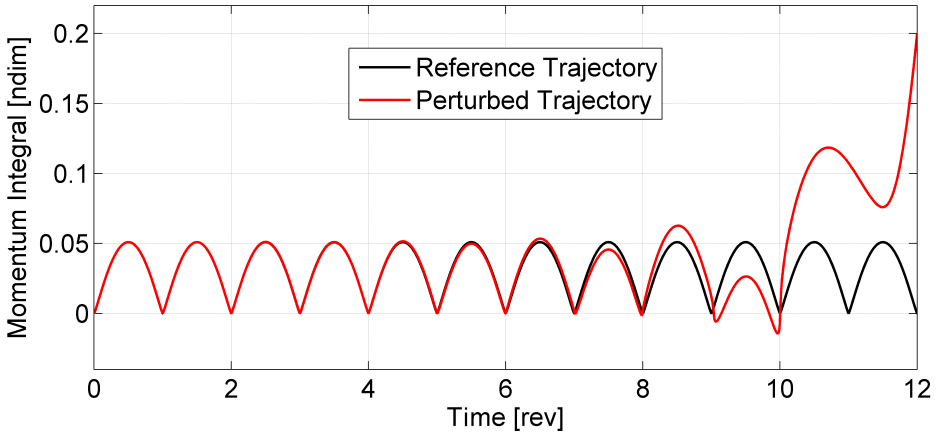

Figure 6.2. Momentum integral evaluated along a periodic orbit and a perturbed trajectory.

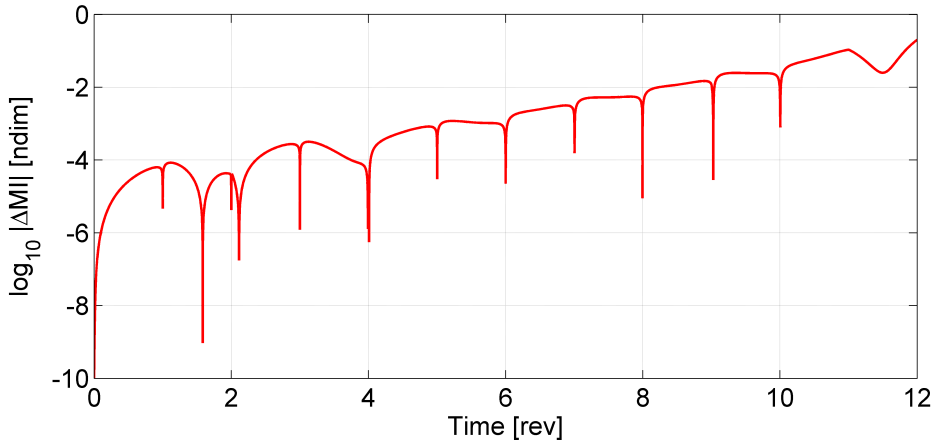

Figure 6.3. Difference in momentum integral between a periodic orbit and a perturbed trajectory.

velocity state change, it is a superior metric than the submatrix $\varphi_{C,v,v}$, thus selected for analysis for the orbit departure problem. For the stationkeeping problem, where the requirement is to minimize the maneuver costs without actively trying to maintain close boundedness to the reference orbit the stretching directions from the submatrix $\varphi_{C,v,v}$ is appropriate. For analyses, the stretching directions are divided into two sets based on their orientation in configuration space and labelled as type 'A' and type 'B', and are plotted in Figures 6.5(a) and 6.5(b), respectively. The type 'A' maximum stretching directions are loosely characterized pointing away from the local velocity direction while type 'B' maximum stretching direc-

tions have component in the local velocity direction. The naming convention is consistent throughout this investigation. Trajectories when propagated after maneuvers along each of type 'A' and type 'B' directions behave differently as observed in Figures 6.6(a) and 6.6(b), respectively. Naturally, their departure characteristics measured in terms of ΔMI in Figures 6.7(a) and 6.7(b) are different. Depending on the locations along the NRHO, maneuvers along type 'A' or type 'B' directions may offer rapid departure. More distinct behavior between trajectories after maneuvers along type 'A' or type 'B' directions is observed as the maneuver magnitude increases, and are detailed in this analyses.

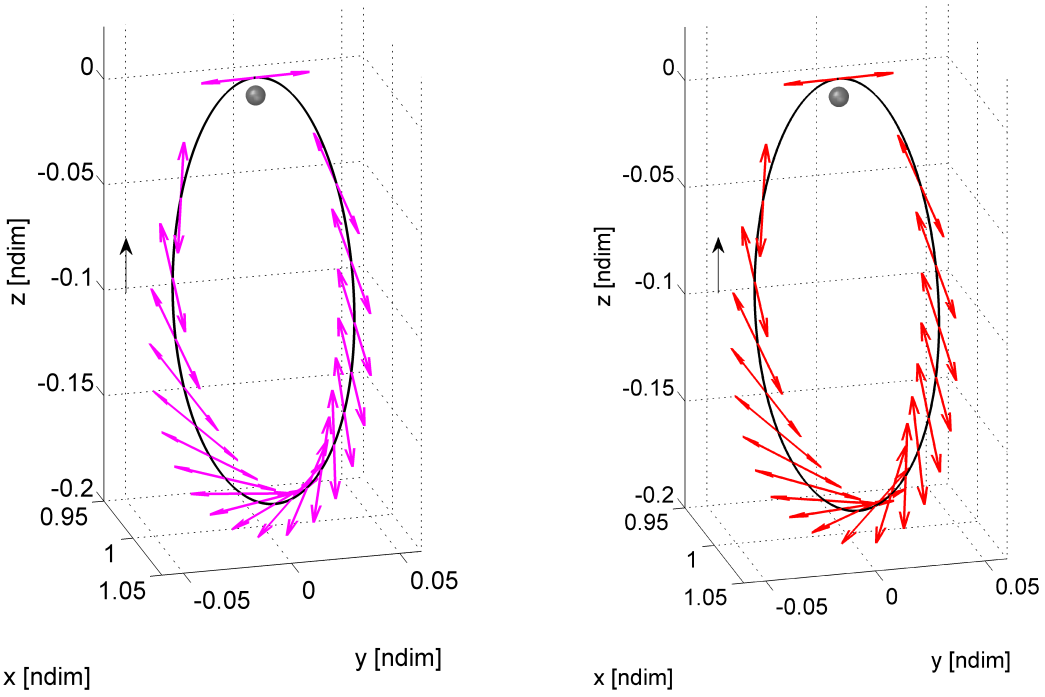

(a) Stretching directions from $\varphi_{C,v,v}(\wp, 0)$ (b) Stretching directions from $\varphi_{C,rv,v}(\wp, 0)$

Figure 6.4. Stretching directions computed using different submatrices of $\varphi_C(\wp, 0)$.

Invariant manifolds have been leveraged extensively for trajectory design applications and disposal [65], [128]–[132]. Although the manifold theory is effective for unstable orbits, relatively stable orbits do not possess well distinguished manifolds and making it less feasible. Since a lot of focus is on the Gateway mission, examples in this investigation are based on the baseline orbit under consideration. The unstable manifolds along the 9:2 synodic resonant southern L2 NRHO with an approximate perilune radius of 3200 km is plotted

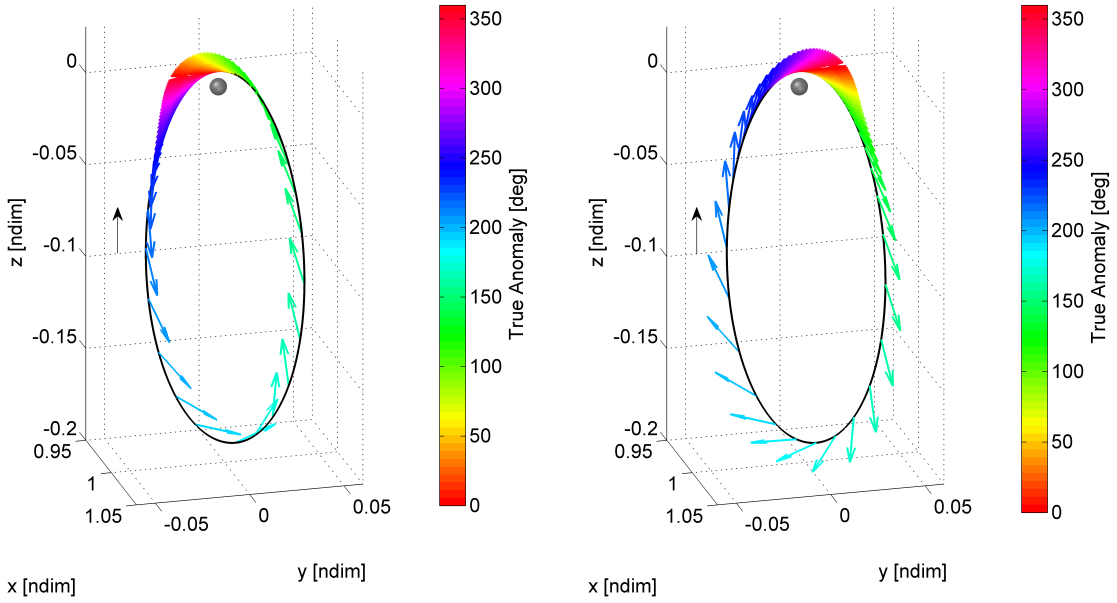

(a) Stretching directions 'A'

(b) Stretching directions 'B'

Figure 6.5. Maximum stretching directions for the 9:2 synodic resonant L2 southern NRHO.

in Figure 6.8(b). For comparison, the maximum stretching directions at the corresponding locations along the 9:2 synodic resonant southern L2 NRHO are plotted in Figure 6.8(a). For each of the plots in Figure 6.8 as well as in this investigation, locations on the NRHO are represented in terms of osculating true anomaly. Clearly, the unstable manifold directions and the maximum stretching directions are distinct. An alternate strategy that leverages maneuvers delivered in the maximum stretching direction is considered in this investigation. Departures along the unstable manifolds offer a reference, to compare the effectiveness of leveraging the maximum stretching directions. Trajectories along the unstable manifold directions are propagated for a duration of 10 revs of the reference NRHO, approximately equal to 65.73 days. These trajectories in the configuration space is plotted in Figure 6.9(a), where the color of each trajectory corresponds to the osculating true anomaly location at which the states along the unstable manifolds are propagated. The corresponding absolute difference in momentum integral evaluated along each of these trajectories relative to the reference NRHO are shown in Figure 6.9(b). For reference, the threshold value of $\Delta\text{MI} = 10^{-1}$ is also displayed, to identify the departed trajectories. A simplified way of classifying

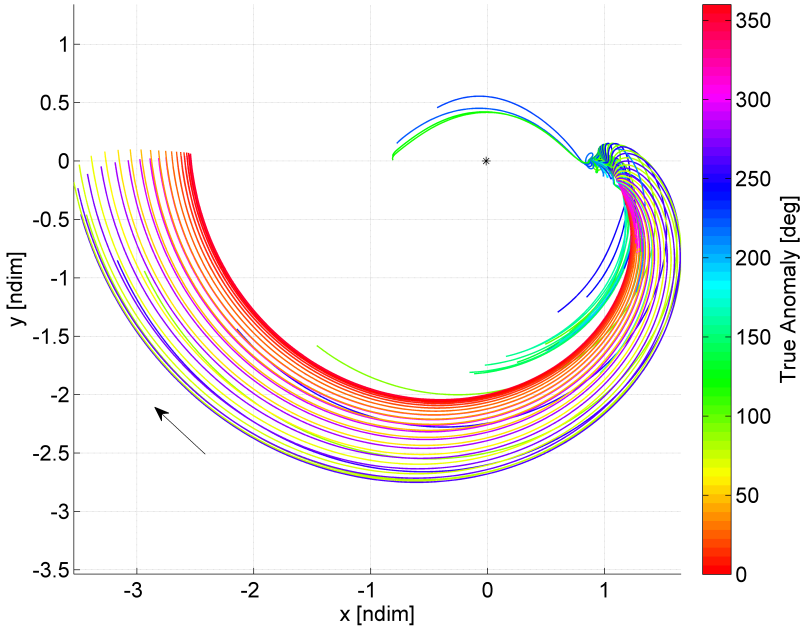

(a) Trajectories propagated after maneuver along direction 'A'

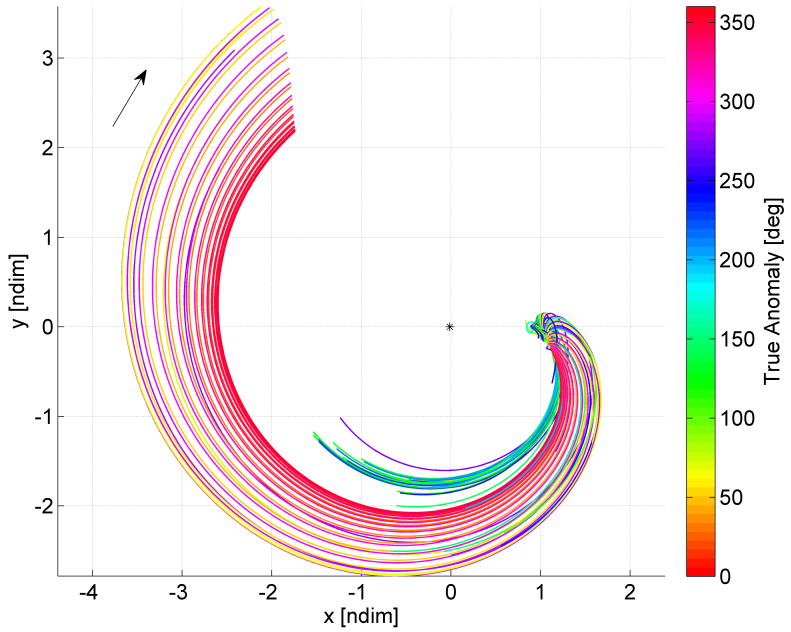

(b) Trajectories propagated after maneuver along direction 'B'

Figure 6.6. Trajectories propagated with maneuvers in the maximum stretching directions.

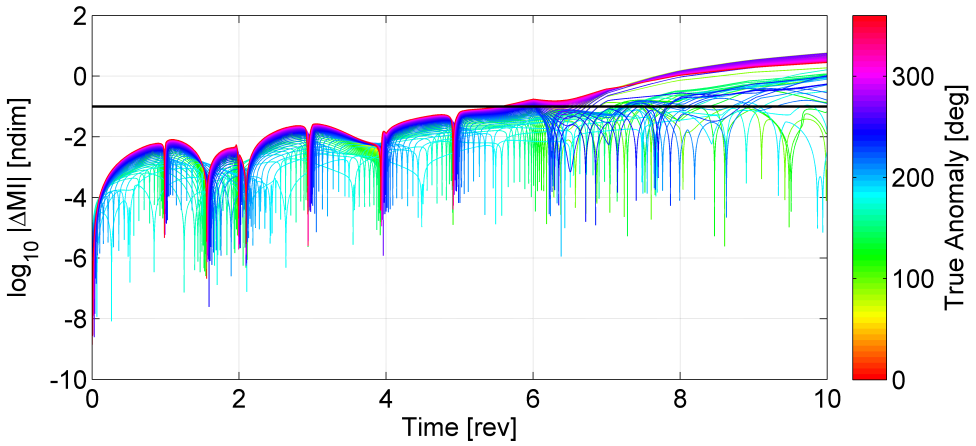

(a) Direction 'A'

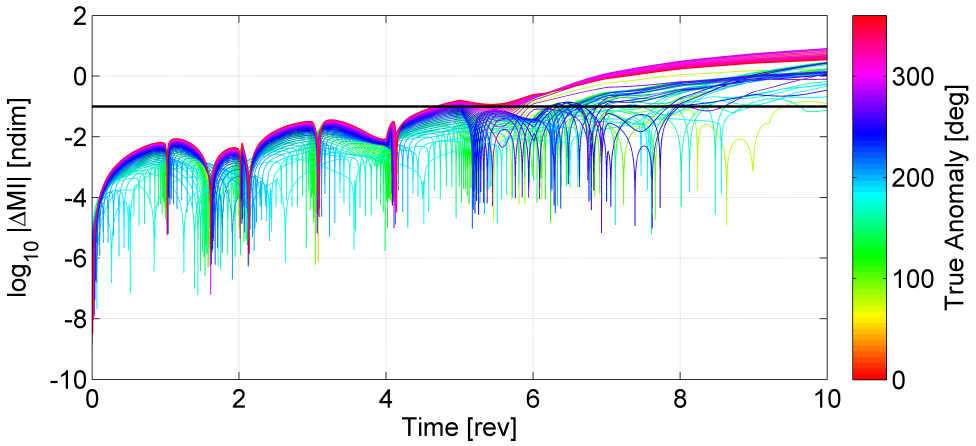

(b) Direction 'B'

Figure 6.7. Change in the momentum integral for trajectories relative to the reference orbit.

the departed trajectories is by identifying the time at which the trajectory exceeds the $\Delta MI = 10^{-1}$ criterion. Some departed trajectories may revert back to $\Delta MI < 10^{-1}$ values due to the underlying nonlinear motion, however, for simplicity, only the time at which the first departure condition is satisfied is recorded. Figure 6.9(c) describes the time for the trajectories along the unstable manifold directions for departure. The blue and the red data points correspond to the two unstable manifold directions at a given osculating true anomaly location on the orbit. For certain osculating true anomaly values, either only one or no data points are recorded, indicating that either only one or none of the unstable

manifolds propagated at that true anomaly does not depart the vicinity of the NRHO for the propagated time duration, respectively. Also, Figure 6.9(d) offers the value of $\Delta\text{MI} = 10^{-1}$ at the end of 65.73 days (10 revs of the reference orbit) of propagation, to identify if the trajectories remain departed. In general, for most true anomaly values, a trajectory along the unstable manifold direction takes at least 50 days to be considered departed.

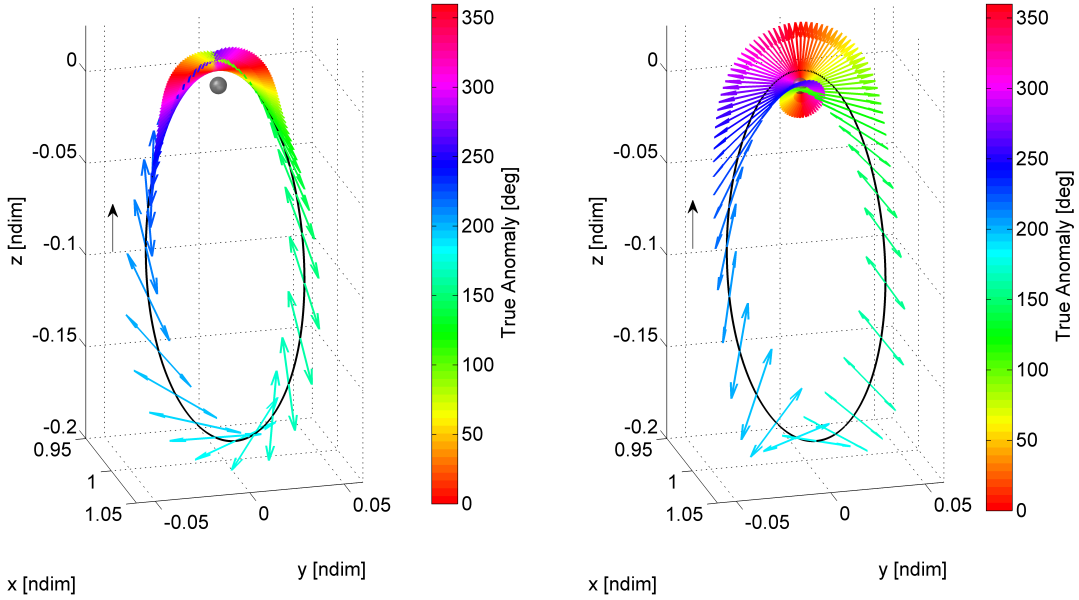

(a) Principal stretching directions (b) Unstable manifold directions

Figure 6.8. Maximum stretching directions and unstable manifold directions at various locations along the 9:2 synodic resonant L2 NRHO with perilune radius 3200 km.

A maneuver along the maximum stretching direction impacts the maximum change in the state magnitude at the end of the propagated arc. In most applications, within trajectory design or disposal, a specific time duration for the propagation may be unknown. For simplicity, the maximum stretching directions are computed along with the monodromy matrix. Of course, for applications with a known time of propagation, maximum stretching directions may be computed over the known propagation duration. The maximum stretching direction computed over a monodromy matrix, inherently assumes that a maneuver delivered at current time causes significantly large step-off over a period of propagation, which consequently aids in rapid departure from the stable orbit.

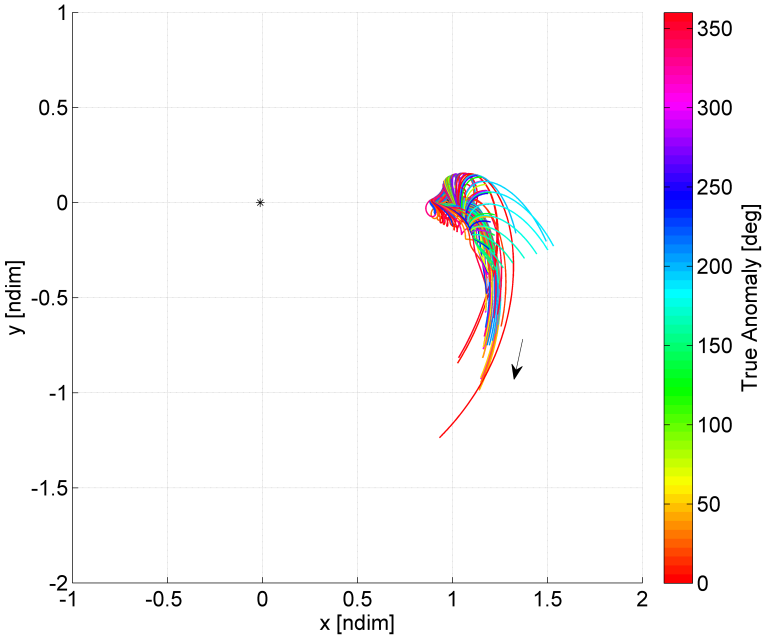

(a) Configuration Space

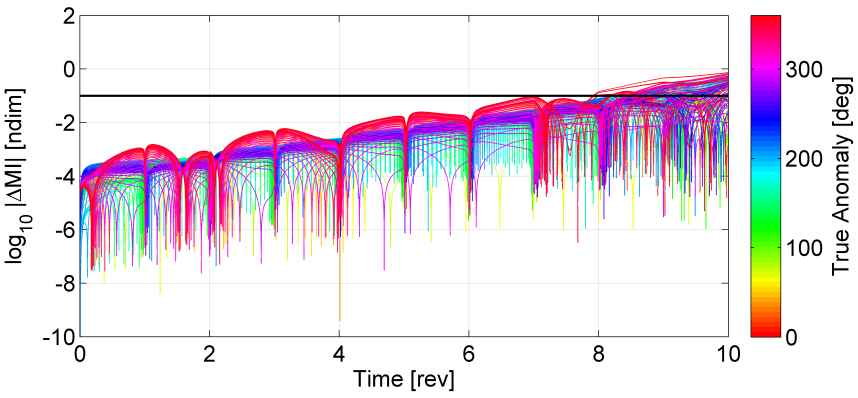

(b) |ΔMI|

Figure 6.9. Departure characteristics leveraging the unstable manifolds. Reference orbit: 9:2 synodic resonant L2 NRHO with a perilune radius of 3200 km.

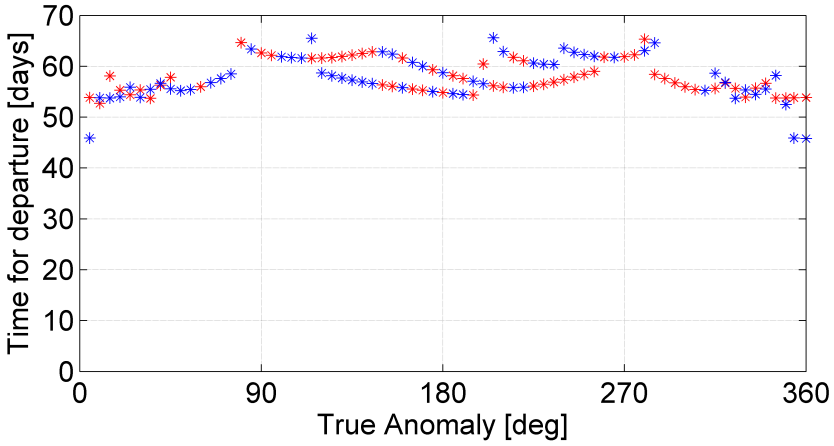

(c) Time for departure

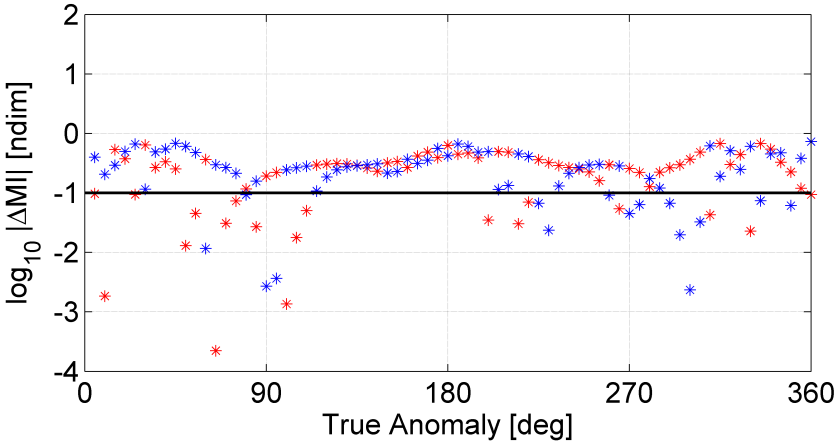

(d) $|\Delta \mathrm{MI}|$ at $t = 10\wp$

Figure 6.9. Departure characteristics leveraging the unstable manifolds. Reference orbit: 9:2 synodic resonant L2 NRHO with a perilune radius of 3200 km. (continued)

Unlike leveraging the unstable manifolds, an actual maneuver is delivered along the maximum stretching direction, along different locations on the NRHO. Similar to the unstable manifolds, there exists two sets of maximum stretching directions, that are labelled as type 'A' and type 'B', as demonstrated in Figures 6.5(a) and 6.5(b). Initial maneuvers of different magnitudes results in different final state changes. Figures 6.10(a), 6.10(b), 6.10(c), 6.10(d), 6.10(e) and 6.10(f) demonstrate the effect of maneuvers of magnitudes 1 m/s, 2 m/s, 4 m/s, 8 m/s, 16 m/s and 100 m/s as viewed in configuration space. In these figures, maneuvers are delivered along maximum stretching directions indicated in both type 'A' and type 'B'. It is to be noted that the Jacobi constant along the unstable manifolds is consistent with the reference NRHO, however, with the delivery of an additional maneuver along the maximum stretching direction, the Jacobi constant of the perturbed trajectory is no longer the same as the reference orbit. Besides, the Jacobi constant or the energy along the trajectory in Type 'A' direction and Type 'B' direction at the corresponding osculating true anomaly location may be different. An increase or decrease in energy of the trajectory does not correlate directly to the rate of departure. The change in the momentum integral evaluated along each of the perturbed trajectories, ones with maneuvers along the maximum stretching directions given in Figures 6.11(a), 6.11(b), 6.11(c), 6.11(d), 6.11(e) and 6.11(f) for maneuver magnitudes of 1 m/s, 2 m/s, 4 m/s, 8 m/s, 16 m/s and 100 m/s, respectively, offers a better assessment of the orbital departures. The direction of the implemented maneuver, i.e., type 'A' or type 'B' directions are more crucial in identifying departing trajectories along with the magnitude of maneuvers. Similar to identifying the time of departure for unstable orbits as in Figure 6.9(c), the time at which the departure conditions are satisfied are recorded for trajectories that incorporate maneuvers delivered along the maximum stretching directions. Figures 6.12(a), 6.12(b), 6.12(c), 6.12(d), 6.12(e) and 6.12(f), correspond to the times of departure, for cases with maneuver magnitudes of 1 m/s, 2 m/s, 4 m/s, 8 m/s, 16 m/s and 100 m/s, respectively. These times correspond to the first time the $|\Delta MI|$ value exceeds the 10^{-1} line in Figures 6.11(a), 6.11(b), 6.11(c), 6.11(d), 6.11(e) and 6.11(f), respectively. In Figure 6.11(a), maneuvers of magnitude 1 m/s are delivered along type 'A' (colored in blue) and type 'B' (colored in red) directions, and across different location on the NRHO are successful in departing over the propagated duration. Certain trajectories depart as

rapidly as 7 days after the onset of the propagation, while most of the trajectories depart within 50 days of the initiation of propagation. Such departure times are easily assessed in comparison to departing along unstable manifold that require at least 50 days to depart. Type 'A' directions are loosely aligned away from the orbit velocity directions while type 'B' directions include significant components in the velocity direction. With an increase in the maneuver magnitudes, the behavior of the trajectories with maneuvers along the type 'A' and type 'B' maneuver direction bifurcates, and are evident from Figures 6.13(a), 6.13(b), 6.13(c), 6.13(d), 6.13(e) and 6.13(f) that describes the value of $|\Delta MI|$ for a sufficiently long propagation duration, 65.73 days (10 revs of the reference orbit) in this case. Clearly, with an increase in the magnitude of maneuvers that are delivered along type 'A' (colored in blue) and type 'B' (colored in red) directions, the behavior. For a significantly large maneuver magnitude of 100 m/s as in Figure 6.12(f), most trajectories along type 'A' direction do not depart the NRHO vicinity in the propagated time duration. By virtue of the direction of maneuver, a loss in energy results in the trajectories getting captured in the lunar vicinity, rather in the Earth-Moon vicinity. Trajectories propagated with a 100 m/s maneuver magnitude along the type 'A' directions, at locations near the Moon, gets captured to Lunar conic orbits as illustrated in Figure 6.14(a). In contrast, the maneuvers along type 'B' directions elevates the rate of departure, and most trajectories depart within 10 days of propagation. Especially for larger maneuver magnitudes, the stark contrast between the behavior of trajectories after maneuvers are delivered in type 'A' and type 'B' directions, are evident as in Figure 6.11(a). The $|\Delta MI|$ value for trajectories that leverage type 'A' maneuver directions offer periodic behavior and boundedness, while $|\Delta MI|$ value for trajectories that leverage type 'B' maneuver directions increase rapidly before approaching an asymptotic behavior as the spacecraft continuously deviates away from the Earth-Moon vicinity in spiral behavior when observed in the rotating frame of view.

Maneuvers along velocity, normal and co-normal (VNC) directions to assist in departure are investigated by Davis et al. [133]. Maneuvers delivered along the rotating velocity directions of the NRHO, implemented close to the periapsis region, offers faster departure [133]. A similar trend is observed in this investigation, where maneuvers delivered along the

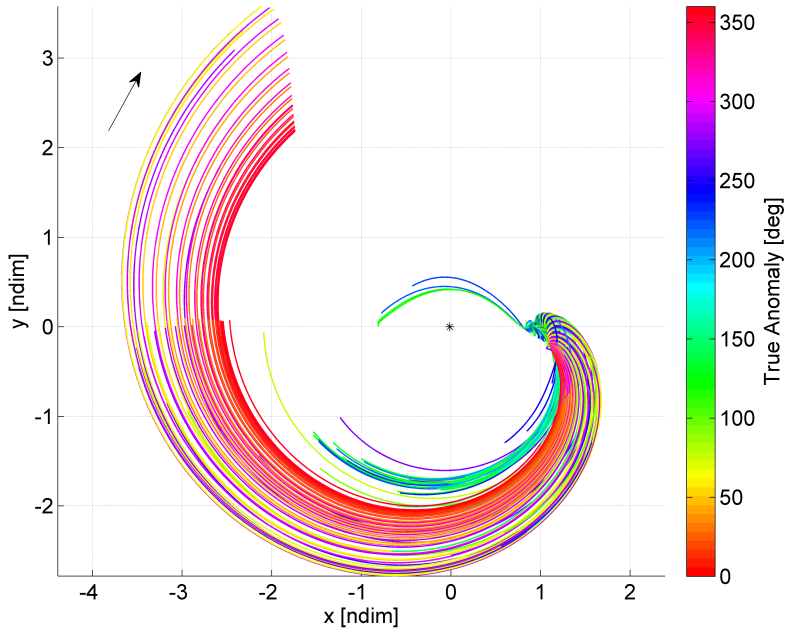

(a) $|\Delta\bar{v}| = 1m/s$

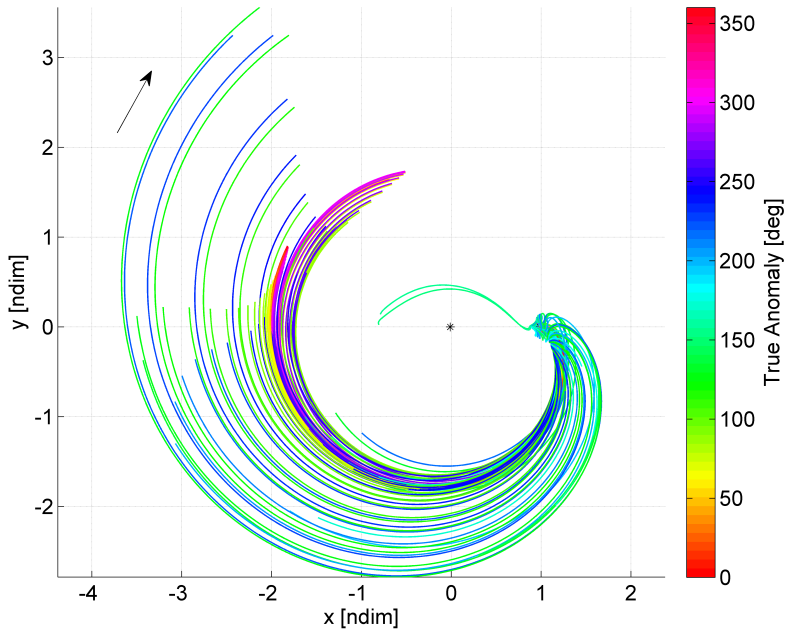

(b) $|\Delta\bar{v}| = 2m/s$

Figure 6.10. Trajectories deviating from the reference orbit after maneuvers along the maximum stretching directions. Maneuver location: variable true anomaly. Time of propagation: $10\wp$ (65.73 days). Reference orbit: 9:2 synodic resonant L2 NRHO with a perilune radius of 3200 km.

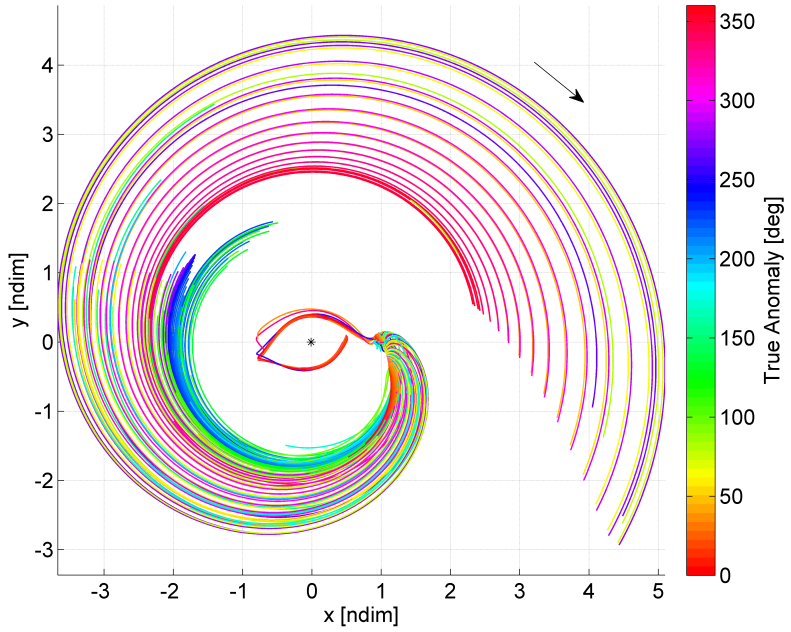

(c) $|\Delta\bar{v}| = 4m/s$

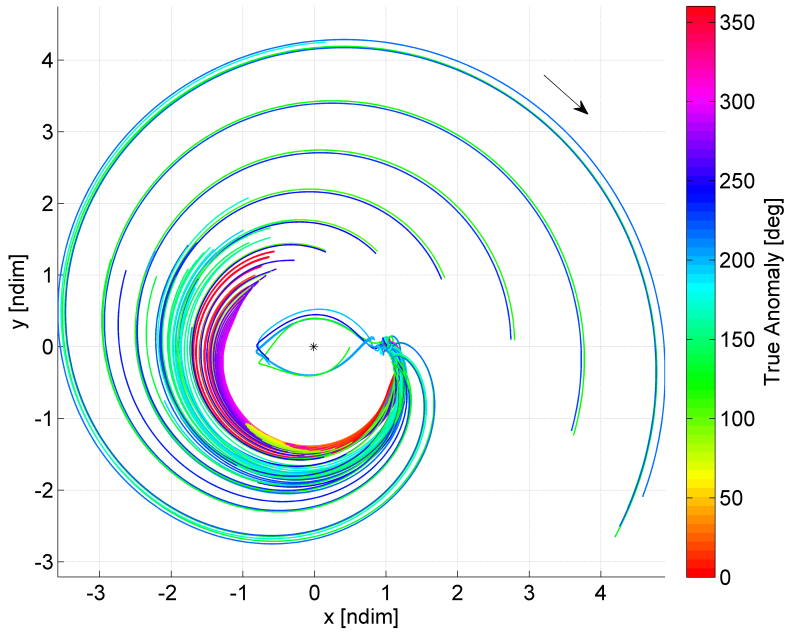

(d) $|\Delta\bar{v}| = 8m/s$

Figure 6.10. Trajectories deviating from the reference orbit after maneuvers along the maximum stretching directions. Maneuver location: variable true anomaly. Time of propagation: $10\wp$ (65.73 days). Reference orbit: 9:2 synodic resonant L2 NRHO with a perilune radius of 3200 km. (continued)

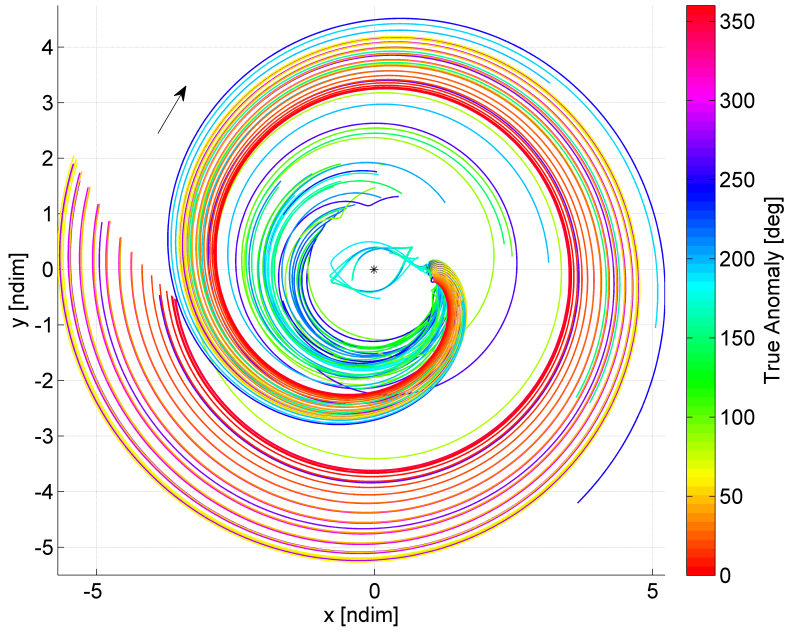

(e) $|\Delta\bar{v}| = 16m/s$

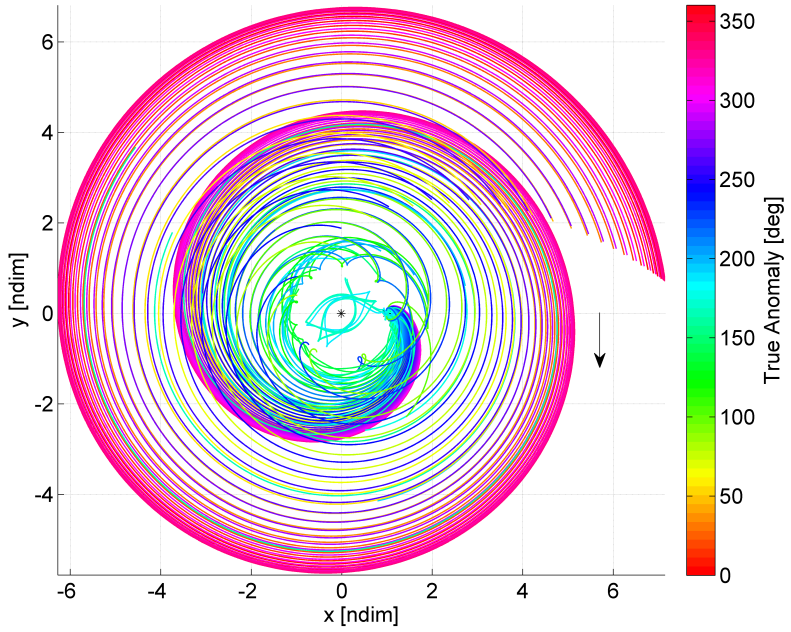

(f) $|\Delta\bar{v}| = 100m/s$

Figure 6.10. Trajectories deviating from the reference orbit after maneuvers along the maximum stretching directions. Maneuver location: variable true anomaly. Time of propagation: $10\wp$ (65.73 days). Reference orbit: 9:2 synodic resonant L2 NRHO with a perilune radius of 3200 km. (continued)

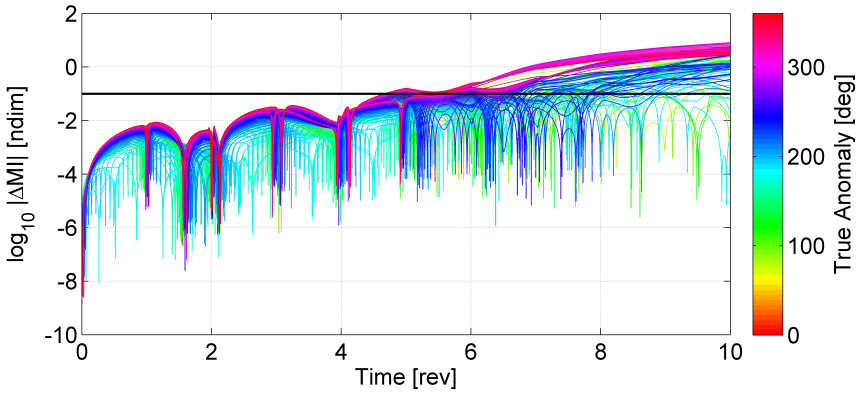

(a) $|\Delta\bar{v}| = 1m/s$

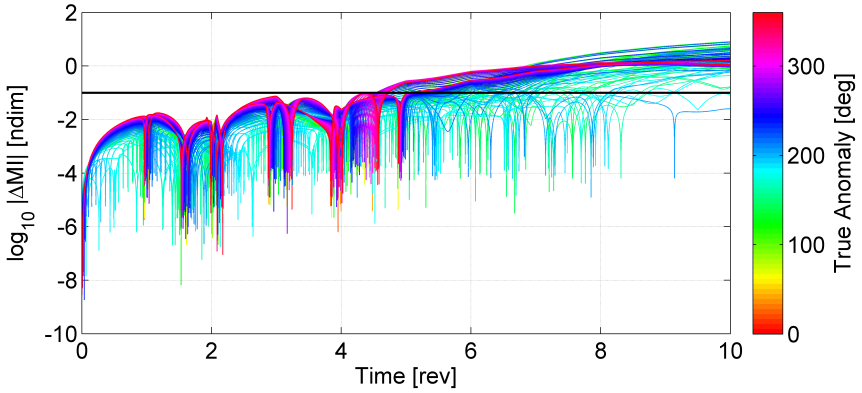

(b) $|\Delta\bar{v}| = 2m/s$

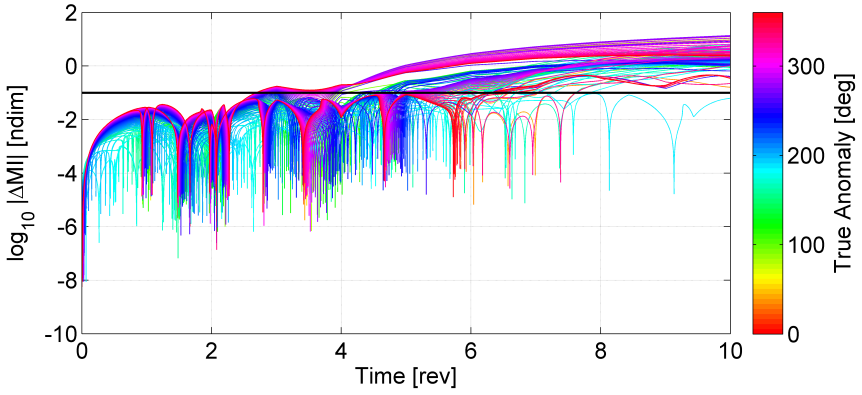

(c) $|\Delta\bar{v}| = 4m/s$

Figure 6.11. Change in the momentum integral with time for trajectories deviating from the reference orbit after maneuvers along the maximum stretching directions, measured at the end of the propagated segment. Maneuver location: variable true anomaly. Reference orbit: 9:2 synodic resonant L2 NRHO with a perilune radius of 3200 km.

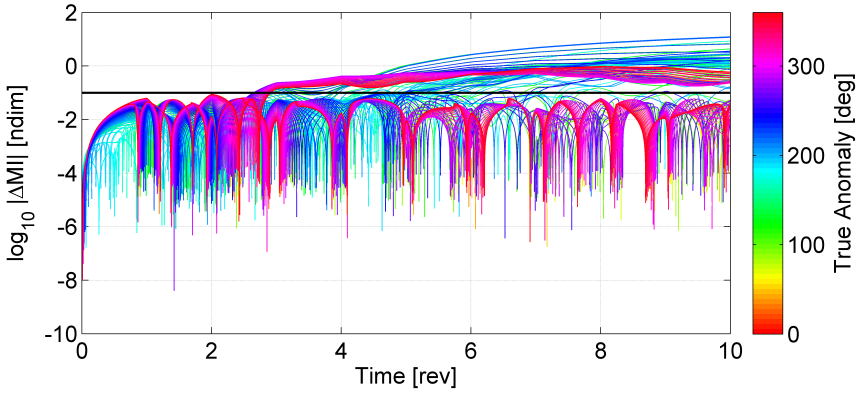

(d) $|\Delta\bar{v}| = 8m/s$

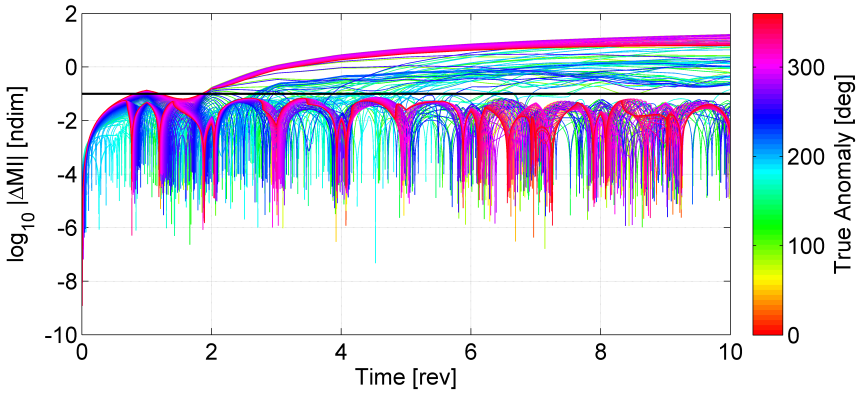

(e) $|\Delta\bar{v}| = 16m/s$

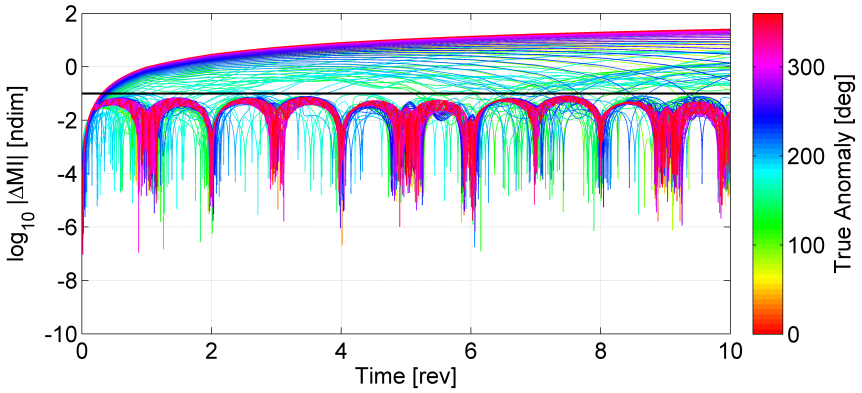

(f) $|\Delta\bar{v}| = 100m/s$

Figure 6.11. Change in the momentum integral with time for trajectories deviating from the reference orbit after maneuvers along the maximum stretching directions, measured at the end of the propagated segment. Maneuver location: variable true anomaly. Reference orbit: 9:2 synodic resonant L2 NRHO with a perilune radius of 3200 km. (continued)

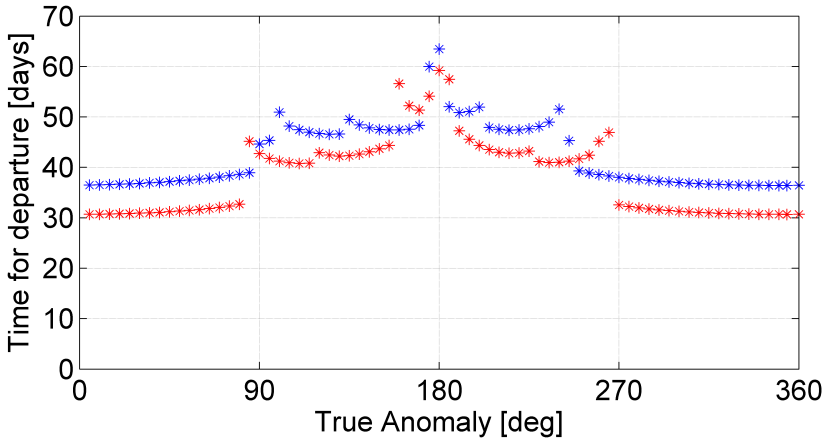

(a) $|\Delta\bar{v}| = 1m/s$

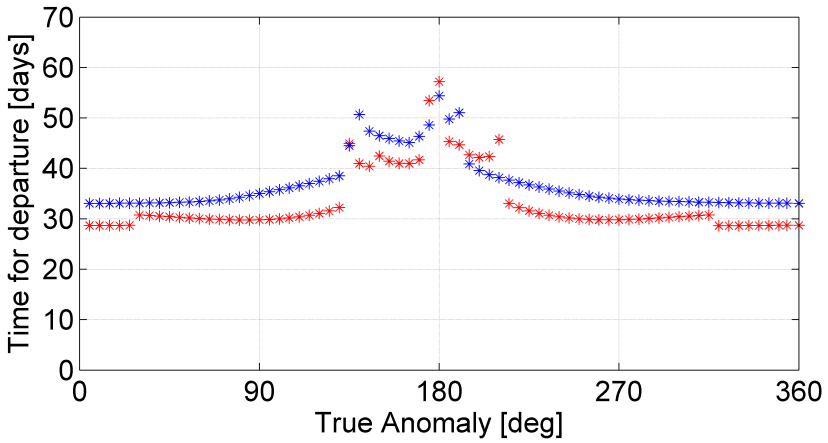

(b) $|\Delta\bar{v}| = 2m/s$

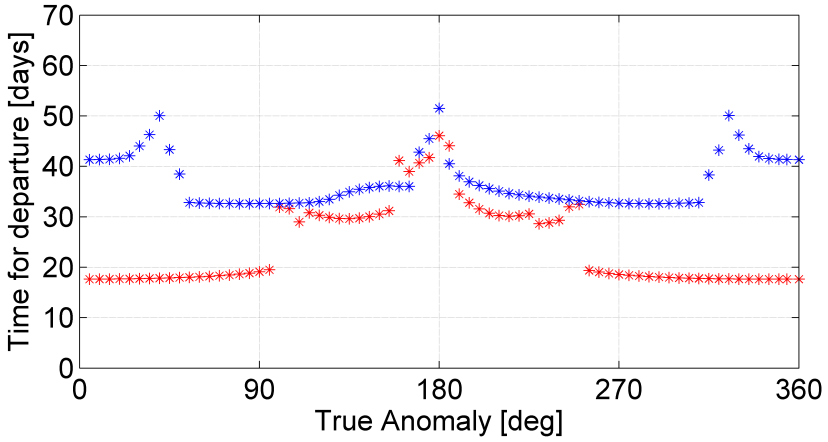

(c) $|\Delta\bar{v}| = 4m/s$

Figure 6.12. Time for departure for trajectories perturbed from the reference NRHO with maneuver of different magnitudes along the maximum stretching directions. Maneuver location: variable true anomaly. Reference orbit: 9:2 synodic resonant L2 NRHO with a perilune radius of 3200 km.

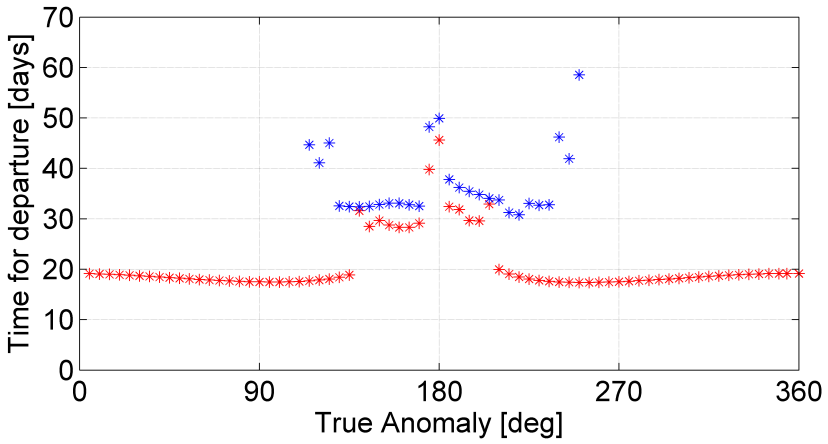

(d) $|\Delta\bar{v}| = 8m/s$

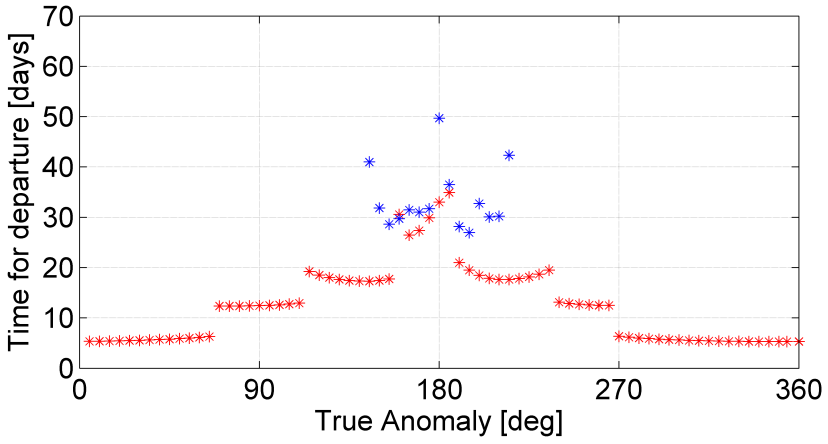

(e) $|\Delta\bar{v}| = 16m/s$

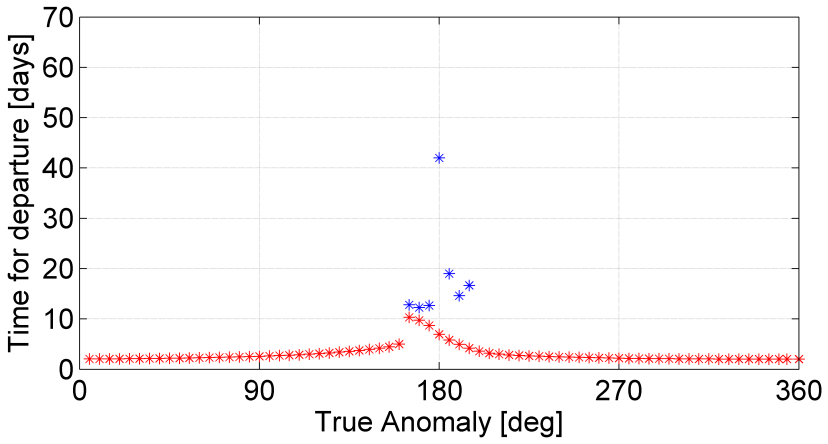

(f) $|\Delta\bar{v}| = 100m/s$

Figure 6.12. Time for departure for trajectories perturbed from the reference NRHO with maneuver of different magnitudes along the maximum stretching directions. Maneuver location: variable true anomaly. Reference orbit: 9:2 synodic resonant L2 NRHO with a perilune radius of 3200 km. (continued)

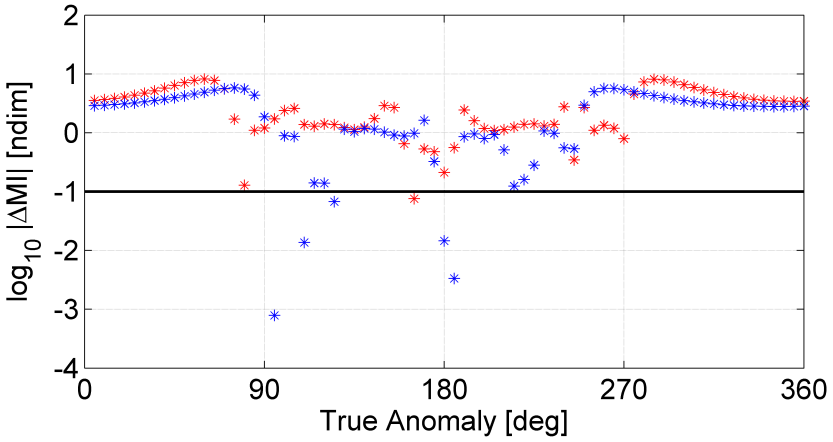

(a) $|\Delta\bar{v}| = 1m/s$

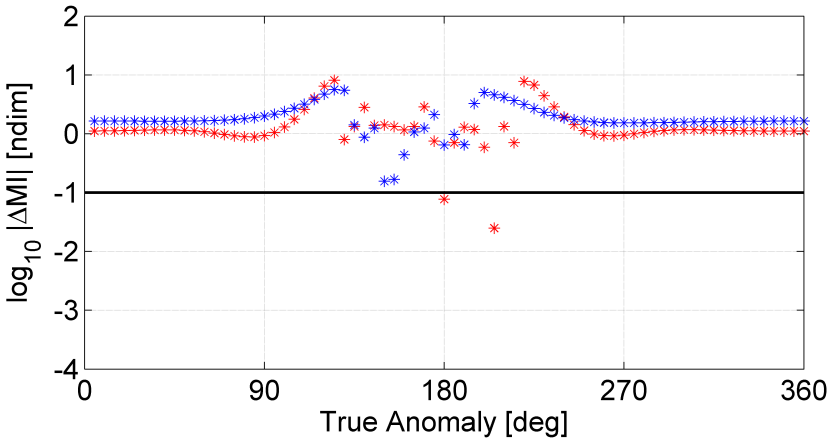

(b) $|\Delta\bar{v}| = 2m/s$

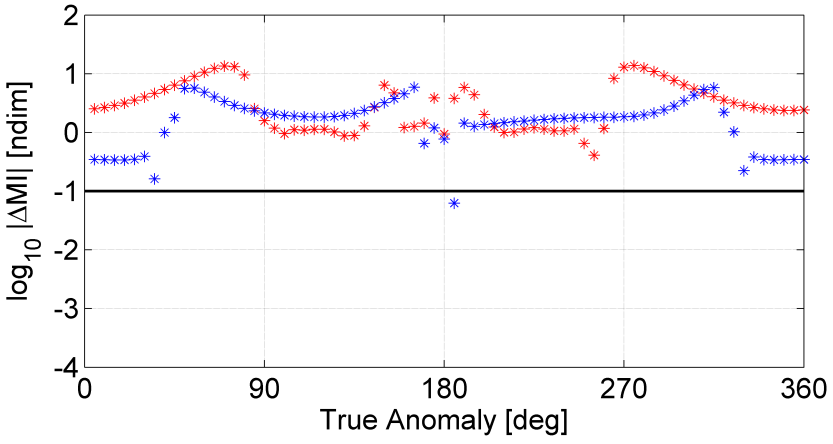

(c) $|\Delta\bar{v}| = 4m/s$

Figure 6.13. Value of $|\Delta\text{MI}|$ for trajectories deviating from the reference orbit measured at the end of the propagated segment. Maneuver location: variable true anomaly. Time of propagation: $10\wp$ (65.73 days). Reference orbit: 9:2 synodic resonant L2 NRHO with a perilune radius of 3200 km.

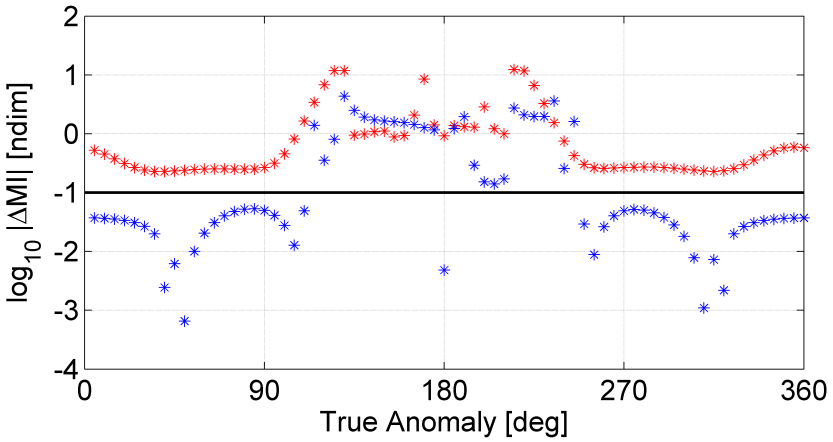

(d) $|\Delta\bar{v}| = 8m/s$

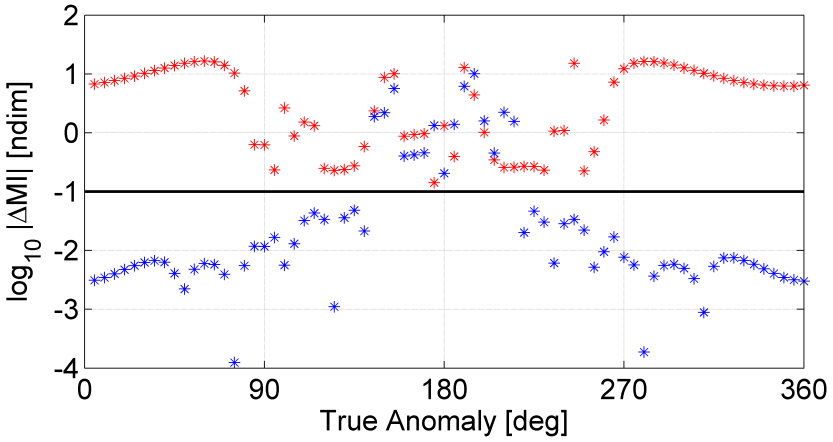

(e) $|\Delta\bar{v}| = 16m/s$

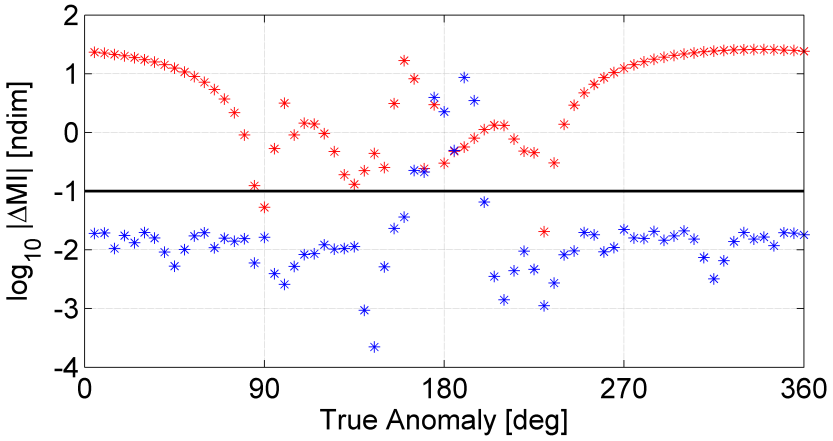

(f) $|\Delta\bar{v}| = 100m/s$

Figure 6.13. Value of $|\Delta\text{MI}|$ for trajectories deviating from the reference orbit measured at the end of the propagated segment. Maneuver location: variable true anomaly. Time of propagation: $10\wp$ (65.73 days). Reference orbit: 9:2 synodic resonant L2 NRHO with a perilune radius of 3200 km. (continued)

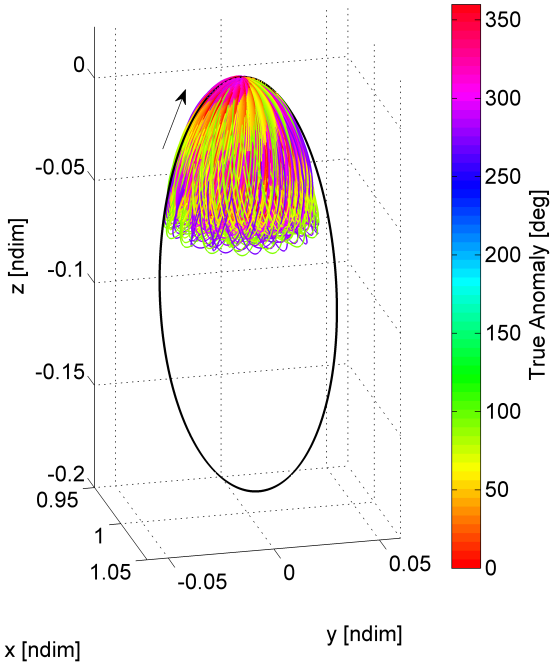

(a) Quasi-periodic trajectories near Moon

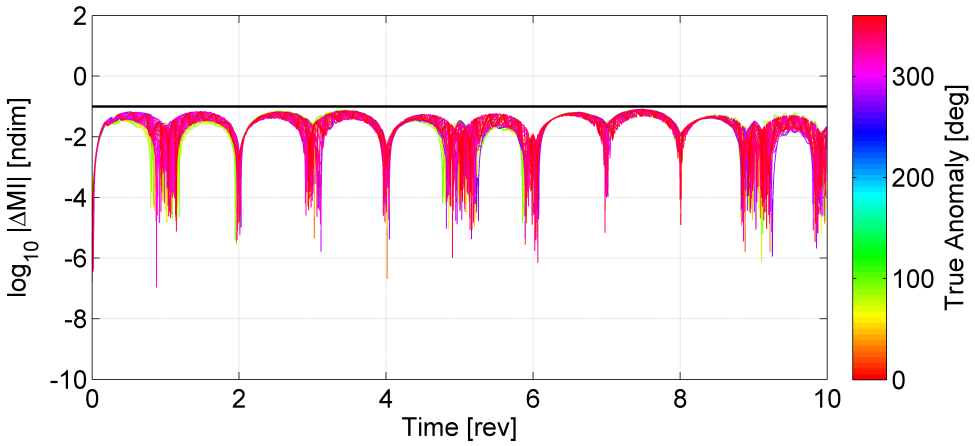

(b) Bounded momemtum integral

Figure 6.14. Bounded quasi-periodic motion near Moon.

type 'B' directions that is aligned close to the rotating velocity direction is more conducive to rapid departure. Maximum stretching direction type 'B' are more conducive to rapid departure relative to type 'A', however, for smaller maneuver magnitudes even type 'A' directions offer departure with marginally larger time of flight.

6.2 Transfer Trajectory Design

Ability to depart an orbit serves as a preliminary step to design transfers between two regions in space. In a nonlinear system it is challenging to determine initial states that drives the spacecraft to the desired final location. Transfers between stable regions in space have utilized intermediate arcs of known orbits, including resonant orbits, and also underlying manifold structures of nearby unstable orbits. Although in the nonlinear regime of the CR3BP there are numerous solutions that may offer suitable options for transfers, having a preconceived notion of the intermediate structures to explore is nontrivial. Furthermore, transfer options may be restricted to evolve along the underlying structures that are incorporated. Direct transfers that use a shooting algorithm to transfer between orbits are also considered in the literature, however, having a suitable initial guess for the shooting algorithm may not be intuitive, thus, the applications of direct transfers may be restricted to orbits that are nearby in the configuration space. Besides, having only two maneuvers along the transfer arc, i.e., a departure and an arrive maneuver may not necessarily be the cost-effective option. Maps offer useful information by reducing the number of free variables. In this investigation, for stable orbits, in the absence of well-defined unstable and stable manifold structures, maneuvers are delivered along the maximum stretching directions and the updated states are propagated until a pre-selected hyperplane crossing. Selection of an hyperplane is application specific. For maps used in this investigation, position coordinates at the hyperplane crossings are recorded. Velocity components may be incorporated as glyphs if necessary, however not included in this work [134], [135]. A combination of trajectory crossings and manifold crossings are also an option subject to the type of departure and arrival orbit and their stability characteristics. It is desirable for transfer trajectory design process to select an appropriate combination of crossings of the departure arcs and the arrival arcs at the hyperplane, with small discontinuity in the position and the velocity

states. An optimization scheme is introduced to generate a continuous transfer between the departure orbit to the arrival orbit that leverages the departure and arrival arc determined from the map. A schematic representation of the transfer trajectory optimization process is illustrated in Fig. 6.15. For reference, orbit colored in cyan is the departure orbit while orbit in magenta is the arrival orbit. The intermediate departure arc and arrival arc are colored in blue and red, respectively. In this investigation, the transfer design process employs three impulsive maneuvers, $\Delta\bar{v}_{dep}$ to transition from the departure orbit to the departure arc, an intermediate maneuver, $\Delta\bar{v}_{int}$, to progress from the departure arc to the arrival arc, and finally $\Delta\bar{v}_{arr}$ to transition from the arrival arc to the arrival orbit. One of the requirements for a space mission is to minimize the propellant consumption, consequently reducing the size of the maneuvers. An optimization scheme minimizes the cost function, J, given by

$$min\ J = |\Delta\bar{v}_{dep}| + |\Delta\bar{v}_{int}| + |\Delta\bar{v}_{arr}| \tag{6.4}$$

$$= \sqrt{\Delta\bar{v}_{dep}^{\mathrm{T}}\Delta\bar{v}_{dep}} + \sqrt{\Delta\bar{v}_{int}^{\mathrm{T}}\Delta\bar{v}_{int}} + \sqrt{\Delta\bar{v}_{arr}^{\mathrm{T}}\Delta\bar{v}_{arr}} \tag{6.5}$$

i.e., the sum of total maneuver magnitudes, $\Delta\bar{v}$. Here,

$$\Delta\bar{v}_{dep} = \bar{v}_{dep-arc}(t=0) \quad - \quad \bar{v}_{dep-orbit}(t=\tau_1) \tag{6.6}$$

$$\Delta\bar{v}_{int} = \bar{v}_{arr-arc}(t=0) \quad - \quad \bar{v}_{dep-arc}(t=ToF_{dep}) \tag{6.7}$$

$$\Delta\bar{v}_{arr} = \bar{v}_{arr-orbit}(t=\tau_2) \; - \; \bar{v}_{arr-arc}(t=ToF_{arr}) \tag{6.8}$$

such that ToF_{dep} is the time of flight along the departure arc while ToF_{arr} is the time of flight along the arrival arc. The total time of flight for the transfer is the sum of ToF_{dep} and ToF_{arr}. The initial and the final position states are constrained to remain on the departure and arrival orbits, respectively. In the optimization process, the departure position states and the arrival position states are free to advance along the orbit and may be different from the initial guess. To constraint the departure and the arrival position states on the orbit, additional τ constraint is incorporated, such that τ_1 and τ_2 are certain time durations from a fixed location on the departure and arrival orbits, respectively. Locally optimal solutions are generated that resemble the geometry predicted by the initial guess.

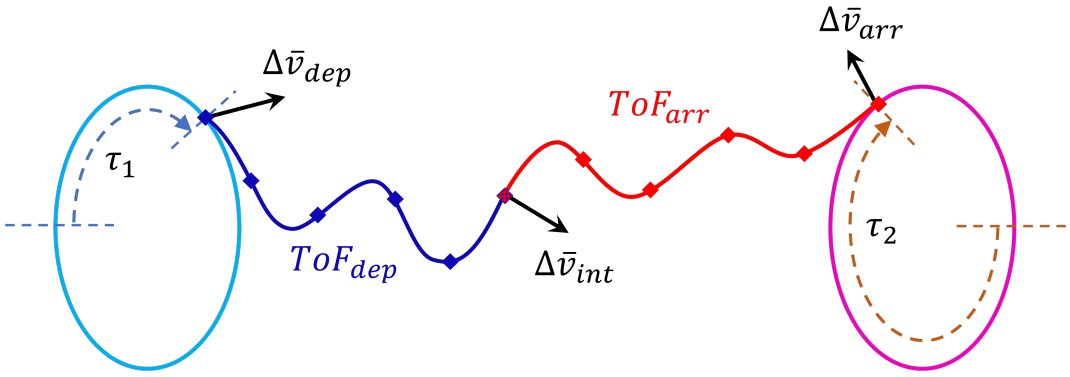

Figure 6.15. Schematic for transfer trajectory optimization.

6.2.1 Transfers between L2 southern 9:2 synodic resonant NRHO to L2 northern 9:2 synodic resonant NRHO

The 9:2 synodic resonant orbit in the southern and northern L2 NRHO families are a current focus for various mission scenarios, primarily due to close passages near the polar regions of the Moon and the relatively stable nature of the orbit. The time period, Jacobi constant and the stability indices of the NRHOs of interest are listed in Table 6.1. Clearly, the magnitudes of the stability indices showcase their almost stable characteristics. A transfer between the two stable orbits are leveraged using maneuvers delivered along the maximum stretching directions. Due to very small unstable eigenvalue for the flow along these NRHOs, the rate of departure is very low. As observed in Figure 6.9(c), leveraging manifold structures may take a significantly longer duration to depart. Besides, for stable orbits, leveraging manifold structures may not even be an option. Maneuvers are delivered along the maximum stretching direction at various locations along the orbit, measured in terms of an osculating true anomaly [82], [83]. Maneuvers of fixed magnitudes are delivered along both sets of maximum stretching direction, type 'A' and type 'B', and the updated states are propagated for a significantly long duration. These trajectories intersect with the selected hyperplanes on multiple occasions. Each crossings at the hyperplane are recorded to generate a comprehensive map. For the transfer between the L2 southern 9:2 synodic resonant NRHO and the L2 northern 9:2 synodic resonant NRHO, two different hyperplanes are considered, the xy-plane and the xz-plane. A 2-sided plane crossings are recorded, i.e., in the positive and the negative velocity directions. Figure 6.16(a) demonstrates the cross-

ings of each of these trajectories propagated from various locations along the NRHO orbits to the $z = 0$ hyperplane, i.e., on the xy plane. Similarly, Figure 6.16(b) demonstrates the crossings on the $y = 0$ hyperplane, i.e., on the xz plane. Blue asterisks (*) correspond to the crossings along the departure arcs that are propagated from the 9:2 synodic resonant L2 southern NRHO forwards in time, while red asterisks (*) correspond to crossings along arrival arcs from the 9:2 synodic resonant L2 northern NRHO that are propagated backwards in time. Along a forward propagated segment, the maximum stretching directions are computed from the matrix $\varphi_{C,rv,v}(\wp, 0)$. In contrast, for a backwards propagated segment, the maximum stretching directions are computed from the matrix $\varphi_{C,rv,v}(0, \wp)$. Here, $\wp$ is the time period of the 9:2 synodic resonant southern and northern L2 NRHO. Common practise for transfer trajectory design is to transition from the departure arc to the arrival arc at the hyperplane, an appropriate choice is to select a combination of a departure crossing and an arrival crossing on the hyperplane with a small state change, in position and velocity. The maps in Figure 6.16 are generated by propagating departure arc and arrival arc following maneuver of size $|\Delta\bar{v}| = 1$ m/s. Maps that result from other $|\Delta\bar{v}|$ values also offer conducive transfers. Besides, the $|\Delta\bar{v}|$ value along the departure arc and the arrival arc need not be of the same magnitude. In the case of transfers between southern and northern NRHO of the same size, the $|\Delta\bar{v}|$ value along the departure arc and the arrival arc are considered the same to exploit the underlying similarity and symmetry in the maps.

Table 6.1. Orbital parameters for 9:2 synodic resonant NRHO with 3200 km perilune radius

Period [days]	6.572983112436425
Jacobi Constant	3.046884268549730
Stability Indices	-1.312122132349322 0.686856822471390 1

Combinations of departure and arrival arc crossings on the maps as in Figure 6.16 near the Moon offer interior transfers, i.e., loosely characterized by the trajectory remaining in

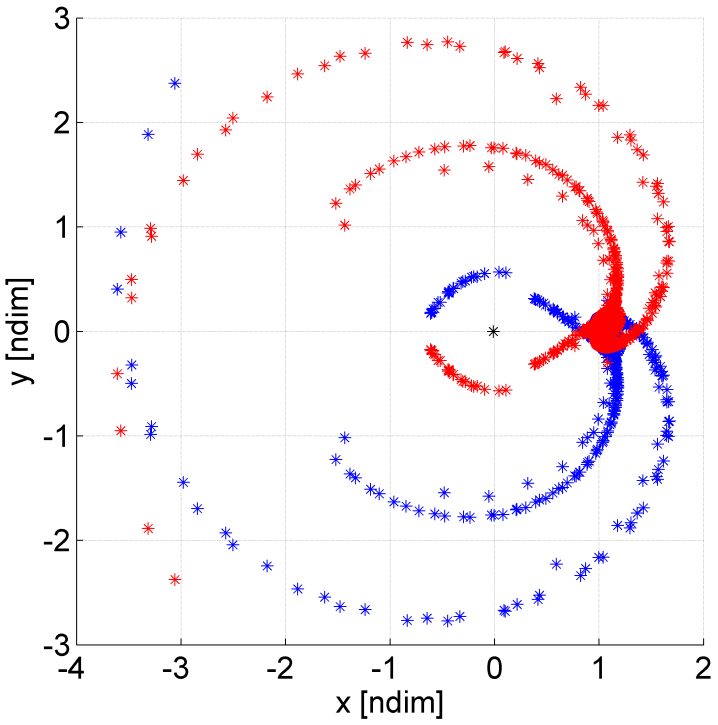

(a) xy-plane crossing map

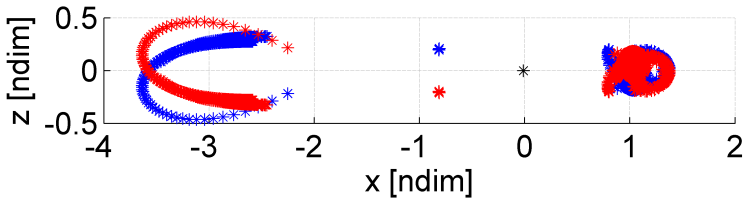

(b) xz-plane crossing map

Figure 6.16. Two sided plane crossing maps. Blue asterisks (*) correspond to departure arcs from southern NRHO propagated forwards in time, while red asterisks (*) correspond to arrival arcs from northern NRHO propagated backwards in time. Map for $|\Delta\bar{v}| = 1$ m/s.

the proximity of the region of interest [136]. Of course several combinations of departure and arrival arcs are possible. These combination offer reliable initial guess for transfer trajectory design. The combination of departure and arrival crossings on the maps may not be continuous in position and velocity. An optimization scheme, as illustrated previously, is adopted to generate a continuous transfer with three maneuvers, $\Delta\bar{v}_{dep}$, $\Delta\bar{v}_{int}$ and $\Delta\bar{v}_{arr}$. Figures 6.17 and 6.18 are examples of locally optimal interior transfer that have similar geometry

in the configuration space but have marginally different time of flight. A different geometry of transfer that exploits motion along the L1 axial orbit is obtained in Figure 6.19. Figure 6.20 offers another geometry of transfer that has multiple loops in the L1 and L2 side of the Moon. The initial guess for each of the locally optimal interior transfers in Figures 6.17, 6.18, 6.19 and 6.20 are identified from the map in Figure 6.16(a) that is generated based of departure and arrival maneuver magnitude of 1 m/s. Of course, the optimal maneuvers, $|\Delta\bar{v}_{dep}|$ and $|\Delta\bar{v}_{arr}|$, may not be precisely the same as the initial guess, i.e., 1 m/s. For cases with small position and velocity discontinuity on the hyperplane crossing maps yield locally optimal solutions that are relatively closer to the initial guess, in contrast to cases where the departure and arrival crossings on the map that have larger discontinuity. The maneuver costs as well as the time of flight for each of the transfers in Figures 6.17, 6.18, 6.19 and 6.20 are detailed in Table 6.2. The osculating true anomaly locations along the departure and arrival orbits for the locally optimal transfers are also listed in Table 6.2.

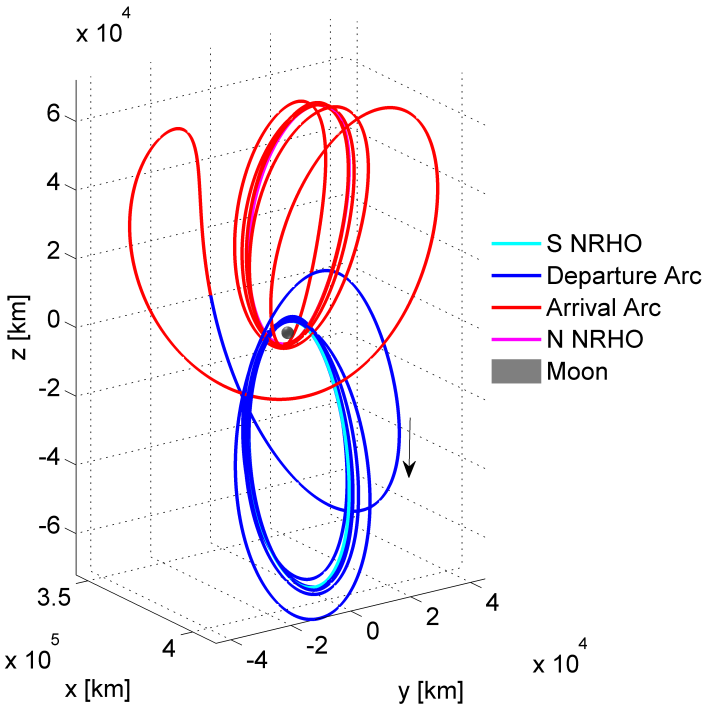

Figure 6.17. Isometric view of an optimal transfer between L2 southern 9:2 synodic resonant NRHO to L2 northern 9:2 synodic resonant NRHO. View for Case 1 transfer.

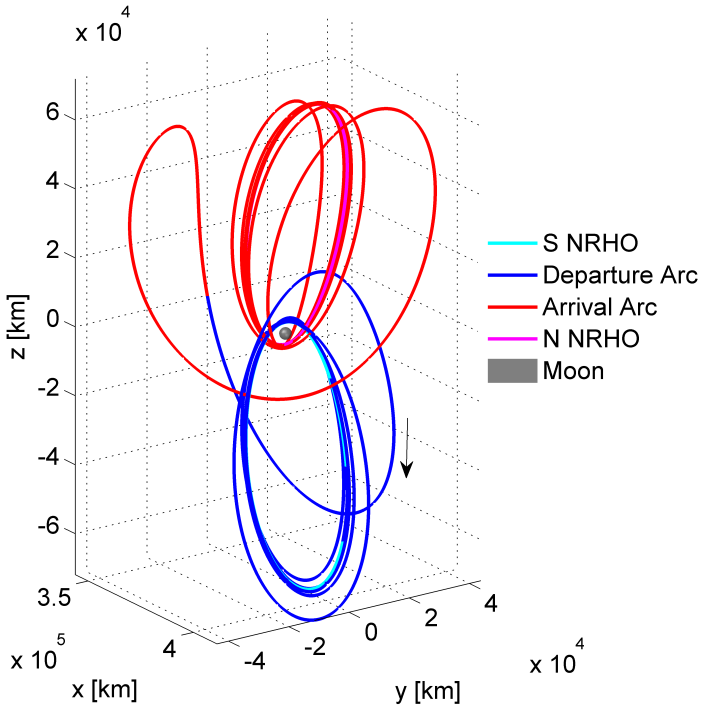

Figure 6.18. Isometric view of an optimal transfer between L2 southern 9:2 synodic resonant NRHO to L2 northern 9:2 synodic resonant NRHO. View for Case 2 transfer.

Trajectories that leave the proximity of the region of interests are loosely characterized as exterior transfer [136]. Hyperplane crossing maps similar to Figure 6.16 are generated for departure and arrival maneuver magnitude of 20 m/s aligned in the maximum stretching directions, type 'A' and type 'B'. Of course, maps of other maneuver magnitudes may also offer transfer trajectory options. The primary motive of this investigation is to demonstrate maximum stretching direction as a tool to assist in transfer trajectory design rather than to determine the most cost-efficient transfer. On the $y = 0$ hyperplane map, i.e., xz plane crossing map, a combination of departure and arrival arc crossings towards the negative x-direction are selected, one that has relatively low position and velocity discontinuity. The selected combination of departure and arrival arc crossing offers an initial guess that is optimized, to reduce maneuver costs and determine a trajectory continuous in position. Figure 6.21 is a locally optimal transfer between the 9:2 synodic resonant southern L2 NRHO to the 9:2 synodic resonant northern L2 NRHO that leverages an exterior type transfer as

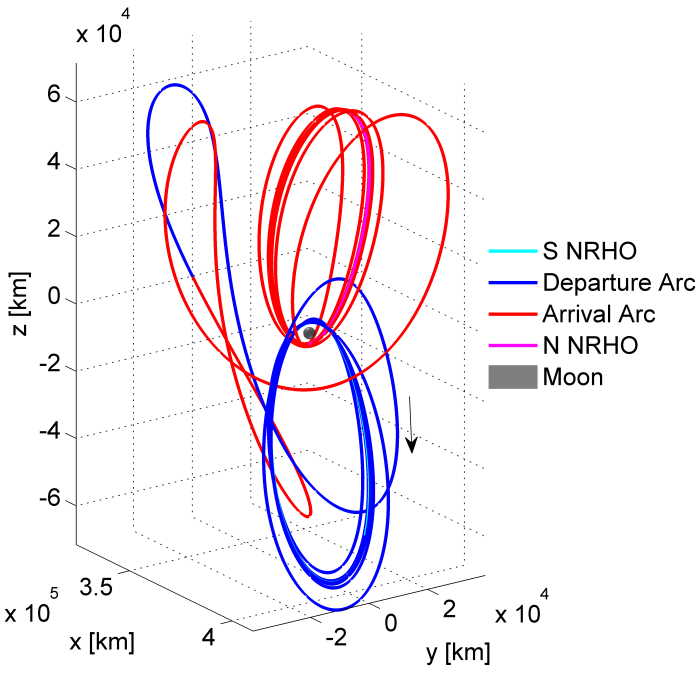

Figure 6.19. Isometric view of an optimal transfer between L2 southern 9:2 synodic resonant NRHO to L2 northern 9:2 synodic resonant NRHO. View for Case 3 transfer.

explained. The transfer has a single loop geometry around the Earth-Moon system. Another combination of departure and arrival arc crossings towards the positive x-direction are selected on the $y = 0$ hyperplane map, i.e., xz plane crossing map, with a relatively low position and velocity discontinuity. The initial guess is optimized to deliver a locally optimal transfer trajectory as in Figure 6.22. The optimal trajectory double loop geometry around the Earth-Moon system in contrast to single loop geometry for optimal transfer in Figure 6.21. Not surprisingly, the time of flight for transfer shown in in Figure 6.22 is longer, however, the overall maneuver costs for both the exterior type transfers demonstrated here are comparable. The details of the maneuver costs, time of flight and the osculating true anomaly of the departure and arrival locations on the corresponding orbits are listed in Table 6.2. The exterior type transfers demonstrated here are generated from 20 m/s maneuvers delivered along the maximum stretching directions, therefore, trajectories depart or arrive the vicinity of the NRHOs more rapidly, and likely to offer shorter time of flight transfer

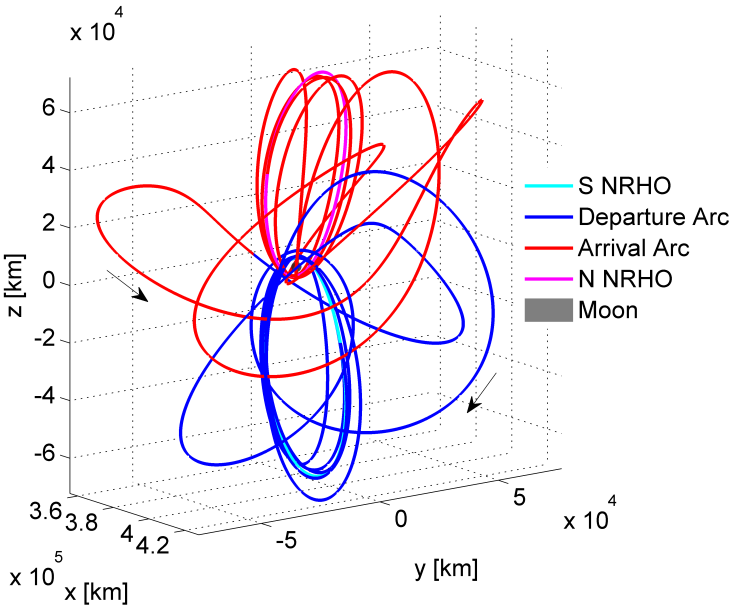

Figure 6.20. Isometric view of an optimal transfer between L2 southern 9:2 synodic resonant NRHO to L2 northern 9:2 synodic resonant NRHO. View for Case 4 transfer.

options. The time of flight and the maneuver costs associated with the transfers are influenced heavily by the combinations selected on the hyperplane crossing maps rather than the initial guess of the departure and arrival maneuver magnitudes alone. Since the 9:2 synodic resonant southern and northern NRHO have the same energy, in theory a ballistic transfer may exist.

An infinitely many transfer trajectory design options are possible, both interior type and exterior type. Different combinations of departure and arrival arc crossings on different hyperplanes offer different solutions. In addition, various magnitudes for departure and arrival maneuvers alter the hyperplane crossing maps thus yielding alternate solutions. The examples in this investigation demonstrate the capability of leveraging the maximum stretching directions for transfer trajectory design to transition between relatively stable orbits. Some of the transfer geometries are consistent with low-thrust transfers available in the literature, along with some that leverage resonant structures [71], [72], [75], [136].

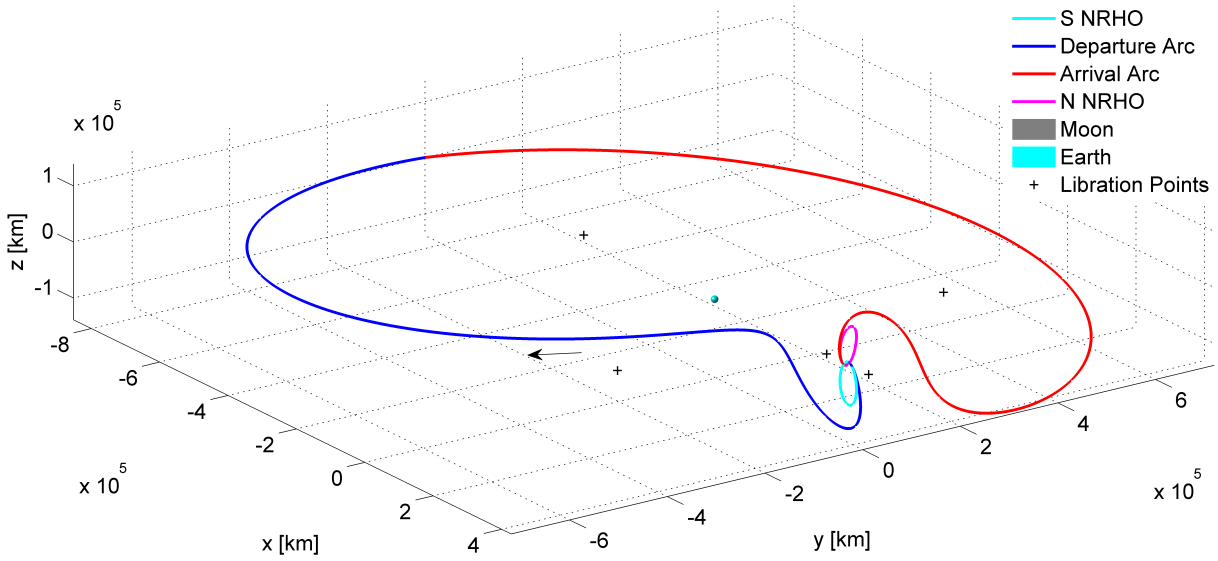

Figure 6.21. Isometric view of an optimal transfer between L2 southern 9:2 synodic resonant NRHO to L2 northern 9:2 synodic resonant NRHO. View for Case 5 transfer.

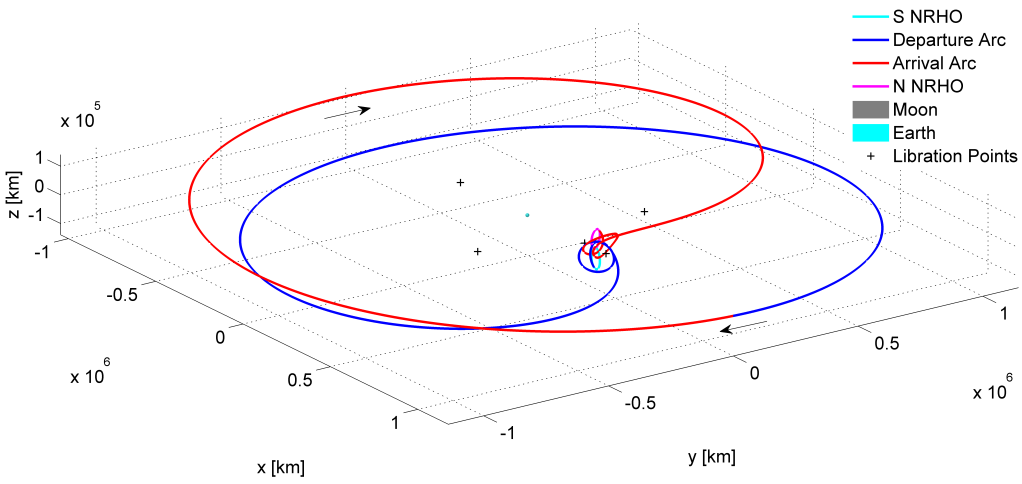

Figure 6.22. Isometric view of an optimal transfer between L2 southern 9:2 synodic resonant NRHO to L2 northern 9:2 synodic resonant NRHO. View for Case 6 transfer.

Table 6.2. Optimal transfers between 9:2 synodic resonant southern L2 NRHO to 9:2 synodic resonant northern L2 NRHO.

Parameter	Case 1	Case 2	Case 3	Case 4	Case 5	Case 6
	Figure 6.17	Figure 6.18	Figure 6.19	Figure 6.20	Figure 6.21	Figure 6.22
$\lvert\Delta\bar{v}_{dep}\rvert$ [m/s]	3.59	2.05	0.88	10.12	27.32	112.34
$\lvert\Delta\bar{v}_{int}\rvert$ [m/s]	0.00	0.00	0.00	0.00	188.55	0.00
$\lvert\Delta\bar{v}_{arr}\rvert$ [m/s]	3.59	2.27	0.88	10.04	27.39	112.36
$\lvert\Delta\bar{v}_{Total}\rvert$ [m/s]	7.18	4.33	1.76	20.17	243.25	224.70
ToF_{dep} [days]	50.08	54.95	61.10	62.35	36.99	58.44
ToF_{arr} [days]	50.08	54.68	61.07	62.19	36.99	58.43
ToF_{Total} [days]	100.16	109.62	122.17	124.54	73.98	116.87
TA_{dep} [deg]	175.52	154.68	164.57	148.27	67.13	193.02
TA_{arr} [deg]	174.84	201.88	195.39	207.49	292.59	166.97
Initial conditions	subsec. B.1.1	subsec. B.1.2	subsec. B.1.3	subsec. B.1.4	subsec. B.1.5	subsec. B.1.6

6.2.2 Transfers between L2 southern 9:2 synodic resonant NRHO to Distant Retrograde Orbit (DRO)

The Lunar Distant Retrograde Orbits are also a choice for upcoming missions, primarily due to their proximity to the Moon and stable nature of the orbits. The family of the distant retrograde orbits in the Earth-Moon system and their corresponding stability indices are presented in Figure 6.23. Clearly they present a range of orbits that are stable or nearly stable. Here, a transfer between the two stable orbits, the 9:2 synodic resonant southern L2 NRHO and the 70,000 km Lunar DRO, are leveraged using initial guesses from maneuvers delivered along the maximum stretching directions. The DRO of interest has a periapsis distance of 70,000 km from the Moon, measured along the x-axis towards the Earth. The time period, Jacobi constant and the stability indices of the NRHOs of interest are listed in Table 6.3. Clearly, the magnitudes of the stability indices indicate that the orbits are stable in nature, therefore, no unstable manifold structures exist. Similar to the southern NRHO to northern NRHO transfers, a map is generated with maneuvers that are

delivered along the maximum stretching directions at various locations along the orbit. The maximum stretching directions along the 70,000 km DRO is demonstrated in Figure 6.24 along a forwards propagated segment and a backwards propagated segment, both for one time period. Along a forwards propagated segment, the maximum stretching directions are computed from the matrix $\varphi_{C,rv,v}(\wp, 0)$ and displayed in Figure 6.24(a), while for a backwards propagated segment, the maximum stretching directions are computed from the matrix $\varphi_{C,rv,v}(0, \wp)$ as in Figure 6.24(b). The quantity $\wp$ is the time period of the DRO. For the DRO, due to relatively consistent angular rate of rotation along the orbit measured with respect to the Moon, Mean Anomaly serves as a simple metric to determine the spacecraft location along the orbit. Maneuvers of fixed magnitudes are delivered along both the sets of maximum stretching direction, type 'A' and type 'B', for both the NRHO and the DRO, and the updated states are propagated for a significantly long duration. The DRO being planar, all the states lie in the xy plane. A $z = 0$ hyperplane, i.e., the xy plane is incorporated with all trajectories emerging from the DRO propagated backwards in time, and all the xy plane crossings for the trajectories emerging from the NRHO propagated forwards in time. A semi-automatic scheme determines a departure arc and an arrival arc at the hyperplane crossing. Within a region of interest on the hyperplane crossing map, the algorithm solves for the value of

$$\mathcal{J} = \left|\left| \begin{bmatrix} \alpha \Delta \bar{r} \\ (1-\alpha)\Delta \bar{v} \end{bmatrix} \right|\right|$$

for each combinations of departure and arrival states on the hyperplane. A combination that minimizes the value of $\mathcal{J}$ is preferred. Here, $\Delta\bar{r}$ and $\Delta\bar{v}$ are the position and velocity discontinuities between the departure arc and the arrival arc at the hyperplane crossing, while α is a scaling factor to selectively control the position and velocity discontinuity. For crossings that are further away from the primary bodies, the optimization algorithm compensates for a relatively larger position error hence a relatively smaller $\alpha \in [0.5, 0.9]$ is used. For crossings that are closer to the primary bodies, a smaller position discontinuity is essential for the optimization algorithm, hence a value of $\alpha \geq 0.9$ is favorable. Multiple maps are generated by propagating departure arcs and arrival arcs following maneuvers of various $|\Delta\bar{v}|$ sizes; an example is provided in Figure 6.25. Different combinations of the departure

and the arrival crossings on the maps offer different transfer geometries, some examples are illustrated in this investigation. For the transfer between the 3200 km L2 NRHO and the 70,000 km DRO, each possessing a different energy level, a ballistic transfer does not exist. A theoretical minimum $|\Delta\bar{v}|$ is required to raise the energy level from the NRHO to meet the energy level for the DRO. The value of theoretical minimum $|\Delta\bar{v}|$ offers an estimate of the minimum maneuver magnitude that must be delivered at various locations along the departing NRHO to meet the energy level for the arriving DRO [75]. For a transfer between the 9:2 synodic resonant L2 NRHO to the planar 70,000 km DRO, the theoretical minimum $|\Delta\bar{v}|$ value along the departing NRHO is illustrated in Figure 6.26. A larger maneuver magnitude is required closer to the apoapsis along the NRHO to meet the energy for the DRO in contrast to departing closer to the periapsis.

Table 6.3. Orbital parameters for 70,000 km DRO

Period [days]	13.934122483289999
Jacobi Constant	2.928898812886901
Stability Indices	-0.716865210258674 0.106755614801400 1

Certain combinations of the departure and arrival arc crossings on the hyperplane that are near the Moon, as in Figure 6.25, offer interior type transfers. There are infinitely many combinations of departure and arrival arcs that are possible. A selected combination offers reliable initial guess for transfer trajectory design between the NRHO and the DRO. An optimization scheme generates a continuous transfer with three maneuvers, $\Delta\bar{v}_{dep}$, $\Delta\bar{v}_{int}$ and $\Delta\bar{v}_{arr}$. Figures 6.27, 6.28 and 6.29 are examples of locally optimal interior transfer where the spacecraft remains in the Lunar vicinity. The initial guess corresponding to Figure 6.27 is extracted from a map generated by propagating trajectories from the NRHO with a maneuver of magnitude 1 m/s along the maximum stretching directions, similarly trajectories are propagated backwards in time from the DRO along the maximum stretching direction

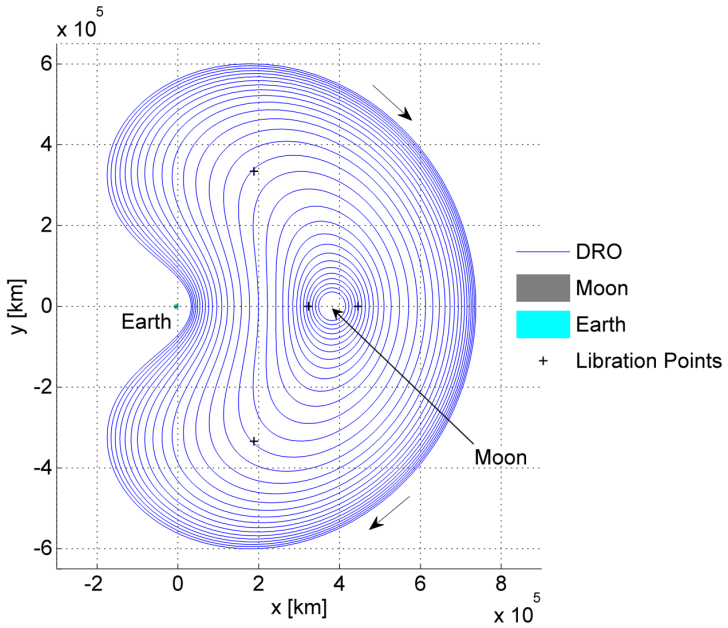

(a) Orbits in configuration space

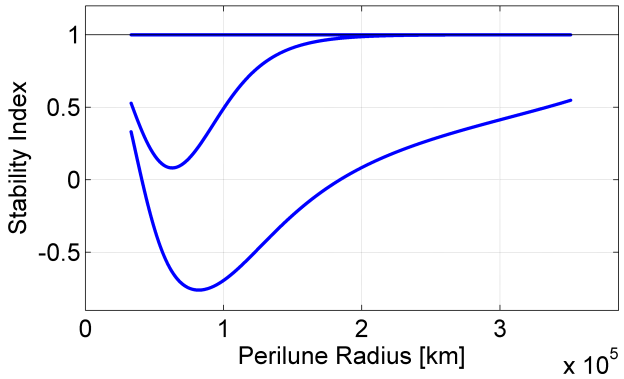

(b) Stability Index

Figure 6.23. Distant Retrograde Orbits in the Earth-Moon system.

with a maneuver of 1 m/s. Figure 6.28 is an outcome of map corresponding to maneuvers of magnitude 5 m/s and 20 m/s delivered on the NRHO and the DRO, respectively. Finally a map with a maneuver magnitude of 20 m/s delivered on both the NRHO and the DRO, yields a geometry that resembles Figure 6.29. As stated previously, the optimal maneuvers, $|\Delta\bar{v}_{dep}|$ and $|\Delta\bar{v}_{arr}|$, may not precisely be the same as the initial guesses, nor precisely aligned along the maximum stretching directions. The maneuver costs as well as the time of flight for each of the transfers in Figures 6.27, 6.28 and 6.29 are listed in Table 6.4. The osculating

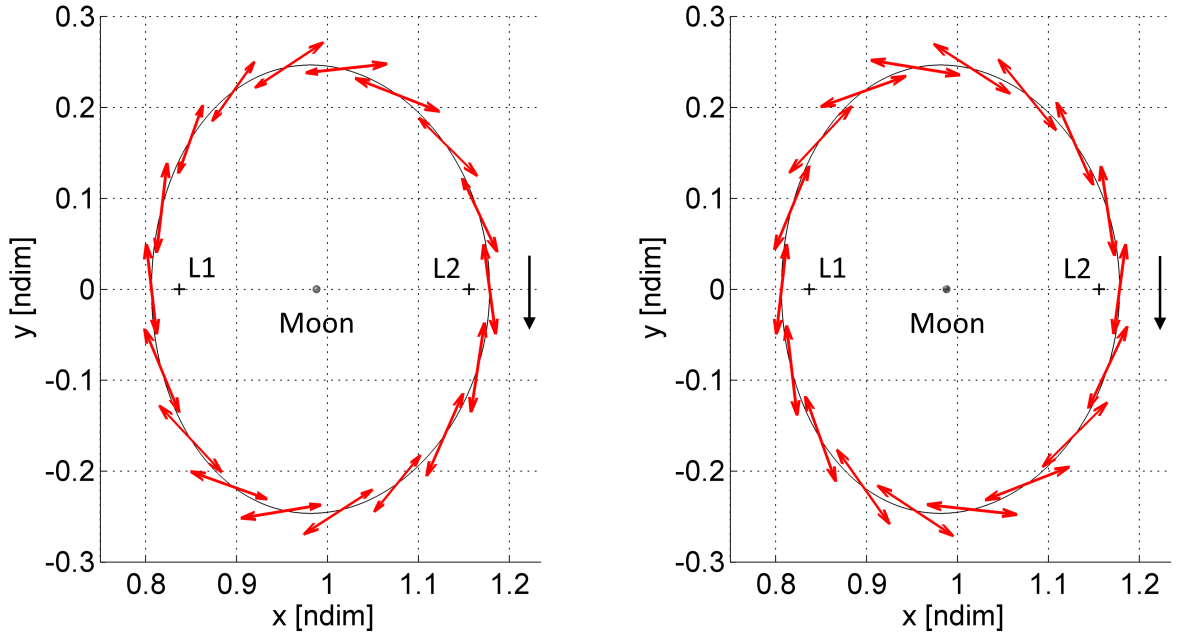

(a) $\varphi_{C,rv,v}(\wp, 0)$ (b) $\varphi_{C,rv,v}(0, \wp)$

Figure 6.24. Maximum stretching direction along the 70,000 km DRO propagated forwards and backwards in time.

true anomaly locations along the departure NRHO and the mean anomaly location on the arrival DRO for the locally optimal transfers are also listed. For the transfers between two NRHOs that are alike in the energy, in theory a $|\Delta\bar{v}| = 0$ transfer exists, however, for the transfer between the 3200 km L2 NRHO and the 70,000 km DRO that have different energy levels, a $|\Delta\bar{v}| = 0$ transfer does not exist. A theoretical minimum $|\Delta\bar{v}|$ is calculated, such that $|\Delta\bar{v}| = 35.48$ m/s must be delivered at the periapsis of the NRHO or $|\Delta\bar{v}| = 261.86$ m/s at the apoapsis of the NRHO to meet the energy of the DRO [75].

Intersections of the departure and arrival arcs on the hyperplane further away from the Moon offer exterior transfers. Hyperplane crossing maps similar to Figure 6.25 are generated for departure and arrival maneuver magnitude of 20 m/s and 40 m/s along the NRHO and the DRO, respectively. The maneuvers are delivered in the maximum stretching directions, type 'A' and type 'B'. Two different combinations of departure and arrival crossings on the map yield transfer geometries as observed in Figures 6.30 and 6.32. In contrast, an optimal

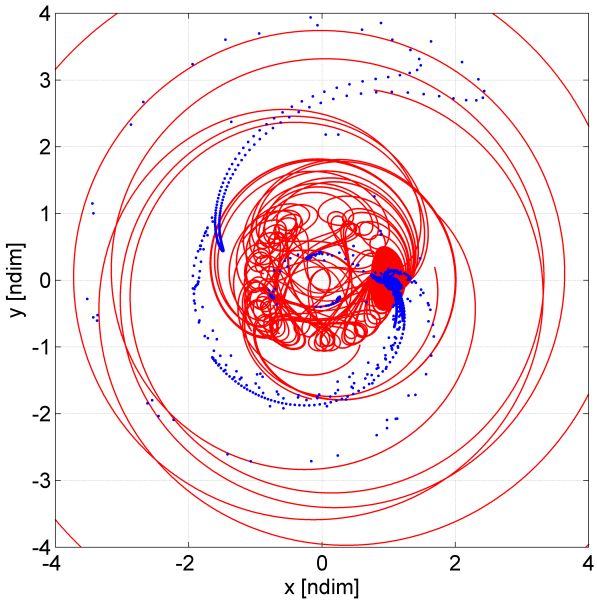

Figure 6.25. Two sided plane crossing maps. Blue dots (.) correspond to departure arc crossings from southern NRHO propagated forwards in time with $|\Delta\bar{v}| = 5$ m/s, while red dots (.) correspond to arrival arcs from DRO propagated backwards in time with $|\Delta\bar{v}| = 20$ m/s.

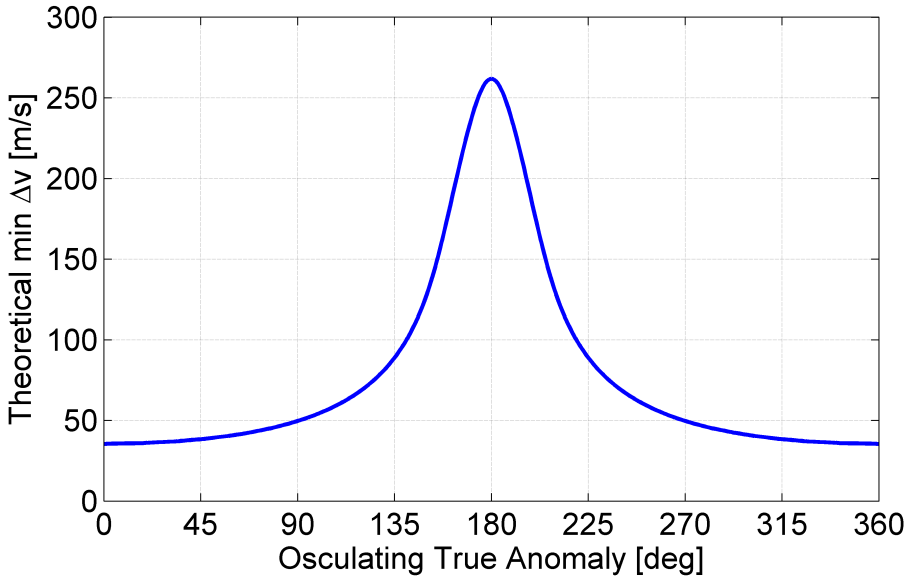

Figure 6.26. Theoretical minimum maneuver magnitude required along different locations on the 9:2 synodic resonant NRHO to meet the energy of the 70,000 km DRO.

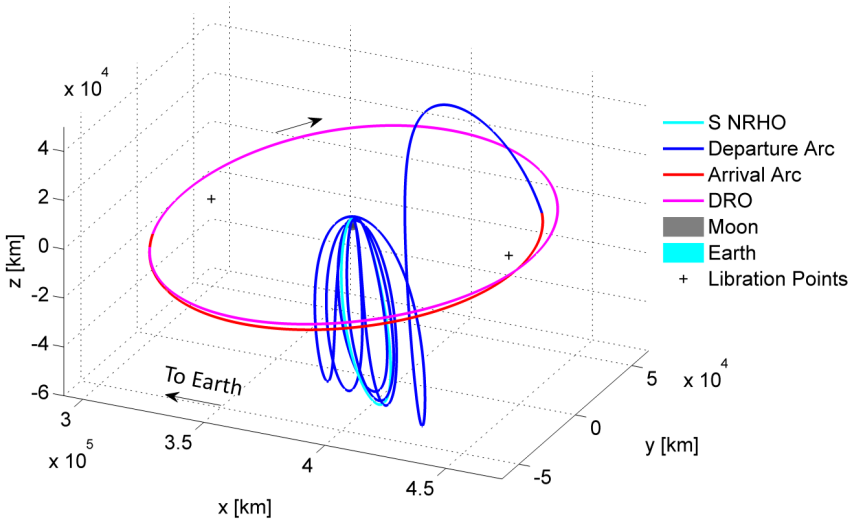

Figure 6.27. Interior type locally optimal transfer between L2 southern 9:2 synodic resonant NRHO to 70,000 km DRO (Case 1).

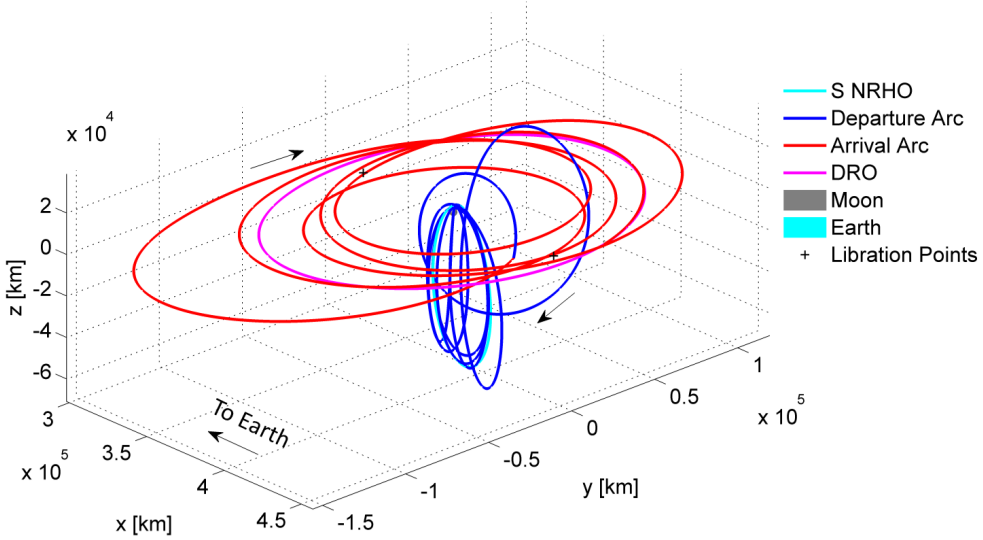

Figure 6.28. Interior type locally optimal transfer between L2 southern 9:2 synodic resonant NRHO to 70,000 km DRO (Case 2).

exterior type geometry in Figure 6.31 is extracted from an initial guess on the map generated by maneuvers of magnitude 20 m/s to depart the NRHO and arrive on the DRO. Maps generated by other maneuver magnitudes may offer other transfer trajectory options. Figure 6.30 illustrates spacecraft motion near the Earth vicinity while Figures 6.31 and 6.32 show trajectories that leave further away from the Earth-Moon vicinity. The maneuver costs, time

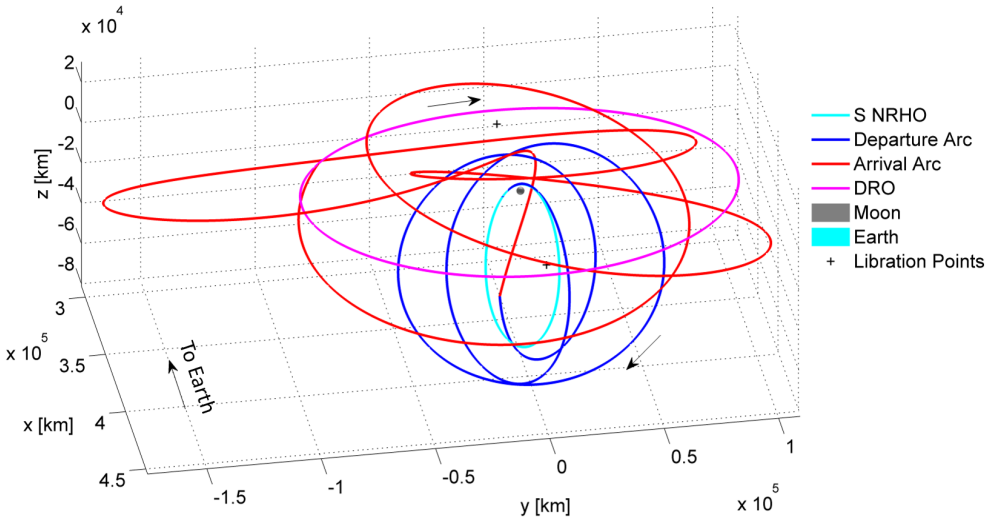

Figure 6.29. Interior type locally optimal transfer between L2 southern 9:2 synodic resonant NRHO to 70,000 km DRO (Case 3).

of flight and the locations on the orbit for departure and arrival are listed in Table 6.4. Note that the NRHO orbit and the DRO orbit have different energy levels, a as a result $|\Delta\bar{v}| = 0$ transfer is not possible in the CR3BP. As noted previously, a theoretical minimum $|\Delta\bar{v}|$ is required to match the energy levels.

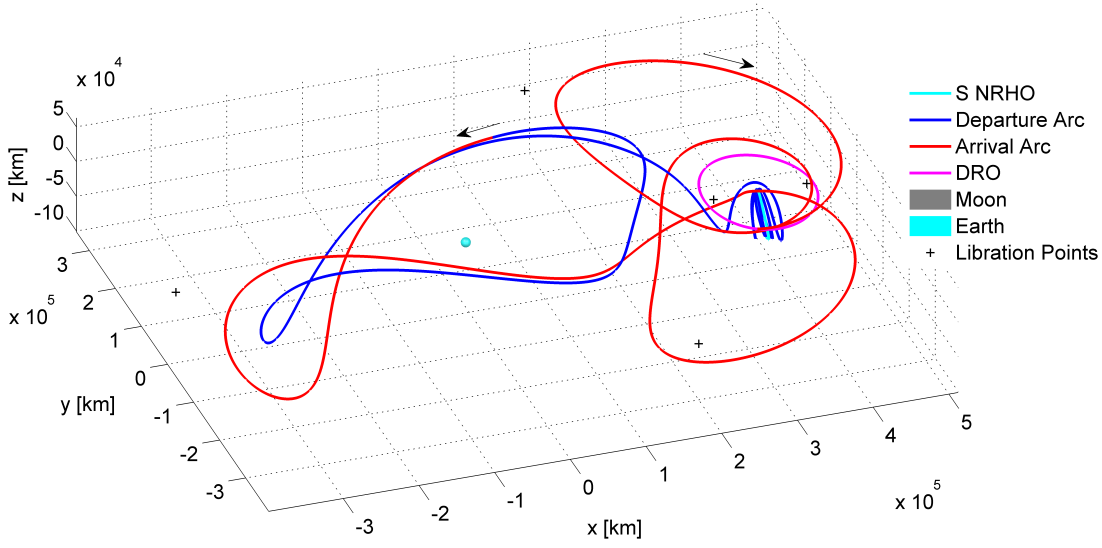

Figure 6.30. Exterior type locally optimal transfer between L2 southern 9:2 synodic resonant NRHO to 70,000 km DRO (Case 4).

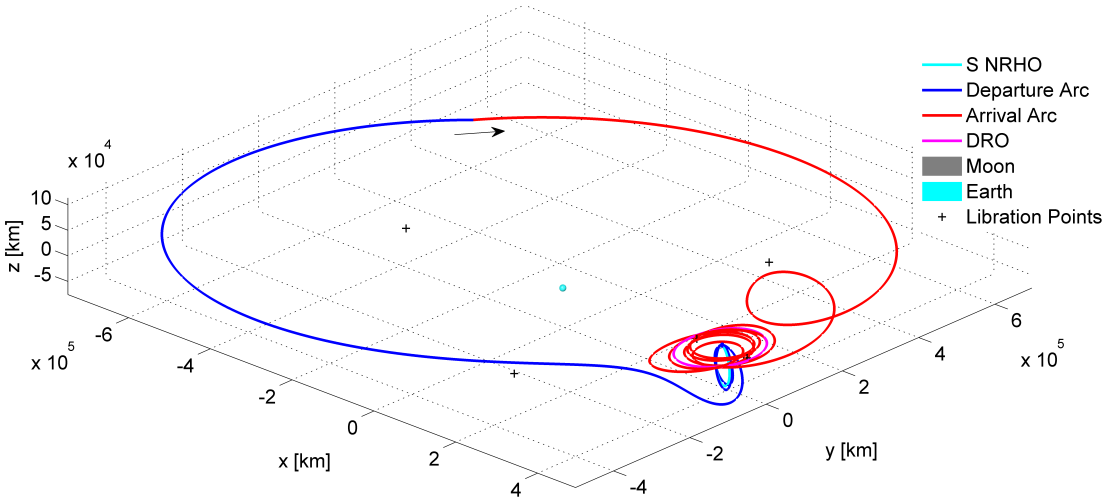

Figure 6.31. Exterior type locally optimal transfer between L2 southern 9:2 synodic resonant NRHO to 70,000 km DRO (Case 5).

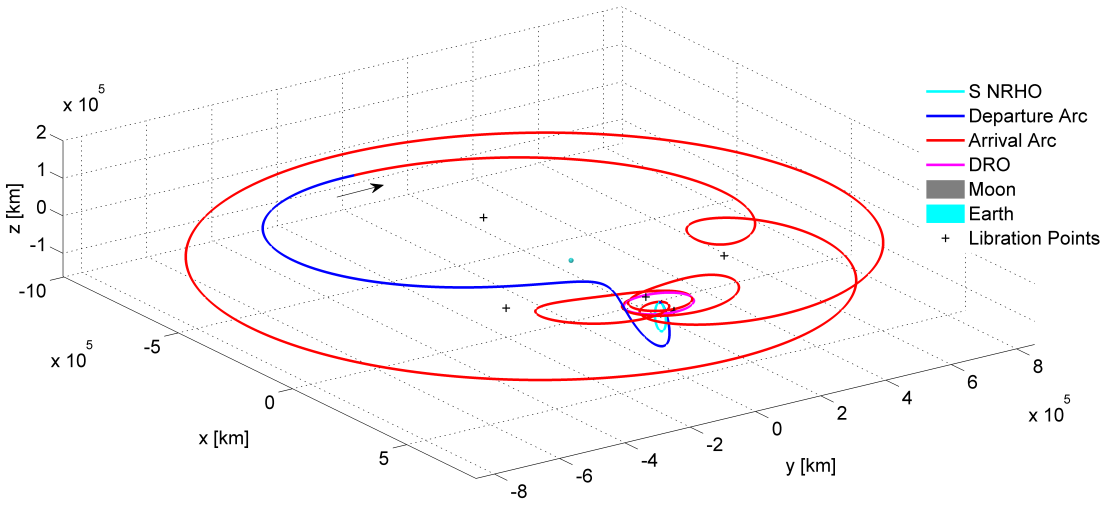

Figure 6.32. Exterior type locally optimal transfer between L2 southern 9:2 synodic resonant NRHO to 70,000 km DRO (Case 6).

Various transfer methodologies have been explored for transfers between the NRHO and the DRO in the literature, including low thrust trajectories, intermediate resonant structures and other known orbits [71]–[73], [75]–[77]. The examples in this investigation demonstrate the capability of leveraging maximum stretching directions for transfer trajectory design process to transition between a 3-dimensional NRHO to a planar DRO, without any prior

Table 6.4. Optimal transfers between 9:2 synodic resonant southern L2 NRHO to 7000O km DRO.

Parameter	Case 1	Case 2	Case 3	Case 4	Case 5	Case 6
	Figure 6.27	Figure 6.28	Figure 6.29	Figure 6.30	Figure 6.31	Figure 6.32
$\lvert\Delta\bar{v}_{dep}\rvert$ [m/s]	4.03	3.81	15.06	12.41	4.41	18.62
$\lvert\Delta\bar{v}_{int}\rvert$ [m/s]	355.51	306.24	172.71	81.38	120.30	296.08
$\lvert\Delta\bar{v}_{arr}\rvert$ [m/s]	12.69	18.77	148.19	106.35	18.16	36.72
$\lvert\Delta\bar{v}_{Total}\rvert$ [m/s]	372.23	328.81	335.97	200.14	142.88	351.41
ToF_{dep} [days]	44.42	50.29	28.28	63.15	54.36	36.51
ToF_{arr} [days]	6.96	64.49	49.69	78.81	111.52	130.65
ToF_{Total} [days]	51.39	114.79	77.97	141.96	165.88	167.15
TA_{dep} [deg]	37.75	7.85	255.08	129.27	339.64	354.57
MA_{arr} [deg]	330.09	165.35	302.78	295.29	137.79	356.64
Initial conditions	subsec. B.2.1	subsec. B.2.2	subsec. B.2.3	subsec. B.2.4	subsec. B.2.5	subsec. B.2.6

knowledge of existing intermediate structures. Some of the transfer geometries, time of flight and maneuver costs are consistent with the literature.

6.2.3 Transfers between L2 southern 9:2 synodic resonant NRHO to planar Lunar Orbit (LO)

The Lunar Orbits (LO) are another choice of orbits for upcoming missions due to close access to Lunar surface. These Lunar Orbits typically resemble a 2-body orbit that are in form of conic solutions, one that are stable in nature. Here, transfers between the two stable orbits, the 9:2 synodic resonant southern L2 NRHO and a 3000 km planar LO, are leveraged using initial guesses from maneuvers that are delivered along the maximum stretching directions. The locations on the almost circular LO is measured in terms of Mean Anomaly (MA) where $MA = 0^o$ is along the negative x-axis direction from the Moon consistent with the approach used for the DRO. The planar LO in focus, is almost circular with a distance of 3000 km from the Moon, measured along the x-axis towards the Earth. The time period, Jacobi constant and the stability indices of the NRHOs of interest are listed in Table 6.5.

The magnitudes of the stability indices indicate that the orbits are stable in nature, therefore, distinct stable and unstable manifold structures do not exist. Maneuvers are leveraged along the maximum stretching directions to arrive on the LOs instead.

Table 6.5. Orbital parameters for 3000 km planar LO

Period [hours]	4.121428550494591
Jacobi Constant	4.533189223937852
Stability Indices	0.999233547406442 0.999218868898944 1

The maximum stretching directions along the 3000 km planar LO offer insight for orbit insertion. The maximum stretching directions, as demonstrated in Figure 6.33, are computed along a forwards propagated orbit and a backwards propagated orbit, with the monodromy matrix. Along a forwards propagated orbit, the maximum stretching directions are computed from the matrix $\varphi_{C,rv,v}(\wp, 0)$ and displayed in Figure 6.33(a), while for a backwards propagated orbit, the maximum stretching directions are computed from the matrix $\varphi_{C,rv,v}(0, \wp)$ as in Figure 6.33(b). The quantity $\wp$ is the time period of the LO. The maximum stretching directions along the LO are aligned nearly parallel or anti-parallel to the orbital velocity directions. For orbits or regions along an orbit that have dominant accelerations from a single gravitational body, the maximum stretching directions are observed to align close to the velocity directions.

Consistent with the approach used in this investigation, a map is generated with maneuvers that are delivered along the maximum stretching directions at various locations along the orbit. Maneuvers of fixed magnitudes are delivered along both sets of maximum stretching direction, type 'A' and type 'B', for both the NRHO and the LO, and the updated states are propagated for a significantly long duration. The LO being planar, all the states lie in the xy plane. A $z = 0$ hyperplane, i.e., the xy plane is considered with all trajectories emerging from the LO propagated backwards in time, and all the xy plane crossings for the

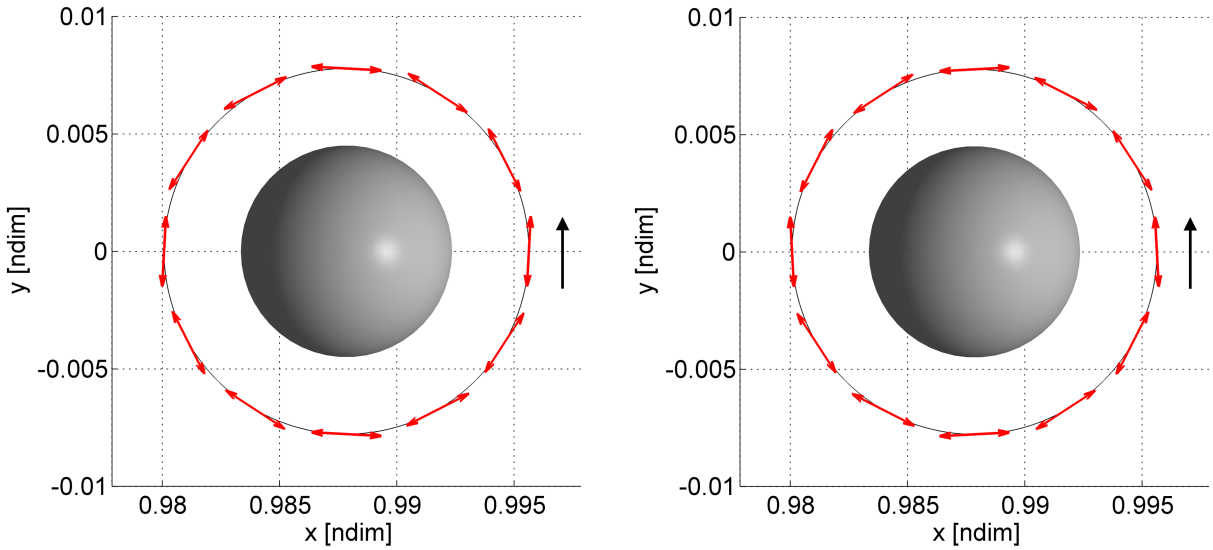

(a) $\varphi_{C,rv,v}(\wp, 0)$ (b) $\varphi_{C,rv,v}(0, \wp)$

Figure 6.33. Maximum stretching direction along 3000 km planar LO propagated forwards and backwards in time.

trajectories emerging from the NRHO propagated forwards in time. As discussed previously, semi-automatic scheme determines the combination of a departure arc and an arrival arc at the hyperplane crossing. Multiple maps are generated by propagating departure arcs and arrival arcs following maneuvers of various $|\Delta\bar{v}|$ sizes, an example is provided in Figure 6.34. Different maps offer different transfer geometries. The transfer geometries illustrated in this investigation are a result of various initial conditions.

Similar to the transfers between the NRHO and the DRO, in theory a ballistic transfer is not possible for transfers between the NRHO and the LO that possess distinct energy levels. To transfer between the 9:2 synodic resonant L2 NRHO to the 3000 km planar LO, a theoretical minimum $|\Delta\bar{v}|$ value, as illustrated in Figure 6.35, must be delivered along various locations on the departing NRHO to meet the energy level for the arriving LO. A larger maneuver magnitude is required closer to the apoapsis along the NRHO to meet the energy level for the LO. In contrast, departing closer to the periapsis requires a relatively smaller value of minimum $|\Delta\bar{v}|$.

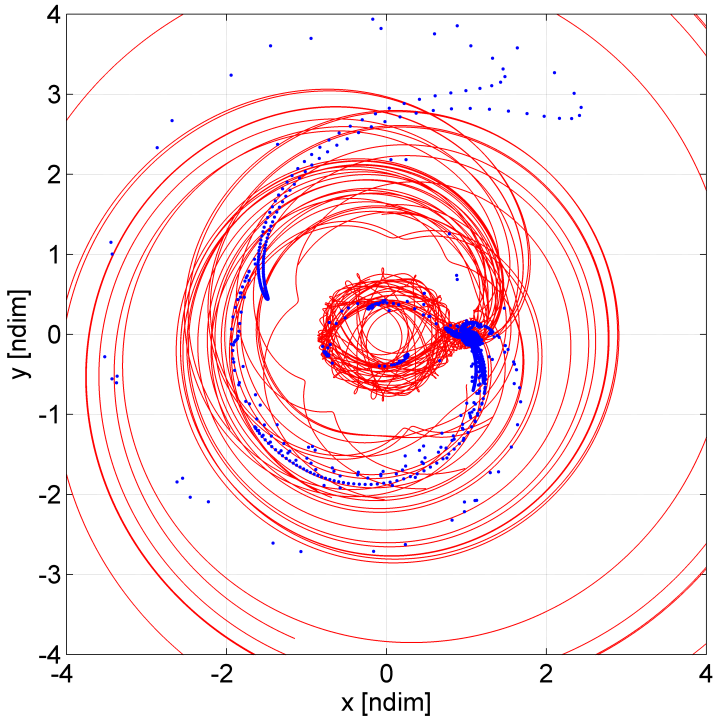

Figure 6.34. Two sided plane crossing maps. Blue dots (.) correspond to departure arc crossings from southern NRHO propagated forwards in time with $|\Delta\bar{v}| = 5$ m/s, while red dots (.) correspond to arrival arcs from LO propagated backwards in time with $|\Delta\bar{v}| = 600$ m/s.

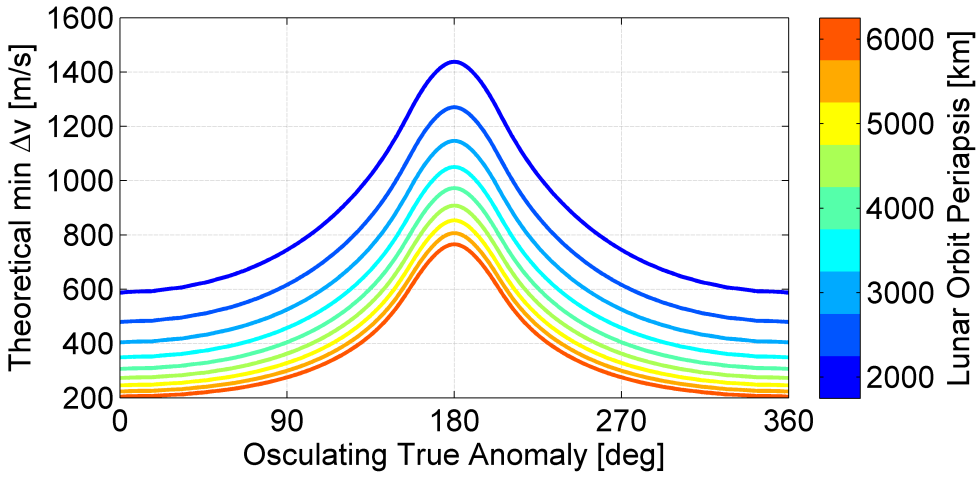

Figure 6.35. Theoretical minimum maneuver magnitude required along different locations on the 9:2 synodic resonant NRHO to meet the energy of different planar LOs.

Interior and exterior type transfers are possible for transfers between an NRHO and a planar LO. Figures 6.36(a) and 6.36(b) are locally optimal interior transfers from the 9:2 synodic resonant L2 NRHO to the 3000 km planar LO. Figure 6.36(a) is based on an initial guess from a map generated by propagating trajectories from the NRHO with a maneuver of magnitude 5 m/s along the maximum stretching directions, similarly trajectories are propagated backwards in time from the LO along the maximum stretching direction with a maneuver of 600 m/s. Figure 6.36(b) is an outcome of map corresponding to maneuvers of magnitude 20 m/s and 500 m/s delivered on the NRHO and the LO, respectively. Locally optimal exterior transfers are illustrated in Figures 6.37(a) and 6.37(b) that are constructed from initial guesses on the map generated by maneuvers of magnitude 5 m/s to depart the NRHO and 600 m/s to arrive on the planar LO. Of course maps generated by other maneuver magnitudes may offer other transfer trajectory options. The maneuver costs, time of flight and the locations on the orbit for departure and arrival are listed in Table 6.6 for both interior and exterior type transfers. Furthermore, the 3200 km L2 NRHO and the 3000 km planar LO have different energy levels therefore a $|\Delta\bar{v}| = 0$ transfer does not exist in the CR3BP. A theoretical minimum $|\Delta\bar{v}|$ magnitude is required along the NRHO to meet the energy of the LO.

Transfers between the NRHO and the LO are offered in the literature, including those that are direct transfers [78]–[80]. Transfer costs depend significantly on the inclination of the LO orbit under consideration. Transfer from an NRHO to a planar LO may incur larger maneuver costs due to large change in orbit planes. Transfers that leverage maximum stretching directions to identify suitable initial guess are offered in this investigation. A broader range of geometries are explored and locally optimal transfers are generated.

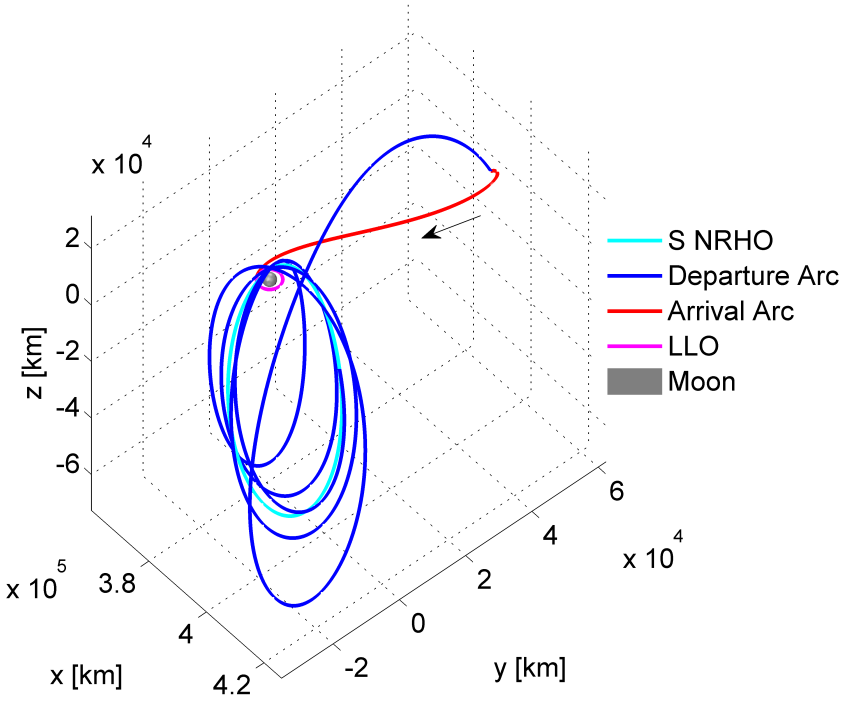

(a) Case 1

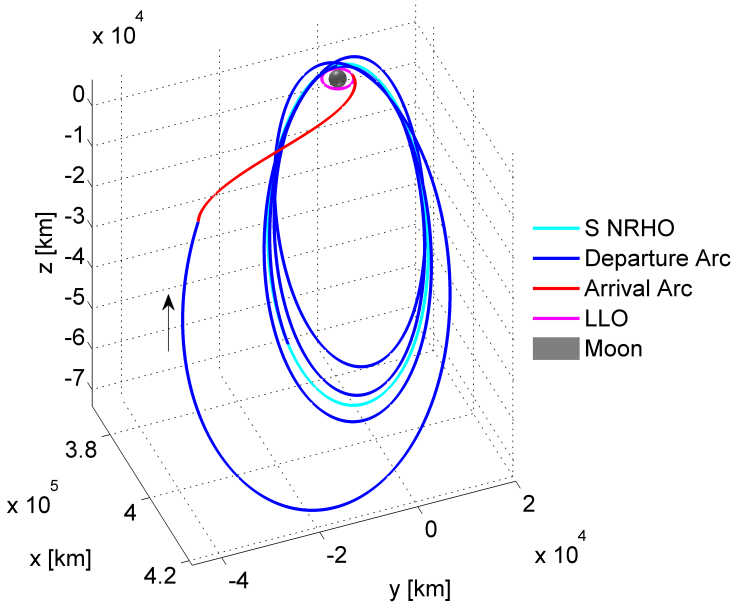

(b) Case 2

Figure 6.36. Interior type locally optimal transfer between L2 southern 9:2 synodic resonant NRHO to 3000 km planar LO.

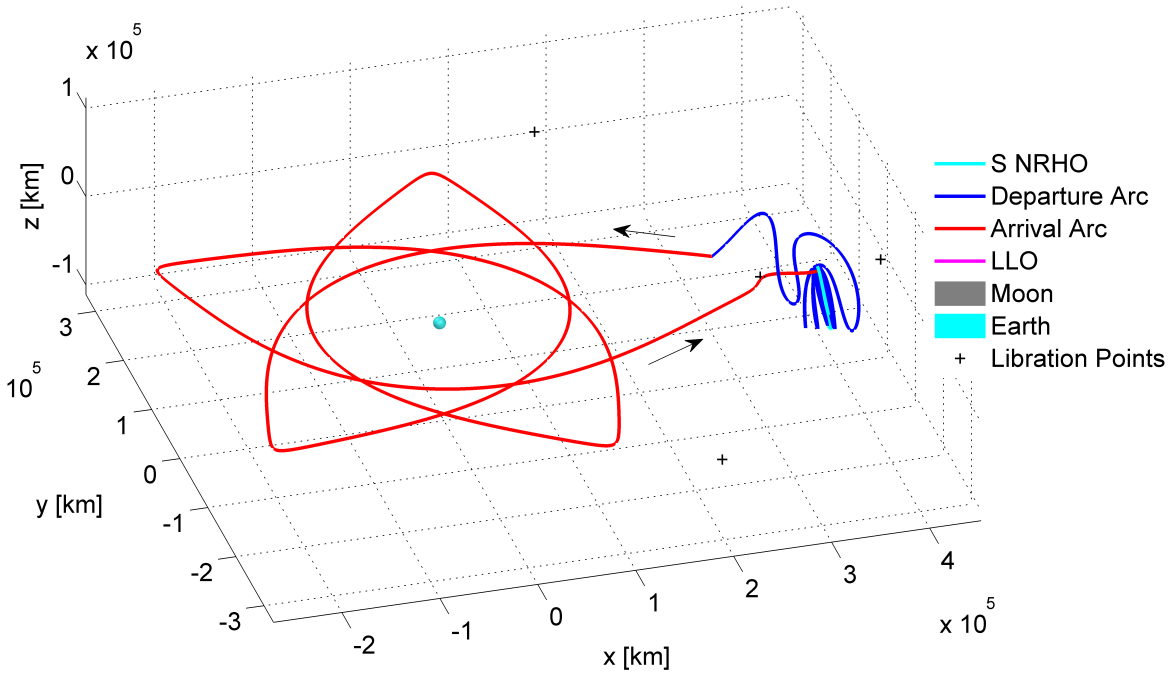

(a) Case 3

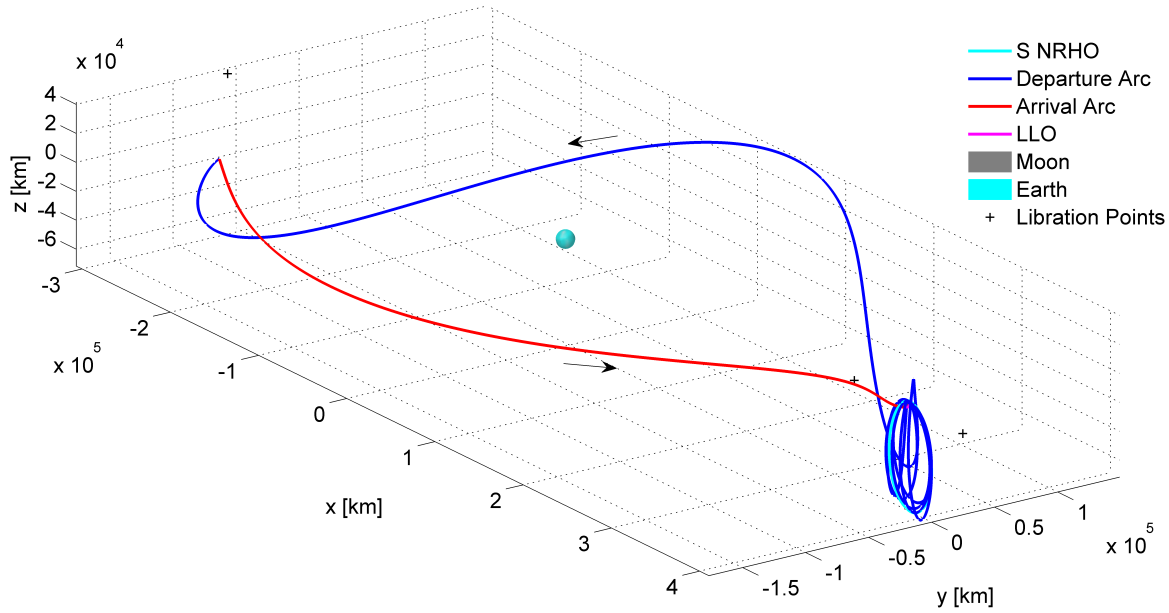

(b) Case 4

Figure 6.37. Exterior type locally optimal transfer between L2 southern 9:2 synodic resonant NRHO to 3000 km planar LO.

Table 6.6. Optimal transfers between 9:2 synodic resonant southern L2 NRHO to 300O km planar LO.

Parameter	Case 1	Case 2	Case 3	Case 4
	Figure 6.36(a)	Figure 6.36(b)	Figure 6.37(a)	Figure 6.37(b)
$\lvert\Delta\bar{v}_{dep}\rvert$ [m/s]	17.60	5.97	3.85	19.27
$\lvert\Delta\bar{v}_{int}\rvert$ [m/s]	230.46	332.37	319.06	280.69
$\lvert\Delta\bar{v}_{arr}\rvert$ [m/s]	492.26	481.73	470.43	500.94
$\lvert\Delta\bar{v}_{Total}\rvert$ [m/s]	740.32	820.06	793.34	800.89
ToF_{dep} [days]	36.31	29.69	55.08	59.46
ToF_{arr} [days]	3.27	1.67	61.32	10.60
ToF_{Total} [days]	39.58	31.36	116.40	70.06
TA_{dep} [deg]	154.15	198.60	359.60	136.99
MA_{arr} [deg]	45.12	273.83	153.04	149.10
Initial conditions	subsec. B.3.1	subsec. B.3.2	subsec. B.3.3	subsec. B.3.4

7. CONCLUDING REMARKS

Cislunar missions continue to generate a growing interest for various mission scenarios. Investigation of the Moon and nearby regions offer enormous potential for scientific discoveries. Stable or nearly stable orbits in regions near the Lunar vicinity are suitable for long terms presence, include those with humans on-board. The orbits of interest, that are stable or nearly stable, reduce the possibility of rapid departure. The stable nature of these orbits also presents a challenge for stationkeeping and, for insertion or departure from the orbit. Stationkeeping and transfer design strategies that leverage stable and unstable manifold structures are not effective for orbits that are stable or nearly stable. An alternate strategy that leverages the stretching directions are explored for two contrasting applications. Maneuvers are delivered away from the most stretching directions to remain bounded near the reference orbit, and, thus, suitable for successful stationkeeping. A contrasting application for departure and transfer trajectory design leverages maneuvers in the most stretching direction to deliberately deviate from the vicinity of the reference orbit, and to eventually arrive on some destination orbit.

7.1 Principal Stretching Directions

The stable and unstable manifold structures have been exploited for various applications in the literature. Stationkeeping strategies that are based on manifold theory such as the Floquet mode approach decomposes any perturbations along different unstable, stable and oscillatory modes, and maneuvers are generated that overcome any component of perturbations along the unstable directions. Similarly, unstable and stable manifolds are used for departing and arriving on the orbits and thus suitable for transfer trajectory design. The lack of well-distinguished stable and unstable manifold structures in the vicinity of a stable or nearly stable orbits requires an alternate strategy to visualize the dynamical flow near a reference orbit. The Cauchy-Green tensor, a function of the State Transition Matrix (STM), offers mutually orthogonal principal stretching directions to visualize the effects of any perturbation downstream, in a linear sense. Principal stretching directions that are based on different submatrices of the state transition matrix yield relevant information for the specific

applications. For the stationkeeping application, where reduction of the propellant costs (minimizing $\Delta\bar{v}$) is a priority, the submatrix of the STM that linearly maps the effect of the initial velocity state change to the velocity state change at final time, is an appropriate choice. For the departure and transfer trajectory design application, the submatrix of the STM that linearly maps the effect of the initial velocity state on the state change in both position and velocity, simultaneously, at final time is suitable for computing the stretching directions. A different application may leverage different submatrices of the STM, but the procedure remains consistent.

7.2 Stationkeeping Applications

An impulsive stationkeeping technique using x-axis crossing control is evaluated from the context of the dynamical foundations and structures that enable the strategy to generally succeed. The algorithm is analyzed for low perilune radius Near Rectilinear Halo Orbits (NRHOs) in the L1 and L2 families, that offer candidate solutions for various cislunar missions including the Gateway mission. The linear dynamical flow between two successive maneuver locations along a ballistic arc is visualized using the principal stretching directions. A systematic and straightforward approach is demonstrated that describes the interaction between the flow evolving from one maneuver location to the next during coast segments and the flow evolution from the maneuver location to the target, to identify likely combinations of maneuver and target locations. The cost of stationkeeping operations as well as boundedness of spacecraft near the virtual reference trajectory using the conventional x-axis crossing control approach is correlated to the mutual interactions between the maneuver direction and the most stretching direction. The understanding of the linear dynamical flow in the circular restricted three-body problem, near the corresponding reference orbit, offers insight into the performance of the x-axis crossing control stationkeeping strategy. In general, it is an effective strategy to deliver maneuvers that are away from the stretching directions.

The x-axis crossing control approach is demonstrated using the framework of the stretching directions for the orbits in the L1 and L2 NRHO families. For the L2 NRHOs with stationkeeping maneuvers only implemented at the apoapsis location, the maneuvers generated

by targeting the rotating $\dot{x}$ value at the xz plane crossing 1.5 rev downstream yield maneuvers that are significantly aligned with the most stretching direction, causing the spacecraft to deviate away from the virtual reference trajectory over time. In contrast, the maneuver generated by targeting the xz plane crossing 6.5 rev downstream is almost aligned in the restoring directions resulting in efficient maneuver characteristics and lower orbit maintenance costs. Unlike the L2 NRHOs, a maneuver implemented at the apoapsis does not necessarily produce effective stationkeeping maneuvers for the L1 NRHOs, due to multiple stretching subspaces for the flow between two successive maneuver locations. Nevertheless, several combinations of maneuver locations that are placed symmetric and asymmetric relative to the apoapsis location along the orbit, and with one or more maneuvers per revolution are explored for stationkeeping. The performance of the impulsive stationkeeping algorithm are evaluated for maneuvers constrained along certain directions, such as $\hat{x}$, $\hat{y}$, or $\hat{z}$ directions, and the vehicle local coordinate axes in the velocity $\hat{V}$, normal $\hat{N}$, or co-normal $\hat{C}$ directions.

The low stationkeeping costs generated by the x-axis control approach is a result of a loose requirement for boundedness around a virtual reference solution, and appropriate in various mission scenarios. The absence of an active phase control, however, causes the actual trajectory to shift in phase from the virtual reference solution. When a tight phase control is required to satisfy mission constraints such as eclipse avoidance, a feedback phase constraint is introduced along with targeting the rotating $\dot{x}$ value to compute a maneuver. Such a strategy maintains tight phasing between the actual and the virtual reference over long duration.

The halo orbits that fall in the transition region are sensitive to epoch dates, hence, the conventional x-axis control algorithm that target only the rotating $\dot{x}$ quantity at a specific xz plane crossing is not effective. By incorporating an additional active phase-control constraint, effective stationkeeping maneuvers are delivered. For the transition halo orbits, the annual cost and boundedness of the spacecraft near the virtual baseline trajectory is observed to be dependent on the underlying natural trajectory.

7.3 Departure and Transfer Trajectory Design

The current focus is on the Gateway mission, that potentially hosts human on-board, and expected to remain along an almost stable 9:2 synodic resonant orbit in the southern L2 NRHO family. An approach suitable to transfer from the baseline NRHO to various locations relatively quickly, as well as, avoiding collisions with any discarded modules is of relevance. In this investigation, maximum stretching directions are leveraged to facilitate departure from the NRHO.

Discarded modules pose a collision threat to the ongoing mission. An accepted approach is to dispose the module to a heliocentric space. An orbit departure serves as a preliminary step to the disposal problem. Impulsive maneuvers along velocity, normal and co-normal directions (VNC) have been offered in the literature. In this investigation, maneuver along the maximum stretching directions are explored as an alternate strategy. Maneuvers along maximum stretching directions offer rapid departure, also rapid capture, and immensely useful for orbits that lack unstable manifold structures.

Maximum stretching direction is also leveraged for transfer trajectory design. Along a forward propagated arc, the maximum stretching direction offers the maneuver that delivers the maximum magnitude of state change at final time and therefore explored for departure. Similarly, the maximum stretching direction along a backward propagated arc, offers the region of maximum access to arrive on the orbit of interest with the smallest maneuver, in a linear sense. The crossings of such forwards and backwards propagated trajectories are recorded over some predetermined hyperplanes. Such hyperplane crossing maps offer initial guess for transfer trajectory generation. A locally optimal trajectory yields a geometry similar to the initial guess determined from the maps that leverages departure and arrival along the maximum stretching directions, however, once optimized, maneuvers may not precisely align with the maximum stretching direction. Three different transfer scenarios are explored in this investigation; a 3-dimensional southern NRHO to a 3-dimensional northern NRHO, a 3-dimensional NRHO to a planar DRO, as well as a 3-dimensional NRHO to a planar

LO transfer. The application is not restricted to any specific mission or any specific epoch date, therefore, this investigation does not focus on determining the most efficient case in the ephemeris model. Rather, to demonstrate the utility of maximum stretching directions for transfer trajectory design. It is known from the literature that certain epoch dates may be conducive to cheaper transfers while some may be more expensive relative to the costs estimated in the CR3BP model. Nevertheless, the CR3BP solution serves as an effective initial guess for the higher-fidelity model. Moreover, the optimal solution in the high-fidelity model generally resembles the architecture of the CR3BP estimate.

7.4 Recommendations for Future Work

The continued interests in cislunar missions keep orbit maintenance strategies and transfer trajectory design popular topics for research. Different approaches offer different qualitative information and have their own advantages. The strategies keep evolving as enhancements are made. Some of the opportunities to advance the stationkeeping and transfer trajectory design strategies that leverage stretching directions are as listed:

1. Variable Target Horizon

   Only a few combinations of coast duration, maneuver locations and target horizon along an L1 NRHO yield maneuver (or maneuvers) away from the most stretching direction. As a consequence, long term stationkeeping is challenging for L1 NRHOs with the current methodology. In the current investigation, maps are generated for the angle between the maneuver and the most stretching direction for a fixed target horizon, and combination of maneuvers are selected on the same map. In such cases, not all the maneuvers are away from the most stretching direction. Nevertheless, for cases where more than one maneuver are placed along an orbit, each maneuver may be generated from a different target, one that is away from the most stretching direction. Of course, the process is more computationally challenging as a combination of maneuver locations are selected from multiple maps at variable target horizons. As a hypothetical example, consider two maneuvers at 150^o and 200^o osculating true

anomaly, such that maneuver at 150^o osculating true anomaly targets the i-th xz plane crossing to deliver a maneuver away from the most stretching direction while the maneuver at 200^o osculating true anomaly targets the j-th xz plane crossing to deliver a maneuver away from the most stretching direction.

2. Stretching directions for stationkeeping on unstable orbits

   The x-axis crossing control approach is evaluated from the context of stretching directions along the stable or nearly stable NRHOs. The strategy with certain modifications may be applicable for the unstable halo orbits as well. Due to unstable nature of the orbits, targeting certain conditions several revolutions downstream may not be possible. A shorter target horizon may be required. Furthermore, the unstable halo orbits are notably far from the Moon, hence, the dynamics near the periapsis and the apoapsis are not significantly different unlike the NRHOs that have very close passage near the Moon. Consequently, target conditions near the apoapsis as well as placing maneuver locations near the periapsis are also a choice, unlike for the NRHOs where maneuver locations are close to the apoapsis and target is near the periapsis. Stationkeeping techniques that rely on manifolds structures also offer insight for the unstable halo orbits. A comparison can be made between the characteristics of the maneuvers (magnitude and direction) that leverages the stretching directions is contrast to the maneuvers that leverages the unstable and stable manifold structures.

3. Transfers between stable and unstable orbits

   Unstable orbits have well-distinguished unstable and stable manifold structures that enable departure and arrival on the orbits. Such structures are exploited for transfers involving the unstable orbits. It is explored in this investigation that leveraging the stretching directions are promising for transfer trajectory design for the stable orbits. This investigation illustrates transfers between two stable orbits, 3-dimensional orbit to planar orbits as well as 3-dimensional orbit to another 3-dimensional orbit. The procedure can be extended for transfers involving an unstable orbit and a stable orbit. For example, a transfer between a stable orbit to an unstable orbit can be constructed from a hyperplane crossing map; one that is generated by recording all crossings of tra-

jectories emerging from the stable orbit after maneuvers are delivered along the most stretching directions and propagated forwards in time, and, recordings of all crossings of stable manifolds originating from the unstable orbit propagated in reverse time. Conversely, a transfer between an unstable orbit to a stable orbit can be leveraged from hyperplane crossing maps that is generated from intersections of unstable manifolds (emerging from the unstable orbit propagated forwards in time) and trajectories originating from the stable orbits once maneuvers are delivered along the stretching directions (propagated backwards in time). Transfer between stable NRHOs to unstable halo orbits, between stable NRHOs and unstable Lyapunov orbits, between unstable halo to stable DROs, etc., can be achieved using such a procedure.

4. Low-Thrust Trajectory Design

   The transfers illustrated in this investigation are based on impulsive maneuvers. Only certain spacecrafts types with chemical engines are able to deliver such a manuever that is effectively close to impulsive. Many missions planned for the cislunar neighborhood include low-thrust engines. To broaden the transfer design applications, a low-thrust dynamics for the transfer trajectories can be incorporated in this regime. The trajectories designed using impulsive maneuvers may serve as a initial guess, and such transfer solutions can be transitioned to a low-thrust model by varying the specific impulse and thrust values.

REFERENCES

[1] M. Mammarella, C. A. Paissoni, N. Viola, R. Fusaro, and T. Andrenussi, "High-power electric propulsion enabling support to the future Deep Space Gateway," in *2018 AIAA SPACE and Astronautics Forum and Exposition*, 2018, p. 5189.

[2] J. C. Crusan, R. M. Smith, D. A. Craig, J. M. Caram, J. Guidi, M. Gates, J. M. Krezel, and N. B. Herrmann, "Deep Space Gateway concept: Extending human presence into cislunar space," in *2018 IEEE Aerospace Conference*, IEEE, 2018, pp. 1–10.

[3] E. M. Zimovan, K. C. Howell, and D. C. Davis, "Near rectilinear halo orbits and their application in cis-lunar space," in *3rd IAA Conference on Dynamics and Control of Space Systems, Moscow, Russia*, 2017, p. 20.

[4] D. Guzzetti, E. M. Zimovan, K. C. Howell, and D. C. Davis, "Stationkeeping analysis for spacecraft in lunar near rectilinear halo orbits," in *AAS/AIAA Space Flight Mechanics Meeting, San Antonio, Texas, USA*, 2017.

[5] W. Wu, Y. Tang, L. Zhang, and D. Qiao, "Design of communication relay mission for supporting lunar-farside soft landing," *Science China Information Sciences*, vol. 61, no. 4, pp. 1–14, 2018.

[6] M. Lemelin, D. M. Blair, C. E. Roberts, K. D. Runyon, D. Nowka, and D. A. Kring, "High-priority lunar landing sites for in situ and sample return studies of polar volatiles," *Planetary and Space Science*, vol. 101, pp. 149–161, 2014.

[7] L. Bucci, M. Lavagna, and R. Jehn, "Station keeping techniques for near rectilinear orbits in the Earth–Moon system," in *Proceedings of 10th international ESA conference on GNC systems, Salzburg, Austria*, vol. 29, 2017.

[8] J. Kepler, M. Caspar, W. von Dyck, and F. Hammer, *Astronomia nova*. CH Beck'sche Verlagsbuchhandlung, 1937.

[9] J. Kepler, *Epitome of Copernican Astronomy and harmonies of the World*. Prometheus Books, 1995.

[10] I. Newton, "Philosophiae naturalis principia mathematica," 1833.

[11] C. E. Sandifer, *The early mathematics of Leonhard Euler*. American Mathematical Soc., 2020, vol. 98.

[12] J. L. Lagrange, *Théorie des fonctions analytiques*. Ve. Courcier, 1813.

[13] C. G. J. Jacobi, *Vorlesungen über dynamik*. 1866.

[14] H. Poincaré, *New methods of celestial mechanics*. Springer Science & Business Media, 1992, vol. 13.

[15] V. Szebehely, "Theory of orbits: The restricted problem of three bodies," *American Journal of Physics*, vol. 36, no. 4, pp. 375–375, 1968.

[16] R. W. Farquhar, *The control and use of libration-point satellites*. Ph.D. Dissertation, Department of Aeronautics and Astronautics, Stanford University, 1968.

[17] R. W. Farquhar and A. A. Kamel, "Quasi-periodic orbits about the translunar libration point," *Celestial Mechanics*, vol. 7, no. 4, pp. 458–473, 1973.

[18] D. L. Richardson, "Halo orbit formulation for the ISEE-3 mission," *Journal of Guidance and Control*, vol. 3, no. 6, pp. 543–548, 1980.

[19] K. C. Howell, "Three-dimensional, periodic, 'halo' orbits," *Celestial Mechanics*, vol. 32, no. 1, pp. 53–71, 1984.

[20] K. Howell and H. Pernicka, "Numerical determination of lissajous trajectories in the restricted three-body problem," *Celestial Mechanics*, vol. 41, no. 1-4, pp. 107–124, 1987.

[21] R. W. Farquhar, D. P. Muhonen, C. R. Newman, and H. S. Heubergerg, "Trajectories and orbital maneuvers for the first libration-point satellite," *Journal of Guidance, Control, and Dynamics*, vol. 3, no. 6, pp. 549–554, 1980.

[22] C. E. Roberts, "Long term missions at the Sun-Earth Libration Point L1: ACE, SOHO, and WIND," in *AAS/AIAA Astrodynamics Specialist Conference, Girdwood, Alaska, USA*, 2011.

[23] D. B. Reisenfeld, R. C. Wiens, B. L. Barraclough, J. T. Steinberg, M. Neugebauer, J. Raines, and T. H. Zurbuchen, "Solar wind conditions and composition during the genesis mission as measured by in situ spacecraft," *Space Science Reviews*, vol. 175, no. 1-4, pp. 125–164, 2013.

[24] N. Jarosik, C. Barnes, C. Bennett, M. Halpern, G. Hinshaw, A. Kogut, M. Limon, S. Meyer, L. Page, D. Spergel, *et al.*, "First-year wilkinson microwave anisotropy probe (wmap)* observations: On-orbit radiometer characterization," *The Astrophysical Journal Supplement Series*, vol. 148, no. 1, p. 29, 2003.

[25] T. A. Pavlak, *Mission Design Applications in the Earth-Moon System: Transfer Trajectories and Stationkeeping*. M.S. Thesis, School of Aeronautics and Astronautics, Purdue University, 2010.

[26] M. Woodard, D. Folta, and D. Woodfork, "ARTEMIS: the first mission to the lunar libration orbits," in *21st International Symposium on Space Flight Dynamics, Toulouse, France*, 2009.

[27] R. Farquhar, D. Muhonen, and L. C. Church, "Trajectories and orbital maneuvers for the ISEE-3/ICE comet mission," in *AIAA/AAS Astrodynamics Conference, Seattle, Washington, USA*, 1984.

[28] H. Heuberger, "Halo orbit station keeping for International Sun-Earth Explorer-C/ISEE-C," in *AIAA/AAS Astrodynamics Specialist Conference, Jackson Hole, Wyoming, USA*, 1977.

[29] J. Erickson and A. Glass, "Implementation of ISEE-3 trajectory control," in *Paper No. AAS 79-128, AIAA/AAS Astrodynamics Specialist Conference, Provincetown, Massachusetts, USA*, 1979.

[30] K. Howell and H. Pernicka, "Stationkeeping method for libration point trajectories," *Journal of Guidance Control and Dynamics*, vol. 16, pp. 151–151, 1993.

[31] H. J. Pernicka, *The Numerical Determination of Nominal Libration Point Trajectories and Development of a Station-Keeping Strategy*. Ph.D. Dissertation, School of Aeronautics and Astronautics, Purdue University, 1990.

[32] G. Gómez, J. Llibre, R. Martínez, and C. Simó, *Dynamics and Mission Design Near Libration Points: Volume I: Fundamentals: The Case of Collinear Libration Points*. World Scientific, 2001, vol. 2.

[33] J. Rodriguez-Canabal and M. Hechler, "Orbital aspects of the SOHO mission design," in *Orbital Mechanics and Mission Design, Proceedings of the AAS/NASA International Symposium, Greenbelt, Maryland, USA*, 1989, pp. 347–357.

[34] P. Sharer, H. Franz, and D. Folta, "WIND Trajectory Design and Control," in *Paper No. MS95/032, CNES International Symposium on Space Dynamics, Toulouse, France*, 1995.

[35] D. Rohrbaugh and C. Schiff, "Stationkeeping approach for the Microwave Anisotropy Probe (MAP)," in *Paper No. AIAA-2002-4429, AIAA/AAS Astrodynamics Specialist Conference, Monterey, California, USA*, 2002.

[36] K. Williams, R. Wilson, M. Lo, K. Howell, and B. Barden, "Genesis halo orbit station keeping design," in *International Symposium: Space Flight Dynamics, Biarritz, France*, 2000.

[37] L. Janes and M. Beckman, "Stationkeeping maneuvers for the James Webb Space Telescope," in *Goddard Flight Mechanics Symposium*, Goddard Space Flight Center Greenbelt, Maryland, USA, 2005.

[38] J. V. Breakwell, A. A. Kamel, and M. J. Ratner, "Station-keeping for a translunar communication station," *Celestial Mechanics*, vol. 10, no. 3, pp. 357–373, 1974.

[39] J. Breakwell, "Investigation of halo satellite orbit control," 1973.

[40] G. Colombo, "The stabilization of an artificial satellite at the inferior conjunction point of the Earth-Moon system," *Smithsonian Contributions to Astrophysics*, vol. 6, p. 213, 1963.

[41] E. A. Euler and E. Yu, "Optimal station-keeping at collinear points," *Journal of Spacecraft and Rockets*, vol. 8, no. 5, pp. 513–516, 1971.

[42] D. Folta, M. Woodard, and D. Cosgrove, "Stationkeeping of the first Earth-Moon libration orbiters: The ARTEMIS mission," in *Paper No. AAS 11-515, AAS/AIAA Astrodynamics Specialist Conference, Girdwood, Alaska, United States*, 2011.

[43] D. Folta, T. Pavlak, K. Howell, M. Woodard, and D. Woodfork, "Stationkeeping of Lissajous trajectories in the Earth-Moon system with applications to ARTEMIS," in *20th AAS/AIAA Space Flight Mechanics Meeting, San Diego, California*, 2010, pp. 10–113.

[44] D. C. Folta, T. A. Pavlak, A. F. Haapala, K. C. Howell, and M. A. Woodard, "Earth–Moon libration point orbit stationkeeping: Theory, modeling, and operations," *Acta Astronautica*, vol. 94, no. 1, pp. 421–433, 2014.

[45] T. Pavlak and K. C. Howell, "Strategy for long-term libration point orbit stationkeeping in the Earth-Moon system," in *AAS/AIAA Astrodynamics Specialist Conference, Girdwood, Alaska, USA*, 2011.

[46] K. Howell and S. Gordon, "Orbit determination error analysis and a station-keeping strategy for Sun-Earth L1 libration point orbits," *Journal of the Astronautical Sciences*, vol. 42, pp. 207–228, 1994.

[47] S. C. Gordon, *Orbit Determination Error Analysis and Station-Keeping for Libration Point Trajectories*. Ph.D. Dissertation, School of Aeronautics and Astronautics, Purdue University, 1991.

[48] T. M. Keeter, *Station-Keeping Strategies for Libration Point Orbits: Target Point and Floquet Mode Approaches*. M.S. Thesis, School of Aeronautics and Astronautics, Purdue University, 1994.

[49] K. Howell and T. Keeter, "Station-keeping strategies for libration point orbits- target point and Floquet mode approaches," *Spaceflight mechanics*, pp. 1377–1396, 1995.

[50] V. Muralidharan, "Orbit Maintenance Strategies for Sun-Earth/Moon Libration Point Missions: Parameter Selection for Target Point and Cauchy-Green Tensor Approaches," M.S. thesis, Purdue University, 2017.

[51] G. Gómez, J. Llibre, R. Martinez, and C. Simó, "Station keeping of libration point orbits," *Final Report: ESOC Contract 5648/83/D/JS (SC)*, 1985.

[52] G. Gómez, K. Howell, J. Masdemont, and C. Simó, "Station-keeping strategies for translunar libration point orbits," *Advances in Astronautical Sciences*, vol. 99, no. 2, pp. 949–967, 1998.

[53] K. C. Howell and T. M. Keeter, "Station-keeping strategies for libration point orbits-Target point and Floquet Mode approaches," *Spaceflight mechanics 1995*, pp. 1377–1396, 1995.

[54] C. Simó, G. Gómez, J. Llibre, and R. Martínez, "Station keeping of a quasiperiodic halo orbit using invariant manifolds," in *Proceed. 2nd Internat. Symp. on spacecraft flight dynamics, Darmstadt, Germany*, 1986, pp. 65–70.

[55] C. Simó, G. Gómez, J. Llibre, R. Martinez, and J. Rodriguez, "On the optimal station keeping control of halo orbits," *Acta Astronautica*, vol. 15, no. 6, pp. 391–397, 1987.

[56] Y. Meng, Y. Zhang, and J. Dai, "Floquet-based design and control approach to spacecraft formation flying in libration point orbits," *Science China Technological Sciences*, vol. 54, no. 3, pp. 758–766, 2011.

[57] D. C. Davis, S. M. Phillips, K. C. Howell, S. Vutukuri, and B. P. McCarthy, "Station-keeping and transfer trajectory design for spacecraft in cislunar space," in *AAS/AIAA Astrodynamics Specialist Conference, Stevenson, Washington, USA*, 2017.

[58] D. Davis, S. Bhatt, K. Howell, J.-W. Jang, R. Whitley, F. Clark, D. Guzzetti, E. Zimovan, and G. Barton, "Orbit maintenance and navigation of human spacecraft at cislunar near rectilinear halo orbits," in *AIAA Space Flight Mechanics Meeting, San Antonio, Texas, USA*, 2017.

[59] D. Folta and F. Vaughn, "A Survey of Earth-Moon Libration Orbits: Stationkeeping Strategies and Intra-Orbit Transfers," in *AIAA/AAS Astrodynamics Specialist Conference, Providence, Rhode Island, USA*, 2004.

[60] D. Folta, T. Pavlak, K. Howell, M. Woodard, and D. Woodfork, "Stationkeeping of Lissajous trajectories in the Earth-Moon system with applications to ARTEMIS," in *AIAA/AAS Astrodynamics Specialist Conference, Toronto, Canada*, 2010.

[61] V. Muralidharan, A. Weiss, and U. V. Kalabic, "Control Strategy for Long-Term Station-Keeping on Near-Rectilinear Halo Orbits," in *AIAA/AAS Space Flight Mechanics Meeting, Orlando, Florida, USA*, 2020.

[62] V. Muralidharan, A. Weiss, and U. Kalabić, "Tracking neighboring quasi-satellite orbits around phobos," *World Congress of the International Federation of Automatic Control (IFAC)-PapersOnLine*, vol. 53, no. 2, pp. 14 906–14 911, 2020.

[63] U. Kalabic, A. Weiss, S. Di Cairano, and I. Kolmanovsky, "Station-keeping and momentum-management on halo orbits around l2: Linear-quadratic feedback and model predictive control approaches," in *AAS/AIAA Space Flight Mechanics Meeting, Williamsburg, Virginia, USA*, 2015.

[64] M. Shirobokov, S. Trofimov, and M. Ovchinnikov, "Survey of station-keeping techniques for libration point orbits," *Journal of Guidance, Control, and Dynamics*, vol. 40, no. 5, pp. 1085–1105, 2017.

[65] K. C. Howell and M. Kakoi, "Transfers between the earth–moon and sun–earth systems using manifolds and transit orbits," *Acta Astronautica*, vol. 59, no. 1-5, pp. 367–380, 2006.

[66] M. Vaquero and K. C. Howell, "Leveraging resonant-orbit manifolds to design transfers between libration-point orbits," *Journal of Guidance, Control, and Dynamics*, vol. 37, no. 4, pp. 1143–1157, 2014.

[67] F. Topputo, M. Vasile, and F. Bernelli-Zazzera, "Low energy interplanetary transfers exploiting invariant manifolds of the restricted three-body problem," *The Journal of the Astronautical Sciences*, vol. 53, no. 4, pp. 353–372, 2005.

[68] E. M. Alessi, G. Gómez, and J. J. Masdemont, "Two-manoeuvres transfers between leos and lissajous orbits in the earth–moon system," *Advances in Space Research*, vol. 45, no. 10, pp. 1276–1291, 2010.

[69] D. Canales, K. C. Howell, and E. Fantino, "Moon-to-moon transfer methodology for multi-moon systems in the coupled spatial circular restricted three-body problem," in *AAS/AIAA Astrodynamics Specialist Conference, Lake Tahoe, California, USA (Virtual)*, 2020.

[70] N. L. Parrish, J. S. Parker, S. P. Hughes, and J. Heiligers, "Low-thrust transfers from distant retrograde orbits to l2 halo orbits in the earth-moon system," in *6th International Conference on Astrodynamics Tools and Techniques*, 2016, pp. 14–17.

[71] R. E. Pritchett, "Strategies for Low-Thrust Transfer Design Based on Direct Collocation Techniques," Ph.D. dissertation, Purdue University, 2020.

[72] B. P. Pino, K. C. Howell, and D. Folta, "An energy-informed adaptive algorithm for low-thrust spacecraft cislunar trajectory design," in *AAS/AIAA Astrodynamics Specialist Conference, South Lake Tahoe, California, United States*, 2020.

[73] A. Das-Stuart, K. C. Howell, and D. C. Folta, "Rapid trajectory design in complex environments enabled by reinforcement learning and graph search strategies," *Acta Astronautica*, vol. 171, pp. 172–195, 2020.

[74] S. L. McCarty, L. M. Burke, and M. McGuire, "Parallel monotonic basin hopping for low thrust trajectory optimization," in *AAS/AIAA Space Flight Mechanics Meeting, Kissimmee, Florida, USA*, 2018.

[75] S. Vutukuri, "Spacecraft trajectory design techniques using resonant orbits," M.S. thesis, Purdue University, 2018.

[76] L. R. Capdevila and K. C. Howell, "A transfer network linking Earth, Moon, and the triangular libration point regions in the Earth-Moon system," *Advances in Space Research*, vol. 62, no. 7, pp. 1826–1852, 2018.

[77] E. M. Zimovan-Spreen and K. C. Howell, "Dynamical structures nearby NRHOs with applications in cislunar space," in *AAS/AIAA Astrodynamics Specialist Conference, Portland, Maine, United States*, 2019.

[78] L. Lu, H. Li, W. Zhou, and J. Liu, "Design and analysis of a direct transfer trajectory from a near rectilinear halo orbit to a low lunar orbit," *Advances in Space Research*, vol. 67, no. 3, pp. 1143–1154, 2021.

[79] M. Rozek, H. Ogawa, S. Ueda, T. Ikenaga, *et al.*, "Multi-objective optimisation of NRHO-LLO orbit transfer via surrogate-assisted evolutionary algorithms," in *AIAC18: 18th Australian International Aerospace Congress (2019): HUMS-11th Defence Science and Technology (DST) International Conference on Health and Usage Monitoring (HUMS 2019): ISSFD-27th International Symposium on Space Flight Dynamics (ISSFD)*, 2019, p. 1001.

[80] C. Thangavelu, "Transfers between Near Rectilinear Halo Orbits and Low Lunar Orbits," M.S. thesis, University of Colorado at Boulder, 2019.

[81] C. R. Short and K. C. Howell, "Lagrangian coherent structures in various map representations for application to multi-body gravitational regimes," *Acta Astronautica*, vol. 94, no. 2, pp. 592–607, 2014.

[82] V. Muralidharan and K. C. Howell, "Stationkeeping in Earth-Moon Near Rectilinear Halo Orbits," in *AAS/AIAA Astrodynamics Specialist Conference, South Lake Tahoe, California, United States*, 2020.

[83] V. Muralidharan and K. C. Howell, "Orbit Maintenance Strategy for Earth-Moon Halo Orbits," in *31st AAS/AIAA Spaceflight Mechanics Meeting, Charlotte, North Carolina, USA (Virtual)*, 2021.

[84] K. Oshima, S. Campagnola, C. H. Yam, Y. Kayama, Y. Kawakatsu, N. Ozaki, Q. Verspieren, K. Kakihara, K. Oguri, and R. Funase, "EQUULEUS mission analysis: Design of the transfer phase," in *International Symposium on Space Technology and Science, ISTS-2017-d-159, Ehime, Japan*, 2017, pp. 3–9.

[85] K. Oguri, K. Oshima, S. Campagnola, K. Kakihara, N. Ozaki, N. Baresi, Y. Kawakatsu, and R. Funase, "EQUULEUS Trajectory Design," *The Journal of the Astronautical Sciences*, vol. 67, no. 3, pp. 950–976, 2020.

[86] N. Baresi, D. A. Dei Tos, H. Ikeda, and Y. Kawakatsu, "Trajectory design and maintenance of the Martian Moons eXploration Mission around Phobos," *Journal of Guidance, Control, and Dynamics*, pp. 1–12, 2020.

[87] C. Spreen, K. Howell, and B. Marchand, "Node placement capability for spacecraft trajectory targeting in an ephemeris model," in *AAS/AIAA Astrodynamics Specialist Conference, Vail, Colorado, United States*, 2015.

[88] C. R. Short, D. Blazevski, K. C. Howell, and G. Haller, "Stretching in phase space and applications in general nonautonomous multi-body problems," *Celestial Mechanics and Dynamical Astronomy*, vol. 122, no. 3, pp. 213–238, 2015.

[89] G. Beutler, *Methods of Celestial Mechanics: Volume I: Physical, Mathematical, and Numerical Principles*. Springer Science & Business Media, 2004.

[90] G. T. Gillies, "The Newtonian gravitational constant: Recent measurements and related studies," *Reports on Progress in Physics*, vol. 60, no. 2, p. 151, 1997. [Online]. Available: http://stacks.iop.org/0034-4885/60/i=2/a=001.

[91] J. S. Nuss, *The Use of Solar Sails in the Circular Restricted Problem of Three Bodies*. M.S. Thesis, School of Aeronautics and Astronautics, Purdue University, 1998.

[92] A. I. S. McInnes, *Strategies for Solar Sail Mission Design in the Circular Restricted Three-Body Problem*. M.S. Thesis, School of Aeronautics and Astronautics, Purdue University, 2000.

[93] R. DiSalle, "Conventionalism and the origins of the inertial frame concept," in *PSA: Proceedings of the Biennial Meeting of the Philosophy of Science Association*, Philosophy of Science Association, 1990, pp. 139–147.

[94] H. G. Walter and O. Sovers, *Astrometry of fundamental catalogues: the evolution from optical to radio reference frames*. Springer Science & Business Media, 2000.

[95] Navigation and Ancillary Information Facility (NAIF), *An Overview of Reference Frames and Coordinate Systems in the SPICE Context*, https://naif.jpl.nasa.gov/pub/naif/toolkit_docs/Tutorials/pdf/individual_docs/17_frames_and_coordinate_systems.pdf (Accessed: 4-4-2021), 2020.

[96] J. M. Howsman, *Investigation of Transfer Trajectories to Periodic Horseshoe Orbits*. M.S. Thesis, School of Aeronautics and Astronautics, Purdue University, 2011.

[97] R. Pritchett, *Numerical Methods for Low-Thrust Trajectory Optimization*. M.S. Thesis, School of Aeronautics and Astronautics, Purdue University, 2016.

[98] A. G. V. Anderlecht, *Tadpole orbits in the L4/L5 region: Construction and links to other families of Periodic Orbits*. M.S. Thesis, School of Aeronautics and Astronautics, Purdue University, 2016.

[99] V. S. Ryaben'kii and S. V. Tsynkov, *A theoretical introduction to numerical analysis*. CRC Press, 2006.

[100] J. V. Breakwell and J. V. Brown, "The 'halo' family of 3-dimensional periodic orbits in the Earth-Moon restricted 3-body problem," *Celestial mechanics and dynamical astronomy*, vol. 20, no. 4, pp. 389–404, 1979.

[101] P. Nath and R. Ramanan, "Precise halo orbit design and optimal transfer to halo orbits from Earth using differential evolution," *Advances in Space Research*, vol. 57, no. 1, pp. 202–217, 2016.

[102] H. R. Malonek and R. De Almeida, "A note on a generalized joukowski transformation," *Applied Mathematics Letters*, vol. 23, no. 10, pp. 1174–1178, 2010.

[103] T. Pavlak and K. Howell, "Strategy for optimal, long-term stationkeeping of libration point orbits in the Earth-Moon system," in *AIAA/AAS Astrodynamics Specialist Conference, Minneapolis, Minnesota, USA*, 2012.

[104] D. Baker, N. Sears, J. Suomals, and R. White, "Lunar Orbit Determination by Star Occultation and MSFN Tracking," *Massachusetts Institute of Technology Instrumentation Lab., Rept. E-1429 (September 1963)*, vol. 68, 1963.

[105] R. Floberghagen, P. Visser, and M. Vasile, "Low lunar orbit analysis, determination and selection for soft landing on the lunar south pole," in *Space Flight Dynamics*, vol. 403, 1997, p. 321.

[106] S. Goossens, K. Matsumoto, D. Rowlands, F. Lemoine, H. Noda, and H. Araki, "Orbit determination of the SELENE satellites using multi-satellite data types and evaluation of SELENE gravity field models," *Journal of Geodesy*, vol. 85, no. 8, pp. 487–504, 2011.

[107] E. Mazarico, D. Rowlands, G. Neumann, D. Smith, M. Torrence, F. Lemoine, and M. Zuber, "Orbit determination of the lunar reconnaissance orbiter," *Journal of Geodesy*, vol. 86, no. 3, pp. 193–207, 2012.

[108] S. Slojkowski, "Lunar reconnaissance orbiter orbit determination accuracy analysis," in *Proceedings of the in Proceedings of 24th International Symposium on Space Flight Dynamics (ISSFD)*, 2014.

[109] S. Qin, Y. Huang, P. Li, Q. Shan, M. Fan, X. Hu, and G. Wang, "Orbit and tracking data evaluation of Chang'E-4 relay satellite," *Advances in Space Research*, vol. 64, no. 4, pp. 836–846, 2019.

[110] Y. Huang, P. Li, and M. Fan, "Orbit determination of ce-5t1 in earth-moon l2 libration point orbit with ground tracking data," *42nd COSPAR Scientific Assembly*, vol. 42, B3–1, 2018.

[111] R. H. Battin and G. M. Levine, "Application of Kalman filtering techniques to the Apollo program (Kalman filtering techniques applied to coasting flight navigation problems of Apollo lunar mission)," 1970.

[112] M. S. Grewal and A. P. Andrews, "Applications of Kalman filtering in aerospace 1960 to the present [historical perspectives]," *IEEE Control Systems Magazine*, vol. 30, no. 3, pp. 69–78, 2010.

[113] M. Woodard, D. Cosgrove, P. Morinelli, J. Marchese, B. Owens, and D. Folta, "Orbit determination of spacecraft in Earth-Moon L1 and L2 libration point orbits," in *AIAA/AAS Astrodynamics Specialist Conference, Girdwood, Alaska, USA*, 2011.

[114] J. Campbell, S. Synnott, and G. Bierman, "Voyager orbit determination at Jupiter," *IEEE Transactions on Automatic Control*, vol. 28, no. 3, pp. 256–268, 1983.

[115] B. D. Tapley, J. Ries, G. Davis, R. Eanes, B. Schutz, C. Shum, M. Watkins, J. Marshall, R. Nerem, B. Putney, *et al.*, "Precision orbit determination for TOPEX/POSEIDON," *Journal of Geophysical Research: Oceans*, vol. 99, no. C12, pp. 24 383–24 404, 1994.

[116] F. Budnik, T. Morley, and R. Mackenzie, "ESOC's system for interplanetary orbit determination: Implementation and operational experience," in *18th International Symposium on Space Flight Dynamics, Munich, Germany*, vol. 548, 2004, p. 387.

[117] K. Muralidharan, *Six sigma for organizational excellence: A statistical approach*. Springer, 2015.

[118] D. C. Folta, T. A. Pavlak, A. F. Haapala, K. C. Howell, and M. A. Woodard, "Earth–Moon libration point orbit stationkeeping: theory, modeling, and operations," *Acta Astronautica*, vol. 94, no. 1, pp. 421–433, 2014.

[119] D. C. Davis, F. S. Khoury, K. C. Howell, and D. J. Sweeney, "Phase Control and Eclipse Avoidance in Near Rectilinear Halo Orbits," in *43rd AAS Guidance, Navigation and Control Conference, Breckenridge, Colorado, United States*, 2020.

[120] G. Haller, "Lagrangian coherent structures from approximate velocity data," *Physics of fluids*, vol. 14, no. 6, pp. 1851–1861, 2002.

[121] R. L. Anderson, M. W. Lo, and G. H. Born, "Application of local Lyapunov exponents to maneuver design and navigation in the three-body problem," in *Paper No. AAS 03-569, AIAA/AAS Astrodynamics Specialist Conference, Big Sky, Montana*, 2003.

[122] J. S. Subirana, J. J. Zornoza, and M. Hernández-Pajares, "GNSS data processing. volume 1: Fundamentals and algorithms," *ESA Communications ESTEC*, vol. 299, p. 2200, 2013.

[123] G. L. Jones, "On the Markov chain central limit theorem," *Probability surveys*, vol. 1, pp. 299–320, 2004.

[124] I. Cavallari, R. Petitdemange, and S. Lizy-Destrez, "Transfer from a Lunar distant retrograde orbit to Mars through Lyapunov orbits," in *27th International Symposium on Space Flight Dynamics (ISSFD), Melbourne, Australia*, 2019, pp. 1393–1398.

[125] R. Martinez, K. E. Goodliff, and R. J. Whitley, "ISECG global exploration roadmap: A stepwise approach to deep space exploration," in *AIAA SPACE 2013 Conference and Exposition, San Diego, California, United States*, 2013.

[126] D. D. Mazanek, R. G. Merrill, J. R. Brophy, and R. P. Mueller, "Asteroid redirect mission concept: A bold approach for utilizing space resources," *Acta Astronautica*, vol. 117, pp. 163–171, 2015.

[127] K. K. Boudad, D. C. Davis, and K. C. Howell, "Disposal trajectories from near rectilinear halo orbits," in *AAS/AIAA Astrodynamics Specialists Conference, Snowbird, Utah, USA*, 2018.

[128] K. Howell, M. Beckman, C. Patterson, and D. Folta, "Representations of invariant manifolds for applications in three-body systems," *The Journal of the Astronautical Sciences*, vol. 54, no. 1, pp. 69–93, 2006.

[129] A. F. Haapala, "Trajectory design using periapse maps and invariant manifolds," M.S. thesis, Purdue University, 2010.

[130] J. Stuart, M. Ozimek, and K. Howell, "Optimal, low-thrust, path-constrained transfers between libration point orbits using invariant manifolds," in *AIAA/AAS Astrodynamics Specialist Conference, Toronto, Canada*, 2010.

[131] S. Soldini, C. Colombo, S. J. Walker, *et al.*, "Solar radiation pressure end-of-life disposal for libration-point orbits in the elliptic restricted three-body problem," in *25th AAS/AIAA Space Flight Mechanics Meeting, Williamsburg, Virginia, USA*, 2015.

[132] Z. Olikara, G. Gómez Muntané, and J. Masdemont Soler, "End-of-life disposal of libration point orbit spacecraft," in *64rd International Astronautical Congress, Beijing, China*, 2013, pp. 1–13.

[133] D. C. Davis, K. K. Boudad, S. M. Phillips, and K. C. Howell, "Disposal, deployment, and debris in near rectilinear halo orbits," in *29th AAS/AIAA Space Flight Mechanics Meeting, Ka'anapali, Maui, Hawaii, USA*, 2019.

[134] M. O. Ward, "A taxonomy of glyph placement strategies for multidimensional data visualization," *Information Visualization*, vol. 1, no. 3-4, pp. 194–210, 2002.

[135] A. F. Haapala and K. C. Howell, "Representations of higher-dimensional poincaré maps with applications to spacecraft trajectory design," *Acta Astronautica*, vol. 96, pp. 23–41, 2014.

[136] B. J. P. Pino, "Energy-Informed Strategies For Low-Thrust Trajectory Design in Cislunar Space," Ph.D. dissertation, Purdue University, 2020.

A. INFLUENCING FORCES ON HALO ORBITS

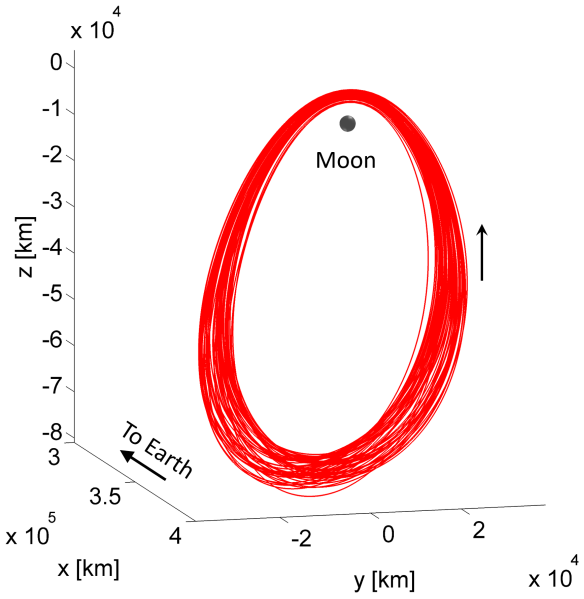

(a) Reference orbit in ephemeris model

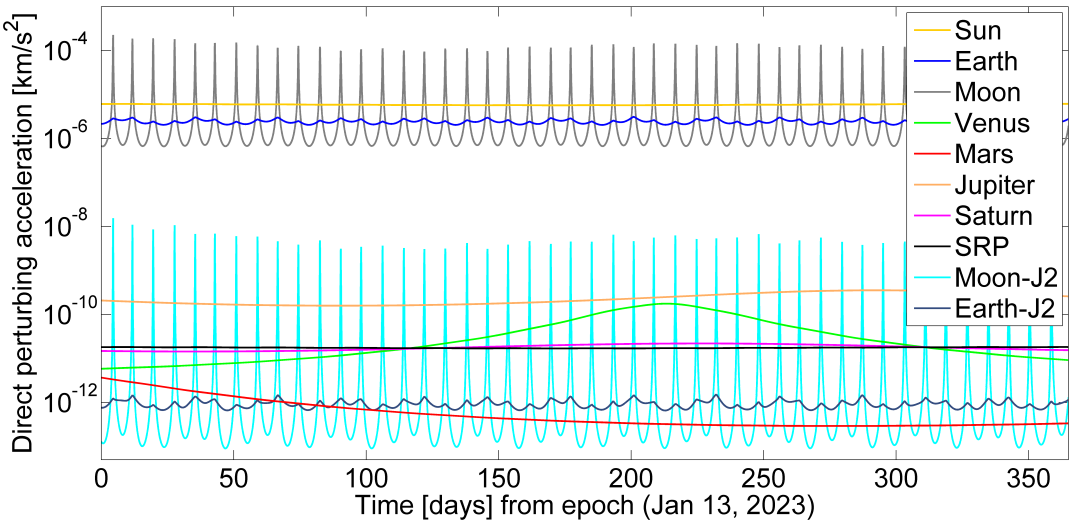

(b) Direct perturbing acceleration

Figure A.1. Spacecraft trajectory and influencing force levels along an L1 southern NRHO with perilune radius 4000 km.

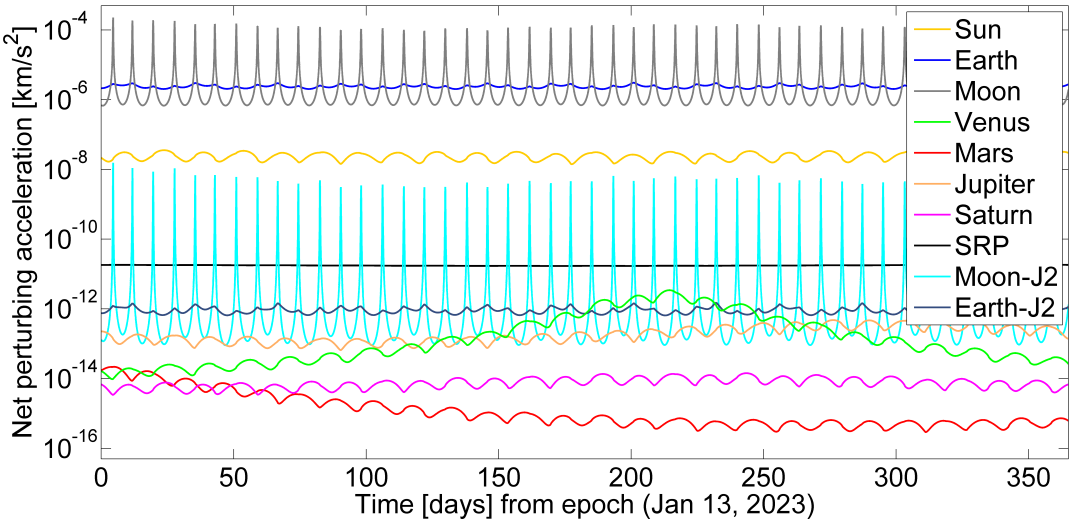

(a) Relative to Earth-Moon Barycenter

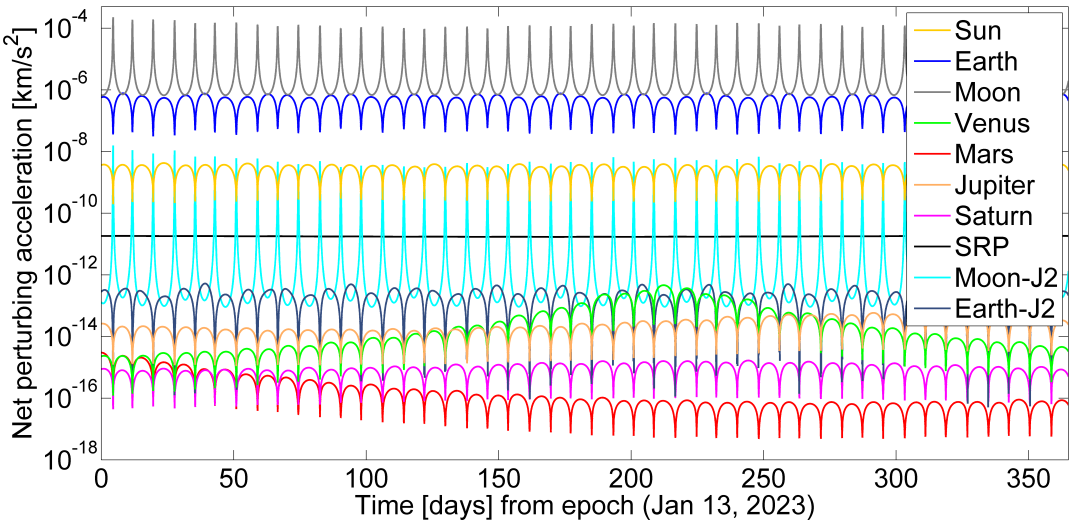

(b) Relative to Moon

Figure A.2. Net perturbing acceleration acting on the spacecraft along an L1 southern NRHO with perilune radius 4000 km.

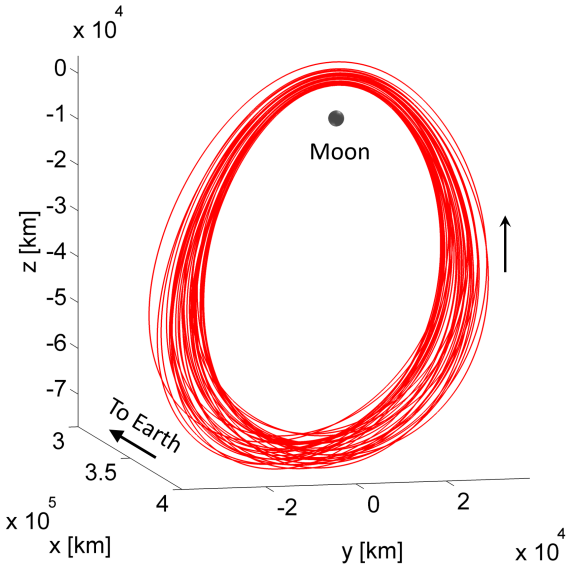

(a) Reference orbit in ephemeris model

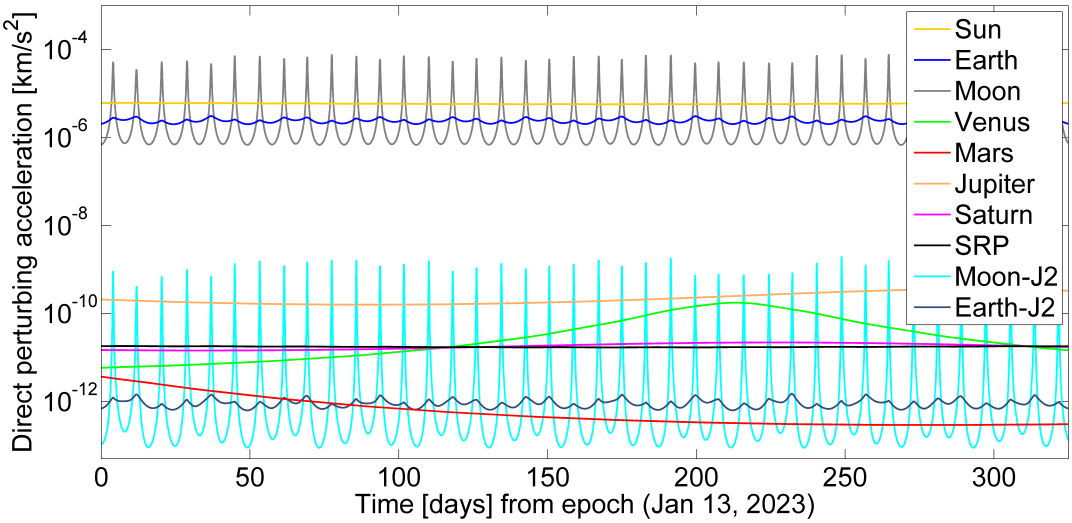

(b) Direct perturbing acceleration

Figure A.3. Spacecraft trajectory and influencing force levels along an L1 southern NRHO with perilune radius 8000 km.

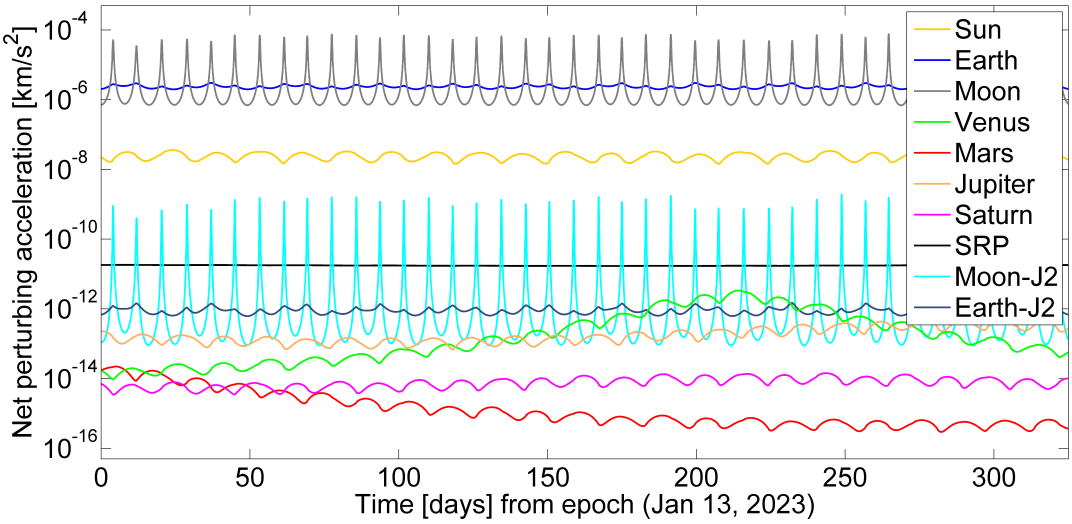

(a) Relative to Earth-Moon Barycenter

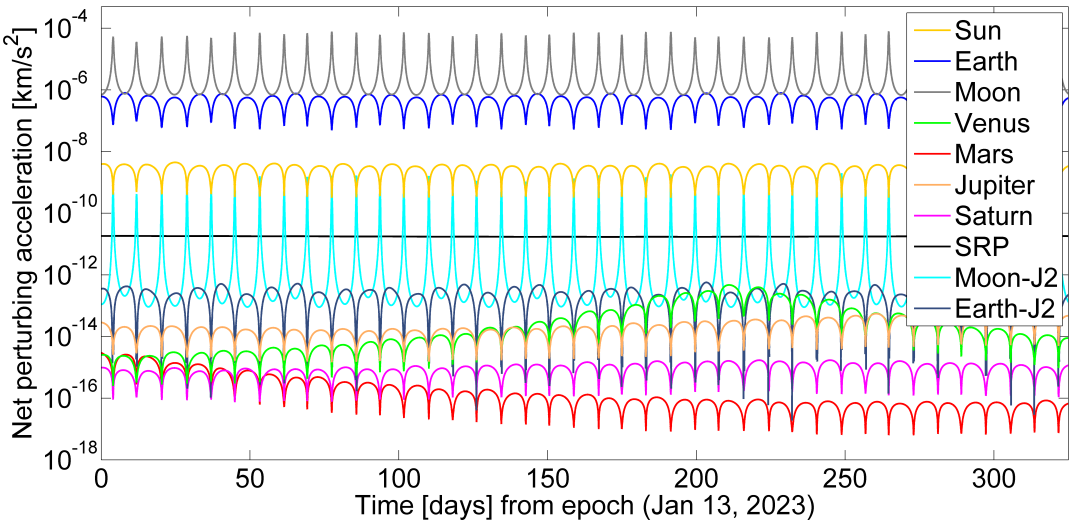

(b) Relative to Moon

Figure A.4. Net perturbing acceleration acting on the spacecraft along an L1 southern NRHO with perilune radius 8000 km.

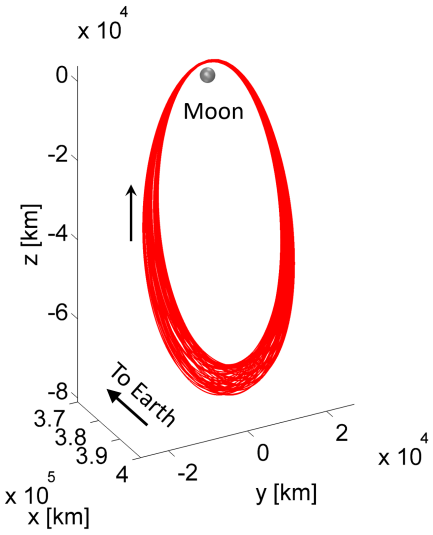

(a) Reference orbit in ephemeris model

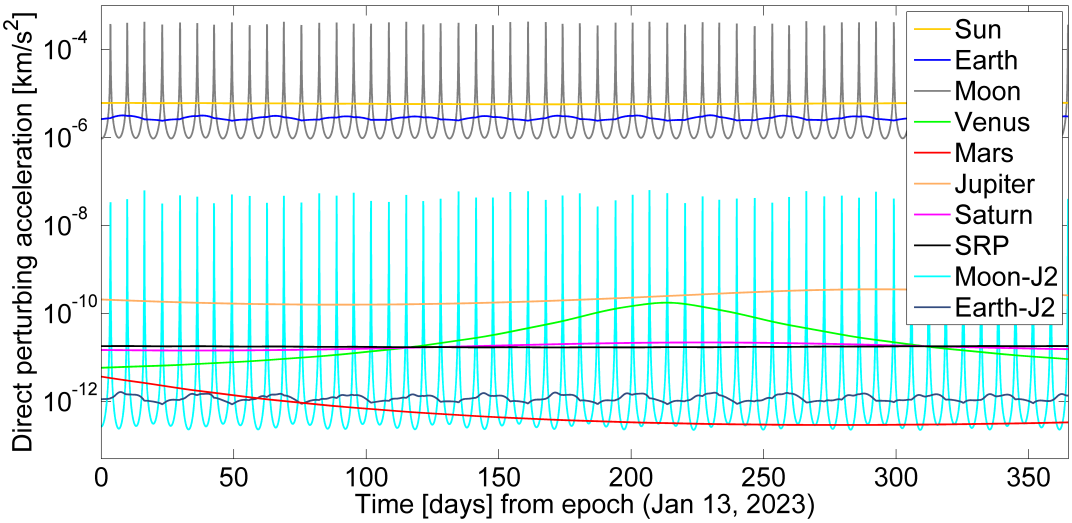

(b) Direct perturbing acceleration

Figure A.5. Spacecraft trajectory and influencing force levels along an L2 southern NRHO with perilune radius 3200 km.

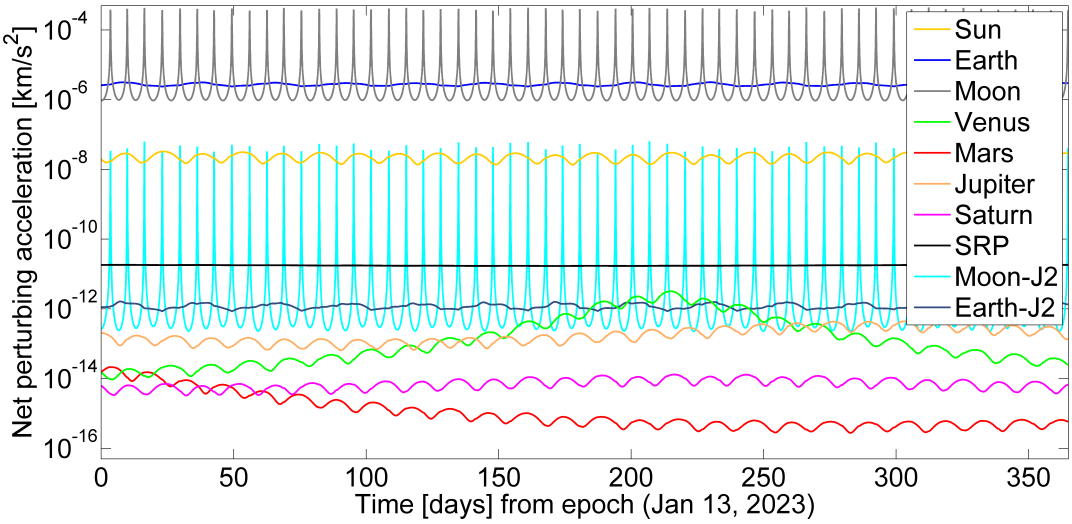

(a) Relative to Earth-Moon Barycenter

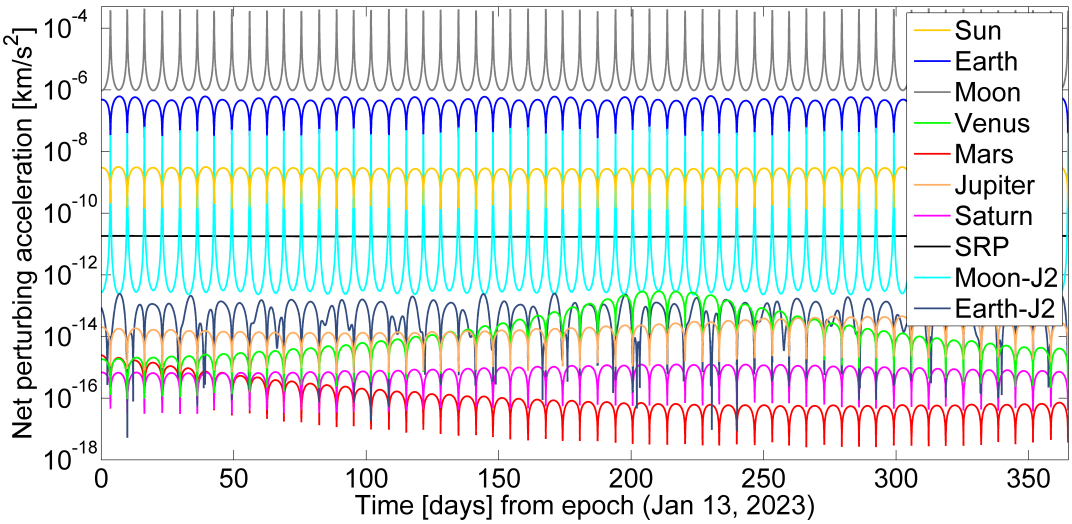

(b) Relative to Moon

Figure A.6. Net perturbing acceleration acting on the spacecraft along an L2 southern NRHO with perilune radius 3200 km.

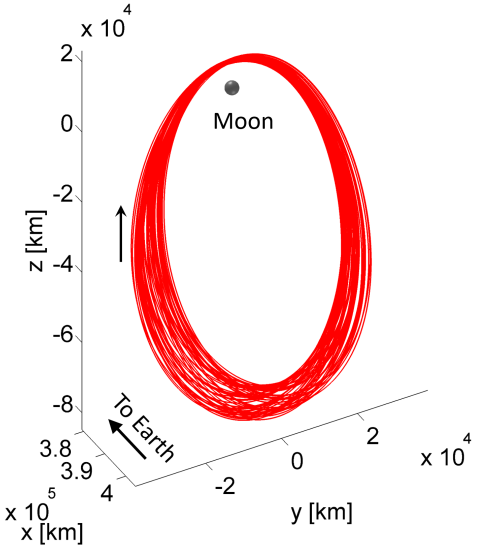

(a) Reference orbit in ephemeris model

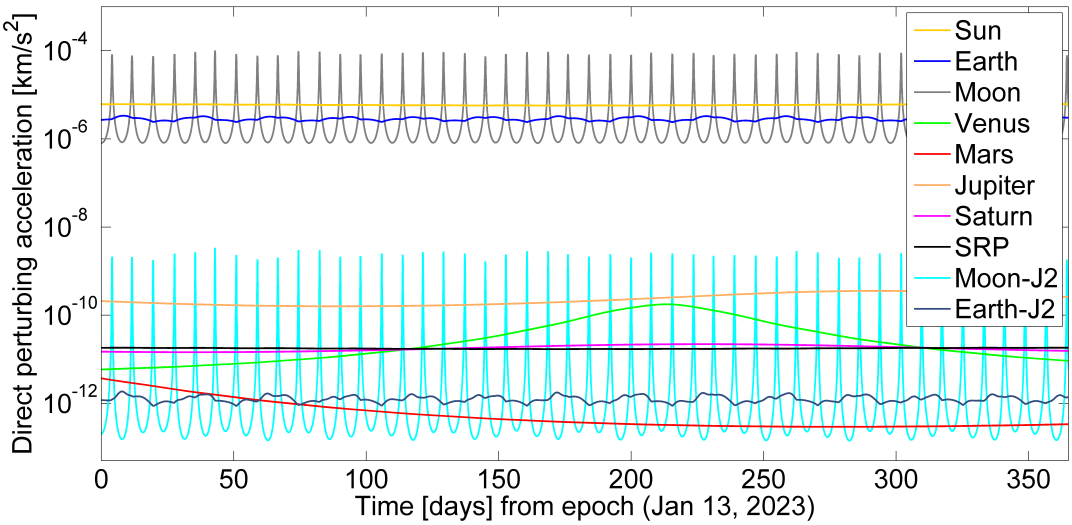

(b) Direct perturbing acceleration

Figure A.7. Spacecraft trajectory and influencing force levels along an L2 southern NRHO with perilune radius 7200 km.

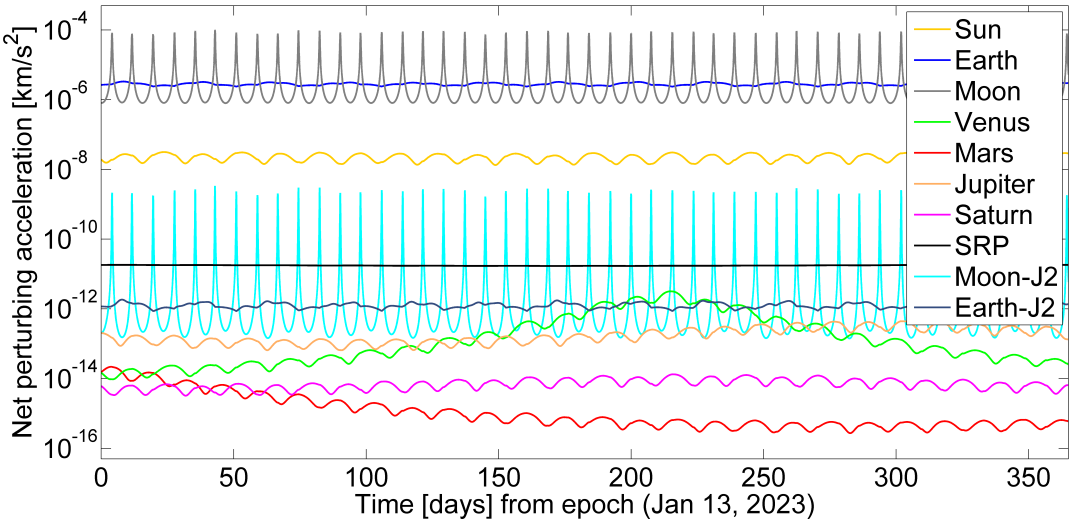

(a) Relative to Earth-Moon Barycenter

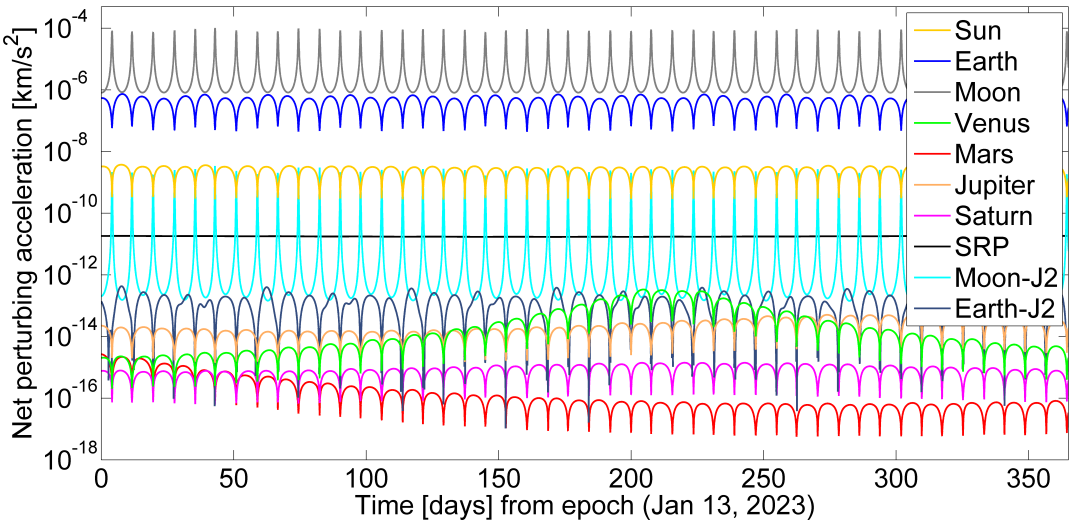

(b) Relative to Moon

Figure A.8. Net perturbing acceleration acting on the spacecraft along an L2 southern NRHO with perilune radius 7200 km.

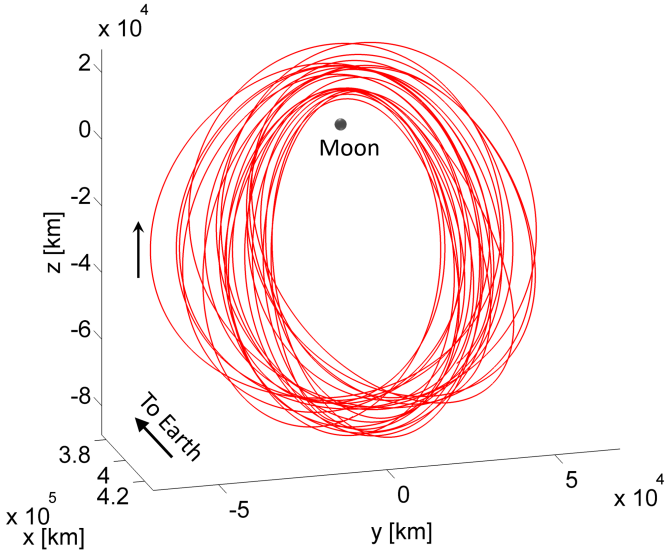

(a) Reference orbit in ephemeris model

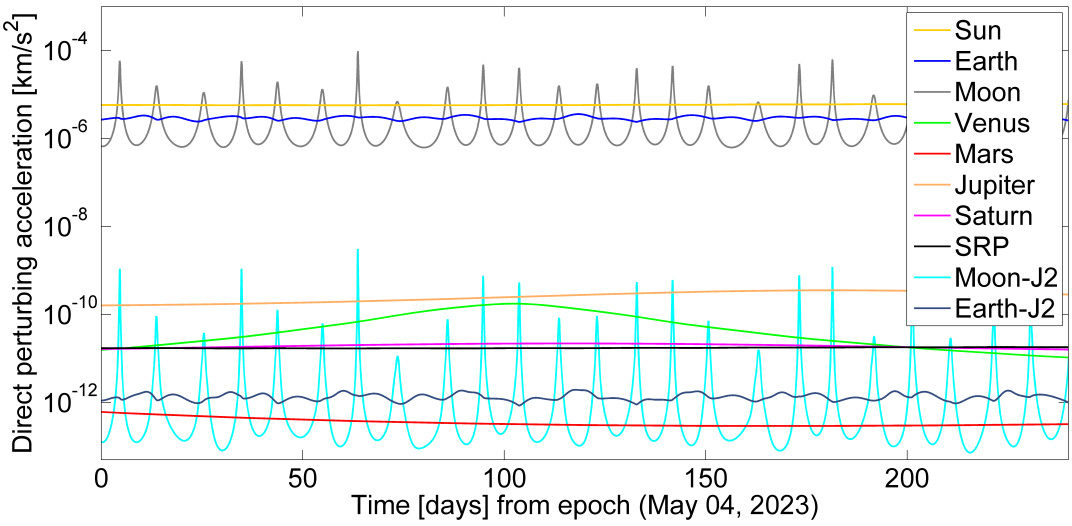

(b) Direct perturbing acceleration

Figure A.9. Spacecraft trajectory and influencing force levels along an L2 southern NRHO with perilune radius 15000 km.

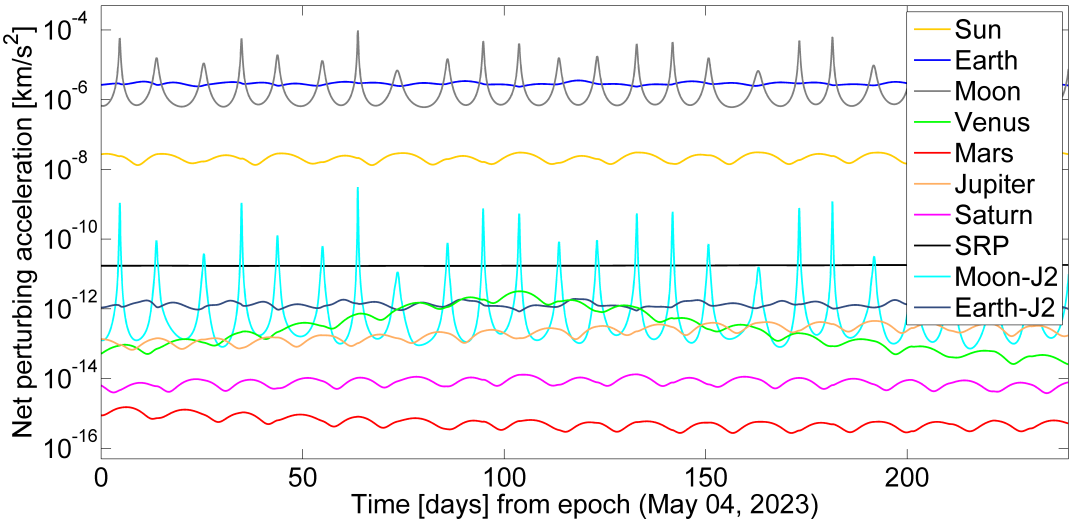

(a) Relative to Earth-Moon Barycenter

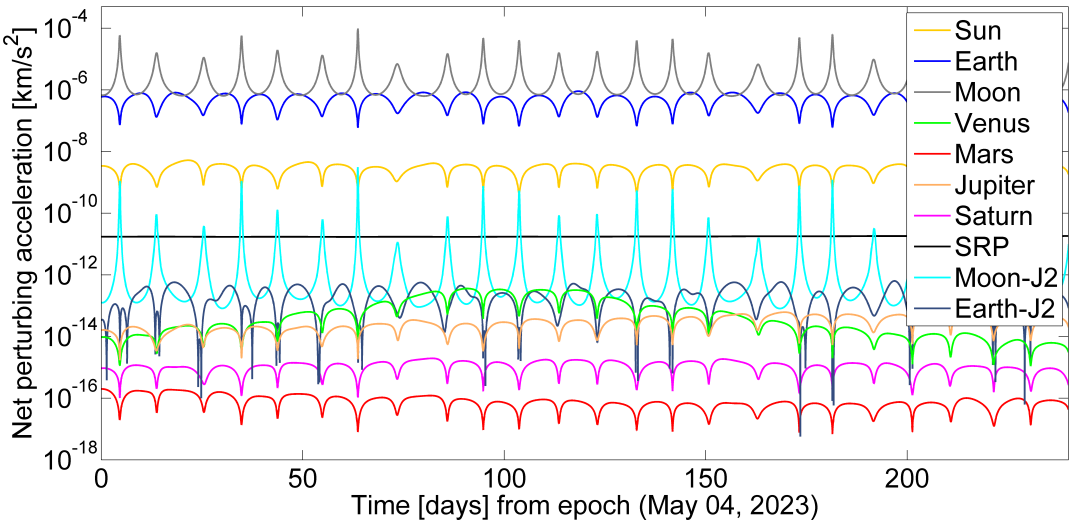

(b) Relative to Moon

Figure A.10. Net perturbing acceleration acting on the spacecraft along an L2 southern NRHO with perilune radius 15000 km.

B. TRANSFER TRAJECTORIES: INITIAL CONDITIONS

B.1 L2 Southern 9:2 synodic resonant NRHO to L2 Northern 9:2 synodic resonant NRHO

B.1.1 Case 1

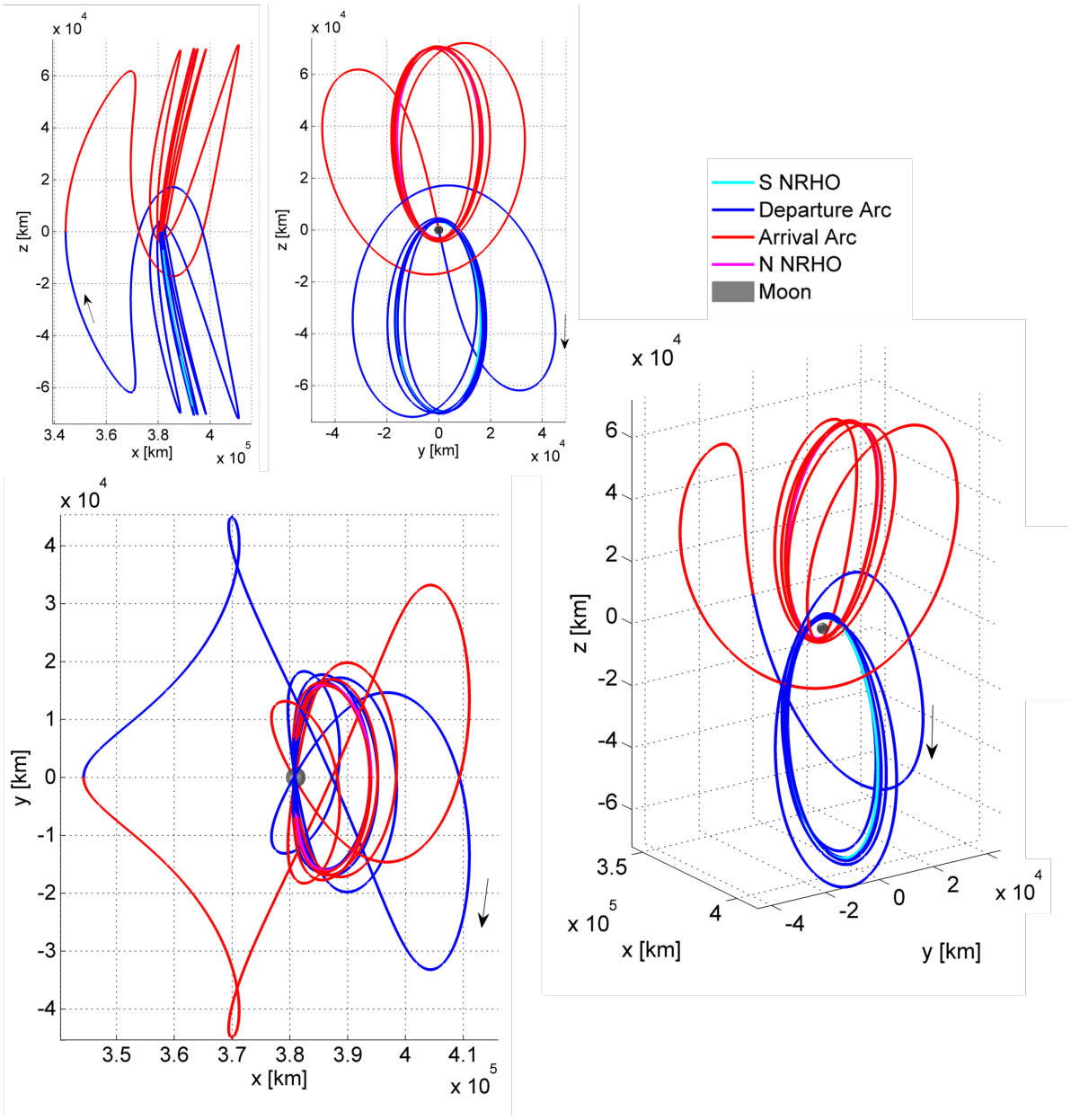

Figure B.1. Locally optimal transfer between L2 southern 9:2 synodic resonant NRHO to L2 northern 9:2 synodic resonant NRHO. Different views for Case 1 transfer.

Table B.1. Initial conditions for transfer from southern 9:2 synodic resonant NRHO to northern 9:2 synodic resonant NRHO (Case 1). Units are in non-dimensional quantities. System mass ratio, $\mu = 0.0121505856096240$.

Initial Conditions	Departure	Arrival
x	0.996927294460369	0.996928684455933
y	-0.0403732064537565	0.0403741246796326
z	-0.0687658508829691	0.0687740941147247
$\dot{x}$	-0.0721210523239770	0.0721197873643325
$\dot{y}$	0.0507544925471208	0.0507341903956708
$\dot{z}$	0.443960420126807	0.443929166676559
Time of Flight	11.4741595643892	-11.4743646922688*
Jacobi Constant of Orbit (actual periodic orbit)	3.04688426854973	3.04688426854973

*Negative Time of Flight indicates propagated backwards in time.

B.1.2 Case 2

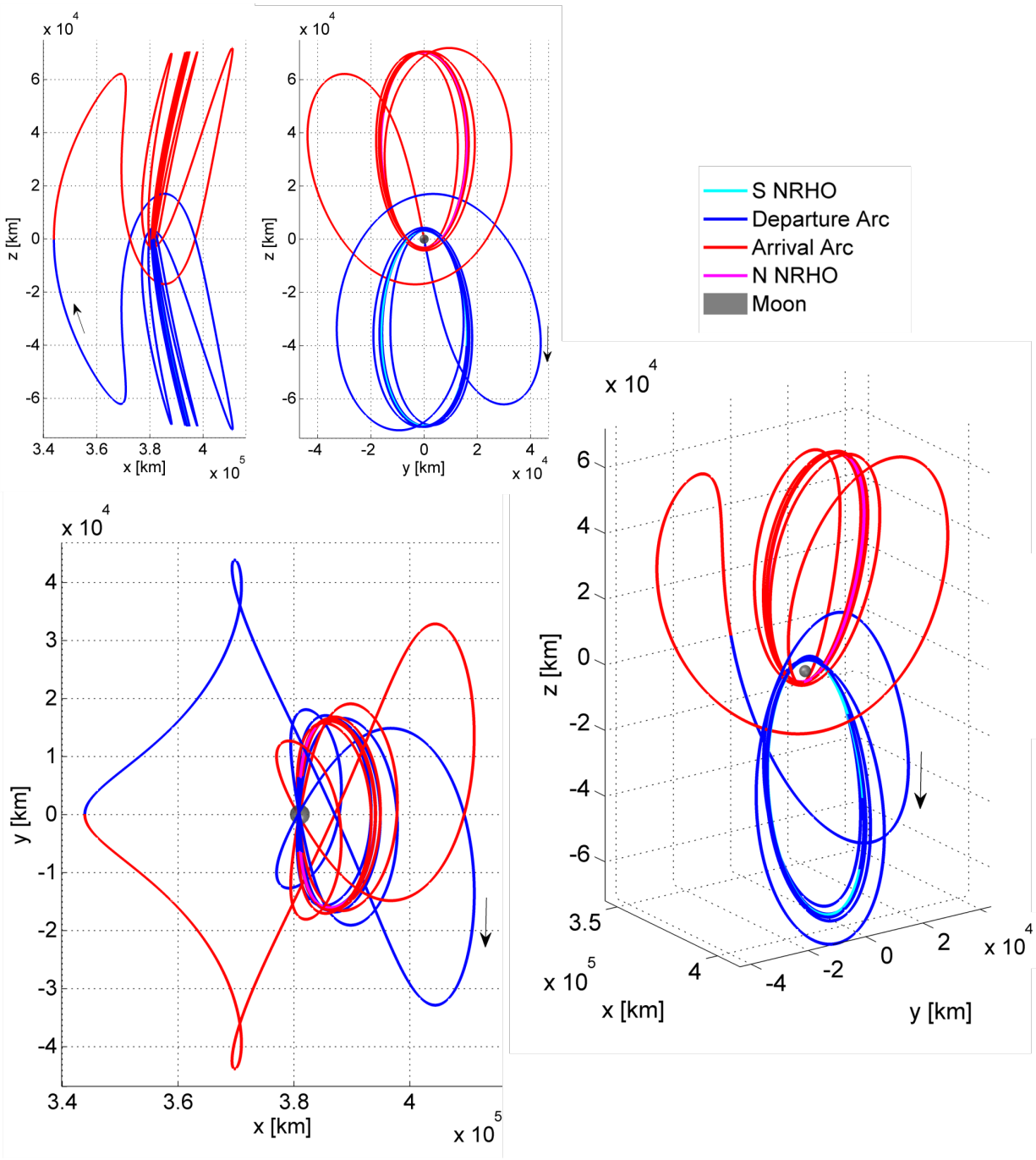

Figure B.2. Locally optimal transfer between L2 southern 9:2 synodic resonant NRHO to L2 northern 9:2 synodic resonant NRHO. Different views for Case 2 transfer.

Table B.2. Initial conditions for transfer from southern 9:2 synodic resonant NRHO to northern 9:2 synodic resonant NRHO (Case 2). Units are in non-dimensional quantities. System mass ratio, $\mu = 0.0121505856096240$.

Initial Conditions	Departure	Arrival
x	1.00349960801801	1.00755126958083
y	0.0414389685145646	-0.0394377964588642
z	-0.104070301847839	0.123267979465757
$\dot{x}$	0.0664262578469378	-0.0594055609962941
$\dot{y}$	-0.0181200047348926	-0.0435437202091242
$\dot{z}$	-0.326672335820773	-0.270856516710595
Time of Flight	12.5895071001317	-12.5278096344325*
Jacobi Constant of Orbit (actual periodic orbit)	3.04688426854973	3.04688426854973

*Negative Time of Flight indicates propagated backwards in time.

B.1.3 Case 3

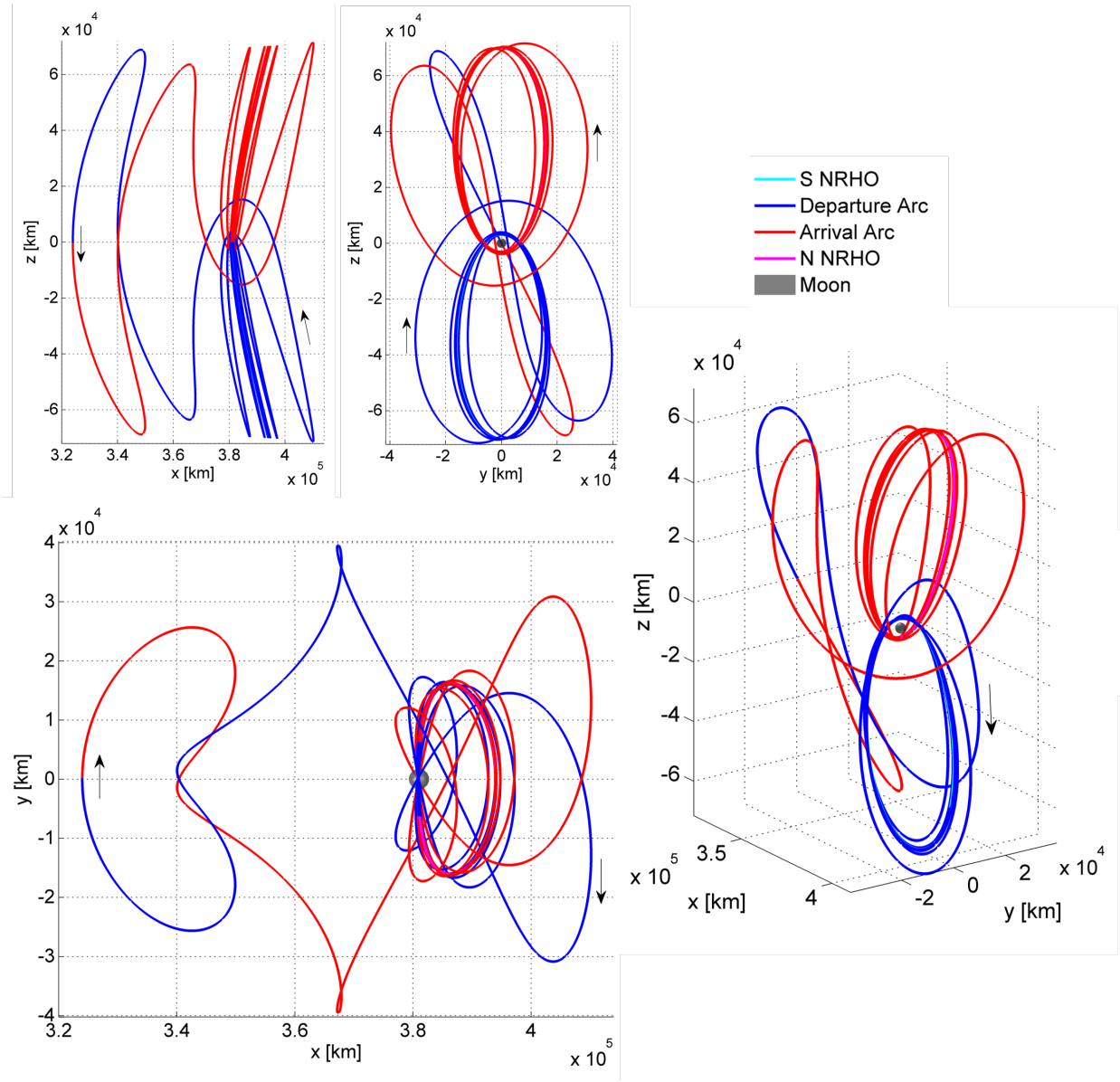

Figure B.3. Locally optimal transfer between L2 southern 9:2 synodic resonant NRHO to L2 northern 9:2 synodic resonant NRHO. Different views for Case 3 transfer.

Table B.3. Initial conditions for transfer from southern 9:2 synodic resonant NRHO to northern 9:2 synodic resonant NRHO (Case 3). Units are in non-dimensional quantities. System mass ratio, $\mu = 0.0121505856096240$.

Initial Conditions	Departure	Arrival
x	1.01470902994341	1.01475339074349
y	0.0307294831461665	-0.0306483605438827
z	-0.154259346316557	0.154442430572550
$\dot{x}$	0.0427952321126951	-0.0426648868355453
$\dot{y}$	-0.0769728043242916	-0.0771550602489779
$\dot{z}$	-0.174093064628739	-0.173464315553202
Time of Flight	13.9993139249227	-13.9933902793874*
Jacobi Constant of Orbit (actual periodic orbit)	3.04688426854973	3.04688426854973

*Negative Time of Flight indicates propagated backwards in time.

B.1.4 Case 4

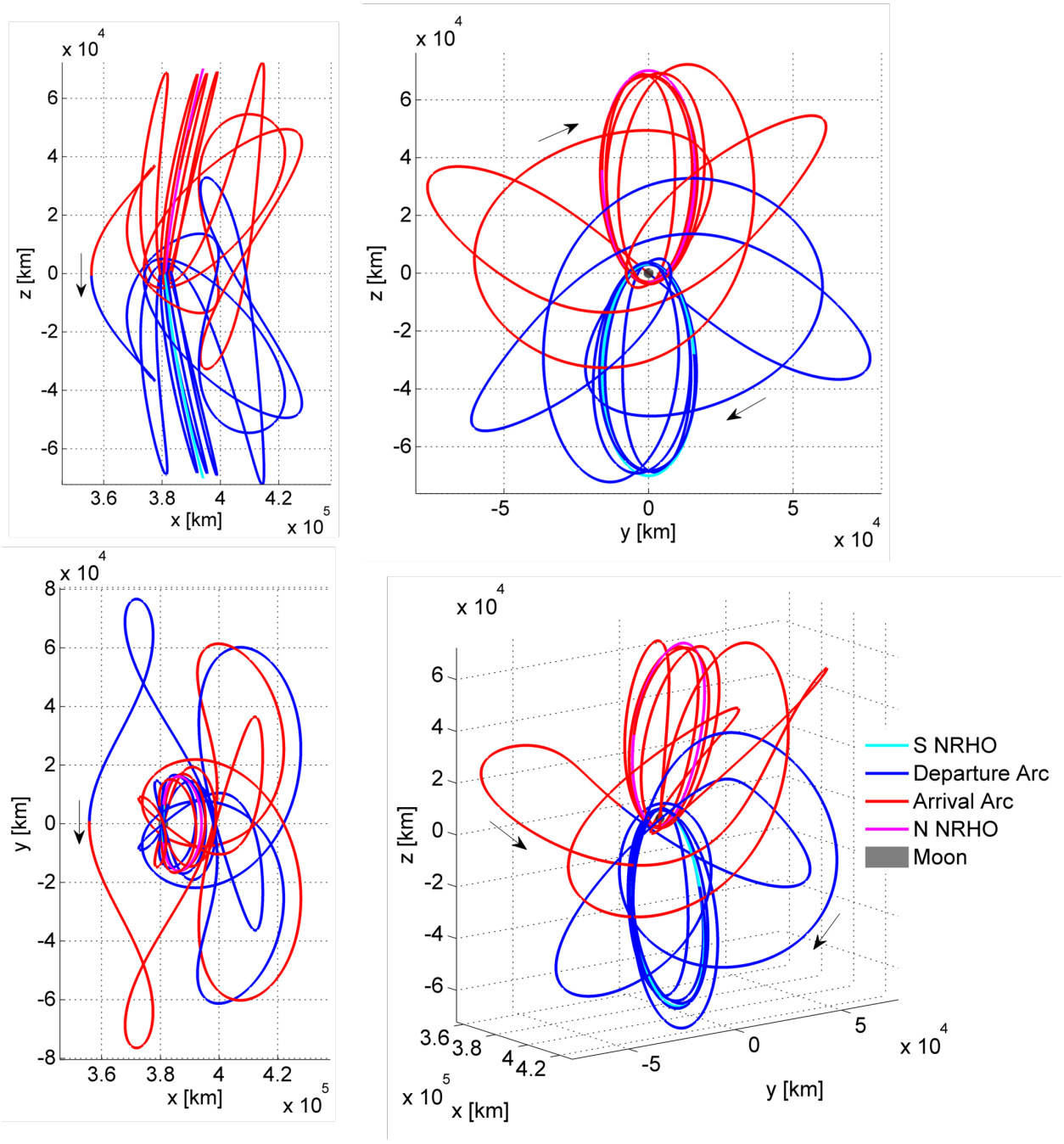

Figure B.4. Locally optimal transfer between L2 southern 9:2 synodic resonant NRHO to L2 northern 9:2 synodic resonant NRHO. Different views for Case 4 transfer.

Table B.4. Initial conditions for transfer from southern 9:2 synodic resonant NRHO to northern 9:2 synodic resonant NRHO (Case 4). Units are in non-dimensional quantities. System mass ratio, $\mu = 0.0121505856096240$.

Initial Conditions	Departure	Arrival
x	0.997585395785009	1.00119900179446
y	0.0407684688219149	-0.0417268385925357
z	-0.0726228210591917	0.0924214359932831
$\dot{x}$	0.0814567143566033	-0.0764649440469417
$\dot{y}$	0.0425379205328191	0.00325680735208123
$\dot{z}$	-0.421764526842971	-0.354274133244900
Time of Flight	14.2863046238343	-14.2490128883756*
Jacobi Constant of Orbit (actual periodic orbit)	3.04688426854973	3.04688426854973

*Negative Time of Flight indicates propagated backwards in time.

B.1.5 Case 5

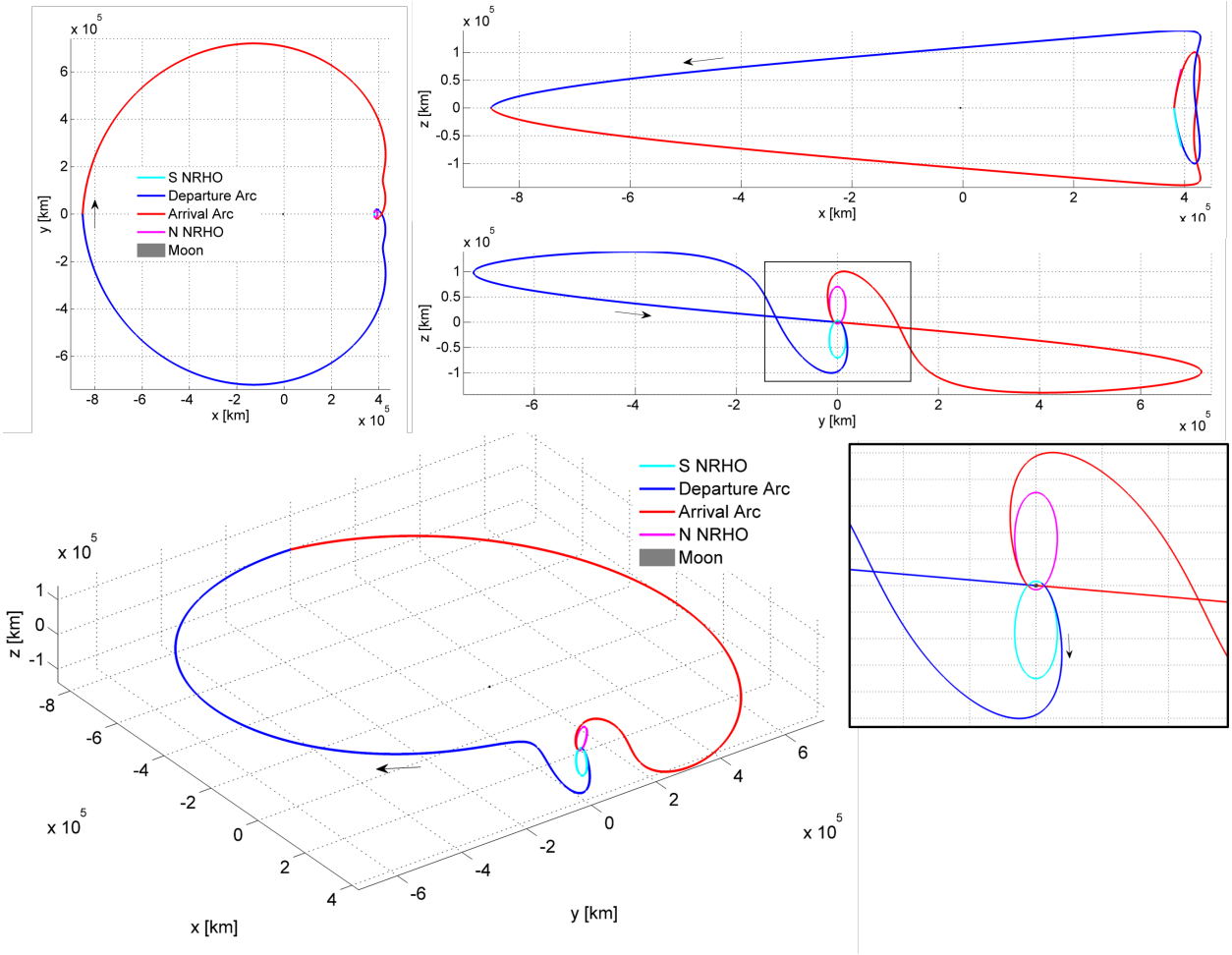

Figure B.5. Locally optimal transfer between L2 southern 9:2 synodic resonant NRHO to L2 northern 9:2 synodic resonant NRHO. Different views for Case 5 transfer.

Table B.5. Initial conditions for transfer from southern 9:2 synodic resonant NRHO to northern 9:2 synodic resonant NRHO (Case 5). Units are in non-dimensional quantities. System mass ratio, $\mu = 0.0121505856096240$.

Initial Conditions	Departure	Arrival
x	0.987677242859851	0.987680776491148
y	0.0108636783679917	-0.0109270397902264
z	0.00455536446415919	-0.00451106342660414
$\dot{x}$	0.0784105615398571	-0.0786710467228080
$\dot{y}$	1.16585917450435	1.16139230499477
$\dot{z}$	0.816501298281286	-0.818424061405115
Time of Flight	8.47580808928797	-8.47538884016890*
Jacobi Constant of Orbit (actual periodic orbit)	3.04688426854973	3.04688426854973

*Negative Time of Flight indicates propagated backwards in time.

B.1.6 Case 6

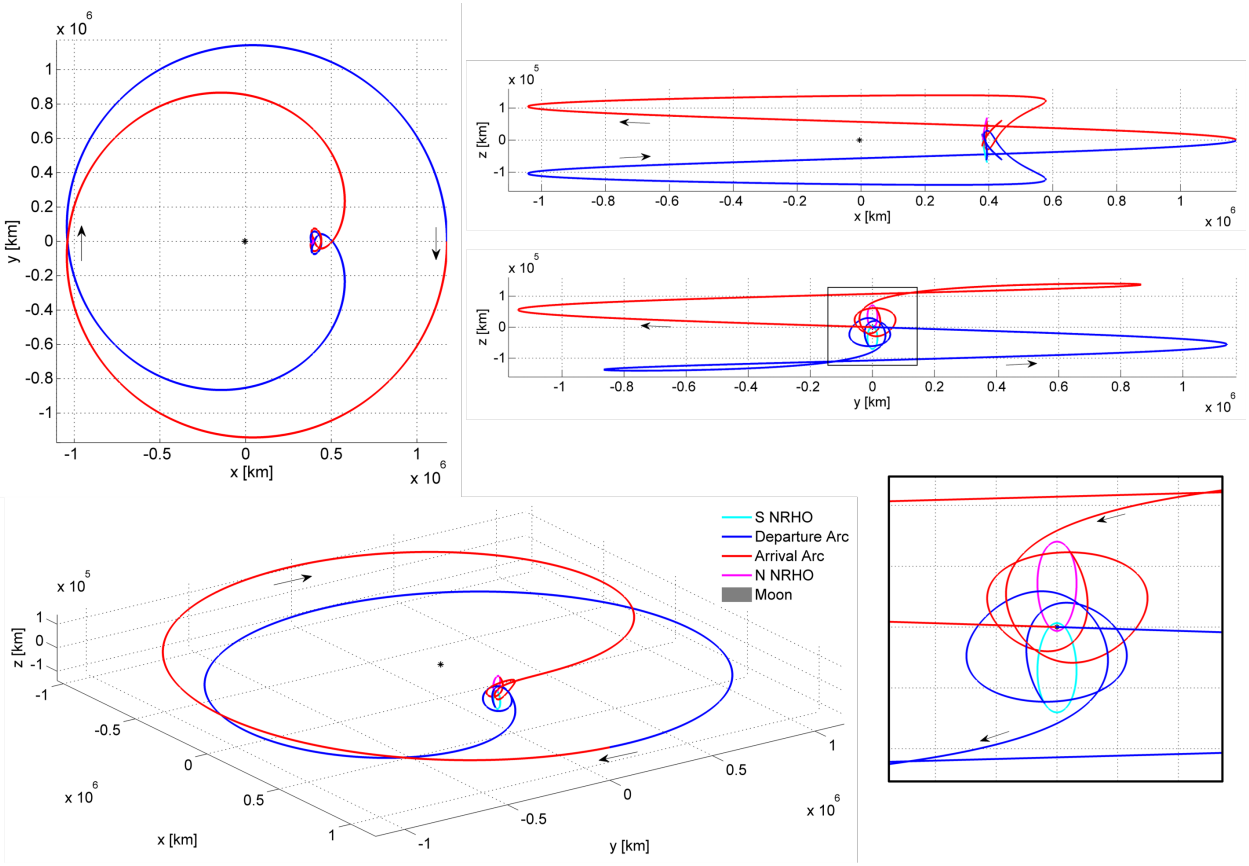

Figure B.6. Locally optimal transfer between L2 southern 9:2 synodic resonant NRHO to L2 northern 9:2 synodic resonant NRHO. Different views for Case 6 transfer.

Table B.6. Initial conditions for transfer from southern 9:2 synodic resonant NRHO to northern 9:2 synodic resonant NRHO (Case 6). Units are in non-dimensional quantities. System mass ratio, $\mu = 0.0121505856096240$.

Initial Conditions	Departure	Arrival
x	1.01678542032983	1.01677806499935
y	-0.0263863087739202	0.0264039713860751
z	-0.162730657384864	0.162700990464794
$\dot{x}$	0.0494346171742251	-0.0494405994312133
$\dot{y}$	-0.138322298439335	-0.138307894550286
$\dot{z}$	0.187619645555199	0.187711975122798
Time of Flight	13.3899567722745	-13.3880639470579*
Jacobi Constant of Orbit (actual periodic orbit)	3.04688426854973	3.04688426854973

*Negative Time of Flight indicates propagated backwards in time.

B.2 L2 Southern 9:2 synodic resonant NRHO to 70000 km DRO

B.2.1 Case 1

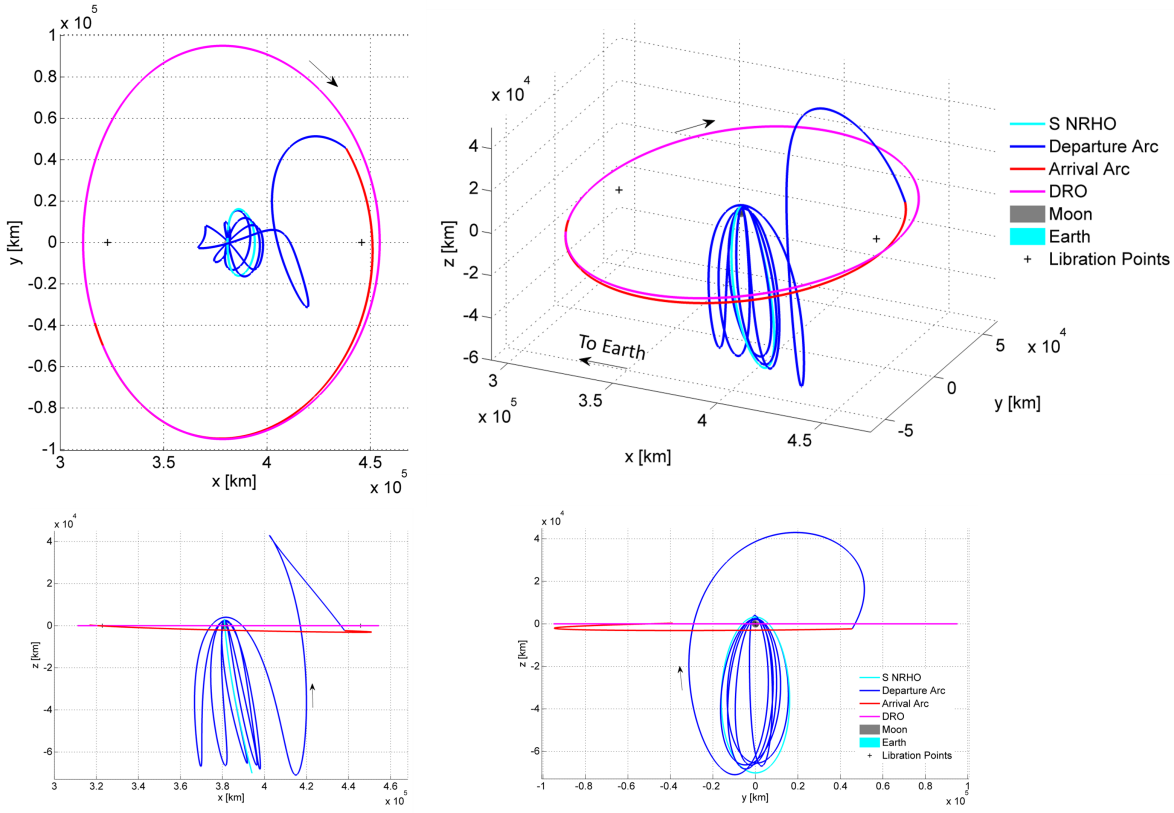

Figure B.7. Locally optimal transfer between L2 southern 9:2 synodic resonant NRHO to 70000 km DRO. Different views for Case 1 transfer.

Table B.7. Initial conditions for transfer from southern 9:2 synodic resonant NRHO to 70000 km DRO (Case 1). Units are in non-dimensional quantities. System mass ratio, $\mu = 0.0121505856096240$.

Initial Conditions	Departure	Arrival
x	0.987465964929823	0.831128407862951
y	0.00569889848311919	-0.129088519251505
z	0.00726850919845108	2.36019311830857e-17
$\dot{x}$	0.0405039953182051	-0.175128524392178
$\dot{y}$	1.49500514185298	0.423135920465187
$\dot{z}$	-0.533431374687675	0.0112509791037591
Time of Flight	10.1784261517383	-1.59562871619429*
Jacobi Constant of Orbit (actual periodic orbit)	3.04688426854973	2.928898812886901

*Negative Time of Flight indicates propagated backwards in time.

B.2.2 Case 2

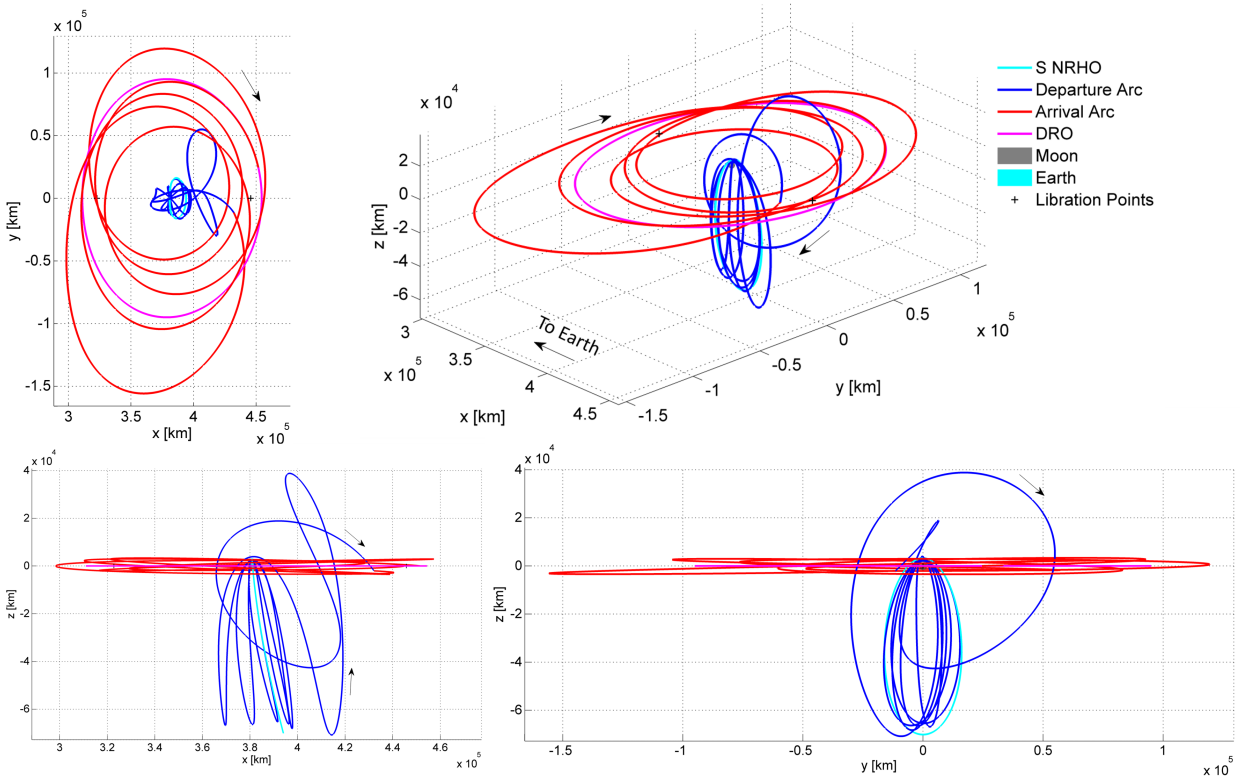

Figure B.8. Locally optimal transfer between L2 southern 9:2 synodic resonant NRHO to 70000 km DRO. Different views for Case 2 transfer.

Table B.8. Initial conditions for transfer from southern 9:2 synodic resonant NRHO to 70000 km DRO (Case 2). Units are in non-dimensional quantities. System mass ratio, $\mu = 0.0121505856096240$.

Initial Conditions	Departure	Arrival
x	0.987392663246718	1.17115183589483
y	0.00115286570760283	0.0636763654251231
z	0.00824153383943731	1.57414296983634e-16
$\dot{x}$	0.00892967502412152	0.104051085290240
$\dot{y}$	1.67144220641279	-0.463563083233762
$\dot{z}$	-0.119352157567163	-0.0118431057512588
Time of Flight	11.5237783505073	-14.7766373384885*
Jacobi Constant of Orbit (actual periodic orbit)	3.04688426854973	2.928898812886901

*Negative Time of Flight indicates propagated backwards in time.

B.2.3 Case 3

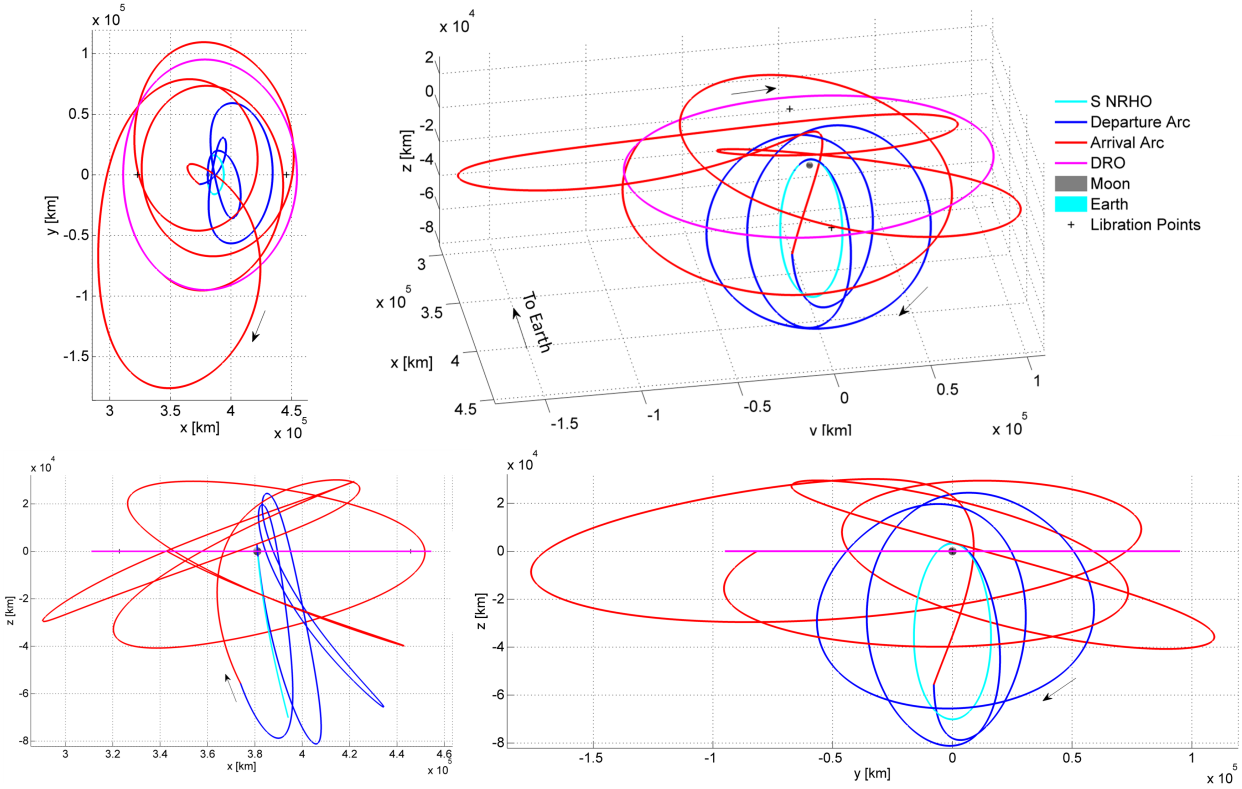

Figure B.9. Locally optimal transfer between L2 southern 9:2 synodic resonant NRHO to 70000 km DRO. Different views for Case 3 transfer.

Table B.9. Initial conditions for transfer from southern 9:2 synodic resonant NRHO to 70000 km DRO (Case 3). Units are in non-dimensional quantities. System mass ratio, $\mu = 0.0121505856096240$.

Initial Conditions	Departure	Arrival
x	0.988551201350836	0.889028163932655
y	-0.0204724150921124	-0.211506195086796
z	-0.00553926825167542	-1.16735942032396e-15
$\dot{x}$	-0.0819628226520406	-0.245707024002011
$\dot{y}$	0.585607691782095	0.235286934263236
$\dot{z}$	0.852843242907566	0.137410569368001
Time of Flight	6.48043596665455	-11.3854792340414*
Jacobi Constant of Orbit (actual periodic orbit)	3.04688426854973	2.928898812886901

*Negative Time of Flight indicates propagated backwards in time.

B.2.4 Case 4

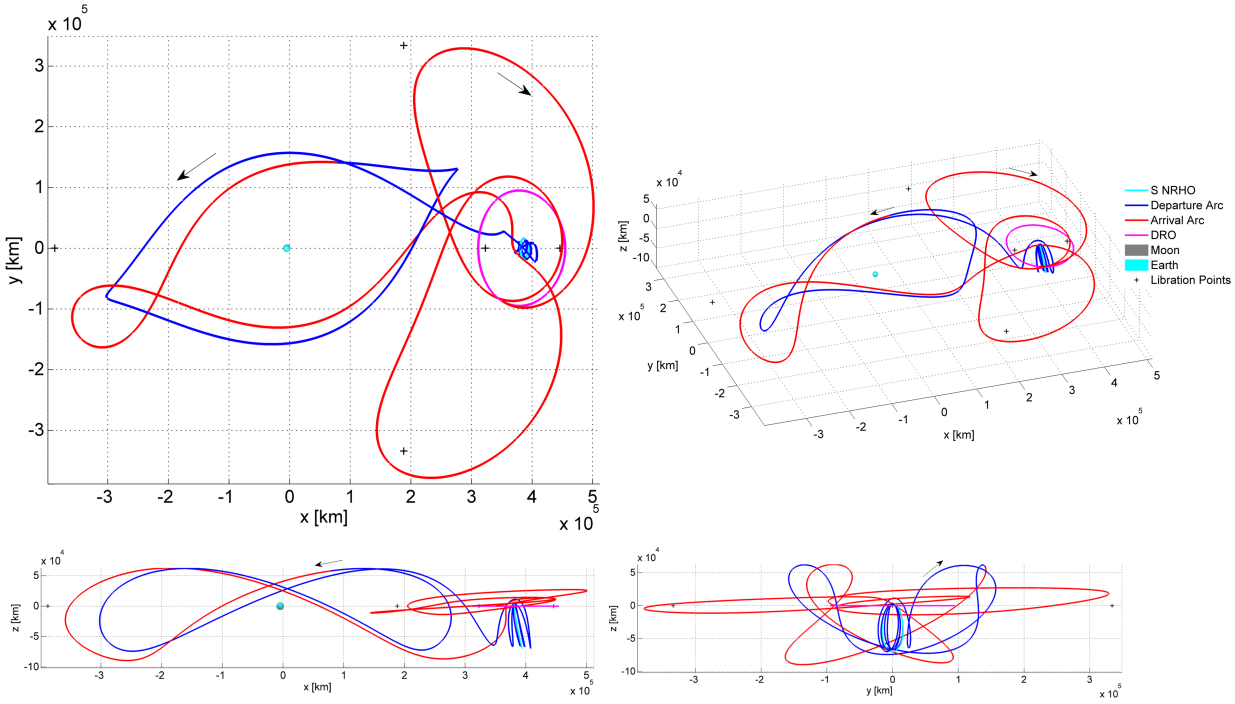

Figure B.10. Locally optimal transfer between L2 southern 9:2 synodic resonant NRHO to 70000 km DRO. Different views for Case 4 transfer.

Table B.10. Initial conditions for transfer from southern 9:2 synodic resonant NRHO to 70000 km DRO (Case 4). Units are in non-dimensional quantities. System mass ratio, $\mu = 0.0121505856096240$.

Initial Conditions	Departure	Arrival
x	0.990688244878795	0.909052731244116
y	0.0305734543621851	-0.225949250841337
z	-0.0256217912635845	5.17460897807125e-16
$\dot{x}$	0.0699105322208542	-0.367262135943777
$\dot{y}$	0.242537453261026	0.235784680933430
$\dot{z}$	-0.661412159026507	-0.0746143551062893
Time of Flight	14.4690304979927	-18.0583317924120*
Jacobi Constant of Orbit (actual periodic orbit)	3.04688426854973	2.928898812886901

*Negative Time of Flight indicates propagated backwards in time.

B.2.5 Case 5

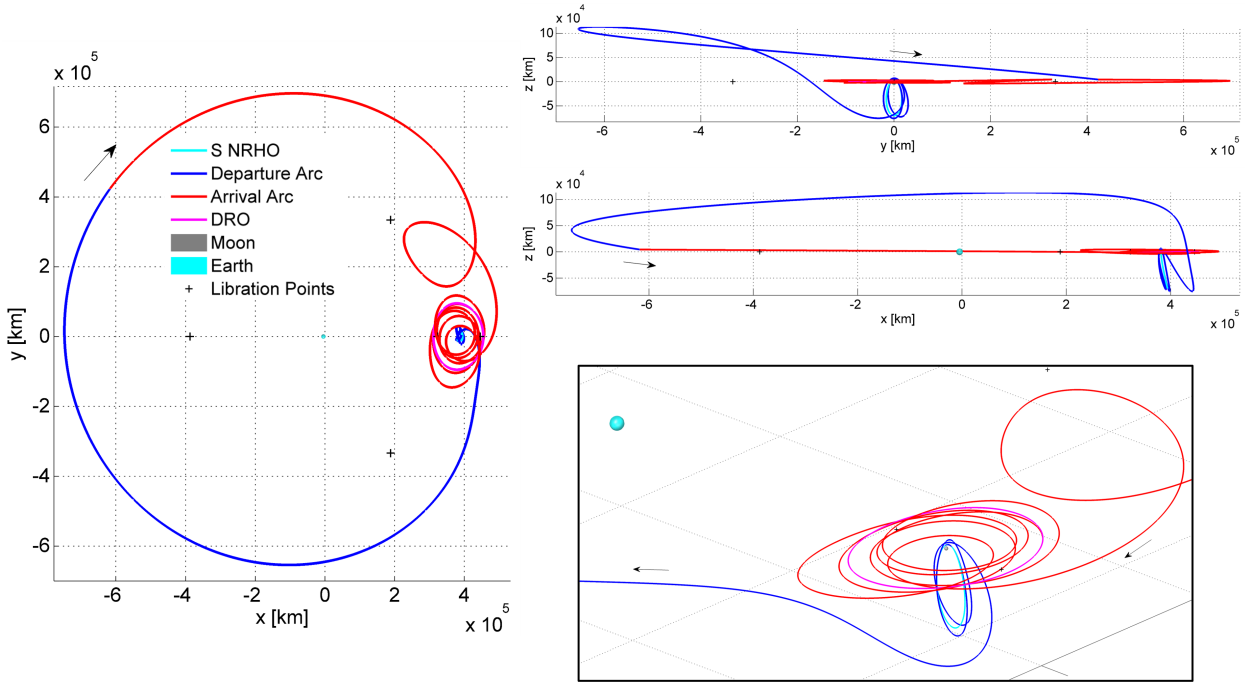

Figure B.11. Locally optimal transfer between L2 southern 9:2 synodic resonant NRHO to 70000 km DRO. Different views for Case 5 transfer.

Table B.11. Initial conditions for transfer from southern 9:2 synodic resonant NRHO to 70000 km DRO (Case 5). Units are in non-dimensional quantities. System mass ratio, $\mu = 0.0121505856096240$.

Initial Conditions	Departure	Arrival
x	0.987410554286670	1.12388657855707
y	-0.00300100599479989	0.167001113427257
z	0.00800243476650756	-7.75128320361883e-17
$\dot{x}$	-0.0228813151980173	0.259409042967061
$\dot{y}$	1.63238967450688	-0.339580098749030
$\dot{z}$	0.305468151095097	0.00941421254137988
Time of Flight	12.4552839786378	-25.5514174249027*
Jacobi Constant of Orbit (actual periodic orbit)	3.04688426854973	2.928898812886901

*Negative Time of Flight indicates propagated backwards in time.

B.2.6 Case 6

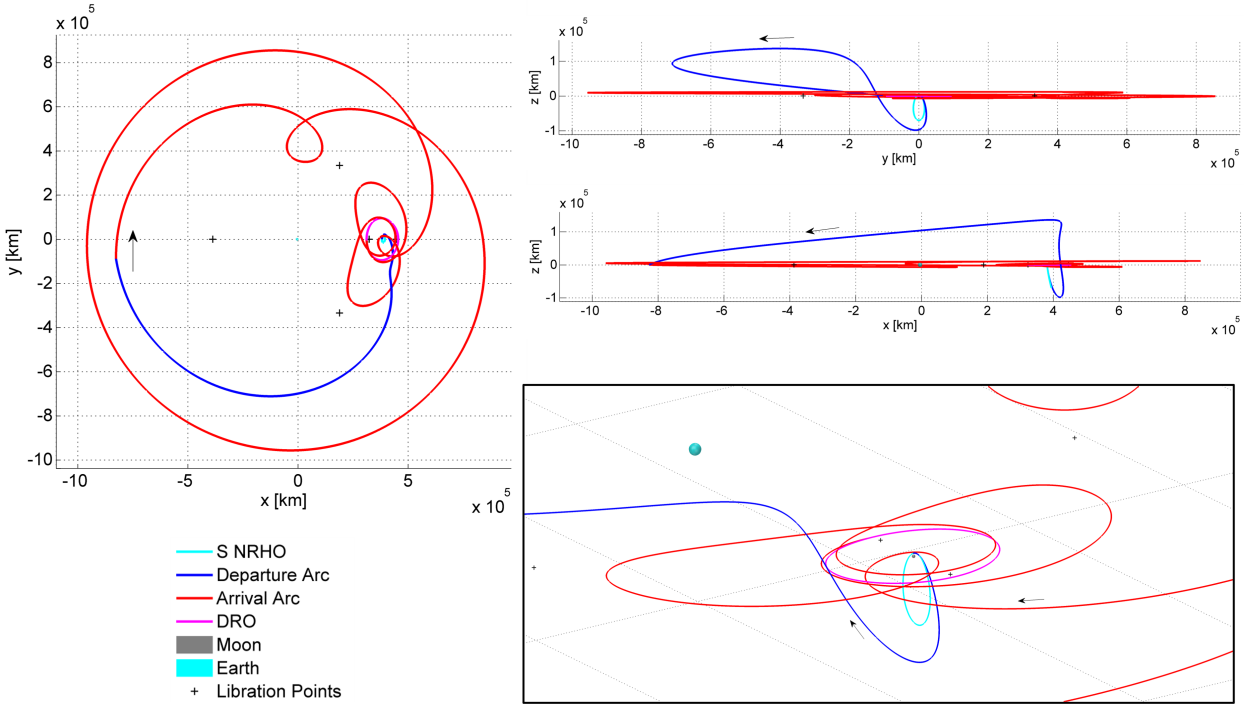

Figure B.12. Locally optimal transfer between L2 southern 9:2 synodic resonant NRHO to 70000 km DRO. Different views for Case 6 transfer.

Table B.12. Initial conditions for transfer from southern 9:2 synodic resonant NRHO to 70000 km DRO (Case 6). Units are in non-dimensional quantities. System mass ratio, $\mu = 0.0121505856096240$.

Initial Conditions	Departure	Arrival
x	0.987391056289568	0.806682694039108
y	-0.000798227279082206	-0.0154398139243511
z	0.00826306134414305	7.28329750026083e-17
$\dot{x}$	-0.00563738325189583	-0.0136768161615825
$\dot{y}$	1.69756053554677	0.549965430384287
$\dot{z}$	0.0848012399582023	-0.0124740069219296
Time of Flight	8.36465290574357	-29.9346586735286*
Jacobi Constant of Orbit (actual periodic orbit)	3.04688426854973	2.928898812886901

*Negative Time of Flight indicates propagated backwards in time.

B.3 L2 Southern 9:2 synodic resonant NRHO to 3000 km planar LO

B.3.1 Case 1

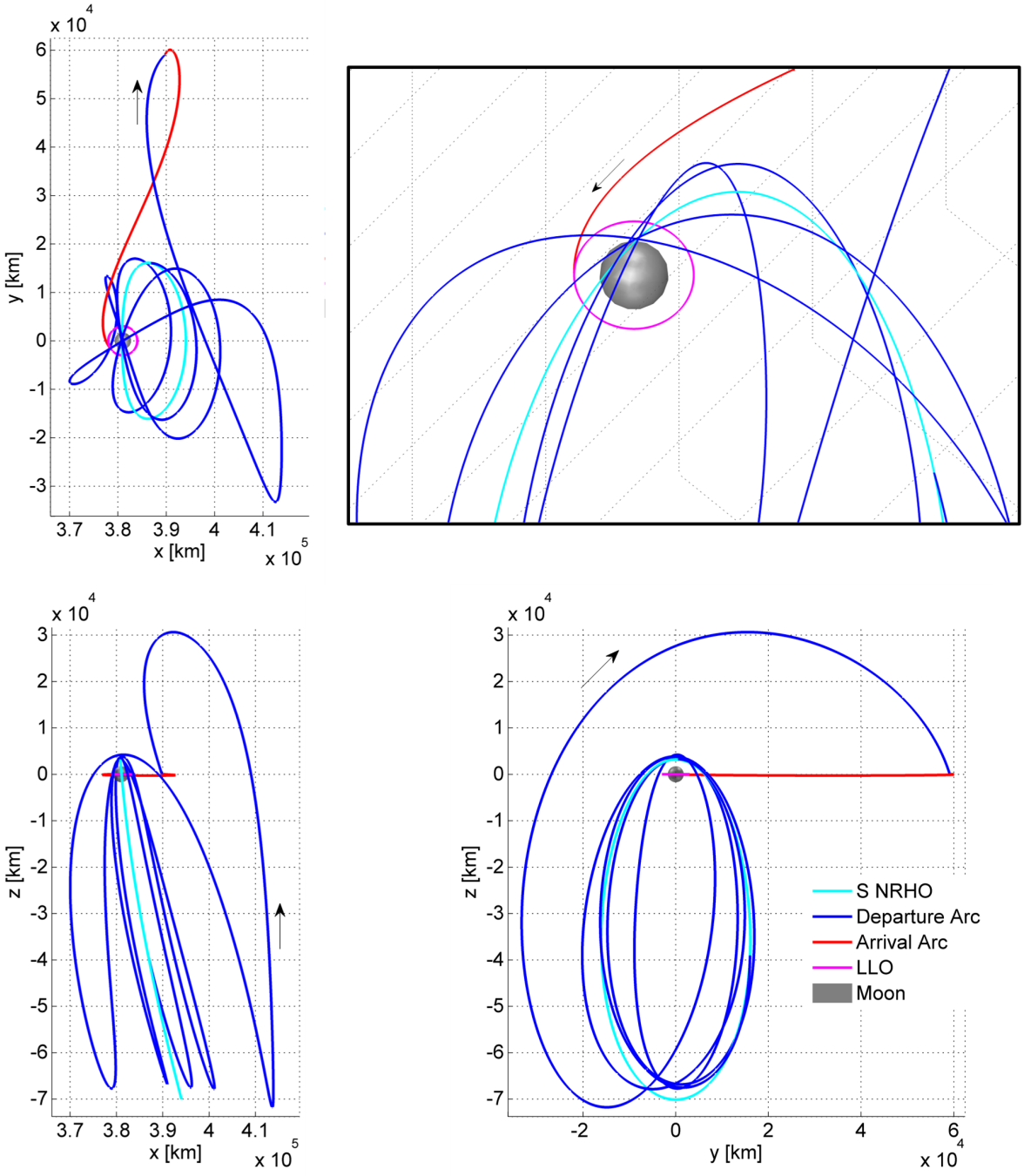

Figure B.13. Locally optimal transfer between L2 southern 9:2 synodic resonant NRHO to 3000 km planar LO. Different views for Case 1 transfer.

Table B.13. Initial conditions for transfer from southern 9:2 synodic resonant NRHO to 3000 km planar LO (Case 1). Units are in non-dimensional quantities. System mass ratio, $\mu = 0.0121505856096240$.

Initial Conditions	Departure	Arrival
x	1.00291966737244	0.982360356173907
y	0.0415711503488223	-0.00551126262660746
z	-0.101192022078972	-9.88767830586200e-17
$\dot{x}$	0.0754243847061982	1.22095419842515
$\dot{y}$	-0.00378200101900460	-1.21448152632087
$\dot{z}$	-0.321876965807617	0.0336592786873775
Time of Flight	8.32070349941637	-0.7490737481784898
Jacobi Constant of Orbit (actual periodic orbit)	3.04688426854973	4.533189223937852

*Negative Time of Flight indicates propagated backwards in time.

B.3.2 Case 2

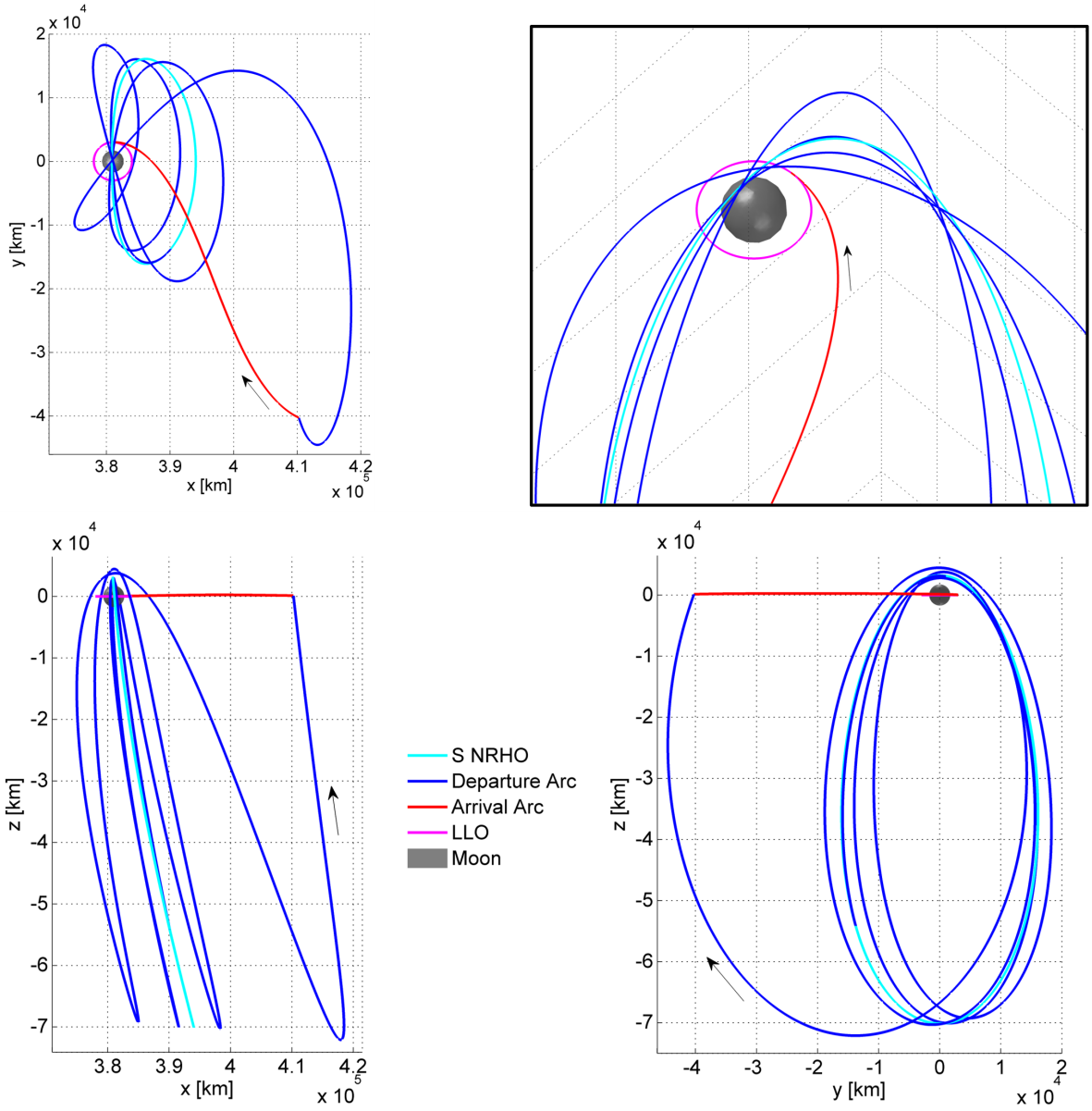

Figure B.14. Locally optimal transfer between L2 southern 9:2 synodic resonant NRHO to 3000 km planar LO. Different views for Case 2 transfer.

Table B.14. Initial conditions for transfer from southern 9:2 synodic resonant NRHO to 3000 km planar LO (Case 2). Units are in non-dimensional quantities. System mass ratio, $\mu = 0.0121505856096240$.

Initial Conditions	Departure	Arrival
x	1.01141626581046	0.987329129425057
y	-0.0356905594441245	0.00776106621332058
z	-0.140385594353981	1.52894056956217e-14
$\dot{x}$	-0.0462424225070656	-1.70803344258009
$\dot{y}$	-0.0588229623360150	-0.112824793010056
$\dot{z}$	0.219368446126931	-0.0335340022029626
Time of Flight	6.80281965879983	-0.382499417844114*
Jacobi Constant of Orbit (actual periodic orbit)	3.04688426854973	4.533189223937852

*Negative Time of Flight indicates propagated backwards in time.

B.3.3 Case 3

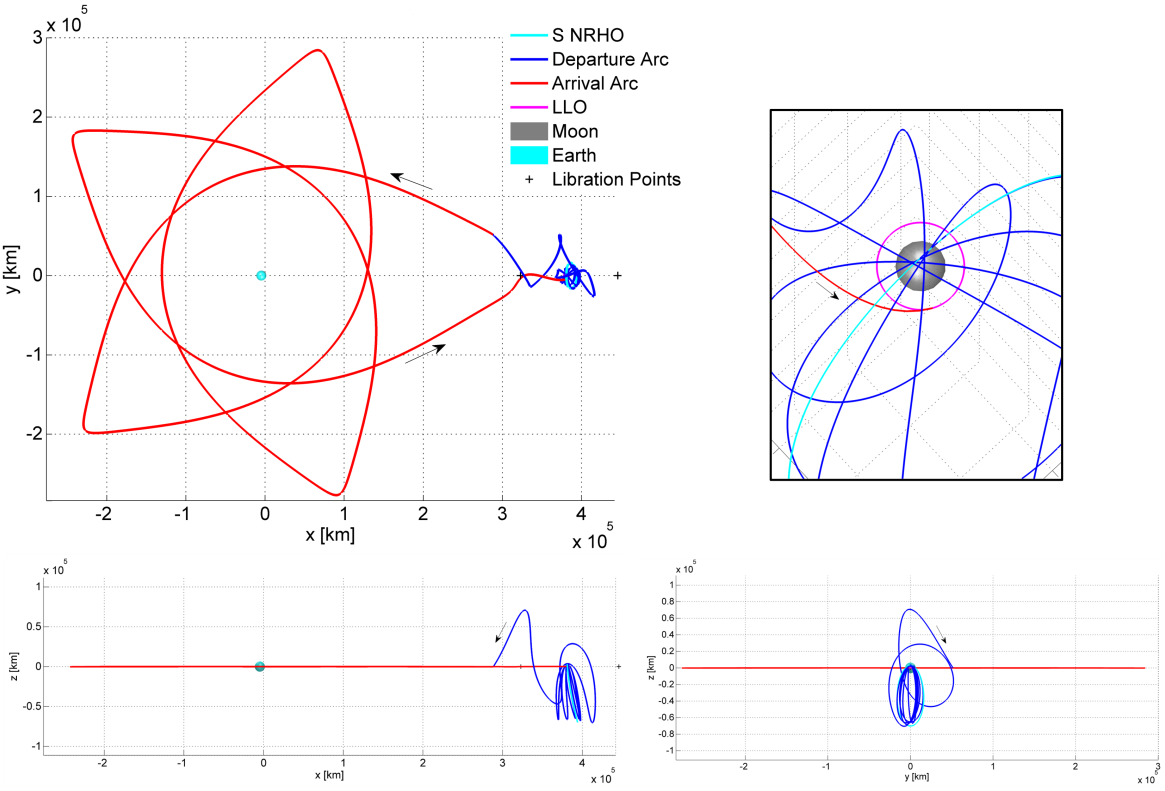

Figure B.15. Locally optimal transfer between L2 southern 9:2 synodic resonant NRHO to 3000 km planar LO. Different views for Case 3 transfer.

Table B.15. Initial conditions for transfer from southern 9:2 synodic resonant NRHO to 3000 km planar LO (Case 3). Units are in non-dimensional quantities. System mass ratio, $\mu = 0.0121505856096240$.

Initial Conditions	Departure	Arrival
x	0.987389585564703	0.994781235894483
y	-5.95466228640473e-05	-0.00352730214343487
z	0.00828277135063308	-1.54615607481677e-17
$\dot{x}$	-0.000477819679628032	0.772968239236952
$\dot{y}$	1.67967135506298	1.51616258348722
$\dot{z}$	0.00589836217491506	-0.0157812992177517
Time of Flight	12.6192525256121	-14.0511647235291*
Jacobi Constant of Orbit (actual periodic orbit)	3.04688426854973	4.533189223937852

*Negative Time of Flight indicates propagated backwards in time.

B.3.4 Case 4

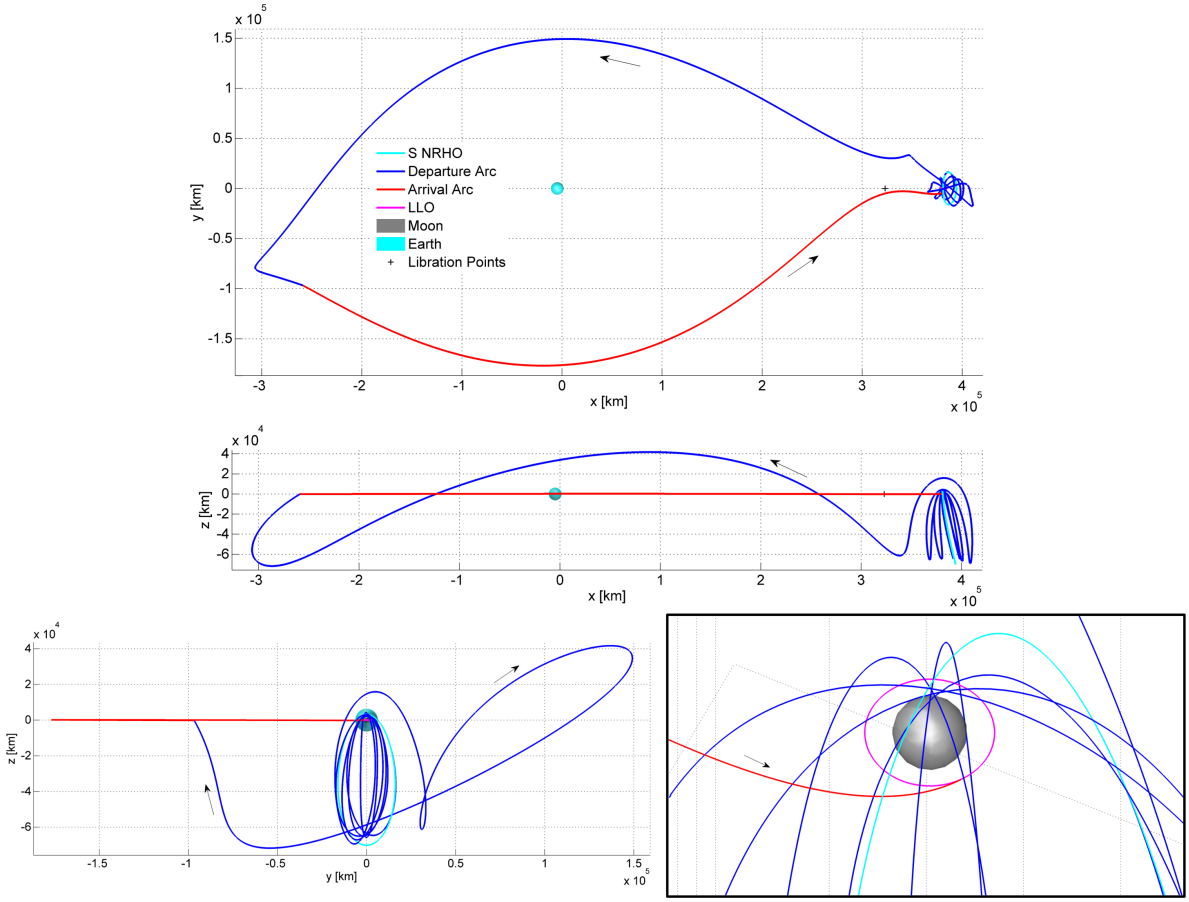

Figure B.16. Locally optimal transfer between L2 southern 9:2 synodic resonant NRHO to 3000 km planar LO. Different views for Case 4 transfer.

Table B.16. Initial conditions for transfer from southern 9:2 synodic resonant NRHO to 3000 km planar LO (Case 4). Units are in non-dimensional quantities. System mass ratio, $\mu = 0.0121505856096240$.

Initial Conditions	Departure	Arrival
x	0.992359520763295	0.994522887113118
y	0.0347667279847131	-0.00399468443341923
z	-0.0387581417955332	3.45272122761889e-16
$\dot{x}$	0.0668759531970413	0.887435040103149
$\dot{y}$	0.163386368728969	1.48651759402216
$\dot{z}$	-0.567103159069688	0.0251740448558707
Time of Flight	13.6240734164924	-2.42779552866416*
Jacobi Constant of Orbit (actual periodic orbit)	3.04688426854973	4.533189223937852

*Negative Time of Flight indicates propagated backwards in time.

VITA

Vivek Muralidharan graduated with a Bachelor of Technology in Mechanical Engineering from the National Institute of Technology Karnataka, Surathkal, India in May 2015. He moved to Purdue University in August 2015 to pursue a Master's in Aeronautics and Astronautics, where he eventually joined Professor Kathleen Howell's Multi-Body Dynamics Research Group. Vivek worked on stationkeeping strategies for the Sun-Earth libration point missions during his masters. In January of 2018, Vivek began his doctoral studies investigating the underlying dynamical structures that assist in stationkeeping and transfer trajectory design. His Ph.D. program was financially supported by the Purdue University Minority Engineering Program. During his graduate career, Vivek interned at the Indian Institute of Space Science and Technology (2016) and Mitsubishi Electric Research Laboratories (MERL) in Massachusetts (2019). Upon graduation, Vivek will join as a Research Associate in vision-based autonomous satellite navigation at the Interdisciplinary Centre for Security, Reliability and Trust (SnT), Université du Luxembourg.